OFFICE OF CIVILIAN RADIOACTIVE WASTE MANAGEMENT
ANALYSIS/MODEL COVER SHEET
Complete Only Applicable Items

1. QA: QA

☐ Analysis — Check all that apply

Type of Analysis:
- ☐ Engineering
- ☐ Performance Assessment
- ☐ Scientific

Intended Use of Analysis:
- ☐ Input to Calculation
- ☐ Input to another Analysis or Model
- ☐ Input to Technical Document
- ☐ Input to other Technical Products

Describe use:

3. ☒ Model — Check all that apply

Type of Model:
- ☐ Conceptual Model
- ☐ Abstraction Model
- ☐ Mathematical Model
- ☐ System Model
- ☒ Process Model

Intended Use of Model:
- ☐ Input to Calculation
- ☒ Input to another Model or Analysis
- ☐ Input to Technical Document
- ☒ Input to other Technical Products

Describe use:

Direct feed to EBS PMR and EBS P&CE Performance Assessment Abstraction Model.

4. Title:

Engineered Barrier System: Physical and Chemical Environment Model

5. Document Identifier (including Rev. No. and Change No., if applicable):

ANL-EBS-MD-000033, REV 00

6. Total Attachments:

18

7. Attachment Numbers - No. of Pages in Each:

I.(13)	II.(3)	III.(5)	IV.(2)	V.(2)	VI.(59)
VII.(69)	VIII.(14)	IX.(38)	X.(8)	XI.(9)	XII.(5)
XIII.(3)	XIV.(7)	XV.(7)	XVI.(7)	XVII.(3)	XVIII.(6)

	Printed Name	Signature	Date
8. Originator	Ernest L. Hardin	E L Hardin	5/12/00
9. Checker	Terry Steinborn	[illegible]	5/12/00
10. Lead/Supervisor	Dwayne A. Chesnut	Dwayne A. Chesnut	5/12/2000
11. Responsible Manager	Dwayne A. Chesnut	Dwayne A. Chesnut	5/12/2000

12. Remarks:

The Following TBV apply to this analysis/model:
TBV-3901, TBV-3471, TBV-3599, TBV-3073, TBV-4475, TBV-4476, TBV-4477, TBV-4478, TBV-4479, TBV-4480, TBV-4481, TBV-4482, TBV-3826, TBV-3588, TBV-3610, TBV-3828, TBV-3902, TBV-4575, TBV-4576, TBV-4586, TBV-4587, TBV-4588, TBV-4623, TBV-4624, TBV-4625, TBV-4626, TBV-3428, TBV-4621, TBV-4628, TBV-3502, TBV-3596, TBV-3904, TBV-3905.

1 CD-ROM is included as part of Attachment I.

WM-11
NH55D7

DISCLAIMER

This contractor document was prepared for the U.S. Department of Energy (DOE), but has not undergone programmatic, policy, or publication review, and is provided for information only. The document provides preliminary information that may change based on new information to be used specifically for Total System Performance Assessment analyses. The document is a preliminary lower-level contractor document and is not intended for publication or wide distribution.

Although this document has undergone technical reviews at the contractor organization, it has not undergone a DOE policy review. Therefore, the views and options of authors expressed may not state or reflect those of the DOE. However, in the interest of the rapid transfer of information, we are providing this document for your information per your request.

OFFICE OF CIVILIAN RADIOACTIVE WASTE MANAGEMENT
ANALYSIS/MODEL COVER SHEET
Complete Only Applicable Items

1. QA: QA

☐ Analysis	Check all that apply	3. ☒ Model	Check all that apply
Type of Analysis	☐ Engineering ☐ Performance Assessment ☐ Scientific	Type of Model	☐ Conceptual Model ☐ Abstraction Model ☐ Mathematical Model ☐ System Model ☒ Process Model
Intended Use of Analysis	☐ Input to Calculation ☐ Input to another Analysis or Model ☐ Input to Technical Document ☐ Input to other Technical Products	Intended Use of Model	☐ Input to Calculation ☒ Input to another Model or Analysis ☐ Input to Technical Document ☒ Input to other Technical Products
Describe use:		Describe use:	Direct feed to EBS PMR and EBS P&CE Performance Assessment Abstraction Model.

4. Title:

Engineered Barrier System: Physical and Chemical Environment Model

5. Document Identifier (including Rev. No. and Change No., if applicable):

ANL-EBS-MD-000033, REV 00

6. Total Attachments:

18

7. Attachment Numbers - No. of Pages in Each:

I.(13)	II.(3)	III.(5)	IV.(2)	V.(2)	VI.(59)
VII.(69)	VIII.(14)	IX.(38)	X.(8)	XI.(9)	XII.(5)
XIII.(3)	XIV.(7)	XV.(7)	XVI.(7)	XVII.(3)	XVIII.(6)

	Printed Name	Signature	Date
8. Originator	Ernest L. Hardin	E L Hardin	5/12/00
9. Checker	Terry Steinborn	[illegible]	5/12/00
10. Lead/Supervisor	Dwayne A. Chesnut	Dwayne A. Chesnut	5/12/2000
11. Responsible Manager	Dwayne A. Chesnut	Dwayne A. Chesnut	5/12/2000

12. Remarks:

The Following TBV apply to this analysis/model:
TBV-3901, TBV-3471, TBV-3599, TBV-3073, TBV-4475, TBV-4476, TBV-4477, TBV-4478, TBV-4479, TBV-4480, TBV-4481, TBV-4482, TBV-3826, TBV-3588, TBV-3610, TBV-3828, TBV-3902, TBV-4575, TBV-4576, TBV-4586, TBV-4587, TBV-4588, TBV-4623, TBV-4624, TBV-4625, TBV-4626, TBV-3428, TBV-4621, TBV-4628, TBV-3502, TBV-3596, TBV-3904, TBV-3905.

1 CD-ROM is included as part of Attachment I.

INFORMATION COPY
LAS VEGAS DOCUMENT CONTROL

OFFICE OF CIVILIAN RADIOACTIVE WASTE MANAGEMENT
ANALYSIS/MODEL REVISION RECORD

Complete Only Applicable Items

2. . Analysis or Model Title:

Engineered Barrier System: Physical and Chemical Environment Model

3. Document Identifier (including Rev. No. and Change No., if applicable):

ANL-EBS-MD-000033, REV 00

4. Revision/Change No.	5. Description of Revision/Change
00	Initial issue.

CONTENTS

Page

1. PURPOSE 17

2. QUALITY ASSURANCE 17

3. COMPUTER SOFTWARE AND MODEL USAGE 18
   3.1 THERMAL HYDROLOGY MODEL 18
      3.1.1 Description of TH Software 25
      3.1.2 Description of TH Software Routines 25
   3.2 GAS FLUX AND FUGACITY MODEL 29
   3.3 CEMENTITIOUS MATERIALS MODEL 30
   3.4 MICROBIAL EFFECTS MODEL 31
   3.5 NORMATIVE PRECIPITATES AND SALTS MODEL 31
   3.6 EBS COLLOIDS MODEL 31
   3.7 CHEMICAL REFERENCE MODEL 32

4. INPUTS 33
   4.1 DATA AND PARAMETERS 33
      4.1.1 Thermal Hydrology Model 33
      4.1.2 Gas Flux and Fugacity Model 45
      4.1.3 Cementitious Materials Model 48
      4.1.4 Microbial Effects Model 52
      4.1.5 Normative Precipitates and Salts Model 53
      4.1.6 EBS Colloids Model 55
      4.1.7 Chemical Reference Model 59
   4.2 CRITERIA 63
   4.3 CODES AND STANDARDS 63

5. ASSUMPTIONS 64
   5.1 THERMAL HYDROLOGY MODEL 64
      5.1.1 Effective Tortuosity Factor 64
      5.1.2 Homogeneous Fracture Continuum 64
      5.1.3 Component Properties 66
      5.1.4 Zero Dispersion Coefficients 66
      5.1.5 Preclosure Ventilation Effects 67
      5.1.6 Environmental Conditions that Promote Corrosion of Drip Shield and Waste Package 67
   5.2 GAS FLUX AND FUGACITY MODEL 67
      5.2.1 Steady-State Gas-Phase Mass-Transfer Conditions 67
      5.2.2 Vertical, One-Dimensional Gas-Phase Transport 68
      5.2.3 J-13 Water Composition 68
      5.2.4 Limited Interaction of CO_2 with Solid-Phase Species 68
      5.2.5 Representative Fracture Porosity and Aqueous Volume Fraction 69
      5.2.6 Average Temperature of the UZ 69

CONTENTS (CONTINUED)

Page

5.3 CEMENTITIOUS MATERIALS MODEL 69
5.3.1 Cement Mineral Assemblage 69
5.3.2 Extent of Carbonation 70
5.3.3 Tobermorite Analogue for Other Cement Phases 70
5.3.4 Stability of Cement Phases 70
5.3.5 Water-Grout Chemical Reaction 71
5.3.6 Thermodynamic Data for Cementitious Materials Model 71
5.3.7 Biotic and Organic Processes 71
5.3.8 Grout Permeability 72
5.3.9 Equilibrium with Quartz Sand 72
5.4 MICROBIAL EFFECTS MODEL 72
5.4.1 Electrical Equipment and Removal of Organics 72
5.4.2 Purity of Backfill and Invert Materials 72
5.4.3 Organic Carbon Content of Host Rock 73
5.4.4 Microbial Growth and Activity on Waste-Package Surface 73
5.4.5 Microbial Effect on Carbon Steel Corrosion Rate 73
5.5 NORMATIVE PRECIPITATES AND SALTS MODEL 74
5.5.1 Portlandite vs. Calcite 74
5.6 EBS COLLOIDS MODEL 74
5.6.1 Size Distribution of Ferric Iron Colloids 74
5.6.2 Spherical Particles 74
5.7 CHEMICAL REFERENCE MODEL 74
5.7.1 Congruent Redissolution and Limited Ionic Strength 74
5.7.2 Corrosion of A572 Structural Steel 75
5.7.3 Humidity Threshold for Corrosion of Structural Steel 75
5.7.4 Humidity Corrosion of Steel for Low-Water Conditions 76
5.7.5 Effects from Corrosion-Resistant Materials 76

6. ANALYSIS/MODEL 76
6.1 THERMAL HYDROLOGY MODEL 77
6.1.1 Thermal Hydrology Calculations Using NUFT 77
6.1.2 Postprocessing NUFT Output 79
6.1.3 Summary of NUFT Calculations and Postprocessing 83
6.1.4 Representing Thermal-Hydrologic Evolution by Uniform Time Intervals 91
6.1.5 Mass-Balance Calculation 91
6.1.6 Conservative Solute Analysis Using Zone Fluxes 92
6.1.7 Selection of a Thermal-Hydrologic Model for Reasonable-Bound Chemical Modeling 99
6.1.8 TH Model Validation 102
6.1.9 Alternative Models and Approaches 102
6.1.10 Summary 103
6.2 GAS FLUX AND FUGACITY MODEL 105
6.2.1 Conceptual Model 105

CONTENTS (CONTINUED)

Page

6.2.2 Background—Oxygen 109
6.2.3 Equilibrium Steady-State CO_2 Transport in the Unsaturated Zone 109
6.2.4 Results—Lower-Bound Estimates for CO_2 Concentration and Flux 123
6.2.5 Results–Lower-Bound Estimates for O_2 Concentration and Flux 123
6.2.6 Summary 125
6.3 CEMENTITIOUS MATERIALS MODEL 132
6.3.1 Grout Description and Evolution 132
6.3.2 Temperature and P_{CO2} Sensitivity 132
6.3.3 Grout Dissolution Rate 139
6.3.4 Flux Through Saturated Grout Cylinder 141
6.3.5 Flux-Scaling 143
6.3.6 Evolution of Leachate Composition 144
6.3.7 Cementitious Materials Model Validation 144
6.3.8 Summary 144
6.4 MICROBIAL EFFECTS MODEL 147
6.4.1 Introduction 147
6.4.2 Conceptual Models for Factors Limiting Microbial Activity 148
6.4.3 Conceptual Models for Microbially Induced Corrosion of Corrosion-Resistant Materials 152
6.4.4 Conceptual Models for Potential Interaction of Yucca Mountain Bacteria with Engineered Barrier System Materials 153
6.4.5 Threshold-Modeling Approach Based on Growth-Limiting Factors 157
6.4.6 Effects of Microbial Activity on the Bulk Physical and Chemical Environment 158
6.4.7 Microbial Effects Model Validation 159
6.4.8 Summary 159
6.5 NORMATIVE PRECIPITATES AND SALTS MODEL 160
6.5.1 Conceptual Model 160
6.5.2 Evaporation Tests with Synthetic J-13 Water and Synthetic Porewater 161
6.5.3 Test Results for Synthetic J-13 Water 169
6.5.4 Test Results for Synthetic Porewater 170
6.5.5 Normative Concept and Predictive Model 171
6.5.6 Supporting Discussion of Mineral Assemblage Stability 173
6.5.7 Application of Normative Model to Laboratory Test Results 179
6.5.8 Normative Model Validation 181
6.5.9 Summary 182
6.6 EBS COLLOIDS MODEL 183
6.6.1 Introduction 183
6.6.2 Conceptual Model 184
6.6.3 Bounding Analysis 185
6.6.4 EBS Colloids Model Validation 196
6.7 CHEMICAL REFERENCE MODEL 196
6.7.1 Simulation of Water Composition in Zone 1/2 197

CONTENTS (CONTINUED)

Page

6.7.2 Simulation of Mineral Precipitation and Water Composition in Zone 3/4 200
6.7.3 Simulation of Mineral Precipitation and Water Composition in Zone 5/6 205
6.7.4 Scoping Calculation of Oxygen Demand 209
6.7.5 Effects of Microbial Activity 211
6.7.6 Corrosion-Resistant Materials 211
6.7.7 CO_2 Consumption in the Engineered Barrier System 212
6.7.8 Chemical Reference Model Validation 214
6.7.9 Discussion and Summary of the Bulk Chemical Environment 215

7. CONCLUSIONS 217
7.1 THERMAL HYDROLOGY 218
7.2 GAS FLUX AND FUGACITY 219
7.3 CEMENTITIOUS MATERIALS 220
7.4 MICROBIAL EFFECTS 221
7.5 PRECIPITATES AND SALTS 222
7.6 COLLOIDS 223
7.7 CHEMICAL REFERENCE MODEL 224

8. INPUTS AND REFERENCES 227
8.1 DOCUMENTS CITED 227
8.2 CODES, STANDARDS, REGULATIONS, AND PROCEDURES 234
8.3 SOURCE DATA 235
8.3.1 Thermal Hydrology Model (See Section 6.1) 235
8.3.2 Gas Flux and Fugacity Model (See Section 6.2) 235
8.3.3 Cementitious Materials Model (See Section 6.3) 236
8.3.4 Microbial Effects Model (See Section 6.4) 237
8.3.5 Normative Precipitates and Salts Model (See Section 6.5) 237
8.3.6 EBS Colloids Model (See Section 6.6) 237
8.3.7 Chemical Reference Model (See Section 6.7) 238
8.4 SOFTWARE SOURCES 238

ATTACHMENT I LISTS OF ELECTRONIC FILES USED FOR EBS PHYSICAL AND CHEMICAL ENVIRONMENT MODEL DEVELOPMENT AND IMPLEMENTATION I-1

ATTACHMENT II SOFTWARE ROUTINE DOCUMENTATION FOR NUFT PRE-PROCESSORS: RME6 V1.1 ..... II-1

CONTENTS (Continued)

		Page
ATTACHMENT III	SOFTWARE ROUTINE DOCUMENTATION FOR NUFT PRE-PROCESSOR: COVER V1.1	III-1
ATTACHMENT IV	SOFTWARE ROUTINE DOCUMENTATION FOR NUFT PRE-PROCESSOR: COLUMNINFILTRATION V1.1	IV-1
ATTACHMENT V	SOFTWARE ROUTINE DOCUMENTATION FOR NUFT PRE-PROCESSORS: CHIM_SURF_TP V1.1 AND CHIM_WT_TP V1.1	V-1
ATTACHMENT VI	SOFTWARE ROUTINE DOCUMENTATION FOR NUFT POST PROCESSOR: MYPLOT V1.1	VI-1
ATTACHMENT VII	SOFTWARE ROUTINE DOCUMENTATION FOR NUFT POST PROCESSOR: ZONEAVG V1.2	VII-1
ATTACHMENT VIII	SOFTWARE ROUTINE DOCUMENTATION FOR NUFT POST PROCESSOR: VFLUXPROF V1.1	VIII-1
ATTACHMENT IX	SOFTWARE ROUTINE DOCUMENTATION FOR THERMAL-HYDROLOGY-GAS MODEL CALCULATION SPREADSHEETS	IX-1
ATTACHMENT X	SOFTWARE ROUTINE DOCUMENTATION FOR RUNGE-KUTTA SOLUTION ALGORITHM	X-1
ATTACHMENT XI	SOFTWARE ROUTINE DOCUMENTATION FOR SD-12 BOREHOLE ^{14}C ACTIVITY AND CO_2 ABUNDANCE DATA PLOTTING AND FITTING SPREADSHEET	XI-1
ATTACHMENT XII	SOFTWARE ROUTINE DOCUMENTATION FOR BOREHOLE ^{14}C ACTIVITY DATA PLOTTING AND FITTING SPREADSHEETS	XII-1

CONTENTS (Continued)

		Page
ATTACHMENT XIII	SOFTWARE ROUTINE DOCUMENTATION FOR LABORATORY EVAPORATION DATA NORMATIVE MINERAL ASSEMBLAGE SPREADSHEETS	XIII-1
ATTACHMENT XIV	SOFTWARE ROUTINE DOCUMENTATION FOR IN-DRIFT UPPER BACKFILL PREDICTIVE MODEL NORMATIVE MINERAL ASSEMBLAGE SPREADSHEETS	XIV-1
ATTACHMENT XV	SOFTWARE ROUTINE DOCUMENTATION FOR IN-DRIFT LOWER BACKFILL/INVERT PREDICTIVE MODEL NORMATIVE MINERAL ASSEMBLAGE SPREADSHEETS	XV-1
ATTACHMENT XVI	SOFTWARE ROUTINE DOCUMENTATION FOR MEASURED DATA FROM COLLOID SAMPLING	XVI-1
ATTACHMENT XVII	SOFTWARE ROUTINE DOCUMENTATION FOR SAND SURFACE AREA CALCULATION SPREADSHEET	XVII-1
ATTACHMENT XVIII	SOFTWARE ROUTINE DOCUMENTATION FOR CO_2 BALANCE CALCULATION SPREADSHEET	XVIII-1

FIGURES

Page

Figure 1. Path of Input and Output Data Through the Codes and Software Routines Used for Thermal Hydrology Calculations 24

Figure 2. Schematic Drawing Showing the Zones Defined for Chemical Modeling and the Connectivity of the Zones 80

Figure 3. Representation of Zone Boundaries in the Model Grid, Showing Boundaries Between Zones 1 through 6 80

Figure 4. Liquid Fluxes Between Zones for the L4C4 Location and the "Upper" Infiltration Distribution 81

Figure 5. Vertical Component of the Gas-Phase Total Mass Flux (Air and Water Vapor) Along a Vertical Profile Passing Through the Drift Center 83

Figure 6. Average Temperature for Zone 4 84

Figure 7. Average Saturation for Zone 4 84

Figure 8. Average Air Mass-Fraction for Zone 4 as a Function of Time 85

Figure 9. Fracture Evaporation Rate Field for the L4C4 Location with the "Upper" Infiltration Distribution at Simulation Time of 1000 yr 87

Figure 10. Plot of Total Evaporation vs. Time for All Zones, Including Fractures + Matrix 88

Figure 11. Vertical Component of the Gas-Phase Total Mass Flux (Air + Water Vapor) Along a Horizontal Profile Passing through the Drift Center 90

Figure 12. Normalized Mass of a Fictive Conservative Solute in Each Zone for Each of Five Time Intervals for the L4C4 Location with the Upper Infiltration Distribution 96

Figure 13. Normalized Mass of a Fictive Conservative Solute in Each Zone for Each of Five Time Intervals for the L4C4 Location with the Lower Infiltration Distribution 96

Figure 14. Normalized Mass of a Fictive Conservative Solute in Each Zone for Each of Five Time Intervals for the L4C1 Location with the Upper Infiltration Distribution 97

Figure 15. Normalized Mass of a Fictive Conservative Solute in Each Zone for Each of Five Time Intervals for the L4C1 Location with the Lower Infiltration Distribution 97

Figure 16. Observed Distribution of ^{14}C Activity with Depth in Borehole SD-12 107

Figure 17. Observed Distribution of Porewater CO_2 Concentration in Core Samples 112

Figure 18. Calculated Flux of $^{14}CO_2$ Required to Maintain Steady-State Isotopic Conditions in the Unsaturated Zone 113

Figure 19. Exponential Model Fit to ^{14}C Activity vs. Depth in Borehole SD-12 116

Figure 20. Exponential Model Fit to ^{14}C Activity vs. Depth in Borehole UZ-6/6S 119

Figure 21. Exponential Model Fit to ^{14}C Activity vs. Depth in Borehole UZ-1 120

Figure 22. Exponential Model Fit to ^{14}C Activity vs. Depth in Borehole NRG-5 121

Figure 23. Exponential Model Fit to ^{14}C Activity vs. Depth in Borehole SD-7 122

Figure 24. Lower-Bound Ratios of the CO_2 Concentration (Fugacity) at Repository Depth 124

Figure 25. Lower-Bound Ratios of the O_2 Concentration (Fugacity) at Repository Depth 125

Figure 26. Evolution of Air Mass-Fraction Calculated for Repository Center and Edge Locations, for the Viability Assessment Repository Design 128

Figure 27. Cumulative Air Flux Flowing Through the Repository Horizon, Calculated for Repository Center and Edge Locations for the Viability Assessment Repository Design 128

Figure 28. Comparison of the 2-D Air Mass-Fraction Approach to Estimating the Available Fluxes of CO_2 and O_2, With the Mass Transfer Model (L4C4 Location; "Upper" Infiltration) 130

Figure 29. Comparison of Reactive Transport Simulation of CO_2 Fugacity, with Results from the Gas Flux and Fugacity Model 131

Figure 30. Particle Size Distribution for Colloids in Groundwater Samples near Yucca Mountain 186

Figure 31. Distribution of Total Number of Colloid Particles per Milliliter in Groundwater Samples Near Yucca Mountain 189

Figure 32. Estimated Diffusion Coefficient as a Function of Particle Size Using the Stokes-Einstein Equation, Compared with Handbook Values from Table 23 194

Figure 33. CO_2 Budget for Reference Model (L4C4 location; "upper" infiltration) 214

Figure 34. Relative Humidity vs. Time Averaged in the Backfill Region Just Above the Upper Drip Shield Surface (Zone 4) 216

Figure 35. Conditions for MIC at the Drip Shield Surface 222

Figure 36. pH vs. Time for the Chemical Reference Model 226

Figure 37. Ionic Strength vs. Time, for the Chemical Reference Model 226

TABLES

Page

Table 1a. Software Codes and Routines Used for Thermal Hydrology Calculations 19

Table 1b. Software Execution 19

Table 2. Input and Output Files and File Types Used by Software Codes and Routines (Attachment I) 20

Table 3. NUFT Input Files for Calculations Described in the Thermal Hydrology Model 21

Table 4. Matrix Hydrologic Properties for Hydrostratigraphic Units, Used in TH Model 36

Table 5. Fracture Hydrologic Properties for Hydrostratigraphic Units, Used in TH Model 38

Table 6. Infiltration Values for Model Locations 40

Table 7. Average Flux Values for Model Locations 40

Table 8. Temperature and Total Pressure Boundary Conditions 41

Table 9. Air Mass-Fraction Boundary Conditions 41

Table 10. Thermal Properties for Hydrostratigraphic Units 43

Table 11. Nominal Property Values Used for Engineered Barrier System Materials 44

Table 12. Gas-Phase CO_2 Concentration Data for the Host-Rock Units, from Analysis of Gas Samples Obtained in Surface-Based Boreholes 46

Table 13. Gas-Phase and Porewater $^{14}CO_2$ Isotopic Data for the Host-Rock Units, from Analysis of Gas Samples and Preserved Rock-Core Samples Obtained from Surface-Based Boreholes 47

Table 14. Comparison of Equilibrium Constants (log10 K values at 25°C) from the PHREEQC and EQ3/6 (data0.com, Attachment I) Databases for Solid Phases Considered in Modeling of Cementitious Materials 50

Table 15. Composition of Fracture Water Used for Cementitious Material Model 52

Table 16. Selected Elements Contained in Considered Corrosion-Resistant Materials 52

Table 17. Corrosion Rates from Polarization-Resistance Experiments 53

Table 18. Major Ion Concentrations for J-13 Well Water 54

Table 19. Average Composition of Synthetic J-13 Water Used in Reported Tests 55

Table 20. Average Composition of SPW Used in Reported Tests 56

Table 21. Colloid Concentrations and Sizes from Nye County Wells 57

Table 22. Colloid Concentrations and Sizes from Yucca Mountain Site Characterization Project Wells 58

Table 23. Diffusion Coefficients and Molecular Diameters for Nonelectrolytes 58

Table 24. Correspondence Between Thermal Hydrology Model Zones and Composite Zones for the Chemical Reference Model 60

Table 25. Input Data Describing Thermal-Hydrologic Conditions and CO_2 and O_2 Gas Fugacities and Fluxes for the Chemical Reference Model 61

Table 26. Size Distribution Data for the Overton Sand Backfill Material 62

Table 27. Mass and Surface Area for Structural Steel Used in the Engineered Barrier System... 62

Table 28. Waste Emplacement Drift System Criteria Addressed by the EBS P&CE Model 65

Table 29. Grout Mineral Assemblage Used for the Cementitious Materials Model 70

Table 30. Intervals During Which Zone Temperatures and Fluxes Are Held Constant 91

Table 31. Zone-Averaged Temperatures, Liquid and Water Vapor Influxes and Outfluxes, and Liquid Masses for Each Zone (L4C4 Location, "Upper" Infiltration) 100

Table 32. Zone-Averaged Temperatures, Liquid and Water Vapor Influxes and Outfluxes, and Liquid Masses for Composite Zones (L4C4 Location, "Upper" Infiltration) 101

Table 33. Calculated Composition of Leachate from Partially Carbonated Grout Assemblage at T = 30°C and Several Values of P_{CO2} 134

Table 34. Calculated Composition of Leachate from Young, Partially Carbonated Grout Assemblage at T = 50°C and Several Values of P_{CO2} 135

Table 35. Calculated Composition of Leachate from Young, Partially Carbonated Grout Assemblage at T = 70°C and Several Values of P_{CO2} 136

Table 36. Calculated Composition of Leachate from Young, Partially Carbonated Grout Assemblage at T = 90°C and Several Values of P_{CO2} 137

Table 37. Solubilities (kg/m^3) of Portlandite and Ettringite at Several Temperatures, with Closed-System CO_2 Conditions Limited to the Influent Dissolved Inorganic Carbon 138

Table 38. Summary of Leaching Conditions for Rockbolt Grout 140

Table 39. Evolution of Leachate Composition with Time 146

Table 40. Summary of Potential Microbial Interactions with EBS Materials, Possible Causes, and Priority for Inclusion in a Model of Microbial Effects 153

Table 41. Evolution of Water Composition in Test with Synthetic J-13 Water (evap1) 162

Table 42. Evolution of Water Composition in Test with Synthetic J-13 Water and Tuff (evap2) 163

Table 43. Evolution of pH in Short-Term Test with Synthetic J-13 Water (evap4) 163

Table 44. Evolution of Water Composition in Short-Term Test with Synthetic J-13 Water (evap4) 164

Table 45. Mineralogical Results from Test with Synthetic J-13 Water (evap1) 164

Table 46. Mineralogic Results from Test with Synthetic J-13 Water and Tuff (evap2) 164

Table 47. Mass of Minerals Formed in Tests with Synthetic J-13 Water (evap1 and evap2) 165

Table 48. Evolution of Water Composition in Test with Synthetic Porewater (evap3) 165

Table 49. Evolution of Water Composition in Test with Synthetic Porewater and Tuff (evap6) 166

Table 50. pH and Carbonate Evolution from Short-Term Test with Synthetic Porewater (evap5) 166

Table 51. Evolution of Water Composition in Short-Term Test with Synthetic Porewater (evap5) 167

Table 52. Mineralogical Results from Test with Synthetic Porewater (evap3) 167

Table 53. Mineralogic Results from Test with Synthetic Porewater and Tuff (evap5) 167

Table 54. Mass of Minerals Formed in Tests with Synthetic Porewater 168

Table 55. Normative Mineral Assemblage Algorithm for Evaporation of Waters Similar to J-13 Under Near-Atmospheric CO_2 Conditions 172

Table 56. Normative Model for Precipitates Formed from Evaporating 1 kg of Synthetic J-13 Water, Compared with Qualitative Laboratory Observations 180

Table 57. Normative Model for Precipitates Formed from Evaporating 1 kg of Synthetic Porewater, Compared with Laboratory Qualitative Observations 181

Table 58. Log-Normal Parameters for Normalized Colloid Size Distributions in Samples from Nine Nye County Wells and Nine Yucca Mountain Wells 188

Table 59. Sorption Coefficient (K_d) Values in mL/g for Sorption of Pu and Am on Hematite, Montmorillonite, and Silica Colloids 190

Table 60. Summary of Calculations for the Colloid Mass at Different Fractiles of the Log-Normal Distribution for the Number of Particles per mL 193

Table 61. Calculated Water Composition in Zone 1/2 for Time Periods 1 through 5 199

Table 62. Normative Evaporative Mineral Assemblage Predicted to Accumulate in Zone 3/4 During Time Period 2 (300 to 700 yr) 201

Table 63. Surface Area Calculation for Quartz-Sand Backfill in Composite Zones 3/4 and 5/6, Expressed as Surface Area per Mass of Solvent 202

Table 64. Composition of Water in Zone 3/4 After Return of Liquid Water Through-Flow and Starting with Redissolution of Evaporative Precipitates in Time Period 3A 204

Table 65. Normative Evaporative Mineral Assemblage Predicted to Accumulate in Zone 5/6 During Time Period 3 (700 to 1500 yr) 206

Table 66. Composition of Water in Zone 5/6 After Return of Liquid Water Through-Flow and Starting with Redissolution of Evaporative Precipitates in Time Period 4A 208

Table 67. CO_2 Consumption in the Engineered Barrier System from Evaporation and Dissolution/Precipitation Processes 213

ABBREVIATIONS AND ACRONYMS

1-D	one-dimensional
2-D	two-dimensional
AFC	active-fracture concept
ANL	Argonne National Laboratory
atm	atmospheres
aw	water activity
CDF	cumulative distribution function
CRM	corrosion-resistant material
CRWMS	Civilian Radioactive Waste Management System
C-S-H	calcium-silicate-hydrate
CSNF	commercial spent nuclear fuel
DHLW	defense high-level waste
DIC	dissolved inorganic carbon
DKM	dual-permeability method
DTN	data-tracking number
EBS	engineered barrier system
EDA	enhanced design alternative
Eh	oxygen potential
EPS	exopolysaccharides
ESF	Exploratory Studies Facility
IC	ion chromatography
ICP	inductively coupled plasma
LANL	Los Alamos National Laboratory
M&O	Management and Operating
MIC	microbially induced corrosion
Mrad	megarad
MTU	metric tons of uranium
NAT-J-13	natural well water from J-13 well
NBS	National Bureau of Standards
NSPC	Nevada State Plane Coordinates
P&CE	physical and chemical environment
pmc	percent modern carbon
ppm	parts per million
ppmv	ppm-volume
QA	quality assurance
RH	relative humidity
SI	saturation index
SPW	synthetic porewater
SRB	sulfate-reducing bacteria
SYN-J-13	synthetic groundwater
SZ	saturated zone
TBD	to be determined
TBV	to be verified
TDMS	Technical Data Management System
TDS	total dissolved solids
TH	thermal hydrology, thermal-hydrologic
TSPA-VA	Total System Performance Assessment–Viability Assessment
USGS	U.S. Geological Survey
UTM	Universal Transverse Mercator
UZ	unsaturated zone
VA	viability assessment
XRD	x-ray diffraction
YM	Yucca Mountain
YMP	Yucca Mountain Site Characterization Project

INTENTIONALLY LEFT BLANK

1. PURPOSE

The conceptual models described in the "Engineered Barrier System Physical and Chemical Environment Model" (EBS P&CE Model) are intended to estimate the evolution of the physical and chemical conditions within the engineered barrier system (EBS) emplacement drifts. The models' output is data intended for use in modeling the performance of the EBS, the waste package, and the waste form. The Yucca Mountain Project developed screening criteria for the grading of data, and determined that the physical and chemical environments on and around the drip shield that is part of the EBS are factors important to the post closure safety case. Further, colloid associated radionuclide transport within the EBS has also been found to be important to the post closure safety case.

The scopes for this model include: a) develop and document a set of process level models which together constitute the EBS P&CE Model; b) perform calculations of the P&CE of the in-drift based on inputfrom other process model reports or responsible organizations, as necessary; and c) evaluate changes in the bulk P&CE affecting drip shield, waste package, and waste form degradation.

Specific tasks and activities of modeling the physical and chemical environment (P&CE) are included in the development plan (CRWMS M&O 1999c). As described in the development plan, the development of this report is coordinated with the development of other EBS analysis/model reports.

This EBS P&CE Model report will provide input to the EBS P&CE Performance Assessment Abstraction Model and the EBS Degradation, Flow, and Transport Process Model. The principal objective of this model and analysis activity is to evaluate the changes in the bulk P&CE that affect drip-shield and waste-package degradation and radionuclide migration.

2. QUALITY ASSURANCE

This report for the EBS P&CE Model has been prepared according to AP-3.10Q (Analyses and Models). AP-3.10Q is the procedure for planning, developing, validating, and documenting analyses and models. A development plan entitled: *Development Plan for EBS Physical & Chemical Environment Model* (CRWMS M&O 1999c) was prepared in accordance with AP-2.13Q ("Technical Product Development Planning"). This report has been prepared according to this development plan and applicable quality assurance (QA) controls presented therein.

The applicability of the QA program is documented in an activity evaluation according to QAP-2-0 (Conduct of Activities). The activity evaluation: *Engineered Barrier System Performance Modeling* (CRWMS M&O 1999a) has concluded that this document is quality-affecting and subject to the QA controls of the *Quality Assurance Requirements and Description* (DOE 2000).

The design analysis: *Classification of the MGR Ex-Container System* (CRWMS M&O 1999b) was performed in accordance with QAP-2-3 (Classification of Permanent Items). The drip shield

and waste package are identified on the *Q-list* (YMP 1998) and are identified as QA-1, important to radiological safety, and as QA-2, important to waste isolation (YMP 1998; p. II-9). The physical and chemical environment is not specifically addressed by the Q-list but is a characteristic of the waste emplacement drift system that primarily affects waste isolation. This analysis/model is identified as quality-affecting, consistent with the *Q-List* assignments, but with a technical focus on the postclosure environment in the emplacement drifts.

Qualified and accepted input data and references have been identified. Unqualified data used in this report are tracked in accordance with AP-3.15Q (Managing Technical Product Inputs). AP-3.10Q (Analyses and Models) requires that output resulting from unqualified software be designated as unqualified—to-be-verified (TBV) in accordance with AP-3.15Q (Managing Technical Product Inputs). Computer software and model usage is discussed in Section 3 of this report.

3. COMPUTER SOFTWARE AND MODEL USAGE

3.1 THERMAL HYDROLOGY MODEL

Software and software routines are used for the Thermal Hydrology (TH) Model portion of the EBS P&CE Model. The resulting output is designated unqualified and must be treated in accordance with AP-3.15Q (Managing Technical Product Inputs). The unqualified software is under configuration management and has software tracking numbers (Table 1a). Further software qualification is required prior to the removal of this TBV. Table 1b contains a list of the CPU's where these programs were executed. For the models described in this report, thermal-hydrology software is used within the range of validation, where such constraint information is available, or within the range of standard practice, where such information is unavailable.

The following subsections describe these codes and routines in more detail. Documentation and validation of some of the software routines are provided in Attachments II through X to this report. Table 2 identifies the types of input and output files used for implementing these codes and routines; it also provides the file-naming extensions assigned to the various input and output files. Table 3 lists the input files used for all NUFT V3.0s runs discussed in this report. Figure 1 illustrates the path of data through the codes and routines.

All input and output data files and electronic copies of software routine sources files have been saved electronically (see Attachment I).

Table 1a. Software Codes and Routines Used for Thermal Hydrology Calculations

Software Name	Type	STN	Attachment
Codes (Unqualified)			
NUFT V3.0s	Simulation Code	10088-3.0s-00	N/A
Routines (qualified per AP-SI.1Q Section 5.1.2)			
YMESH V1.53	NUFT preprocessor	10172-1.53-00	N/A
XTOOL 10.1	NUFT preprocessor	10208-10.1-00	N/A
CONVERTCOORDS V1.1	NUFT preprocessor	10209-1.1-00	N/A
Routines (see Attachments for Qualification/Validation Documentation)			
RME6 V1.1	NUFT preprocessor	N/A	II
COVER V1.1	NUFT preprocessor	N/A	III
COLUMNINFILTRATION V1.1	NUFT preprocessor	N/A	IV
CHIM_SURF_TP V1.1 & CHIM_WT_TP V1.1	NUFT preprocessors	N/A	V
MYPLOT V1.1	NUFT postprocessor	N/A	VI
ZONEAVG V1.2	NUFT postprocessor	N/A	VII
VFLUXPROF V1.1	NUFT postprocessor	N/A	VIII
TH+GASMODEL spreadsheets (Version 4; see text)	Excel Spreadsheets	N/A	IX
SoluteRK MathCad Files (V1.2; see text)	MathCad Files	N/A	X

Table 1b. Software Execution

Workstation/PC Name	Physical Location
s139	LLNL, T1487 Rm 150A
s89	LLNL, T1487 Rm 150
s116	LLNL, T1401 Rm 1119
s117	LLNL, T1487 Rm 112
s187	LLNL, T1487 Rm 153
s70	LLNL, T1487 Rm 149
s11	LLNL, T1487 Rm 146
s08	LLNL, T1487 Rm 145
s28	LLNL, T1487 Rm 154
s13	LLNL, T1487 Rm 124
s188	LLNL, T1487 Rm 138
s175	LLNL, T1487 Rm 114
Dell PowerEdge 2200 #112524	Las Vegas, Rm 611
Dell Optiplex #116400	Las Vegas, Rm 1031F

Table 2. Input and Output Files and File Types Used by Software Codes and Routines (Attachment I)

Software Name	Number or Validation	Input Filename(s)	Output Filename(s)
NUFT V3.0s	10088-3.0s-00	L4C*.in vtough.pkg dkm-afc-NBS4512= dkm-afc-EBS* outputtime LDTH-SDT-0.3Qheat* run_control_param*	L4C*.f.ext L4C*.m.ext L4C*Gflux*.dat L4C*Lflux*.dat
YMESH V1.53	10172-1.53-00	LBL99_YMESH	L4C4.col.units, lvc1.col.units
XTOOL V10.1	10208-10.1-00	L4C*.ext	Plot files may be produced
CONVERT-COORDS V1.1	10209-1.1-00	pa_pchl1.dat pa_pchm1.dat pa_pchu1.dat pa_monl1.dat pa_monm1.dat pa_monu1.dat pa_glal1.dat pa_glam1.dat pa_glau1.dat	Glaciall.NV Glacialm.NV Glacialu.NV Monsoonl.NV Monsoonm.NV Monsoonu.NV Yml.NV Ymm.NV Ymu.NV
RME6 V1.1	Attachment II	tspa99_primary_mesh UZ99_3.grd L4C*.dat	LBL99_YMESH
COVER V1.1	Attachment III	dft1.dat	Shape1.dat
COLUMN-INFILTRATION V1.1	Attachment IV	Glaciall.NV, Glacialm.NV Glacialu.NV, Monsoonl.NV Monsoonm.NV, Monsoonu.NV Yml.NV, Ymm.NV Ymu.NV	Display output
CHIM_SURF-_TPV1.1 & CHIM_WT-_TP V1.1	Attachment V	bcs_99.txt tspa99_primary_mesh	Display output
MYPLOT V1.1	Attachment VI	L4C*Gflux*.dat	L4C*.exl
ZONEAVG V1.2	Attachment VII	L4C*.f.ext L4C*.m.ext	L4C*.f.ext.zavg
VFLUXPROF V1.1	Attachment VIII	L4C*.f.ext L4C*.m.ext	L4C*.m.ext.vflux
TH+GAS-MODEL spreadsheets (Version 4; see text)	Attachment IX	L4C*.exl L4C*.f.ext.zavg L4C*.m.ext.zavg L4C*.f.ext.vflux	Display output
SoluteRK spreadsheets (V1.2; see text)	Attachment X	SoluteRK*.xls	Display output

Table 3. NUFT Input Files for Calculations Described in the Thermal Hydrology Model

File Type	Filename
Model: A-1 L4C4 location; "upper" infiltration; 60 MTU/acre (preclosure)	
NUFT input (.in) file	L4C4-LDTH60-1Dds_mc-ui-01v.in
Rock properties file	dkm_afc-1Dds-mc-ui-00
EBS properties file	dkm-afc-pbf-EBS_Rev00
Physical properties files	modprop_dr-up-00v
Heat generation file	LDTH-SDT-0.3Qheat-1e6y_vent-00v
Solver control file	vtough.pkg
Run control file	run_control_param_LDTH-v01
Time steps for.ext file output	output.times-00v
Model: A-2 L4C4 location; "upper" infiltration; 60 MTU/acre (postclosure)	
NUFT input (.in) file	L4C4-LDTH60-1Dds_mc-ui-01.in
Rock properties file	dkm_afc-ds-NBS-u_inf
EBS properties file	dkm-afc-EBS_Rev10
Heat generation file	LDTH-SDT-0.3Qheat-50y_vent-00
Solver control file	vtough.pkg
Run control file	run_control_param_LDTH-v00
Time steps for .ext file output	outputtime
Model: A-3 L4C4 location; "upper" infiltration; 60 MTU/acre (initialization without excavation)	
NUFT input (.in) file	L4C4-LDTH60-1Dds_ui-00-i.in
Rock properties file	dkm_afc-ds-NBS-u_inf
Solver control file	vtough.pkg
Run control file	run_control_param_LDTH-v00
Model: B-1 L4C1 location; "lower" infiltration; 60 MTU/acre (preclosure)	
NUFT input (.in) file	L4C4-LDTH60-1Dds_mc-li-01v.in
Rock properties file	dkm_afc-1Dds-mc-li-00
EBS properties file	dkm-afc-pbf-EBS_Rev10
Heat generation file	LDTH-SDT-0.3Qheat-1e6y_vent-00v
Physical properties files	modprop_dr-up-00v
Solver control file	vtough.pkg
Run control file	run_control_param_LDTH-v01
Time steps for .ext file output	output.times-00v
Model: B-2 L4C4 location; "lower" infiltration; 60 MTU/acre (postclosure)	
NUFT input (.in) file	L4C4-LDTH60-1Dds_mc-li-01.in
Rock properties file	dkm_afc-ds-NBS-l_inf
EBS properties file	dkm-afc- EBS_Rev10
Heat generation file	LDTH-SDT-0.3Qheat-50y_vent-00
Solver control file	vtough.pkg
Run control file	run_control_param_LDTH-v00
Time steps for .ext file output	outputtime

File Type	Filename
Model: B-3 L4C4 location; "lower" infiltration; 60 MTU/acre (initialization without excavation)	
NUFT input (.in) file	L4C4-LDTH60-1Dds_li-00-i.in
Rock properties file	dkm_afc-ds-NBS-l_inf
Solver control file	vtough.pkg
Run control file	run_control_param_LDTH-v00
Model: C-1 L4C1 location; "upper" infiltration; 36 MTU/acre (preclosure)	
NUFT input (.in) file	L4C1-LDTH36-1Dds_mc-ui-01v.in
Rock properties file	dkm_afc-1Dds-mc-ui-00
EBS properties file	dkm-afc-pbf-EBS_Rev00
Physical properties files	modprop_dr-up-00v
Heat generation file	LDTH-SDT-0.3Qheat-1e6y_vent-00v
Solver control file	vtough.pkg
Run control file	run_control_param_LDTH-v01
Time steps for .ext file output	output.times-00v
Model: C-2 L4C1 location; "upper" infiltration; 36 MTU/acre (postclosure)	
NUFT input (.in) file	L4C1-LDTH36-1Dds_mc-ui-01.in
Rock properties file	dkm_afc-ds-NBS-u_inf
EBS properties file	dkm-afc-EBS_Rev10
Heat generation file	LDTH-SDT-0.3Qheat-50y_vent-00
Solver control file	vtough.pkg
Run control file	run_control_param_LDTH-v00
Time steps for .ext file output	outputtime
Model: C-3 L4C1 location; "upper" infiltration; 36 MTU/acre (initialization without excavation)	
NUFT input (.in) file	L4C1-LDTH36-1Dds_ui-00-i.in
Rock properties file	dkm_afc-ds-NBS-u_inf
Solver control file	vtough.pkg
Run control file	run_control_param_LDTH-v00
Model: D-1 L4C1 location; "lower" infiltration; 36 MTU/acre (preclosure)	
NUFT input (.in) file	L4C1-LDTH36-1Dds_mc-li-01v.in
Rock properties file	dkm_afc-1Dds-mc-li-00
EBS properties file	dkm-afc-pbf-EBS_Rev10
Heat generation file	LDTH-SDT-0.3Qheat-1e6y_vent-00v
Solver control file	vtough.pkg
Run control file	run_control_param_LDTH-v01
Time steps for.ext file output	output.times-00v
Model: D-2 L4C1 location; "lower" infiltration; 36 MTU/acre (postclosure)	
NUFT input (.in) file	L4C1-LDTH36-1Dds_mc-li-01.in
Rock properties file	dkm_afc-ds-NBS-l_inf
EBS properties file	dkm-afc-EBS_Rev10
Heat generation file	LDTH-SDT-0.3Qheat-50y_vent-00
Solver control file	vtough.pkg
Run control file	run_control_param_LDTH-v00
Time steps for .ext file output	outputtime

File Type	Filename
Model: D-3 L4C1 location; "lower" infiltration; 36 MTU/acre (initialization without excavation)	
NUFT input (.in) file	L4C1-LDTH36-1Dds_li-00-i.in
Rock properties file	dkm_afc-ds-NBS-l_inf
Solver control file	vtough.pkg
Run control file	run_control_param_LDTH-v00

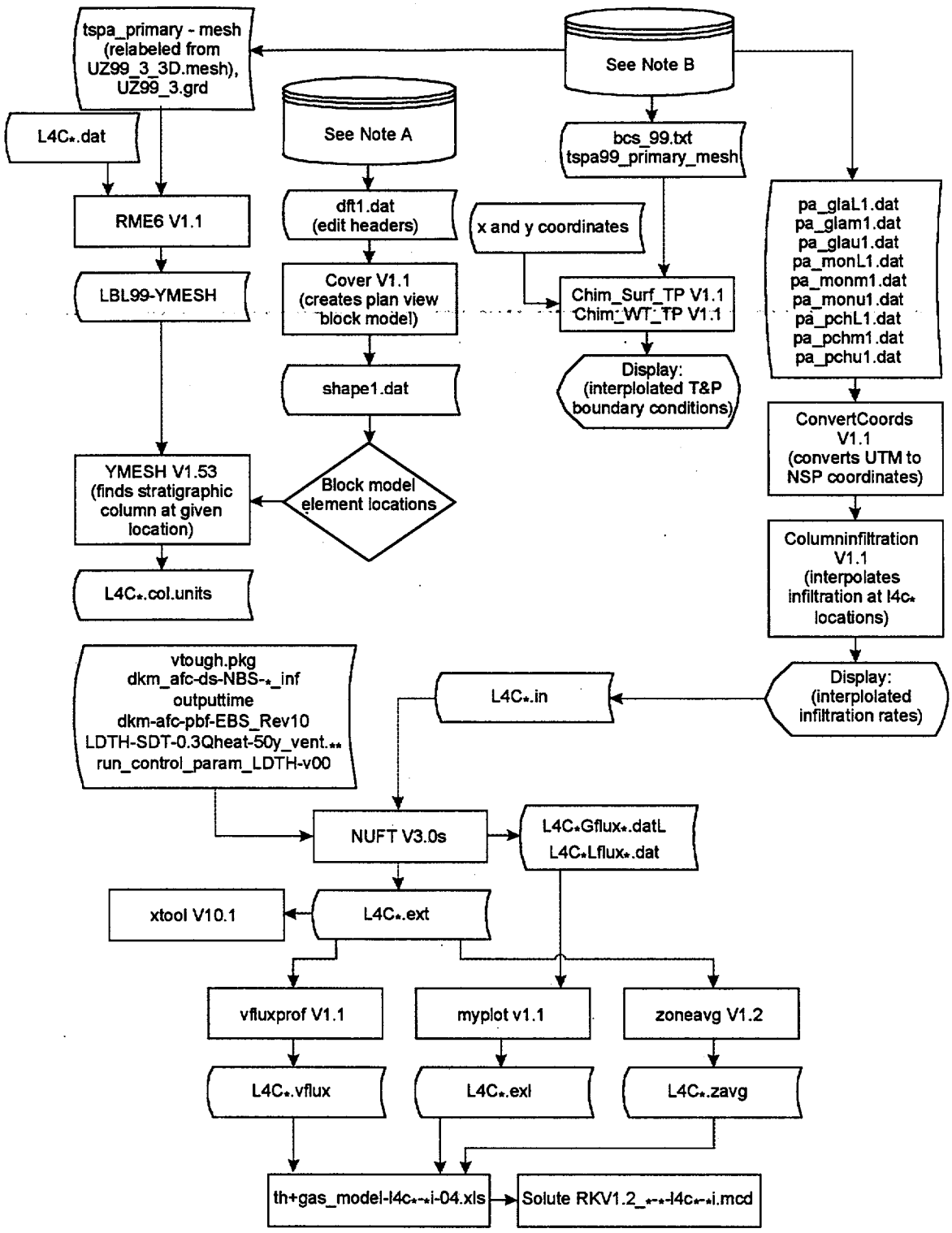

FIGURE 1.CDR.Q.DOCUMENTS.AMR.ANL-EBS-MD-000033/4-6-00

NOTES: A DTN: MO9911MWDEBSWD.000 (uses same input files as Water Drainage Model)
B DTN: LB99EBS1233129.001 (TBV-3826)

Figure 1. Path of Input and Output Data Through the Codes and Software Routines Used for Thermal Hydrology Calculations

3.1.1 Description of TH Software

3.1.1.1 NUFT

NUFT V3.0s (STN: 10088-3.0s-00) is an unqualified software code per AP-SI.1Q (Software Management) and obtained from configuration management (Table 1) (TBV-3828). The key options used for the NUFT V3.0s simulations include the dual permeability model (DKM) and the active-fracture concept (AFC). These modeling methods are options selected in the NUFT V3.0s input files (L4C*.in). NUFT was run on a Sun Ultra 10 workstation with a SunOS 5.6 operating system. NUFT is used to predict the conditions in the EBS and NBS. NUFT is appropriate for this task.

This is a thermal-hydrologic simulation code that was selected for the following reasons. NUFT has been used extensively for designing field tests, and interpreting results from those tests. NUFT has flexible input requirements and menu-type code structure. Model grids, including nested meshes, are readily generated and changed if necessary. NUFT implements a set of code features, including vapor pressure lowering, that is needed for thermal-hydrologic modeling. In summary, NUFT includes all code features needed for state-of-the-art modeling of thermal-hydrologic processes, is readily applied, and has been used extensively in conjunction with field testing in welded tuff.

3.1.2 Description of TH Software Routines

The types of input files, sources of input data, and types of output files used by the routines are shown in Table 2. Figure 1 further illustrates the path of data through routines supported by software packages Microsoft Excel 97, Mathcad 8 Professional, and Matlab.

3.1.2.1 YMESH

YMESH V1.53 is a qualified software routine per AP-SI.1Q (Software Management) and was obtained from configuration management (Table 1). YMESH V1.53 is used to develop the model grid to represent Yucca Mountain. It uses as input the grid and mesh files for the UZ model. The thickness of hydrostratigraphic units, as represented in the input files, is interpolated to locations required for TH modeling. YMESH V1.53 was developed for this task and is appropriate software for this application. It was used within the range of validation. YMESH was run on a Sun Ultra 2 workstation with a SunOS 5.5.1 operating system. This routine implements specific processing steps for preparation of input data for NUFT. The routine is a tool that performs specific functions needed to use NUFT, and no further justification for selection of this routine is needed.

3.1.2.2 CONVERTCOORDS

CONVERTCOORDS V1.1 is a qualified software routine per AP-SI.1Q (Software Management) and was obtained from configuration management (Table 1a). It is used to convert location data from Universal Transverse Mercator (UTM) coordinates to Nevada State Plane Coordinates (NSPC) and to reformat the input data on net infiltration (Attachment I). The input files are in a matrix format, and the output format is in columns for easting, northing, and infiltration value.

CONVERTCOORDS was run on a Sun Ultra 2 workstation with a SunOS 5.5.1 operating system. CONVERTCOORDS was developed for this task and is appropriate software for this application. It was used within the range of validation. The routine is a tool that performs specific functions needed to use NUFT, and no further justification for selection of this routine is needed.

3.1.2.3 XTOOL

XTOOL V10.1 is a qualified software routine per AP-SI.1Q (Software Management) and was obtained from configuration management (Table 1a). XTOOL is used for graphical visualization of NUFT V3.0s output. The input data are contained in output files from NUFT V3.0s (*.ext). XTOOL was run on a Sun Ultra 10 workstation with a SunOS 5.6 operating system. XTOOL was developed for this task and is appropriate software for this application. It was used within the range of validation. The routine is a tool that performs specific functions needed to use NUFT, and no further justification for selection of this routine is needed.

3.1.2.4 RME6

RME6 V1.1 is a software routine per AP-SI.1Q and is qualified in Attachment II. The purpose of RME6 is to reformat and combine specific input files ("tspa_primary_mesh", "UZ99_3.grd", and L4C*.dat). The resulting file ("LBL00_YMESH") is used by YMESH V1.53 (Figure 1 and Table 1a). The results of this routine meet the objectives, and the routine is determined to be valid for its intended use. Rme6 was run on a Sun Ultra 2 workstation with a SunOS 5.5.1 operating system. Rme6 was developed using a C++ vSC4.2 compiler. The routine is a tool that performs specific functions needed to use NUFT, and no further justification for selection of this routine is needed.

3.1.2.5 COVER

COVER V1.1 is a software routine per AP-SI.1Q, and is qualified in Attachment III. The purpose of COVER is to develop a block model of the plan view of the repository that approximates the area and location of emplacement areas. The results of this routine meet the objectives, and the routine is determined to be valid for its intended use. Cover was run on a Sun Ultra 2 workstation with a SunOS 5.5.1 operating system. Cover was developed using Matlab V 5.3.0.10183. The routine is a tool that performs specific functions needed to use NUFT, and no further justification for selection of this routine is needed.

3.1.2.6 COLUMNINFILTRATION

COLUMNINFILTRATION V1.1 is a software routine per AP-SI.1Q and is qualified in Attachment IV. The purpose of COLUMNINFILTRATION is to interpolate the infiltration at a given point using a Gaussian weighting function. This routine executes the mathematical operations accurately and is determined to be valid for its intended use. This routine was run on a Sun Ultra 2 workstation with a SunOS 5.5.1 operating system. ColumnInfiltration was developed

using C++ vSC 4.2 compiler. The routine is a tool that performs specific functions needed to use NUFT, and no further justification for selection of this routine is needed.

3.1.2.7 CHIM_SURF_TP and CHIM_WT_TP

CHIM_SURF_TP V1.1 and CHIM_WT_TP V1.1 are software routines per AP-SI.1Q and are qualified in Attachment V. The purpose of these routines is to interpolate, using the inverse-distance method, the temperature and pressure at the ground surface and at the water table at a given location. These routines execute the expected mathematical operations accurately and are determined to be valid for the intended use. Chim_surf_TP was run on a Sun Ultra 2 workstation with a SunOS 5.5.1 operating system. Chim_surf_TP was developed using a Fortran v SC 4.2 compiler. These routines are tools that perform specific functions needed to use NUFT, and no further justification for selection of these routines is needed.

3.1.2.8 MYPLOT

MYPLOT V1.1 is a software routine per AP-SI.1Q and is qualified in Attachment VI. The purpose of this routine is to sort NUFT V3.0s ".ext" file output to produce tables of fluxes between zones in the model domain. The zones are identified by unique material (unit) names in the NUFT V3.0s ".in" and "rocktab" files. MYPLOT produces one ".exl" file for each set of gas or liquid flux output files from NUFT V3.0s (*.dat). Both fracture and matrix fluxes are included by NUFT V3.0s in the output files (*.dat); therefore, both are included in the output from this routine (*.exl). The results of this routine meet the objectives, and the routine is determined to be valid for the intended use. Myplot was run on a Sun Ultra 2 workstation with a SunOS 5.5.1 operating system. Myplot was developed using MatlabV 5.3.0.10183. This routine implements specific processing steps for sorting and visualization of NUFT output. The routine is a tool that performs specific functions needed to use NUFT, and no further justification for selection of this routine is needed.

3.1.2.9 ZONEAVG

ZONEAVG V1.2 is a software routine per AP-SI.1Q and is qualified in Attachment VII. The purpose of this routine is to sort NUFT V3.0s output file (*.ext) and to process the information to produce tables of scalar variables averaged over all the grid blocks in each zone. The contribution from each grid block is weighted by the ratio of the cross-sectional area of the block to the total area of the zone. ZONEAVG produces a set of output files (*.zavg) from each NUFT V3.0s output file (*.ext). The results of this routine meet the objectives, and the routine is determined to be valid for the intended use. The routine is written in the "perl" scripting language of SunOS 5.5.1 C shell for Unix, and is compatible with any 5.x version of the perl compiler. The routine was run on a Sun Ultra 2 workstation with SunOS 5.5.1 operating system. The routine is a tool that performs specific functions needed to use NUFT, and no further justification for selection of this routine is needed.

3.1.2.10 VFLUXPROF

VFLUXPROF V1.1 is a software routine per AP-SI.1Q and is qualified in Attachment VIII. The purpose of this routine is to sort NUFT V3.0s output files (*.ext) to produce tables containing profiles of the vertical gas-phase flux along the vertical line of grid points passing through the drift center. VFLUXPROF produces a set of output files (*.vflux) from each NUFT V3.0s output file (*.ext). The results of this routine meet the objectives, and the routine is determined t0o be valid for the intended use. The routine is written in the "perl" scripting language of SunOS 5.5.1 C shell for Unix, and is compatible with any 5.x version of the perl compiler. The routine was run on a Sun Ultra 2 workstation with SunOS 5.5.1 operating system. The routine is a tool that performs specific functions needed to use NUFT, and no further justification for selection of this routine is needed.

3.1.2.11 TH+GASMODEL Spreadsheets

The TH+GASMODEL spreadsheets (file: "th+gas_model-L4C4-ui-04" and related spreadsheet routines; see Attachment IX) are software routines per AP-SI.1Q and are qualified in Attachment IX. These routines implement sorting and simple processing steps which use input based on NUFT output. Specific limitations on the use of these routines, pertaining to the way that the thermal-hydrologic evolution of the EBS is discretized both spatially and temporally, are identified in the attached software routine documentation. The filenames indicate the specific application of these routines, for example, file: "th+gas_model-L4C4-ui-04" is an Excel spreadsheet used for the L4C4 location and the "upper" infiltration conditions. The related routines are used for the "lower" infiltration condition, and for the L4C1 location. These routines are nearly identical except for the input data, with the qualification that the timing of TH changes in the four models requires slightly different organization (clearly indicated by comments in the electronic files, as well as in the attached documentation).

For TH calculations, the purpose of these routines is to sort the post-processed output of NUFT V3.0s (*.exl, *.zavg, and *.vflux), organize data on the state of the EBS environment over time, and calculate specific measures of the EBS environment. The routines parse the time axis into a number of discrete steps for which the thermal and hydrologic conditions are held constant to allow for chemical modeling (Section 6.7). The continuously variable-state functions, such as temperature and mass flux, are represented in a stepwise manner.

The input data that are organized and parsed in this manner include total (fracture + matrix) liquid and gas fluxes between zones, total (fracture + matrix) liquid water mass in each zone, temperature, fracture air mass-fraction, and total influx and outflux data for use in the SoluteRK calculation. Input is transferred directly (manually) from ZONEAVG V1.2 and MYPLOT V1.1 output files (*.zavg and *.exl). In addition, minimum and maximum values of the fracture air-mass fraction and the fracture vertical gas-phase flux, respectively, are transferred directly (manually) from the VFLUXPROF V1.1 output files (*.vflux). The results of these routines meet the objectives, and the routines are determined to be valid for the intended use. The routines are Excel 97 (SR-2) spreadsheets. These routines were run on a Dell Poweredge 2200 PC (Pentium Pro; Windows 95 4.00.950 B).

3.1.2.12 SOLUTERK

The SoluteRK MathCad files (V1.2) are a collection of software routines per AP-SI.1Q and are qualified in Attachment X. The purpose of these routines is to process the zone influx and outflux data from the TH+GASMODEL spreadsheets, and to estimate the mass accumulation of an ideal conservative solute caused by evaporation in the EBS. For each stepwise period in time, a system of linear, ordinary differential equations is solved to describe mass transport between zones. Input data are transferred manually from the TH+GASMODEL spreadsheets. The results of these routines meet the objectives, and the routines are determined to be valid for the intended use. These routines were developed and compiled using Mathcad 8 Professional (MathSoft 1998), run on a Dell Poweredge 2200 PC (Pentium Pro; Windows 95 V4.00.950 B).

3.2 GAS FLUX AND FUGACITY MODEL

The estimation approach for gaseous mass-transfer developed in this part of the EBS P&CE Model is implemented using several Microsoft Excel 97 spreadsheets that are classified as software routines:

- **gasC14-SD-12-1996dataV1.2.xls** —Compile and plot CO_2 data from borehole SD-12; compile and plot unit contact depths, matrix saturation, matrix porosity, and fracture porosity for SD-12; compile and plot gas-phase flux and temperature data from NUFT output; and calculate and plot exponential solution for gaseous mass transfer.

- **gasC14-UZ-6-1995dataV1.2.xls**—Compile and plot CO_2 data from borehole UZ-6 for comparison to the mass-transfer model developed using SD-12 data.

- **gasC14-UZ-1-1985dataV1.2.xls**—Compile and plot CO_2 data from borehole UZ-1 for comparison to the mass-transfer model developed using SD-12 data.

- **gasC14-NRG-5-1996dataV1.2.xls**—Compile and plot CO_2 data from borehole NRG-5 for comparison to the mass-transfer model developed using SD-12 data.

- **gasC14-SD-7-1996dataV1.2.xls**—Compile and plot CO_2 data from borehole SD-7 for comparison to the mass-transfer model developed using SD-12 data.

The foregoing routines are documented and qualified in Attachments XI and XII. The routines accurately implement the required mathematical functions, and are determined to be valid for the intended uses. The routines was run on a Dell Poweredge 2200 PC (Pentium Pro; Windows 95 4.00.950 B) located in Rm # 611 of Summerlin Facilities. In addition, the following routines were discussed previously, and are used in this model:

- **th+gas_model_L4C4-ui-04.xls**—Compile NUFT output for Multiscale Model location L4C4 with the upper distribution of infiltration flux; and calculate and plot lower-bound flux and fugacity for CO_2 and O_2. Features of this routine are also used for the TH modeling sections of this report.

- **th+gas_model_L4C4-li-04.xls**—Compile NUFT output for Multiscale Model location L4C4 with the lower distribution of infiltration flux; and calculate and plot lower-bound flux and fugacity for CO_2 and O_2. Features of this routine are also used for the TH modeling sections of this report.

- **th+gas_model_L4C1-ui-04.xls**—Compile NUFT output for Multiscale Model location L4C1 with the upper distribution of infiltration flux; and calculate and plot lower-bound flux and fugacity for CO_2 and O_2. Features of this routine are also used for the TH modeling sections of this report.

- **th+gas_model_L4C1-li-04.xls**—Compile NUFT output for Multiscale Model location L4C1 with the lower distribution of infiltration flux; and calculate and plot lower-bound flux and fugacity for CO_2 and O_2. Features of this routine are also used for the TH modeling sections of this report.

These routines are documented and qualified in Attachment IX, where they are determined to be valid for the intended use.

The NUFT calculations used in the Gas Flux and Fugacity Model, development of the input data for the NUFT calculations, and postprocessing of the NUFT calculations (before the data are entered in the "th+gas_model" spreadsheets described previously) are described in the TH modeling sections of this report.

3.3 CEMENTITIOUS MATERIALS MODEL

The U.S. Geological Survey (USGS) solution equilibrium modeling code PHREEQC V2.0 (**pH-RE**dox **EQ**uilibrium equation program in **C** language; STN: 10068-2.0-00) is qualified software, used for the Cementitious Materials Model to assess three types of geochemical effects:

- Changes in water and solid composition resulting from groundwater contacting grout

- Effects from grout-modified groundwater interacting with the CO_2 in the gas phase in the emplacement drift

- Effects of the grout- and gas-modified groundwater contacting backfill material

PHREEQC is based on an ion-association aqueous model. It uses an equation solver that optimizes a set of equalities subject to both equality and inequality constraints. Constraints are used to determine the thermodynamically stable set of phases in equilibrium with a solution. The PHREEQC code was obtained from configuration management. Two capabilities of PHREEQC were used for this model: (1) speciation and saturation-index (SI) calculations and (2) reaction-path calculations involving specified irreversible reactions and mineral or gas-phase equilibria.

All input and output files used for this model were saved (Attachment I). PHREEQC is appropriate for this task and is used only within the range of validation in accordance with AP-SI.1Q. The software was run on a Dell PC OptiPlex (Pentium and Windows P5 4.00950B) located in Rm # 1031F of Summerlin Facilities.

3.4 MICROBIAL EFFECTS MODEL

No software was used in developing the microbial effects model.

3.5 NORMATIVE PRECIPITATES AND SALTS MODEL

An Excel 97 spreadsheet algorithm is used to implement the normative model for precipitates formed by evaporation of waters within a range of composition. The results are used in the Chemical Reference Model to describe the relative abundance of various precipitates formed by evaporation. The algorithm is repeated for those few zones and time periods during which evaporation is represented as complete or nearly so. In addition, it is repeated for high-CO_2 and low-CO_2 conditions to address differences between the laboratory test conditions and predicted repository conditions.

The algorithm starts with the qualitative mineral assemblage observed from laboratory tests and the calculated composition of water transferred from zone to zone in the Chemical Reference Model and subject to evaporation. Minerals are then assigned to the evaporite suite to account for the chemical constituents of the water.

The algorithm was applied to the laboratory test data, in the following spreadsheets:

- **normative_hiCO2_synJ13V1.2.xls**—Minerals formed by complete evaporation of the synthetic J-13 water used in laboratory tests
- **normative_hiCO2_SPWV1.2.xls**—Minerals formed by complete evaporation of synthetic tuff matrix porewater used in laboratory tests

These routines are documented in Attachment XIII, where they are determined to be valid for the intended use. Following are the spreadsheets for the L4C4 location and the "upper" infiltration distribution:

- **normative_hiCO2_L4C4_ui-zone34-500V1.2.xls**—Minerals formed in Zones 3 and 4 (backfill) during the time period from 300 to 700 yr (nominally 500 yr), assuming high-CO_2 conditions
- **normative_hiCO2_L4C4_ui-zone56-1000V1.2.xls**—Minerals formed in Zones 5 and 6 (lower backfill and invert) during the time period from 700 to 1500 yr (nominally 1000 yr), assuming high-CO_2 conditions

These routines are documented in Attachments XIV and XV, where they are determined to be valid for the intended uses. These routine were run on a Dell Poweredge 2200 PC (Pentium Pro; Windows 95 4.00.950 B) located in Rm # 611 of Summerlin Facilities.

3.6 EBS COLLOIDS MODEL

An Excel 97 spreadsheet is used to compile, plot, and fit curves to colloid size and abundance data. The routine is implemented in file: "gwcolloidsV1.2.xls" and is documented in Attachment XVI, where it is determined to be valid for the intended use. The routine was run on a Dell

Poweredge 2200 PC (Pentium Pro; Windows 95 4.00.950 B) located in Rm # 611 of Summerlin Facilities.

3.7 CHEMICAL REFERENCE MODEL

The chemical reaction modeling code EQ3/6 V7.2b (qualified software, STN: LLNL:UCRL-MA-110662) is used for the Chemical Reference Model. The EQ3/6 V7.2b code was obtained from configuration management. Types of problems to which the code was applied include the following:

- Changes in reference water composition resulting from elevated temperature, contact with the host rock, minor gains or losses of solvent water due to condensation/ evaporation, and changes in CO_2 fugacity at far-field and near-field locations

- Redissolution of precipitates previously formed in the EBS by complete evaporation of influent waters. (The original formation of such precipitates was modeled outside the code using a normative calculation.)

- Changes in water composition caused by evaporative concentration (incomplete evaporation) of influent waters, rate-limited interaction with backfill, and changes in temperature and CO_2 fugacity within the EBS

- Changes in water composition resulting from the processes described in the previous bulleted item and from rate-limited interaction with EBS materials

Two capabilities of EQ3/6 were used for this model: (1) the speciation-solubility code EQ3NR and (2) the reaction-path mass-transfer code EQ6. All input and output files used for these calculations were saved (Attachment I). EQ3/6 is appropriate for this task and is used only within the range of validation in accordance with AP-SI.1Q. EQ3/6 results are tabulated and plotted using Excel 97, for which validation is not required, in accordance with AP-SI.1Q. EQ 3/6 was run on a Gateway PC (Pentium II; Windows 98) located in LLNL, T1487 Rm 145.

Two software routines introduced for the Normative Precipitates and Salts Model are used to develop mineral assemblages that form when waters evaporate to dryness in the EBS:

- **normative_hiCO2_L4C4_ui-zone34-500V1.2.xls**—Calculates the assemblage of precipitates formed in Zone 3/4 (backfill), during the Time Period 2, from 300 to 700 yr, and the mass of groundwater required to redissolve them in the next time period (based on a water composition modeled using EQ3/6)(for validation see Attachment XIV).

- **normative_hiCO2_L4C4_ui-zone56-1000V1.2.xls**—Calculates the assemblage of precipitates formed in Zone 5/6 (lower backfill and invert) during the Time Period 3, from 700 to 1500 yr, and the mass of groundwater required to redissolve them in the next time period (based on a water composition modeled using EQ3/6) (for validation see Attachment XV).

Input data values for the Chemical Reference Model (L4C4 location, "upper" infiltration distribution) are generated in another routine that was introduced for the Thermal Hydrology Model:

- **th+gas_model-L4C4-ui-04.xls, worksheet: CHEMprobL4C4upper**— Compiles data on temperature, liquid influx, liquid outflux, evaporative concentration factor, CO_2 fugacity, and O_2 fugacity for each composite zone modeled in the Chemical Reference Model (for validation see Attachment IX.)

- **th+gas_model-L4C4-ui-04.xls, worksheet: Steel**— Compiles data on zone temperatures and water composition and computes steel corrosion rates (for validation see Attachment IX).

In addition, a spreadsheet was developed to calculate the surface area of the quartz sand backfill:

- **OvertonSandAreaV1.2.xls**—Computes the surface area from a grain-size distribution (for validation see Attachment XVII).

Finally, the CO_2 mass balance across all zones, and including the effects of cement leaching, was calculated using another spreadsheet:

- **CO2balanceV1.2.xls**—Computes the net CO_2 budget for different types of chemical reactions in the EBS (for validation see Attachment XVIII).

These routines are implemented using Excel 97 and are equivalent except for the zone and time period of application. All of these routines are further described and validated in attachments to this report. These Excel 97 spreadsheet routines were run on a Dell Poweredge 2200 PC (Pentium Pro; Windows 95 4.00.950 B) located in Rm # 611 of Summerlin Facilities.

4. INPUTS

4.1 DATA AND PARAMETERS

Data and parameters used in this section are derived for the specific use of this model if not otherwise indicated. These data and parameters are therefore appropriate for the intended purpose.

4.1.1 Thermal Hydrology Model

Drift-scale, two-dimensional (2-D) TH calculations are reported here for the L4C4 and L4C1 locations. These model calculations are performed using the same approach developed for the Multiscale Thermal-Hydrologic Model (CRWMS M&O 2000f) with minor modifications. The Multiscale Model represents variation of TH conditions throughout the repository by 31 distributed locations. The TH calculations described in this report are limited to two of those, the L4C4 and L4C1 locations. The rationale for selecting the L4C4 and L4C1 locations for investigation of the in-drift physical and chemical environment, is as follows:

- L4C4 is typical for locations internal to the repository layout. It is located near the geographic center, where temperatures and evaporation rates will be relatively high. Thermal loading for the L4C4 model is equivalent to the average for the repository layout (corresponds to areal spent-fuel mass loading of 60 MTU/acre required by management guidance; Wilkins and Heath 1999). The projected infiltration flux is near the average for the layout, as discussed subsequently.

- L4C1 is located at the repository edge, where the rate of cooling will be greatest because of conductive heat loss to unheated external regions. 36 MTU/acre thermal loading is used for the L4C1 model, which is appropriate for edge locations subject to cooling effects.

For each of these locations, TH conditions are simulated, using the "lower" and "upper" infiltration distributions described in the Multiscale Model (CRWMS M&O 2000f), for different flux conditions. Note that the data used to describe the "lower" and "upper" infiltration distributions were obtained from the same sources used for the Multiscale Model, and not directly from the Multiscale Model. Different hydrologic property sets are associated with the different infiltration conditions.

Separate but linked NUFT V3.0s runs are used to initialize the models and to represent preclosure and postclosure conditions. The initialization model calculates equilibrium saturation and temperature conditions for the stratigraphic column with the imposed boundary conditions, but without a drift opening. The preclosure model uses the calculated equilibrium as initial data, adds the drift opening without backfill, and adds heating. The postclosure model uses the final preclosure saturation and temperature fields as initial data, adds backfill, and increases heating to account for the cessation of ventilation. This necessitates separate NUFT V3.0s input and output files. Restart files (*.res) are used to store the TH conditions from the initialization and preclosure models, for use as initial conditions in the preclosure and postclosure models, respectively. Restart files are only used internally to NUFT calculations but are saved with the other input and output files (Attachment I). In summary, as listed in Table 3, twelve NUFT V3.0s models are required to calculate the four TH cases included in this report.

For calculated postclosure results, there also are separate output files for fracture and matrix data. Further discussion of the NUFT V3.0s inputs for these models is provided in the following subsections.

4.1.1.1 Hydrostratigraphic Unit Thicknesses, Contact Elevations, and Extents

The 31 model locations selected for the Multiscale Model were developed using an algorithm (COVER V1.1) to represent the repository layout as a contiguous array of blocks having uniform geometry. The center of each block is the nominal location. Coordinates for the repository outline provided as input to COVER were transmitted by subsurface design (CRWMS M&O 2000a) (TBV-3902).

The UZ model unit thicknesses, contact elevations, and lateral extents are honored in these calculations. Integration with the UZ model was accomplished using YMESH V1.53 to read mesh and grid files from the UZ model (Figure 1 and Table 2). Input data from the UZ model

were received from CRWMS M&O (1999d) (TBV-3901). The results from this operation consisted of a file (L4C*.col.units) containing contact elevations for each of the 31 model locations. This information was manually incorporated into the NUFT V3.0s input files (L4C*.in).

In summary, for the calculations described in the TH portion of this report, the results from the operations described previously consist of stratigraphic columns for the L4C4 and L4C1 locations and additional information, as discussed in the following subsections. Note that some stratigraphic units at the site are discontinuous over the repository area because of geologic variation. These results are essentially the same as results obtained for the Multiscale Model, but were developed independently, using the same input data.

4.1.1.2 Hydrostratigraphic Unit Properties

The hydrologic properties used in the TH portion of this report are fully consistent with the one-dimensional (1-D), drift-scale property sets from the UZ model. The property values for units in the L4C4 and L4C1 columns are exactly those given for these units by the following:

- DTN LB990861233129.002 (1-D, drift-scale, "upper" infiltration)
- DTN LB990861233129.003 (1-D, drift-scale, "lower" infiltration)

These property sets include porosity, saturated permeability, and parameters for water potential vs. liquid-phase saturation and relative permeability vs. saturation relationships, based on the analytical expressions developed by van Genuchten (1980) and Mualem (1976). Each property set contains similar descriptions for the rock matrix and for the fracture network for each hydrostratigraphic unit (Tables 4 and 5). The fracture network is assumed to behave as a continuous porous medium in these calculations, and the continuum properties are assumed to be homogeneous within each hydrostratigraphic unit (Assumption 5.1.3).

The property sets listed previously also include values for parameters that describe nonequilibrium fracture–matrix interaction using the AFC, which are input directly to NUFT V3.0s. These parameters include fracture spacings and the γ-parameter for each unit (Table 5).

Table 4. Matrix Hydrologic Properties for Hydrostratigraphic Units, Used in TH Model

	Matrix Parameters					
Model Layer	Permeability k_m (m^2)	Porosity ϕ_m	van Genuchten α_m (1/Pa)	van Genuchten m_m	Residual Saturation S_{lrm}	Satiated Saturation S_{lsm}
"Upper" Infiltration Distribution (DTN: LB997141233129.002)						
tcw11	3.98E-15	0.253	4.27E-5	0.484	0.07	1.00
tcw12	3.26E-19	0.082	2.18E-5	0.229	0.19	1.00
tcw13	1.63E-16	0.203	2.17E-6	0.416	0.31	1.00
ptn21	1.26E-13	0.387	1.84E-4	0.199	0.23	1.00
ptn22	5.98E-12	0.439	2.42E-5	0.473	0.16	1.00
ptn23	3.43E-13	0.254	4.06E-6	0.407	0.08	1.00
ptn24	3.93E-13	0.411	5.27E-5	0.271	0.14	1.00
ptn25	1.85E-13	0.499	2.95E-5	0.378	0.06	1.00
ptn26	6.39E-13	0.492	3.54E-4	0.265	0.05	1.00
tsw31	9.25E-17	0.053	7.79E-5	0.299	0.22	1.00
tsw32	5.11E-16	0.157	4.90E-5	0.304	0.07	1.00
tsw33	1.24E-17	0.154	1.97E-5	0.272	0.12	1.00
tsw34	7.94E-19	0.110	3.32E-6	0.324	0.19	1.00
tsw35	1.42E-17	0.131	7.64E-6	0.209	0.12	1.00
tsw36	1.34E-18	0.112	3.37E-6	0.383	0.18	1.00
tsw37	7.04E-19	0.094	2.70E-6	0.447	0.25	1.00
tsw38	4.47E-18	0.037	5.56E-7	0.314	0.44	1.00
tsw39	3.12E-17	0.173	1.82E-5	0.377	0.29	1.00
ch1z	8.46E-20	0.288	4.23E-7	0.336	0.33	1.00
ch1v	4.36E-14	0.273	4.23E-5	0.363	0.03	1.00
ch2v	3.89E-13	0.345	4.86E-5	0.312	0.07	1.00
ch3v	3.89E-13	0.345	4.86E-5	0.312	0.07	1.00
ch4v	3.89E-13	0.345	4.86E-5	0.312	0.07	1.00
ch5v	3.89E-13	0.345	4.86E-5	0.312	0.07	1.00
ch2z	1.16E-17	0.331	1.13E-6	0.229	0.28	1.00
ch3z	1.16E-17	0.331	1.13E-6	0.229	0.28	1.00
ch4z	1.16E-17	0.331	1.13E-6	0.229	0.28	1.00
ch5z	1.16E-17	0.331	1.13E-6	0.229	0.28	1.00
ch6	3.32E-20	0.266	3.57E-7	0.502	0.37	1.00
pp4	2.00E-18	0.325	1.83E-7	0.683	0.28	1.00
pp3	1.47E-14	0.303	1.02E-5	0.395	0.10	1.00
pp2	1.05E-16	0.263	2.43E-6	0.367	0.18	1.00
pp1	5.49E-17	0.280	1.01E-6	0.393	0.30	1.00
bf3	2.98E-14	0.115	3.83E-6	0.490	0.11	1.00
bf2	3.86E-17	0.259	2.29E-7	0.582	0.18	1.00
"Lower" Infiltration Distribution (DTN: LB997141233129.003)						
tcw11	4.63E-15	0.253	1.61E-5	0.460	0.07	1.00
tcw12	8.87E-20	0.082	2.89E-5	0.241	0.19	1.00
tcw13	6.61E-17	0.203	1.42E-6	0.368	0.31	1.00
ptn21	1.86E-13	0.387	6.13E-5	0.165	0.23	1.00
ptn22	3.27E-12	0.439	1.51E-5	0.390	0.16	1.00
ptn23	4.20E-13	0.254	2.04E-6	0.367	0.08	1.00
ptn24	3.94E-13	0.411	2.32E-5	0.210	0.14	1.00
ptn25	2.22E-13	0.499	2.04E-5	0.296	0.06	1.00
ptn26	5.43E-13	0.492	1.82E-4	0.264	0.05	1.00
tsw31	6.38E-17	0.053	2.81E-5	0.317	0.22	1.00
tsw32	6.28E-16	0.157	6.35E-5	0.279	0.07	1.00
tsw33	1.82E-17	0.154	2.44E-5	0.248	0.12	1.00

Matrix Parameters

Model Layer	Permeability k_m (m^2)	Porosity ϕ_m	van Genuchten α_m (1/Pa)	van Genuchten m_m	Residual Saturation S_{lrm}	Satiated Saturation S_{lsm}
tsw34	**3.50E-19**	0.110	**3.54E-6**	**0.309**	0.19	1.00
tsw35	**1.27E-17**	0.131	**7.57E-6**	**0.187**	0.12	1.00
tsw36	**1.19E-18**	0.112	**3.74E-6**	**0.328**	0.18	1.00
tsw37	**5.63E-19**	0.094	**3.28E-6**	**0.423**	0.25	1.00
tsw38	**1.44E-18**	0.037	**3.72E-6**	**0.291**	0.44	1.00
tsw39	**1.09E-17**	0.173	**2.37E-5**	**0.321**	0.29	1.00
ch1z	**2.75E-20**	0.288	**7.26E-7**	**0.304**	0.33	1.00
ch1v	**2.05E-14**	0.273	**9.86E-6**	**0.402**	0.03	1.00
ch2v	**3.17E-13**	0.345	**1.91E-5**	**0.326**	0.07	1.00
ch3v	**3.17E-13**	0.345	**1.91E-5**	**0.326**	0.07	1.00
ch4v	**3.17E-13**	0.345	**1.91E-5**	**0.326**	0.07	1.00
ch5v	**3.17E-13**	0.345	**1.91E-5**	**0.326**	0.07	1.00
ch2z	**6.28E-18**	0.331	**2.44E-6**	**0.135**	0.28	1.00
ch3z	**6.28E-18**	0.331	**2.44E-6**	**0.135**	0.28	1.00
ch4z	**6.28E-18**	0.331	**2.44E-6**	**0.135**	0.28	1.00
ch5z	**6.28E-18**	0.331	**2.44E-6**	**0.135**	0.28	1.00
ch6	**8.20E-20**	0.266	**5.06E-7**	**0.445**	0.37	1.00
pp4	**2.05E-18**	0.325	**1.83E-7**	**0.653**	0.28	1.00
pp3	**1.91E-14**	0.303	**1.53E-5**	**0.355**	0.10	1.00
pp2	**1.08E-16**	0.263	**2.08E-6**	**0.399**	0.18	1.00
pp1	**6.52E-17**	0.280	**9.40E-7**	**0.392**	0.30	1.00
bf3	**9.47E-15**	0.115	**3.75E-6**	**0.509**	0.11	1.00
bf2	**1.27E-17**	0.259	**1.38E-7**	**0.568**	0.18	1.00

NOTES: Values in bold type are constrained by hydrologic calibration process.

Table 5. Fracture Hydrologic Properties for Hydrostratigraphic Units, Used in TH Model

Fracture Parameters

	Perme-ability	Porosity	van Genuchten	van Genuchten	Residual Satura-tion	Satiated Satura-tion	Active Fracture Parameter	Fre-quency	Fracture to Matrix Connection Area
	k_f (m^2)	ϕ_f (-)	α_f (1/Pa)	m_f (-)	S_{lrf} (-)	S_{lsf} (-)	γ (-)	f (1/m)	A (m^2/m^3)
"Upper" Infiltration Distribution (DTN: LB997141233129.002)									
tcw11	**2.75E-12**	3.7E-2	**4.67E-3**	**0.636**	0.01	1.00	**0.31**	0.92	1.56
tcw12	**1.00E-10**	2.6E-2	**2.18E-3**	**0.633**	0.01	1.00	**0.31**	1.91	13.39
tcw13	**2.26E-12**	1.9E-2	**1.71E-3**	**0.631**	0.01	1.00	**0.31**	2.79	3.77
ptn21	**1.00E-11**	1.4E-2	**2.38E-3**	**0.611**	0.01	1.00	**0.08**	0.67	1.00
ptn22	**1.00E-11**	1.5E-2	**1.26E-3**	**0.665**	0.01	1.00	**0.08**	0.46	1.41
ptn23	**1.96E-13**	3.2E-3	**1.25E-3**	**0.627**	0.01	1.00	**0.08**	0.57	1.75
ptn24	**4.38E-13**	1.5E-2	**2.25E-3**	**0.631**	0.01	1.00	**0.08**	0.46	0.34
ptn25	**6.14E-13**	7.9E-3	**1.00E-3**	**0.637**	0.01	1.00	**0.08**	0.52	1.09
ptn26	**3.48E-13**	4.6E-3	**3.98E-4**	**0.367**	0.01	1.00	**0.08**	0.97	3.56
tsw31	**2.55E-11**	7.1E-3	**1.78E-4**	**0.577**	0.01	1.00	**0.09**	2.17	3.86
tsw32	**2.83E-11**	1.2E-2	**1.32E-3**	**0.631**	0.01	1.00	**0.38**	1.12	3.21
tsw33	**3.07E-11**	8.5E-3	**1.50E-3**	**0.631**	0.01	1.00	**0.38**	0.81	4.44
tsw34	**1.35E-11**	1.0E-2	**4.05E-4**	**0.579**	0.01	1.00	**0.38**	4.32	13.54
tsw35	**3.58E-11**	1.5E-2	**9.43E-4**	**0.627**	0.01	1.00	**0.38**	3.16	9.68
tsw36	**5.57E-11**	2.0E-2	**8.21E-4**	**0.623**	0.01	1.00	**0.38**	4.02	12.31
tsw37	**5.57E-11**	2.0E-2	**8.21E-4**	**0.623**	0.01	1.00	**0.38**	4.02	12.31
tsw38	**4.06E-13**	1.6E-2	**7.69E-4**	**0.622**	0.01	1.00	**0.38**	4.36	13.34
tsw39	**5.69E-13**	5.9E-3	**1.30E-3**	**0.633**	0.01	1.00	**0.38**	0.96	2.95
ch1z	**5.70E-13**	2.2E-4	**1.29E-3**	**0.631**	0.01	1.00	**0.10**	0.04	0.11
ch1v	**7.90E-13**	8.8E-4	**1.66E-3**	**0.656**	0.01	1.00	**0.10**	0.10	0.30
ch2v	**4.64E-13**	1.1E-3	**1.45E-3**	**0.626**	0.01	1.00	**0.10**	0.14	0.43
ch3v	**4.64E-13**	1.1E-3	**1.45E-3**	**0.626**	0.01	1.00	**0.10**	0.14	0.43
ch4v	**4.64E-13**	1.1E-3	**1.45E-3**	**0.626**	0.01	1.00	**0.10**	0.14	0.43
ch5v	**4.64E-13**	1.1E-3	**1.45E-3**	**0.626**	0.01	1.00	**0.10**	0.14	0.43
ch2z	**2.64E-14**	5.5E-4	**8.45E-4**	**0.628**	0.01	1.00	**0.10**	0.14	0.43
ch3z	**2.64E-14**	5.5E-4	**8.45E-4**	**0.628**	0.01	1.00	**0.10**	0.14	0.43
ch4z	**2.64E-14**	5.5E-4	**8.45E-4**	**0.628**	0.01	1.00	**0.10**	0.14	0.43
ch5z	**2.64E-14**	5.5E-4	**8.45E-4**	**0.628**	0.01	1.00	**0.10**	0.14	0.43
ch6	**2.21E-14**	2.2E-4	**1.31E-3**	**0.631**	0.01	1.00	**0.10**	0.04	0.11
pp4	**1.07E-13**	5.5E-4	**7.99E-4**	**0.633**	0.01	1.00	**0.10**	0.14	0.43
pp3	**7.10E-12**	1.4E-3	**1.29E-3**	**0.749**	0.01	1.00	**0.56**	0.20	0.61
pp2	**2.53E-13**	1.4E-3	**1.65E-3**	**0.629**	0.01	1.00	**0.56**	0.20	0.61
pp1	**6.25E-13**	5.5E-4	**8.18E-4**	**0.630**	0.01	1.00	**0.10**	0.14	0.43
bf3	**1.43E-12**	1.4E-3	**1.50E-3**	**0.636**	0.01	1.00	**0.56**	0.20	0.61
bf2	**2.26E-14**	5.5E-4	**8.18E-4**	**0.631**	0.01	1.00	**0.10**	0.14	0.43
"Lower" Infiltration Distribution (DTN: LB997141233129.003)									
tcw11	**2.70E-12**	3.7E-2	**2.40E-3**	**0.598**	0.01	1.00	**0.25**	0.92	1.56
tcw12	**1.00E-10**	2.6E-2	**2.05E-3**	**0.608**	0.01	1.00	**0.25**	1.91	13.39
tcw13	**1.79E-12**	1.9E-2	**9.21E-4**	**0.600**	0.01	1.00	**0.25**	2.79	3.77
ptn21	**1.00E-11**	1.4E-2	**1.66E-3**	**0.503**	0.01	1.00	**0.01**	0.67	1.00
ptn22	**1.00E-11**	1.5E-2	**9.39E-4**	**0.651**	0.01	1.00	**0.01**	0.46	1.41
ptn23	**1.84E-13**	3.2E-3	**1.28E-3**	**0.518**	0.01	1.00	**0.01**	0.57	1.75
ptn24	**4.31E-13**	1.5E-2	**2.02E-3**	**0.594**	0.01	1.00	**0.01**	0.46	0.34
ptn25	**7.12E-13**	7.9E-3	**7.42E-4**	**0.555**	0.01	1.00	**0.01**	0.52	1.09
ptn26	**3.08E-13**	4.6E-3	**2.00E-4**	**0.401**	0.01	1.00	**0.01**	0.97	3.56
tsw31	**2.55E-11**	7.1E-3	**4.42E-4**	**0.545**	0.01	1.00	**0.06**	2.17	3.56

Fracture Parameters

	Perme-ability	Porosity	van Genuchten	van Genuchten	Residual Satura-tion	Satiated Satura-tion	Active Fracture Parameter	Fre-quency	Fracture to Matrix Connection Area
	k_f (m^2)	ϕ_f (-)	α_f (1/Pa)	m_f (-)	S_{lrf} (-)	S_{lsf} (-)	γ (-)	f (1/m)	A (m^2/m^3)
tsw32	**2.83E-11**	1.2E-2	**1.21E-3**	**0.603**	0.01	1.00	**0.23**	1.12	3.21
tsw33	**3.07E-11**	8.5E-3	**1.36E-3**	**0.600**	0.01	1.00	**0.23**	0.81	4.44
tsw34	**1.35E-11**	1.0E-2	**2.48E-4**	**0.515**	0.01	1.00	**0.23**	4.32	13.54
tsw35	**3.58E-11**	1.5E-2	**6.26E-4**	**0.612**	0.01	1.00	**0.23**	3.16	9.68
tsw36	**5.57E-11**	2.0E-2	**4.90E-4**	**0.540**	0.01	1.00	**0.23**	4.02	12.31
tsw37	**5.57E-11**	2.0E-2	**4.90E-4**	**0.540**	0.01	1.00	**0.23**	4.02	12.31
tsw38	**5.65E-13**	1.6E-2	**4.00E-4**	**0.603**	0.01	1.00	**0.23**	4.36	13.34
tsw39	**3.12E-13**	5.9E-3	**6.43E-4**	**0.605**	0.01	1.00	**0.23**	0.96	2.95
ch1z	**1.87E-13**	2.2E-4	**1.00E-3**	**0.611**	0.01	1.00	**0.12**	0.04	0.11
ch1v	**9.03E-13**	9.8E-4	**1.43E-3**	**0.668**	0.01	1.00	**0.12**	0.10	0.30
ch2v	**1.94E-13**	1.1E-3	**6.84E-4**	**0.544**	0.01	1.00	**0.12**	0.14	0.43
ch3v	**1.94E-13**	1.1E-3	**6.84E-4**	**0.544**	0.01	1.00	**0.12**	0.14	0.43
ch4v	**1.94E-13**	1.1E-3	**6.84E-4**	**0.544**	0.01	1.00	**0.12**	0.14	0.43
ch5v	**1.94E-13**	1.1E-3	**6.84E-4**	**0.544**	0.01	1.00	**0.12**	0.14	0.43
ch2z	**4.10E-14**	5.5E-4	**2.08E-4**	**0.613**	0.01	1.00	**0.12**	0.14	0.43
ch3z	**4.10E-14**	5.5E-4	**2.08E-4**	**0.613**	0.01	1.00	**0.12**	0.14	0.43
ch4z	**4.10E-14**	5.5E-4	**2.08E-4**	**0.613**	0.01	1.00	**0.12**	0.14	0.43
ch5z	**4.10E-14**	5.5E-4	**2.08E-4**	**0.613**	0.01	1.00	**0.12**	0.14	0.43
ch6	**1.12E-14**	2.2E-4	**6.10E-4**	**0.604**	0.01	1.00	**0.12**	0.04	0.11
pp4	**3.40E-14**	5.5E-4	**4.86E-4**	**0.635**	0.01	1.00	**0.12**	0.14	0.43
pp3	**2.23E-12**	1.4E-3	**5.93E-4**	**0.699**	0.01	1.00	**0.43**	0.20	0.61
pp2	**1.42E-13**	1.4E-3	**7.62E-4**	**0.608**	0.01	1.00	**0.43**	0.20	0.61
pp1	**7.15E-14**	5.5E-4	**3.90E-4**	**0.638**	0.01	1.00	**0.12**	0.14	0.43
bf3	**3.43E-13**	1.4E-3	**7.60E-4**	**0.611**	0.01	1.00	**0.43**	0.20	0.61
bf2	**9.21E-15**	5.5E-4	**4.18E-4**	**0.598**	0.01	1.00	**0.12**	0.14	0.43

NOTES: Values in bold type are constrained by hydrologic calibration process.

4.1.1.3 Net Infiltration Boundary Conditions

Software routine CONVERTCOORDS V1.1 is used to convert infiltration grid files obtained from the U.S. Geological Survey (USGS) (LB99EBS1233129.004) from UTM to NSPC (metric), while reformatting the file from matrix to column format. Infiltration values at selected model locations are then interpolated using software routine COLUMNINFILTRATION V1.1. In the climate model represented by these files, the monsoonal values are assigned to begin at 600 yr after waste emplacement, and the glacial values are assigned to begin at 2000 yr (LB99EBS1233129.004).

The resulting infiltration values for the model locations are shown in Table 6.

Table 6. Infiltration Values for Model Locations

Location	Infiltration Distribution	Present-Day (mm/yr)	Monsoonal (mm/yr)	Glacial (mm/yr)
l4c4	"lower"	0.00	10.13	1.99
	"upper"	24.29	47.61	82.01
l4c1	"lower"	0.18	4.80	3.32
	"upper"	10.98	19.40	34.44

NOTE: Source: Spreadsheet "infiltration.xls" (Attachment I)

These values are included in the NUFT V3.0s input file (*.in). The infiltration flux values for the 31 locations in the multiscale TH Model, produced in the manner described previously, are compiled in the spreadsheet "infiltration.xls" (Attachment I). For comparison purposes, the average flux values for all 31 locations are shown in Table 7.

Table 7. Average Flux Values for Model Locations

Location	Infiltration Distribution	Present-Day (mm/yr)	Monsoonal (mm/yr)	Glacial (mm/yr)
Average	"lower"	0.56	5.98	2.99
(31 locations)	"upper"	14.56	26.17	46.73

NOTE: Source: Spreadsheet "infiltration.xls" (Attachment I)

4.1.1.4 Temperature and Total Pressure Boundary Conditions

For the 2-D models used in these calculations, the model domain extends from the ground surface to the water table, and temperature and total pressure conditions are specified at each boundary. This information is required for both the L4C1 and the L4C4 locations. The values were obtained directly from the UZ model files ("bcs_99.dat" and "tspa99_primary_mesh"; LB99EBS1233129.001), which are read directly into the CHIM_SURF_TP V1.1 software routine. Inverse-squared distance weighting is used to interpolate the UZ model information at the required L4C1 and L4C4 locations.

Table 8. Temperature and Total Pressure Boundary Conditions

Model Location	Ground Surface		Water Table	
	Temperature (°C)	Pressure (Pa)	Temperature (°C)	Pressure (Pa)
L4C1	16.994	85,587	32.360	92,000
L4C4	15.910	84,511	32.544	92,000

NOTE: Source: Software routine CHIM_SURF_TP V1.1 and CRWMS M&O (2000f)

The temperature and total pressure boundary conditions used in this report are shown in Table 8.

Air Mass-Fraction Boundary Conditions

The air mass-fraction at the ground surface is calculated from the temperature and total pressure such that the relative humidity is 100 percent. This prevents water from diffusing upward through the ground surface when NUFT V3.0s calculates initial, steady conditions prior to the application of heat. The air mass-fraction is calculated from

$$W = 0.622 \frac{p_v}{p_b - p_v} \qquad \text{(Eq. 1)}$$

where

W = specific humidity, weight of water per unit weight of dry air

p_v = partial pressure of water vapor

p_b = barometric pressure

At the water table, the air mass-fraction is assigned a small value (comparable to the solubility of air-constituent gases in water). The air mass-fraction boundary condition values used in this report are shown in Table 9.

Table 9. Air Mass-Fraction Boundary Conditions

Model Location	Ground Surface Air Mass-Fraction	Water Table Air Mass-Fraction
L4C1	0.98584	1.0×10^{-6}
L4C4	0.98660	1.0×10^{-6}

NOTE: Source: Equation 1, using barometric pressure
Vapor pressures are obtained for the ground surface temperatures indicated in Table 8, using a vapor pressure table (Weast and Astle 1981, p. D-168).

4.1.1.5 Thermal Properties for Natural Barrier Materials

The thermal properties used by NUFT V3.0s are dry thermal conductivity (zero liquid saturation), wet thermal conductivity (100 percent water saturation), specific heat, and grain density. The values used for these calculations are shown in Table 10. For partial saturation, the NUFT V3.0s code is instructed in the input file (L4C*.in) to linearly interpolate between dry and wet values, based on liquid saturation. Linear interpolation is appropriate because only two constraint data points (dry and wet) are available. Notice that the data are not used directly in producing a technical output that provides estimates for any of the principal factors or potentially diruptive process events.

4.1.1.6 Thermal and Hydrologic Properties for EBS Materials

The EBS backfill and invert materials are designated as quartz sand (Overton Sand) and crushed tuff, respectively. These materials are unfractured but are represented in the DKM by splitting the total property value between the fracture and matrix continua. For example, half the backfill porosity is assigned to the matrix continuum, and half is assigned to the fracture continuum. Density, specific heat, thermal conductivity, permeability, and other hydrologic properties are assigned the same way. The AFC is not used for EBS material properties. The nominal property values (not split between continua) used for EBS materials are shown in Table 11.

4.1.1.7 Component Properties

Vapor-pressure lowering is active for these calculations. This feature of the NUFT V3.0s code simulates the interaction between capillary water potential and the vapor pressure governing water mass transfer between the liquid and gas phases. The vapor pressure is lowered by an amount determined from the capillary pressure using the Kelvin Equation (Atkins 1990, Equation 13b, p. 148). The capillary radius for this calculation is computed from the capillary pressure (Atkins 1990, Equation 12, p. 148). This increases the boiling temperature for partially saturated capillary media, which is the point at which vapor pressure equals the total pressure.

The components air and water are distributed in the gas and liquid phases. The physical properties of each component in each phase are given in a NUFT V3.0s input file ("vtough.pkg" in Attachment I). These properties include some assumed values (Assumption 5.1.4).

4.1.1.8 Thermal Loading and Aging of Waste Inventory

The thermal output of the waste decays with time, and this decay information is incorporated in a NUFT V3.0s input file (LDTH-SDT-0.3Qheat-50y_vent-00, Attachment I). For these calculations, the waste packages are represented as a line-averaged heat source oriented perpendicular to the plane of the vertical, 2-D model domain. The line source strength decays with time in a manner that represents radioactive decay of spent fuel and defense high-level waste. A composite of different waste package types is used (DTN SN9907T0872799.001; file: "heatTSPA-SR-99184-Ta.xls"; column F) (TBV-3599).

The line source strength is modified for the heat-removal effect of ventilation in the preclosure period. The referenced data (DTN SN9907T0872799.001) (TBV-3599) are calculated assuming that, during the 50-yr preclosure period, the preclosure ventilation will remove 50 percent of the

thermal output. For these calculations, 70 percent heat removal was used in accordance with management guidance (CRWMS M&O 2000c). Accordingly, the referenced data are corrected by multiplying the line-source strength values by the ratio 0.3/0.5 from time zero until 50 yr.

Table 10. Thermal Properties for Hydrostratigraphic Units

Model Layer	Rock Grain Density (kg/m3)	Rock Grain Specific Heat (J/kg–K)	Dry Conductivity (W/m–K)	Wet Conductivity (W/m–K)
tcw11	2550	823	1.60	2.00
tcw12	2510	851	1.24	1.81
tcw13	2470	857	0.54	0.98
ptn21	2380	1040	0.50	1.07
ptn22	2340	1080	0.35	0.50
ptn23	2400	849	0.44	0.97
ptn24	2370	1020	0.46	1.02
ptn25	2260	1330	0.35	0.82
ptn26	2370	1220	0.23	0.67
tsw31	2510	834	0.37	1.00
tsw32	2550	866	1.06	1.62
tsw33	2510	882	0.79	1.68
tsw34	2530	948	1.56	2.33
tsw35	2540	900	1.20	2.02
tsw36	2560	865	1.42	1.84
tsw37	2560	865	1.42	1.84
tsw38	2360	984	1.69	2.08
tsw39	2360	984	1.69	2.08
ch1z	2310	1060	0.70	1.31
ch1v	2310	1060	0.70	1.31
ch2v	2240	1200	0.58	1.17
ch3v	2240	1200	0.58	1.17
ch4v	2240	1200	0.58	1.17
ch5v	2240	1200	0.58	1.17
ch2z	2350	1150	0.61	1.20
ch3z	2350	1150	0.61	1.20
ch4z	2350	1150	0.61	1.20
ch5z	2350	1150	0.61	1.20
ch6	2440	1170	0.73	1.35
pp4	2410	577	0.62	1.21
pp3	2580	841	0.66	1.26
pp2	2580	841	0.66	1.26
pp1	2470	635	0.72	1.33
bf3	2570	763	1.41	1.83
bf2	2410	633	0.74	1.36

DTN: LB990861233129.001

Table 11. Nominal Property Values Used for Engineered Barrier System Materials

Property	Units	Backfill Value	Invert Value
Permeability	m^2	1.43E–11	6.15E–10
Porosity	none	0.41	0.545
van Genuchten α	Pa^{-1}	2.7523E–4	1.2232E–3
van Genuchten β	none	2.00	2.70
Residual Saturation	none	0.024	0.092
Grain Density	kg/m^3	2700	2530
Grain Specific Heat	J/kg–K	795.492	948
Thermal Conductivity	W/m–K	0.33	0.66

DTN SN9908T0872799.004; file: "indriftgeom_rev01.doc" (TBV-3471)

4.1.1.9 Geometry of the Drift and Drip Shield and Waste Package

Geometric data consistent with management guidance (Wilkins and Heath 1999) were compiled for use in TH models (DTN SN9908T0872799.004; file: "indriftgeom_rev01.doc") (TBV-3471). The drift diameter is 5.5 m. For this report, the waste package, drip shield, and pedestal supporting the waste package are combined into a single body with outside dimensions representing those of the drip shield. The rectilinear NUFT V3.0s grid is designed with spacings so that this composite body as well as the drift, invert, and backfill are represented. The cross-sectional areas of each component (drift, invert, backfill, waste package/drip shield) in the grid are approximately the same as specified (DTN SN9908T0872799.004) (TBV-3471).

4.1.1.10 Properties of the Waste Package

The waste package is modeled as a uniform solid body, with thermal conductivity and heat capacity scaled to represent the response of the composite body. The waste package is assigned a thermal conductivity of 14.42 W/m–K, specific heat of 488.86 J/kg–K, and density of 8189.2 kg/m^3 (DTN SN9908T0872799.004; file: "indriftgeom_rev01.doc") (TBV-3471). These values are based on area-averaging using prescribed geometry and materials (Wilkins and Heath 1999) for the waste package and drip shield. Treatment of the drip shield, waste package, and waste package supports as a composite body, is consistent with the objectives of this model, which include investigation of the bulk environment but not the fine-scale variability of conditions in the spaces enclosed by the drip shield. In addition, the temperature in the bulk environment during the thermal period will be determined by the processes that convey heat away from the drifts, but not by heat transfer within the spaces enclosed by the drip shields. The space between the drip shield and waste package remains warmer, and therefore drier, than the bulk environment during cooldown, so aqueous processes will take place primarily outside the drip shield for these conditions. Finally, the storage of sensible heat by the waste package and drip shield will not be significant to the bulk environment, because temperature changes will occur very slowly. Accordingly, the calculated results are insensitive to the value of specific heat, used to represent the composite body.

4.1.1.11 Model Gridding and Numerical Control Parameters

NUFT V3.0s input files (vtough.pkg; run_control_param_LDTH-v00; L4C*.in in Attachment I) specify control parameters such as numerical-convergence tolerances, time-step control, and parameters for controlling implementation of the nonlinear relations among saturation, relative permeability, and potential. When NUFT V3.0s is qualified, the values used can be evaluated against the ranges specified in the verification and validation documentation.

4.1.2 Gas Flux and Fugacity Model

4.1.2.1 CO_2 and ^{14}C Data from SD-12 and Other Surface-Based Boreholes

Total gas-phase CO_2 concentration data from several surface-based boreholes, in the form of averages computed from the reported data values, are shown in Table 12. This table includes all the qualified measurements of this type for the welded host rock. The data in Table 12 are used to support the average value of 1000 ppm for the concentration of CO_2 in the UZ gas phase, which is used in this report.

Gas-phase $^{14}CO_2$ activity data from several surface-based boreholes, in the form of averages computed from the reported data values, are shown in Table 13. Also tabulated is ^{14}C activity of dissolved inorganic carbon from porewater extracted from several core samples acquired from within the depth extent of the Topopah Spring welded tuff. This table includes all the qualified measurements of this type for the welded host rock. The individual data that were used to generate the averages in Table 13 are plotted against depth and used to support the gas-phase CO_2 advective-dispersive transport model in this report.

Notice that the data in Tables 12 and 13 are not used directly in producing a technical output that provides estimates for any of the principal factors or potentially diruptive process events.

4.1.2.2 Additional Input Data Used to Analyze CO_2 Transport at Borehole SD-12

In addition to the CO_2 and ^{14}C activity data for SD-12 cited in Table 12 and Table 13, additional input data consist of the following:

- Composition (i.e., bicarbonate concentration) of porewater samples extracted from samples of SD-12 drill core: DTNs GS970908312271.003 (TBV-3588), GS961108312271.002 (TBV_3610), and LL990702804244.100

- Hydrostratigraphic unit definitions and properties (fracture and matrix porosities): LB990861233129.001

- Stratigraphic contact elevations for stratigraphic units in borehole SD-12: DTN MO9811MWDGFM03.000, file "pix98usgs.xls" (TBV-3073).

- Correlation between stratigraphic units and hydrostratigraphic units: based on TSPA-VA stratigraphy (Bodvarsson et al. 1997, Table 3.4-1) interpreted for this model at the location of borehole SD-12, and including newly defined hydrostratigraphic units TSw37, TSw38, and TSw39.

- Matrix saturation for hydrostratigraphic units intercepted by borehole SD-12, estimated from the information of matrix saturation (Bodvarrson et al. 1997, Figure 6.4.10)

Notice that the data are not used directly in producing a technical output that provides estimates for any of the principal factors or potentially diruptive process events. The information used from the preceding sources is reproduced directly in the spreadsheet (both worksheets of the file "gasC14-SD-12-1996data.xls").

Table 12. Gas-Phase CO_2 Concentration Data for the Host-Rock Units, from Analysis of Gas Samples Obtained in Surface-Based Boreholes

Borehole (Year Data Collection Finished)	Sampled Depth Range (ft)	Topopah Spring Welded Tuff Depth Range (ft) [A]	Average CO_2 (ppm) [B]	Number of Samples	DTN
NRG-6 (1994)	490–1215	465–TD [C]	1080	22	GS941208312261.008
NRG-7 (1994)	600–1215	518–1415	1000	20	GS941208312261.008
UZ-6 (1994)	1225	610–1333	2500	3	GS940708312261.005
UZ-6 (1995)	800–1195	610–1333	701 1181 [D]	34 20	GS950808312261.004
The following line is provided as unqualified, corroborative data only.					
UZ-1 (1985)	501–1207	470–TD [C]	200	19	GS930508312271.021

NOTES: A Stratigraphic picks obtained from DTN MO9811MWDGFM03.000, file: "pix98usgs.xls" (TBV-073)
B Average of reported data in the specified Topopah Spring welded tuff depth range
C Total depth
D Calculated in the same manner except excluding nondetects and measurements less than 0.005 percent or 50 ppm CO_2

Table 13. Gas-Phase and Porewater $^{14}CO_2$ Isotopic Data for the Host-Rock Units, from Analysis of Gas Samples and Preserved Rock-Core Samples Obtained from Surface-Based Boreholes

Surface-Based Borehole Gas Samples					
Borehole (Year Data Collection Finished)	**Sampled Depth Range (ft)**	**Topopah Spring Welded Tuff Depth Range (ft)** [A]	**Average ^{14}C (pmc)** [B]	**Number of Samples**	**DTN**
NRG-5 (1996)	572–799	565–TD [C]	59.0	4	GS970283122410.002
NRG-5 (1996)	1225	565–TD [C]	93.1	1	GS941208312261.008
NRG-6 (1994)	600–925	465–TD [C]	88.7	2	GS941208312261.008
NRG-7 (1994)	890	518–1415	111.0 [D]	1	GS941208312261.008
SD-12 (1996)	561–1265	470–1278	45.5	8	GS961108312271.002 (TBV-3610)
SD-7 (1996)	339–1558.5	248–1090	62.8	11	GS970283122410.002
UZ-6 (1995)	800–1195	610–1333	84.4	4	GS960208312261.002
The following line is provided as unqualified, corroborative data only.					
UZ-1 (1985)	501–1207	470–TD [C]	65.3	7	GS930508312271.021
Surface-Based Borehole Extracted Porewater Samples					
SD-12 (1996)	693.5	470–1278	60.2	1	GS970908312271.003 (TBV-3588)
SD-7 (1996)	339.0	248–1090	74.1	3	GS961108312271.002 (TBV-3610)

NOTES: A Stratigraphic picks obtained from DTN MO9811MWDGFM03.000, file "pix98usgs.xls" (TBV-073)
B Average of reported data in the specified Topopah Spring welded tuff depth range
C Total depth
D Values of pmc > 100% indicate influence from nuclear-age carbon

4.1.2.3 Infiltration Flux

Three values of the infiltration flux are used to represent the range of conditions in the UZ hydrologic model. The values used for interpreting SD-12 data are averages over the repository layout for the lower, mean, and upper infiltration-flux distributions (LB99EBS1233129.004). The average values for all Multiscale Model locations, for present-day Yucca Mountain conditions are as follows:

- Present-day average for "lower" distribution = 0.56 mm/yr
- Present-day average for "mean" distribution = 5.98 mm/yr
- Present-day average for "upper" distribution = 14.56 mm/yr

These values were obtained from spreadsheet "infiltration.xls" (Attachment I) which is described—along with the data manipulation process used to derive the multi-scale model locations and flux values—in the TH Model sections of this report.

4.1.3 Cementitious Materials Model

4.1.3.1 Thermodynamic Data

The unqualified PHREEQC thermodynamic database file "wateq4f.dat" (CRWMS M&O 1999f, Attachment B) was modified by adding data for certain cement minerals, to form the database file "wateqcem.dat" used in these calculations (Attachment I). The additional thermodynamic data were obtained from the "com" database provided with the EQ3/6 modeling code (Wolery 1992a). The "com" database used for this purpose is contained in the file "data0.com" (Attachment I).

Additional detail on how chemical data (dissociation equilibrium constant and enthalpy of formation) for ettringite and tobermorite were obtained from the "data0.com" file and modified for use in the "wateqcem.dat" file is provided below.

Equilibrium Constant for Ettringite

The dissociation reaction

$$Ca_6Al_2(SO_4)_3(OH)_{12} : 26H_2O + 12H^+ = 6Ca^{2+} + 2Al^{3+} + 3SO_4^{2-} + 38H_2O$$

(Eq. 2)

is the same in the EQ3/6 "com" database and is the same basis species used for the PHREEQC database; thus, the equilibrium constant value log K = 62.5362 is used without transformation.

Enthalpy of Reaction for Ettringite

Using the dissociation reaction (Equation 2), the enthalpy of reaction ΔH_r for ettringite is found from the following:

$$\Delta H_r = \sum \nu_i \Delta H_{f,i}$$

(Eq. 3)

where

ν_i = stoichiometric coefficients (positive for products, negative for reactants)

$\Delta H_{f,i}$ = enthalpies of formation for each species

Using the $\Delta H_{f,i}$ value for ettringite from the "data0.com" EQ3/6 database (Attachment I) and values for all other species from Robie, et al. (1979, pp. 12, 19, and 21) yields

$$\Delta H_r = 4193.000 - 6(129.74) - 2(126.91) - 3(217.32) - 32(68.315) = -87.19 \text{ kcal/mol}$$

(Eq. 4)

Equilibrium Constant for Tobermorite-14Å

The equilibrium constant for tobermorite is calculated using the relationship (Stumm and Morgan 1981, combining Equation 230 and Equation 234, page 58):

$$\Delta G^0 = -RT \ln K = \sum_{\substack{\text{products} \\ -\text{reactants}}} \nu_i \mu_i^0$$

(Eq. 5)

where

ΔG^0	=	standard free energy of reaction (kcal/mol)
R	=	universal gas constant (8.312 Pa-m^3/mol-K or J/mol-°K)
T	=	absolute temperature (°K)
μ^0_i	=	standard free energies of formation for each product and reactant

The equilibrium coefficient for tobermorite at 298 K is calculated for the dissociation reaction

$$Ca_5Si_6H_{21}O_{27.5} + 10H^+ = 5Ca^{2+} + 6H_4SiO_4 + 3.5H_2O$$

(Eq. 6)

A value of –2647.300 kcal/mol for the standard free energy of formation for tobermorite-14Å is obtained from the "data0.com" file for EQ3/6 (Attachment I). Values for the other species are obtained from Garrels and Christ (1965, pp. 408, 418, and 421) (TBV-4576). The resulting calculation yields

$$\Delta G^0 = 5(-132.18) + 6(-300.3) + 3.5(-56.69) - (-2647.300) - 10(0) = -13.82 \text{ kcal/mol}$$

(Eq. 7)

The corresponding ln K value is found for T = 298 K using Equation 5, converting joules to kcal (4.18×10^3 J/kcal), and converting to $\log_{10}$ ($2.3026 \log_{10} x = \ln x$)

$$\log K = \left(\frac{1}{2.3026}\right)\ln K = -(-13.82)\frac{(4.18\times 103)}{(2.3025)}(8.312)(298) = 10.13$$

(Eq. 8)

which wis used in the PHREEQC simulations.

Enthalpy of Reaction for Tobermorite-14Å

Using dissociation reaction (Equation 6), the enthalpy of reaction ΔH_r for tobermorite-14Å is found using Equation 2.

Using the $\Delta H_{f,i}$ value for tobermorite-14Å from the EQ3/6 database and values for all other species from Robie et al. (1978) yields

$$\Delta H_r = 2911.25 - 5(129.74) - 6(348.95) - 3.5(68.315) = 70.25\ \text{kcal/mol}$$

(Eq. 9)

The PHREEQC dissociation constant values for solid species used in this model are compared to the SUPCRT database used with the EQ3/6 modeling code (Wolery 1992a) contained in file "data0.sup" (Attachment I). The comparison is shown in Table 14. Notice that the SUPCRT database is contained in the EQ3/6 code.

Table 14. Comparison of Equilibrium Constants (log10 K values at 25°C) from the PHREEQC and EQ3/6 (data0.com, Attachment I) Databases for Solid Phases Considered in Modeling of Cementitious Materials

Phase	Reaction	EQ3/6 [A] log K	PHREEQC log K
Anhydrite	$CaSO_4(s) = Ca^{2+} + SO_4^{2-}$	–4.3064	–4.36
Brucite	$Mg(OH)_2(s) + 2H^+ = Mg^{2+} + 2H_2O$	16.298	16.84
Calcite	$CaCO_3(s) + H^+ = Ca^{2+} + HCO_3^-$	1.8487	1.849
Chalcedony	$SiO_2(s) = SiO_2$	–3.7281	–3.55
$CO_2(g)$	$HCO_3^- + H^+ = H_2O + CO_2(g)$	7.8136	7.820
Ettringite	$Ca_6Al_{12}(SO_4)_3(OH)_{12}{\cdot}26H_2O(s) + 12H^+ = 2Al^{3+} + 6Ca^{2+} + 3SO_4^{2-} + 38H_2O$	62.5362	N/A
Gypsum	$CaSO_4{\cdot}2H_2O(s) = Ca^{2+} + SO_4^{2-} + 2H_2O$	–4.4823	–4.58
Portlandite	$Ca(OH)_2(s) + 2H^+ = Ca^{2+} + 2H_2O$	22.5552	22.8
Quartz	$SiO_2(s) = SiO_2$	–3.9993	–3.98
Amorphous silica	$SiO_2(s) = SiO_2$	–2.7136	–2.71
Tobermorite-14Å	$Ca_5Si_6H_{21}O_{27.5}(s) + 10H^+ = 5Ca^{2+} + 6SiO_2(aq) + 15.5H_2O$	63.8445	N/A

NOTE: A EQ3/6 log K data are from the SUPCRT database (file: "data0.sup" in Attachment I) except for gypsum, ettringite, portlandite, and tobermorite, which are from the "com" database (file: "data0.com" in Attachment I). The PHREEQC database does not include log K values for ettringite and tobermorite; these were obtained from the "com" database.

4.1.3.2 Type of Grout

Type-K expansive cement will be used for rockbolt anchorage (CRWMS M&O 2000a) (TBV-4587). The following additional mix parameters are specified:

- Water-cement mass ratio between 0.4 and 0.6 to promote strength and durability
- Silica fume admixture (5 percent of dry weight) to increase durability by limiting porosity and permeability
- Superplasticizer (1 percent of dry weight) for workability

4.1.3.3 Excess Grout

Total grout used for each rockbolt will be limited to three times that needed to fill the annulus around the steel bolt (CRWMS M&O 2000a, TBV-4621). Rockbolt Design

The rockbolts evaluated for this model are nominally 2.15-m long, 1.125-in. diameter steel bolts grouted into 2.5-inch diameter holes (CRWMS M&O 2000a) (TBV-4588). Rockbolts will be installed in radial arrays of six bolts installed in the roof of the drift; this will be repeated every 1.5 m along drift. The rockbolts will be used in addition to steel sets only where the repository is constructed in the middle nonlithophysal unit of the Topopah Springs tuff.

The mass of cement used in the grout will be 22.65 kg per rockbolt (including the threefold excess). With six rockbolts every 1.5 m along the drift opening, the cement usage will be 91 kg/m (only in the portion of the potential repository where grouted rockbolts are used).

4.1.3.4 Composition of Fracture Water in the Unsaturated Zone

The grout will be fluid-saturated when first installed. Moisture potential equilibrium will be reached with the adjacent rock matrix, whereupon the grout will be partially saturated. The grout permeability in this condition will be low (a fraction of the saturated permeability in Assumption 5.3.5). For significant leachate to form and flow into the drifts, the source of the water will be fracture flow because the relative permeability of the grout at likely values of the in situ matrix moisture potential will be low. Accordingly, the initial composition of water that interacts with the grout and flows into the drifts is that of fracture water.

Naturally occurring percolating fracture waters have not been observed in the host rock, possibly because fracture flow is episodic. Consequently, groundwater from well J-13 is used as an analogue for fracture water that percolates through the host rock and may seep into drifts. The basis for this is documented by Harrar et al. (1990, DTN LL980711104242.054). Notice that this data set is not used directly in producing a technical output that provides estimates for any of the principal factors or potentially diruptive process events.

The Cementitious Materials Model concerns only major changes in water composition; thus, only the major chemical constituents of J-13 water (Table 15) are used in models of leachate composition.

Table 15. Composition of Fracture Water Used for Cementitious Material Model

pH = 7.41					
	Concentration			Concentration	
Element	(mg/L) [A]	(mol/kg) [B]	Species	(mg/L) [A]	(mol/kg) [B]
Na	45.8	1.99E-003	F^-	2.18	1.15E-004
K	5.04	1.29E-004	Cl^-	7.14	2.02E-004
Ca	13.0	3.24E-004	NO^{3-}	8.78	3.19E-005
Mg	2.01	8.27E-005	SO_4^{2-}	18.4	1.92E-004
Si	28.5	1.02E-003	HCO_3^-	128.9	2.11E-003

Notes:

A. Source DTN: LL980711104242.054, B. Source: file "grout301.out" (Section 6.3; Attachment I)

Composition of matrix porewater in the UZ is variable, and greater concentrations for certain constituents have been observed than are present in J-13 water. For example, matrix porewater chloride concentration data for various tuff units at Yucca Mountain (GS970908312271.003 and GS961108312271.002) (TBV-3588) may be compared with the average chloride concentration for J-13 water (discussed in Section 4.1.2.2). Compared to other waters such as matrix porewater, calculated results for the Cementitious Materials Model are relatively insensitive to the use of J-13 water as an initial composition because, for the repository CO_2 and temperature conditions considered, leachate composition tends to be dominated by solutes such as calcium and sulfate, which are derived from the cement.

Grout make-up water also has the same chemical composition as J-13 well water in this model. Groundwater that is used for construction will be similar in composition to J-13 water. Compared to other waters (e.g., matrix porewater), calculated results are relatively insensitive to the use of J-13 for make-up water for the same reasons given previously.

4.1.3.5 Temperature and CO_2 Fugacity

The temperature and CO_2 fugacity conditions used for the Cementitious Materials Model, for the L4C4 model location with the "upper" infiltration distribution, are calculated in Section 6.1 and Section 6.2 of this report.

4.1.4 Microbial Effects Model

Those corrosion-resistant materials (CRMs) under consideration in the current repository design (DTN: LL991203505924.094) contain carbon, phosphorus, and sulfur in the amounts shown in Table 16.

Table 16. Selected Elements Contained in Considered Corrosion-Resistant Materials

CRM	Carbon	Phosphorus	Sulfur
Ti Gr.7 [A]	0.08%	0%	0%
Alloy-22 [A]	0.015%	0.02%	0.02%
316L [B]	0.03%	0.045%	0.03%

NOTES: A ASTM 1994, pp.110-116, 410–413
B ASTM 1997b, pp. 36–42

Corrosion rates for carbon steel and Alloy-22 are shown in Table 17. These rates came from electrochemical polarization resistance measurement on coupons that were incubated in tuff cultures. The data in Table 17 constitute best available information regarding the acceleration of corrosion by microbial effects.

Table 17. Corrosion Rates from Polarization-Resistance Experiments

Tested Sample Initial Condition	Average Corrosion Rate (μm/yr)
Carbon Steel Alloy 1020 + YM microbes	8.800
Sterile Carbon Steel Alloy 1020	1.400
Alloy-22 + YM microbes	0.022
Sterile Alloy-22	0.011

DTN: LL991203505924.094

NOTES: YM = Yucca Mountain
Blank fields indicate not analyzed
n.d. = not detected

4.1.5 Normative Precipitates and Salts Model

4.1.5.1 J-13 Water Composition

Well J-13 is a producing water well that is screened in the Topopah Spring welded tuff. J-13 water is of the dilute $NaHCO_3$ type, and its composition is used as a chemical analogue for fracture waters in the repository host rock. As described in the following text, this is a conservative approach with respect to prediction of high-pH conditions. The concentrations for various analytes, computed as mean values over 19 analyses, are shown in Table 18.

A synthetic J-13 well water was created for use in evaporation tests, by combining several inorganic compounds with deionized water, mixing and stirring for several days. The procedure was undertaken at room temperature, under ambient atmospheric gas composition conditions. The batch was decanted and analyzed for metals (Ca, Mg, Na, K, and Si) by inductively coupled plasma spectrometry, for anions (chloride, fluoride, nitrate, and sulfate) by ion chromatography, and for bicarbonate by infra-red analysis (spectral absorption by purged CO_2). The pH was also measured. The composition of synthetic J-13 water is compared with sampled J-13 water in Table 19. The significance of differences in composition is discussed in Section 6.5.4.

Table 18. Major Ion Concentrations for J-13 Well Water

	Qualified?	Al µg/L	B µg/L	Ca mg/L	Cl mg/L	F mg/L	Fe µg/L	HCO_3[A] mg/L	K mg/L	Li µg/L	Mg mg/L	Mn µg/L	Na mg/L	NO_3 mg/L	PO_4 µg/L	Si mg/L	SO_4 mg/L	Sr µg/L	pH[B]
1	Y	—	—	14	8.4	2	160	124	6.6	40	2.4	240	46	5.6[D]	120	26.7	25[D]	100	7
2	Y	62	140	14	7.4	2.4	40	136	5	—	1.8	110	48	4.5[D]	< 10	27.1	23[D]	—	6.8
3	Y	—	—	13	7.2	2.7	< 10	126	4.8	40	2.1	30	44	6.8	< 10	28.5	18	90	7.6
4	Y	8	130	14	5.4[D]	2.4	< 10	124	5.4	40	2.5	< 10	44	9	< 10	26.7	18	90	7.3
5	Y	—	—	12	7.1	2.4	< 10	124	5	40	2.1	< 10	42	7.2	< 10	26.7	17	20	7.4
6	Y	—	—	13	7.7	1.7	0.0[D,E]	130	4.7	50	2	—	47	—	—	—	21	60	7.3
7	Y	—	—	13	7.5	1.7	0.0[D,E]	130	4.7	50	2	—	50	—	—	—	20	40	7.3
8	Y	8	—	12	6.4	2.1	11	170[D]	5.5	—	1.7	12	46	9.9	—	31	18	40	
9	Y	26	—	11.5	6.4	2.1	44	143	5.5	70	1.73	11	45	10.1	100[D,G]	30	18	40	6.9
10	Y	40	—	14	6.3	1.8	39	127	5	59	2.2	14	50	9.1	< 100	37.6[D]	18	45	8.3
11	Y			12	8.1	2.2		120	4.5		1.9		44	8.1		28.5	17		7.7
12	Y			12	7	2.2		120	3.7		2		44	8.3		26.6	19		7.6
13	Y	30	—	11.5	6.4	2.1	40	143	5.3	60	1.8	1	45	10.1	—	30	18	—	6.9
14	Y	12	128	12.5[G]	6.9[G]	2.2[H]	6	125[F,H]	5.1[H]	42	1.9[H]	—	44	9.6	—	27[H]	18.7[H]	35	7.6
15	Y	—	142	12.5	7	2.2	—	—	4.8	—	1.9	—	45	8.4	< 100	27.2	18.1	—	—
16	Y			—	—	—		—	—		—		45	—		27.2	—		—
17	Y	< 100	130	14	—	—	< 10	—	—	49	2.1	< 5	47	—	—	30.9	—	41	—
18	Y	110	< 100	15	7.3	2.7	—	118	5.5	—	2.1	—	50	8.7	2800[D,G]	31.9	18.8	—	7.2
19	Y	< 100	—	13	7.1	2.1	< 10	143	4.5	40	2	—	45	8.9	—	30	18.7	40	8.2
N		8	5	18	16	8	7	13	17	12	18	7	19	13	1	16	15	12	15
Avg		37	134	12	6.7	4.4	49	139	4.7	48	1.9	60	46	8.8	120	26.8	17	53	6.8–8.3

Source DTN: LL980711104242.054 (Harrar et al. 1990)

NOTES: Blank fields represent analyses that were not made.

Symbol "—" indicates below detection limit of the analytical methods.

A Alkalinity expressed as bicarbonate

B pH is not average but is expressed as the total range of measured values

C Date and source identifiers exactly as they appear in source DTN

D Not used in calculation of mean value; also, non-detects or less-than values are not used in calculation of mean.

E Data from reference 3 of the source report, as cited in source DTN

F Data from reference 10 of the source report, as cited in source DTN

G Value indicated as "probably erroneous" in source DTN.

H These values represent averages over a 12-month period, as reported by the source DTN.

4.1.5.2 Synthetic Porewater Composition

A second set of tests was performed to investigate precipitates that could be produced by evaporation of matrix porewater, a reference water composition based qualitatively on reported analyses for porewater extracted from the Topopah Spring welded tuff (DTN: LB991200DSTTHC.001) (TBV-4575). Such waters have substantially less Na and K and more Ca and Mg than does J-13 water, and the anionic species are dominated by sulfate and chloride instead of bicarbonate.

A synthetic porewater (SPW) was created for use in evaporation tests by combining several inorganic compounds with deionized water, mixing, and stirring for several days. The procedure was undertaken at room temperature, under ambient atmospheric gas compositional conditions. The batch was then decanted to remove undissolved reagents, and the resulting solution was analyzed for metals (Ca, Mg, Na, K, and Si) by inductively coupled plasma spectrometry, for anions (chloride, fluoride, nitrate, and sulfate) by ion chromatography, and for bicarbonate by alkalinity titration. The pH was also measured. The average of measured compositions for several batches of synthetic porewater is given in Table 20.

4.1.6 EBS Colloids Model

4.1.6.1 Steel Contained in Engineered Barrier System Components

See Table 27, Mass and Surface Area for Structural Steel Used in the Engineering Barrier System.

4.1.6.2 Groundwater Chemistry

See Table 18, Major Ion Concentrations for J-13 Well Water.

Table 19. Average Composition of Synthetic J-13 Water Used in Reported Tests

Species	Synthetic J-13 Water (mg/L)	Average J-13 Water (mg/L)
Ca	6.4	12
Cl^-	6.9	6.7
F^-	2.2	4.4
HCO_3^-	108	139
K	5.3	4.7
Mg	2.2	1.9
Na	46	46
NO_3^-	8.0	8.8
SO_4^{2-}	18.1	17
Si(aq)	11.3	57.3
pH	7.84	6.8-8.3

DTN: LL991008104241.042 and LL980711104242.054

NOTE: Average J-13 water composition from Table 18.

Table 20. Average Composition of SPW Used in Reported Tests

Ions	Synthetic Porewater (mg/L)	Average Porewater (mg/L) [A]
Ca^{2+}	57.3 ± 1.80	101
Cl^-	76.6 ± 1.30	117
F^-	2.16 ± 0.09	0.86
HCO_3^-	20.3 ± 4.30	200 [B]
K^+	4.0 ± 0.27	8.0
Mg^{2+}	11.8 ± 0.20	17
Na^+	8.56 ± 0.32	61.3
NO_3^-	10.7 ± 0.29	Note C
SO_4^{2-}	83.9 ± 1.90	116
$SiO_2(aq)$	22.2 ± 2.1	70.6
pH	7.55 ± 0.12	8.32 (25°C)

DTN: LL991008004241.041 and LB991200DSTTHC.001 (TBV-4575)

NOTES: A Averages from porewater samples ESF-HD-PERM1(30.1'-30.5').

B Total dissolved inorganic carbon reported as bicarbonate; calculated from charge balance.

C Not analyzed.

4.1.6.3 Size Distribution of Groundwater Colloids

The size and concentration distributions for colloids in groundwaters, are used as analogues for colloid distribution in waters that may flow through the EBS. A number of wells in the vicinity of Yucca Mountain have been sampled (from the saturated zone), and the resulting data are shown in Tables 21 and 22.

4.1.6.4 Sorption Coefficients of Pu and Am on Hematite, Montmorillonite, and Sillica Colloids

Sorption Coefficient values for sorption of Pu and Am on Hematite, Montmorillonite, and Sillica Colloids are presented in Table 59 in Section 6.6.3.2. The source DTNs of the data are LA0003NL831352.002 and LA0005NL831352.001 (TBV).

4.1.6.5 Miscellaneous Parameters, Equations, and Physical Constants

The specific gravity of anhydrous hematite is assigned a value of 5.24 (Perry and Chilton, 1973, B-109). Diffusion coefficients and molecular diameters for nonelectrolytes are listed in Table 23.

Table 21. Colloid Concentrations and Sizes from Nye County Wells

Colloid Size (nm)	Nye County NC-EWDP-01S, @~170 ft (5/18/99) (counts/mL)	Nye County NC-EWDP-01S, 250 ft (5/17/99) (counts/ mL)	Nye County NC-EWDP-03S, @~449 ft (5/20/99) (counts/mL)	Nye County NC-EWDP-03S, @~390 ft (5/20/99) (counts/mL)	Nye County NC-EWDP-09SX, @~310 ft (5/18/99) (counts/ mL)	Nye County NC-EWDP-09SX. @~270 ft (5/19/99) (counts/mL)	Nye County NC-EWDP-09SX, @~150 ft (5/19/99) (counts/mL)	Nye County NC-EWDP-09SX, @~112 ft (5/19/99) (counts/mL)	Nye County Airport Well AD-2 (6/10/99) (counts/mL)
50	9.27E+05	2.33E+06	5.47E+07	2.79E+08	6.28E+06	1.10E+07	1.19E+07	1.07E+07	7.90E+06
60	1.01E+06	2.79E+06	6.86E+07	3.14E+08	6.24E+06	1.35E+07	1.33E+07	1.36E+07	1.11E+07
70	8.64E+05	2.57E+06	6.77E+07	3.38E+08	6.43E+06	1.14E+07	1.27E+07	1.22E+07	1.06E+07
80	8.01E+05	1.92E+06	5.37E+07	2.86E+08	5.78E+06	9.76E+06	1.18E+07	8.86E+06	1.12E+07
90	8.51E+05	1.44E+06	4.31E+07	2.02E+08	4.40E+06	9.25E+06	1.27E+07	7.82E+06	9.10E+06
100	1.14E+06	2.09E+06	3.06E+07	1.30E+08	3.41E+06	5.26E+06	8.44E+06	5.62E+06	7.06E+06
110	8.01E+05	1.93E+06	1.34E+07	6.52E+07	1.84E+06	4.08E+06	6.85E+06	3.55E+06	5.36E+06
120	7.26E+05	9.90E+05	5.10E+06	5.04E+07	1.11E+06	1.83E+06	5.01E+06	2.47E+06	2.96E+06
130	5.26E+05	7.90E+05	7.88E+06	2.96E+07	8.42E+05	1.61E+06	3.42E+06	1.53E+06	3.11E+06
140	6.26E+05	7.27E+05	3.25E+06	2.82E+07	6.89E+05	1.19E+06	2.79E+06	1.48E+06	2.96E+06
150	5.76E+05	5.26E+05	2.32E+06	1.48E+07	3.06E+05	9.34E+05	1.75E+06	7.19E+05	2.12E+06
160	4.51E+05	5.89E+05	1.85E+06	2.22E+07	3.45E+05	7.64E+05	1.51E+06	7.19E+05	1.62E+06
170	4.13E+05	6.02E+05	9.28E+05	7.42E+06	2.30E+05	3.82E+05	1.35E+06	7.64E+05	1.06E+06
180	3.13E+05	4.76E+05	1.39E+06	7.42E+06	1.53E+05	5.94E+05	1.19E+06	5.39E+05	9.88E+05
190	3.63E+05	4.76E+05	1.39E+06	4.45E+06	1.92E+05	2.12E+05	1.35E+06	2.25E+05	9.88E+05
200	3.51E+05	6.02E+05	4.62E+05	5.93E+06	2.68E+05	5.94E+05	1.19E+06	6.29E+05	1.41E+06
Total 50 to 200 nm Colloid Particles (counts/mL)	1.07E+07	2.09E+07	3.56E+08	1.78E+09	3.85E+07	7.24E+07	9.71E+07	7.14E+07	7.95E+07

DTN: LA0002SK831352.001

Table 22. Colloid Concentrations and Sizes from Yucca Mountain Site Characterization Project Wells

Colloid Size (nm)	J13 Unfiltered (3/2/99) (counts/mL)	SD6 Unfiltered (6/2/99) (counts/mL)	SD6 Unfiltered (6/8/99) (counts/mL)	WT-17 Unfiltered (7/1/98) (counts/mL)	WT-3 Unfiltered (6/22/98) (counts/mL)	WW20 0.45 Unfiltered (11/5/97) (counts/mL)	UE29A1 Unfiltered (11/06/97) (counts/mL)	UE29A2 Unfiltered (11/06/97) (counts/mL)	C Well Unfiltered (2/18/99) (counts/mL)
50	2.00E+05	6.36E+07	1.49E+07	2.57E+08	8.75E+05	8.19E+06	8.01E+05	3.54E+06	4.64E+05
60	2.50E+05	7.91E+07	1.72E+07	3.02E+08	8.50E+05	1.06E+07	1.03E+06	5.15E+06	5.88E+05
70	2.05E+05	8.80E+07	1.69E+07	3.01E+08	1.08E+06	9.69E+06	9.70E+05	4.76E+06	6.06E+05
80	1.64E+05	7.17E+07	1.48E+07	2.64E+08	6.25E+05	7.34E+06	8.31E+05	4.70E+06	4.84E+05
90	1.32E+05	5.74E+07	1.24E+07	2.39E+08	6.50E+05	5.25E+06	7.36E+05	3.81E+06	3.24E+05
100	7.22E+04	4.26E+07	8.67E+06	2.04E+08	5.75E+05	4.71E+06	6.92E+05	3.23E+06	5.93E+05
110	3.98E+04	2.64E+07	4.46E+06	1.28E+08	4.75E+05	2.92E+06	5.57E+05	2.45E+06	3.99E+05
120	1.93E+04	1.71E+07	3.85E+06	9.42E+07	3.50E+05	1.95E+06	3.18E+05	1.93E+06	2.36E+05
130	2.74E+04	1.63E+07	3.49E+06	6.28E+07	5.50E+05	1.49E+06	3.08E+05	1.58E+06	1.55E+05
140	2.30E+04	6.59E+06	1.93E+06	6.16E+07	2.50E+05	1.30E+06	2.94E+05	1.33E+06	1.34E+05
150	1.99E+04	1.16E+07	1.93E+06	4.59E+07	2.25E+05	1.01E+06	1.89E+05	1.25E+06	1.19E+05
160	8.72E+03	6.59E+06	8.43E+05	4.35E+07	1.25E+05	8.51E+05	1.79E+05	7.64E+05	1.04E+05
170	1.12E+04	6.59E+06	9.63E+05	3.02E+07	2.50E+05	6.89E+05	1.79E+05	5.13E+05	1.09E+05
180	4.98E+03	5.81E+06	1.08E+06	2.54E+07	1.50E+05	3.76E+05	1.14E+05	6.26E+05	1.24E+05
190	9.34E+03	5.04E+06	4.82E+05	2.66E+07	3.75E+05	3.13E+05	1.19E+05	4.38E+05	9.02E+04
200	4.36E+03	3.10E+06	1.20E+06	2.54E+07	3.75E+05	5.26E+05	1.29E+05	5.01E+05	1.04E+05
Total 50 to 200 nm Colloid Particles (counts/ml)	1.19E+06	5.07E+08	1.05E+08	2.11E+09	7.78E+06	5.72E+07	7.45E+06	3.66E+07	4.63E+06

DTN: LA0002SK831352.002

Table 23. Diffusion Coefficients and Molecular Diameters for Nonelectrolytes

Diffusion Coefficient ($cm^2/sec*10^5$	Diameter (Å)
2.2	2.9
0.7	6.2
0.25	13.2
0.11	28.5
0.05	62.0
0.025	132.0

NOTE: Source: Perry and Chilton, 1973, Table 17-10, p. 17-38

4.1.7 Chemical Reference Model

The required inputs for EQ3/6 modeling are described in Section 4.1.7.1 through Section 4.1.7.8.

4.1.7.1 Reference Chemical Composition of Fracture Water in the Host Rock

Naturally occurring percolating fracture waters have not been observed in the host rock, possibly because fracture flow is episodic. Groundwater from well J-13 is chemically analogous to fracture water that percolates through the host rock and may seep into drifts. The basis for this was originally documented by Harrar et al. (1990). The major chemical constituents of J-13 water are shown in Table 18. As discussed in Section 6.5.7, J-13 water, compared with matrix porewaters that contain more chloride and sulfate, produces higher pH conditions when evaporated.

4.1.7.2 Thermal-Hydrologic Conditions

Zone-averaged temperature, liquid fluxes, vapor fluxes, and liquid masses are calculated by the TH Model. Repository center and edge locations, and the "lower" and "upper" infiltration distributions, are considered in the TH Model for four cases. The L4C4 location, with the "upper" infiltration distribution, is selected as the reference case for chemical analysis.

The six zones defined for the TH Model, plus the far-field host rock (Zone 0), as shown in Figure 2 and Figure 3 (Section 6.1.2.1) are combined into four composite zones for the Chemical Reference Model, as represented in Table 24. The use of composite zones for the reference model is discussed in Section 6.7.

In the reference model, for each time period, the necessary fluxes between composite zones, liquid masses for each composite zone, average temperatures for each composite zone, and evaporative concentration factors for each composite zone are calculated and compiled as discussed in Section 3.1.2.8 (e.g., file: "th+gas_model-L4C4-ui-04.xls"; worksheet: CHEMprobL4C4upper). The values used for the Chemical Reference Model are shown in Table 25.

4.1.7.3 CO_2 and O_2 Fugacities

For chemical modeling, the necessary CO_2 and O_2 fugacities for each time period are compiled as discussed in Section 3.2 (e.g., file: "th+gas_model-L4C4-ui-04.xls"; worksheet: CHEMprobL4C4upper). These fugacities are considered uniform throughout the zones modeled. The values used for the Chemical Reference Model are shown in Table 25.

4.1.7.4 Thermodynamic Data

The thermodynamic data used for these calculations consists of the "data0.com" supplied with EQ3/6 V7.2b (Attachment I). Only a subset of the data in this file are important to the chemical modeling presented in this report. Many of the data values are also part of the "data0.sup.R2" file (Attachment I).

Table 24. Correspondence Between Thermal Hydrology Model Zones and Composite Zones for the Chemical Reference Model

TH Model Zones	Chemical Reference Model Composite Zones
Zone 0 (far-field host rock)	Zone 0
Zone 1 (host rock)	Zone 1/2
Zone 2 (drift wall)	
Zone 3 (backfill)	Zone 3/4
Zone 4 (drip-shield surface)	
Zone 5 (lower backfill)	Zone 5/6
Zone 6 (invert)	

A number of potential minerals were removed from the calculations by artificially suppressing their formation. This is done in geochemical modeling, when the chemical database includes minerals that either cannot form, or are unlikely to form, at the environmental conditions of the model. The database includes a superset of mineral species that can be used for many different types of geochemical problems, but some of these must typically be suppressed for a particular problem. Also, Gibb's phase rule (Stumm and Morgan, 1981, p. 304) limits the number of compositionally similar minerals that can coexist in a solvable geochemical problem.

Mineral suppression was accomplished in part by using the suppression option in EQ3/6. However, because the number of minerals to be suppressed exceeded the hard-coded array limits in version 7.2b, a number of these minerals were eliminated from a special copy of the "data0.com" data file, named "data0.elh" (Attachment I). A list of the suppressed phases is included in each EQ3/6 input file.

The rationale for suppressing certain minerals is twofold. First, it is recognized that kinetics generally prevents the formation of certain phases under the conditions of temperature, pressure, etc., in the systems modeled here (on the pertinent time scales). Second, it is recognized that the existing thermodynamic database overestimates the stability of a number of silicate minerals with respect to clay minerals. Both arguments are supported by observed mineral assemblages, including those at Yucca Mountain in both fractures and the tuff matrix. The mineral assemblages in the calculations are thus partially controlled by judgment, and not just by the available thermodynamic data. Rationale for phase suppression used in the Chemical Reference Model is provided in Section 6.7.1.

Table 25. Input Data Describing Thermal-Hydrologic Conditions and CO_2 and O_2 Gas Fugacities and Fluxes for the Chemical Reference Model

Zone 0 (tsw35 host rock)							
Nominal Time (yr)	Simulation Time From (yr)	Simulation Time To (yr)	Estimated P_{CO2} (atm)	Estimated P_{O2} (atm)	Air-Mass Fraction		Temperature (°C)
100	50	300	9.0845E-07	2.3840E-04	6.646E-01		73.64
500	300	700	1.8052E-06	4.7360E-04	3.788E-01		87.30
1000	700	1500	1.5361E-06	4.0304E-04	4.142E-01		86.31
2000	1500	2500	5.4053E-06	1.4165E-03	6.156E-01		78.21
5000	2500	10000	3.3135E-05	8.6089E-03	9.073E-01		50.19
Zone 1/2 (tsw35 rock)							
Nominal Time (yr)	Simulation Time From (yr)	Simulation Time To (yr)	Liquid Influx from Zone 0 (kg/m-sec)	Liquid Mass (kg/m)	Liquid Flux Out (kg/m-sec)	Evaporation or Condensation Factor [A]	Temperature (°C)
100	50	300	3.491E-05	7.417E+04	-3.209E-05	1.088E+00	80.81
500	300	700	3.353E-05	7.867E+04	-3.429E-05	9.778E-01	90.05
1000	700	1500	6.165E-05	8.241E+04	-7.020E-05	8.782E-01	88.42
2000	1500	2500	6.103E-05	8.277E+04	-6.168E-05	9.895E-01	79.96
5000	2500	10000	1.049E-04	8.234E+04	-1.050E-04	9.995E-01	51.69
Zone 3/4 (quartz sand)							
Nominal Time (yr)	Simulation Time From (yr)	Simulation Time To (yr)	Liquid Influx from Zone 1/2 (kg/m-sec)	Liquid Mass (kg/m)	Liquid Flux Out (kg/m-sec)	Evaporation or Condensation Factor [A]	Temperature (°C)
100	50	300	0.000E+00	0.000E+00	0.000E+00		189.77
500	300	700	2.510E-06	2.500E+00	0.000E+00		111.16
1000	700	1500	1.105E-05	2.553E+02	-1.039E-06	1.064E+01	96.05
2000	1500	2500	5.646E-06	3.933E+02	-5.156E-06	1.095E+00	86.95
5000	2500	10000	8.684E-06	4.412E+02	-8.647E-06	1.004E+00	56.95
Zone 5/6 (quartz sand with crushed tuff)							
Nominal Time (yr)	Simulation Time From (yr)	Simulation Time To (yr)	Liquid Influx from Zone 3/4 (kg/m-sec)	Liquid Mass (kg/m)	Liquid Flux Out (kg/m-sec)	Evaporation or Condensation Factor [A]	Temperature (°C)
100	50	300	0.000E+00	0.000E+00	0		200.53
500	300	700	0.000E+00	0.000E+00	0		127.29
1000	700	1500	1.039E-06	7.242E+00	0		99.13
2000	1500	2500	5.156E-06	2.043E+02	-4.931E-06	1.046E+00	88.46
5000	2500	10000	8.647E-06	2.232E+02	-8.625E-06	1.003E+00	58.90

NOTE: A Evaporative concentration is indicated by values greater than unity; condensative dilution is indicated by values less than unity.

4.1.7.5 Grain-Size Distribution for Backfill

Grain-size distribution for the Overton Sand backfill material (unsieved) was obtained from DTN: MO9912EBSPWR28.001. The size distribution data used in this model are shown in Table 26. Notice that the data are not used directly in producing a technical output that provides estimates for any of the principal factors or potentially diruptive process events.

4.1.7.6 Surface Area of Exposed Structural Steel

The surface area of steel that will be used for ground support and the invert structural supports shown in Table 27.

Table 26. Size Distribution Data for the Overton Sand Backfill Material

	Size (diameter)					
	0.053 to 0.100 mm	0.10 to 0.25 mm	0.25 to 0.50 mm	0.5 to 1.0 mm	1.0 to 2.0 mm	
Sample #	**Percentage Mass**					**Total Percentage**
99-0001	1.8	56.8	37.7	3.6	0	99.90
99-0002	2.4	58.9	35.9	2.7	0	99.90
99-0003	1.9	52.3	42.2	3.6	0	100.00
99-0004	1.8	50.9	44.2	3.1	0	100.00
99-0005	2.5	59	36.2	2.3	0	100.00
Averages (%)	2.08	55.58	39.24	3.06	0	99.96

NOTES: Source: DTN MO9912EBSPWR28.001

A Additional mass may reside in a clay-size fraction.

Table 27. Mass and Surface Area for Structural Steel Used in the Engineered Barrier System

Zone	Steel Mass (kg/m)	Surface Area (m^2/m)	Remark
3	260	6.95	Ground support above springline (full drift)—maximum value developed for 30% of drifts in which rockbolts will be installed
5	140	1.49	Ground support and other structures above invert and below springline (full drift)
6	785	2.50	Ground support and other structures within the invert (full drift)
Composite 1/2	0	0	
Composite 3/4	260	6.95	
Composite 5/6	925	3.99	

Source: CRWMS M&O 1999e

4.1.7.7 Corrosion Rate for Structural Steel

Rate equation for general corrosion of A516 steel were obtained from laboratory test results (CRWMS M&O 2000b) (TBV-4586). The reported results were measured with vapor-phase coupon samples at temperatures as great as 90°C, with saturated humidity, and in the presence of chemical constituents from the aqueous phase (a synthetic concentrated J-13 water). The correlation developed by the authors for Case 2 data is

$$r = \exp\left(b_0 + b_1 \frac{1000}{T + 273} + b_2 \cdot pH + b_3 \cdot C_{NaCl}\right)$$

(Eq. 10)

where

r	= penetration rate (μm/yr)
b_0	= –10.035
b_1	= –0.4657
b_2	= 1.5795
b_3	= 1.8258
T	= Temperature (°C)
C_{NaCl}	= Concentration of NaCl in the aqueous phase, expressed in weight percentage

4.2 CRITERIA

The EBS P&CE Model is developed to provide the methodology, and specific results, for demonstrating compliance with the system criteria shown in Table 28 (CRWMS M&O 2000c). Pillar and drift-wall temperature criteria (1.2.1.3 through 1.2.1.5) will not be addressed by the models developed in this report, because for a given thermal power output, they are controlled by the host rock rather than the engineered system.

4.3 CODES AND STANDARDS

The following twol ASTM standards are cited to document the mineral composition of steels (Alloy-22 and 316L) used in the Microbial Effects Model:

ASTM B 575-94. 1994. *Standard Specification for Low-Carbon Nickel-Molybdenum-Chromium, Low-Carbon Nickel-Chromium-Molybdenum, and Low-Carbon Nickel-Chromium-Molybdenum-Tungsten Alloy Plate, Sheet, and Strip.* Philadelphia, Pennsylvania: American Society for Testing and Materials. TIC: 237683.

ASTM A 240/A 240M-97a. 1997b. *Standard specification for heat-resisting chromium and chromium-nickel stainless steel plate, sheet, and strip for pressure vessels.* West Conshohocken, PA: American Society for Testing and Materials. TIC: 241744.

5. ASSUMPTIONS

The assumptions listed in this section describe model inputs, or factors considered in selecting model features, for which special justification is provided. For each assumption in the sections below, a statement is made as to whether additional justification is required, and if so then what impacts on the model results may be expected.

5.1 THERMAL HYDROLOGY MODEL

5.1.1 Effective Tortuosity Factor

A value of 0.7 is assumed for the effective tortuosity factor (τ) for gas-phase diffusive mass transfer for all hydrostratigraphic units. This factor is the ratio of the vapor diffusion enhancement factor (shown to be unity for welded tuff in laboratory tests; Wildenschild and Roberts 1999, Equation 10 and pp. 19–20) to the path tortuosity (a number representing the ratio of actual distance traveled by diffusing species in the gas phase to the straight-line distance). Thus the tortuosity factor (t) is proportional to tortuosity as defined by Bear (1988; Eq. 4.8.26). The value developed by Bear (2/3) is rounded to 0.7. The use of effective tortuosity in NUFT V3.0s is discussed in Hardin et al. (1998, Section 3.3.4.2).

For liquid-phase mass transfer, an effective tortuosity (τ) of zero is assumed. Liquid-phase diffusive mass transfer is insignificant compared to the corresponding gas-phase process because diffusion coefficients are much smaller in liquids (Incropera and DeWitt 1996, Table A-8, p. 849; compare diffusion coefficients for gases and dilute solutions). Also, for TH calculations the diffusion of liquid water in an aqueous phase is unimportant.

This assumption is used in the calculations described in Section 6.1. No further justification of this assumption is required.

5.1.2 Homogeneous Fracture Continuum

In the conceptual basis for NUFT V3.0s, the fracture network is assumed to behave as a continuous porous medium with homogeneous properties within each hydrostratigraphic unit. This assumption is used in development of the UZ model, from which the unit properties used in this report were obtained, and therefore applies to this model. Any tendency to underestimate seepage, resulting from this assumption, is compensated in the TH models developed for this report, through the use of backfill as discussed in Section 6.1.1. This assumption is consistent with the purpose of the TH calculations reported here, which is to calculate the average response to heating under a range of effective seepage inflow conditions.

This assumption is used in the calculations described in Section 6.1. No further justification of this assumption is required.

Table 28. Waste Emplacement Drift System Criteria Addressed by the EBS P&CE Model

Criterion	Description
1.2.1	**System Performance Criteria**
1.2.1.8	For 10,000 years, the system shall allow free-liquid-phase water to drain out of emplacement drifts, via the emplacement drift floor, at a rate of: 2 cubic meters per meter of emplacement drift, with duration of 1 week, and frequency of 1 per year (TBV-284).
1.2.1.9	The invert structural members shall be composed of carbon steel.
1.2.1.10	The invert ballast shall maintain the pH of water within the ballast to between 6.7 and 10.2 (TBV-3881) for 10,000 years.
1.2.1.11	The invert ballast material shall be granular.
1.2.1.19	The backfill shall maintain the pH of water within the backfill to between 6.7 and 10.2 (TBV-3881) for 10,000 years.
1.2.2	**Safety Criteria**
1.2.2.2	**Non-nuclear Safety Criteria**
1.2.2.2.1	The selection of invert ballast and backfill materials shall consider the known health and safety hazards of the materials.
1.2.3	**System Environment Criteria**
1.2.3.8	Values representing the initial condition of the Natural Barrier shall be obtained from the Technical Data Management System.
1.2.4	**System Interfacing Criteria**
1.2.4.1	The system shall be designed in accordance with the interface agreements defined in "Interface Control Document for Waste Packages and the Mined Geologic Disposal System Repository Subsurface Facilities and Systems for Mechanical and Envelope Interfaces."
1.2.4.4	The system shall accommodate a maximum WP thermal output of 11.8 kW at the time of emplacement.
1.2.4.5	The system shall accommodate removal of 70 percent of the heat generated by WPs by the Subsurface Ventilation System during the preclosure period.
1.2.4.8	The system shall accommodate a nominal spacing of 81 m between emplacement drifts.
1.2.4.9	The system shall accommodate a nominal drift excavated diameter of 5.5 m.
1.2.4.13	The system shall accommodate an emplacement drift ground support system composed primarily of carbon steel (steel sets and/or rock bolts and mesh).
1.2.4.14	The system shall affect the emplacement drift environment such that WP near field environments are maintained as follows: Temperature and humidity (TBD-234) Microbial 10^{14} microbes/year/m of drift (TBV-3881) Colloidal 8×10^{-6} (TBV-3881) to 6×10^{-5} mg/ml (TBV-3881) Water pH 6.7 to 10.2 (TBV-3881)
1.2.6.2	The system shall comply with the applicable assumptions contained in the "Monitored Geologic Repository Project Description Document."

Source: CRWMS M&O 2000c

NOTE: For specific references to system functions, other requirements, and applicable regulations, the reader is referred to the source document.

5.1.3 Component Properties

The properties of components air and water, distributed in the gas and liquid phases, are incorporated in a NUFT V3.0s input file (vtough.pkg, Attachment I). The values used are approximations that are suitable either because different values would have a negligible effect on the NUFT V3.0s results, or because they are not used in TH simulations such as these which do not use the contaminant transport features of NUFT V3.0s. For those parameters that are used in TH simulations, the assumed values consist of the following:

- Equivalent molecular weight of air: 29.0 g/mol
- Molecular weight of water: 18.0 g/mol
- Binary diffusivity for water vapor into air in the gas phase:

$$D = \tau\phi S_g D_{va}\left(\frac{T + 273.15}{273.15}\right)\theta \qquad \text{(Eq. 11)}$$

where

D_{va} = 2.13×10^{-5} m^2/sec
θ = 1.8 (dimensionless)
T = temperature in °C
τ = effective tortuosity coefficient
S_g = gas saturation (calculated by NUFT)
ϕ = porosity

- Diffusivity of air in liquid water: 10–9 m2/sec
- Specific heat of air (C_p): 1009 J/kg–K

This assumption is used in the calculations described in Section 6.1. No further justification of this assumption is required.

5.1.4 Zero Dispersion Coefficients

For TH problems, the use of zero dispersion for the gas phase is equivalent to an assumption that dispersive behavior is small relative to diffusion or that velocities are small. For gas-phase mass flux rates, gas densities, and fracture porosities and apertures used in this report, the resulting Peclet Number is much less than unity, therefore dispersion can be neglected in TH simulations in accordance with established principles (Bear, 1988; p.608).

This assumption is used in the calculations described in Section 6.1. No further justification of this assumption is required.

5.1.5 Preclosure Ventilation Effects

For this report, the effects of preclosure ventilation on the TH state of the host rock is taken into account by running NUFT V3.0s for 50 yr without backfill, then adding backfill and restarting the code. Preclosure ventilation is not included except to decrease effective thermal output by 70 percent. The drying effects of ventilation on the host rock and precipitation of solutes predominantly in the rock matrix are neglected in this model. The result is that the TH model overpredicts the water and humidity present in the drift environment for the first few tens or hundreds of years after closure. This tends to shorten the time until return of moisture to the environment, and is therefore conservative in conjunction with the assumed environmental conditions that promote corrosion (Assumption 5.1.6).

This assumption is used in Section 6.1.4. No further justification of this assumption is required.

5.1.6 Environmental Conditions that Promote Corrosion of Drip Shield and Waste Package

The following environmental conditions are assumed to accelerate corrosion rates and accumulation of damage from general, localized, and stress-cracking mechanisms:

- Duration of exposure to adverse conditions
- Temperature at which adverse chemical conditions occur
- Precipitation of salts that provide ions needed for some corrosion processes and that promote aqueous conditions at higher temperatures by osmolality
- Alkaline (high-pH) conditions in the bulk chemical environment, which are associated with low CO_2 fugacity caused by evaporation that decreases the air mass-fraction
- Fluoride, chloride, and sulfate are of principal importance for corrosion of titanium and Alloy-22.

This assumption is used in Section 6.1.7. This assumption is to-be-verified (TBV-4475).

5.2 GAS FLUX AND FUGACITY MODEL

Following are the assumptions made in estimating chemical boundary conditions for fluxes and fugacities of CO_2 and O_2 to support modeling of the EBS in-drift chemical environment:

5.2.1 Steady-State Gas-Phase Mass-Transfer Conditions

Steady-state conditions are assumed for interpretation of present-day isotopic conditions and mass transfer. Hydrologic conditions have been relatively stable during the Holocene period, which is approximately two half-lives of ^{14}C; thus, any pre-Holocene influence on radiocarbon distribution in the UZ has decayed to 25 percent or less of its maximum magnitude. The observed variations in ^{14}C activity that are interpreted for this model are generally greater than

25 percent. Also, the amount of $^{14}CO_2$ present in the UZ is large compared with the potential annual mass transfer; thus, observed data are insensitive to short-term changes in flux.

Use of natural ^{14}C abundance to describe gas-phase transport in the UZ is a unique approach to modeling both gas flux and fugacity, which is justified because these measures are uncertain. Results from the ^{14}C approach are compared with other approaches in Section 6.2.6.2.

This assumption is used in Section 6.2.3.1 and Section 6.2.3.4. No further justification of this assumption is required.

5.2.2 Vertical, One-Dimensional Gas-Phase Transport

One-dimensional vertical transport is assumed for interpretation of present-day conditions and for prediction of repository conditions. One-dimensional liquid flow in the UZ above the potential repository is likely because conditions are unsaturated. Assumption of 1-D transport conditions during repository heating supports lower-bound estimates for CO_2 and O_2 availability because multidimensional flow produces circulation with mixing and lateral components of mass flux, which increase efficiency of transport into the drifts. Thus this assumption produces conservative, bounding results in conjunction with Assumption 5.1.6.

This assumption is used in Section 6.2.3.1 and Section 6.2.1.4. No further justification of this assumption is required.

5.2.3 J-13 Water Composition

The composition of water from well J-13 is a chemical analogue for fracture waters in the UZ under ambient conditions (Harrar et al. 1990, p. 21; DTN LL980711104242.054). J-13 well water is found in the same Topopah Spring tuff at similar temperature, oxidizing conditions, and CO_2 fugacity. For the analyses reported by Harrar, et al., the nominal bicarbonate alkalinity is 128.9 mg/L, which is converted to a CO_2(aq) concentration of 94 mg/L using molecular weights of 61 g and 44 g for bicarbonate and CO_2, respectively. This is an approximate value that could vary in response to different values of the CO_2 fugacity, temperature, etc. The J-13 value of 94 mg/L of CO_2 is assumed for use in a general interpretation of CO_2 observations in borehole SD-12 and in developing the 1-D mass-transfer model for gas-phase CO_2 transport.

Greater concentrations of dissolved inorganic carbon (as CO_2) have been inferred for matrix porewaters (DTN: LB991200DSTTHC.001) (TBV-4575) but these would lead to greater gas-phase CO_2 transport (required to replace ^{14}C decay in the ambient system). Thus the use of J-13 water as a reference composition for interaction with gas-phase CO_2 transport is a conservative approximation (i.e. yields lower values of flux and fugacity).

This assumption is used in Section 6.2.1.1 and Section 6.2.3.1. No further justification of this assumption is required.

5.2.4 Limited Interaction of CO_2 with Solid-Phase Species

CO_2 interaction with solid-phase carbonates is assumed to be limited. For ambient conditions, this is consistent with a dynamic steady-state whereby:

- Equilibrium of waters with calcite is maintained throughout the UZ
- Gas-phase CO_2 concentration tends to be uniform
- Mass transfer of CO_2 between gas, liquid, and solid phases can occur in response to small changes in solubility produced by evaporation or temperature changes that are limited in magnitude.

For thermal conditions, the exsolution of CO_2 by evaporating waters and the acquisition of dissolved CO_2 by condensate waters are assumed to be compensating processes with respect to the average gas-phase CO_2 fugacity in the host rock. In other words, the effects of evaporation or boiling and of mineral and gas dissolution in condensation regions are assumed to involve similar amounts of CO_2 and to be localized relative to the spatial scale of gas-phase diffusion, for the time scale of postclosure performance. This argument is supported by the CO_2 balance described in Section 6.7.

This assumption is used in Section 6.2.1.3. No further justification of this assumption is required.

5.2.5 Representative Fracture Porosity and Aqueous Volume Fraction

The depth-averaged volume fractions for fracture porosity and liquid-filled porosity for borehole SD-12 are representative of other boreholes and of the L4C4 Multiscale Model location. This is justified because the stratigraphy is similar across the site area and because the mass-transfer model is relatively insensitive to changes in the gas-volume fraction (ϕ_{gas}) and aqueous-volume fraction (ϕ_{aq}) compared with sensitivity to the diffusion-dispersion coefficient D_{gas}.

This assumption is used in Section 6.2.3.3. No further justification of this assumption is required.

5.2.6 Average Temperature of the UZ

Average temperature in the UZ for ambient conditions is assumed to be 30°C for calculating a composite partition coefficient for CO_2. Estimated temperatures at the ground surface and water table are shown in Table 8. The value of 30°C is an approximation of the ambient UZ temperature. Because temperature in Equation 26 uses absolute temperature, the difference between temperature at the ground surface and water table is insignificant.

This assumption is used in Section 6.2.3.1. No further justification of this assumption is required.

5.3 CEMENTITIOUS MATERIALS MODEL

5.3.1 Cement Mineral Assemblage

The cement mineral assemblage shown in Table 29 is assumed. This is based on the assemblage for "young" cement grout (Hardin et al. 1998, Table 6-2, p. 6-15) with modification (Assumption 5.3.2 and Assumption 5.3.3). Mineral assemblages representing modification of Portland cement by aging and carbonation are available from the same information source, but they tend to produce less alkaline leachate; thus, young cement minerals are assumed in accordance with Assumption 5.1.6. The effects of aging and carbonation, which may decrease

the pH and concentrations of key constituents in leachate over time, are neglected in this bounding model.

This assumption is used in Section 6.3.1. No further justification of this assumption is required.

Table 29. Grout Mineral Assemblage Used for the Cementitious Materials Model

Phase	Weight %	Mass per Rockbolt [A] (kg)
Tobermorite (also representing C-S-H [1.7] gel and gehlenite hydrate)	57.5	13.0
Ettringite	18.0	4.08
Portlandite	21.5	4.87
Brucite	3.0	0.68

NOTE: A Mass of each mineral in the grout used for one rockbolt, including 3x excess grout use, totaling 22.65 kg per rockbolt per CRWMS M&O 2000a (TBV-3902)

5.3.2 Extent of Carbonation

Cement carbonation begins, but is not complete, at the time percolating water contacts the cement grout. Calcite is assumed to represent the solid-phase products of partial carbonation, and a minor amount of calcite is assumed to be present in the grout. This is a reasonable-bound assumption (in accordance with Assumption 5.1.6) because it maximizes the pH of leachate.

This assumption is used in Sections 6.3.1 and 6.3.6. No further justification of this assumption is required.

5.3.3 Tobermorite Analogue for Other Cement Phases

In developing this assemblage in Table 29, the C-S-H gel and gehlenite hydrate phases in young cement are represented by tobermorite, which has better known characteristics and similar elemental composition. This assumption is justified because aging of the cement at elevated temperature during the preclosure period of 50 years or more will cause the C-S-H gel to crystallize, and tobermorite is a likely product. The gehlenite hydrate is a minor phase used to account for aluminum in the assemblage that is not incorporated in ettringite. Thermodynamic solubility data are not available for gehlenite hydrate, so it is represented by tobermorite (instead of ettringite, thereby preserving the ratio between ettringite and portlandite).

This assumption is used in Section 6.3.1. No further justification of this assumption is required.

5.3.4 Stability of Cement Phases

Ettringite is assumed to be thermally stable over the temperature range predicted for the potential repository near-field host rock (from 25°C to approximately 150°C, with limited water availability above 96°C). This is consistent with assemblages developed for thermally treated concrete (Hardin et al., 1998; Section 7.1.2). Pozzolanic reactions are assumed to consume the silica fume.

This assumption is used in Section 6.3.1. This assumption is to-be-verified (TBV-4476).

5.3.5 Water-Grout Chemical Reaction

Chemical equilibrium is assumed along the cement-water reaction path; thus, equilibrium controls the composition of leachate from the grout. This assumption is suitable for slowly changing low-flux conditions that will be encountered in the grout.

Reaction of groundwater with the grout is assumed to be closed with respect to gas-phase constituents, particularly CO_2. This is justified because of the following:

- The grout will be very fine-grained, and the pore structure will retain capillary water; thus, gas saturation will be small.
- The assumed intrinsic permeability is low (also see Assumption 5.3.8). Low permeability confers resistance to diffusion.
- The grout column around each rock bolt will be surrounded by the intact rock matrix over much of its length. Exposure of the grout to gas-phase CO_2 is thus limited by the surrounding host rock.

Flowing water and gas-phase CO_2 will most readily access the grout column at fracture intersections. If the grout is near liquid saturation, access by gas-phase CO_2 to unreacted grout within the grout column will be limited.

If cracks form in the grout from shrinkage or disruption, water and gas will penetrate them. More surface area could become available for diffusion of CO_2, but the leachate composition would still be bounded by the closed-system calculations.

This assumption is used in Sections 6.3.1 and 6.3.2.1. No further justification of this assumption is required.

5.3.6 Thermodynamic Data for Cementitious Materials Model

Chemical dissociation constants for tobermorite and ettringite solids from the "com" database (file: "data0.com"; Attachment I) are assumed to be consistent with the PHREEQC chemical database (file: "wateqcem.txt"; Attachment I). Quantitative verification of thermodynamic data consistency was not performed for this report.

This assumption is used in Section 6.3.1. This assumption is to-be-verified (TBV-4477).

5.3.7 Biotic and Organic Processes

Biotic and organic processes, including contributions from the presence of superplasticizer and the steel rockbolt, are assumed to have negligible effect on leachate composition for as long as high-pH conditions prevail in the grout; these processes are neglected in this model. Biotic and organic processes will be limited (although not totally eliminated) by the high-pH environment and by the availability of necessary nutrients such as phosphate and organic carbon. The organic

content in superplasticizer will not be degraded by microbial or other activity at a rate that is great enough to affect leachate composition.

This assumption is used in Sections 6.3.2 and 6.3.3. This assumption is to-be-verified (TBV-4478).

5.3.8 Grout Permeability

Saturated permeability is assumed to be 0.1 μdarcy ($10^{-19}m^2$) for all conditions. For initial permeability of the grout (early time), this value is as justified by cited literature (Onofrei et al. 1992, p. 137). As aging and carbonation of the grout proceed over time, permeability is assumed to remain at this value for purposes of calculating leachate composition. Additional water flow may occur through cracks that can form, but such flow will tend to bypass unreacted cement and is neglected for this reasonable-bound model.

This assumption is used in Sections 6.3.4 and 6.3.8. No further justification of this assumption is required.

5.3.9 Equilibrium with Quartz Sand

Calculations described in Section 6.3 show that when leachate emerges from the grout, it is strongly aggressive with respect to dissolution of silica and silicate minerals. For this model, the leachate is assumed to equilibrate chemically with the quartz sand backfill. The importance of this assumption is that silica-buffer activity is obtained (thus, pH is decreased) from dissolution of quartz. This is a reasonable approximation because substantial silica-buffer activity is obtained even if quartz dissolution does not proceed to equilibrium.

This assumption is used in Section 6.3.6. No further justification of this assumption is required.

5.4 MICROBIAL EFFECTS MODEL

5.4.1 Electrical Equipment and Removal of Organics

Haulage will be electrically driven (i.e., no hydrocarbon fuels will be used in the emplacement drifts). Hydrocarbon-based lubricants and other organic materials will be used in construction equipment but will be recovered from the drift environment prior to waste emplacement. This is justified because it is consistent with currently used methods for exploratory excavation and construction in the potential repository host rock.

This assumption is used in Section 6.4.2.2. This assumption is to-be-verified (TBV-4479).

5.4.2 Purity of Backfill and Invert Materials

Backfill and invert materials will be washed and contain only trace amounts of organic matter. In addition, backfill material will contain only trace amounts of phosphate. This is justified because washing of granular materials, and sourcing of backfill material with the indicated purity, are within standard engineering practice.

This assumption is used in Sections 6.4.2.2 and 6.4.6. This assumption is to-be-verified (TBV-4480).

5.4.3 Organic Carbon Content of Host Rock

The organic carbon of the host welded-tuff rock units is negligible as a carbon source to support microbial activity and growth. Inorganic carbon is present, principally in the form of speciated CO_2, and is available for microbial utilization. Microbes can utilize the inorganic carbon to produce biomass, which can be a source of organic carbon. Therefore, the presence of a small concentration of organic matter in the host rock (if it exists) is negligible.

This assumption is used in Section 6.4.2.2. No further justification of this assumption is required.

5.4.4 Microbial Growth and Activity on Waste-Package Surface

Microbial growth and activity on the waste-package surface (Alloy-22) are negligible for humid conditions (not liquid-saturated or dripping), even for RH greater than 90 percent, as long as:

- Liquid groundwater (with its endogenous complement of nutrients) has not penetrated the drip shield
- Rock dust present on waste-package surfaces does not provide nutrients for microbial growth
- Alloy-22 does not provide nutrients such as phosphate which are necessary for growth

This assumption is consistent with published information on microbial metabolism, and the microbial ecology in the potential host rock, as discussed in Section 6.4. It is used in Section 6.4.5.1 and 6.4.5.2. No further justification of this assumption is required.

5.4.5 Microbial Effect on Carbon Steel Corrosion Rate

Preliminary data, as yet unpublished, suggest an approximate one-order-of-magnitude increase in the corrosion rate for C1020 steel, once moisture returns to the emplacement drifts, due to microbial activity for environmental conditions representative of the potential repository. Carbon steel used for ground support and invert material is assumed to have similar behavior. The technical basis for this assumption is that the average corrosion rate for carbon steel Alloy 1020 was a factor of 6 higher than sterile carbon steel as presented in Table 17. The assumption of an increase of one order of magnitude in the corrosion rate is conservative and requires confirmation.

This assumption is used in Sections 6.4.4.1 and 6.4.6. This assumption is to-be-verified (TBV-4481).

5.5 NORMATIVE PRECIPITATES AND SALTS MODEL

5.5.1 Portlandite vs. Calcite

Laboratory tests were performed, whereby synthetic J-13 water and synthetic porewater were evaporated under atmospheric gas composition conditions. Calcite but not portlandite was detected in the final mineral suites. For low-CO_2 conditions that may be encountered in the potential repository during the thermal period, it is assumed that sufficient CO_2 will be present to produce thermonatrite ($Na_2CO_3 \cdot H_2O$) and calcite ($CaCO_3$). This approach is justified by the thermodynamic arguments presented in Section 6.5.5.2. However, the thermodynamic argument is approximate, and if this assumption is incorrect, the result could be precipitation of portlandite or sodium hydroxide on the drip-shield surface.

This assumption is used in Section 6.5.5. This assumption is to-be-verified (TBV-4482).

5.6 EBS COLLOIDS MODEL

5.6.1 Size Distribution of Ferric Iron Colloids

The size distribution of ferric iron colloids is assumed to be identical to the size distributions of natural colloids referenced in this report. The justification for this assumption is that colloids outside the observed range will probably not be transported over long distances, either because they are unstable or because they become attached to the porous media through which the water flows.

This assumption is used in Section 6.6.2. No further justification of this assumption is required.

5.6.2 Spherical Particles

Spherical colloid particle geometry is assumed for relating colloid frequency and size to the mass of sorbent material. This is a conservative assumption because sorptive capacity is strongly related to the surface area, and the surface area is minimized by spherical geometry.

This assumption is used in Section. 6.6.3.3. No further justification of this assumption is required for this bounding analysis.

5.7 CHEMICAL REFERENCE MODEL

5.7.1 Congruent Redissolution and Limited Ionic Strength

When liquid water returns to the EBS during the thermal period, there is assumed to be congruent dissolution of precipitates formed by evaporation (i.e., all the different types of precipitates present, dissolve together and are eventually depleted at the same time). The ionic strength of the solution formed by congruent dissolution of precipitates is assumed to be 1 molal.

Importantly, the activity model used with the EQ3/6 code in these simulations (B-dot equation; Wolery 1992a; Section 3.3, p. 39–42) is generally recognized as suitable only for ionic strengths not exceeding 1 molal. Other activity models can be used with EQ3/6 (e.g., Pitzer equation;

Wolery 1992a; Section 3.5; p. 44–64) but data support is lacking for some of the species of interest, especially at elevated temperatures.

Accumulation of precipitates and eventual redissolution is sensitive to the spatial and temporal granularity of the model in a manner such that (a) less precipitate mass may accumulate at one time, but (b) elevated temperature and chemically concentrated conditions could persist in the EBS for a longer time than predicted by this model.

This assumption does not necessarily lead to a bounding model for chemical performance measures such as pH, but instead produces a reference model (Section 6.7). For example, redissolution could be incongruent, causing a short-duration pulse of high-pH brine, possibly in response to episodic hydrologic conditions. Or, redissolution could be hindered if flow is bypassed through a portion of the EBS, which could lead to long-duration aggressive chemical conditions on part of the drip shield. The 1-molal calculations are used as a reference model for the bulk chemical environment, but modeling chemical conditions on the surface of the drip shield or waste package must consider the presence of salts in the humidity environment. In other words, solution conditions in the potential repository drifts may not be as dilute as the conditions calculated using the reference model, and models of drip shield or waste package corrosion should take this into account.

These assumptions are addressed in Sections 6.7.2.3 and 6.7.3.3. No further justification is required for reference model development.

5.7.2 Corrosion of A572 Structural Steel

Alloy A572 has been identified for use in ground support and the invert (CRWMS M&O 2000a, TBV-3902). However, long-term controlled test data are not available for A572 steel, and the A516 data are assumed to apply. Corrosion rates for A516 steel were measured for oxic, vapor-phase, elevated temperature conditions in proximity to concentrated synthetic J-13 water (Section 4.1.7.7). The tests were performed because alloy A516 was selected as the corrosion-allowance waste-package material for the Viability Assessment design. This assumption is justified because the two alloys contain similar amounts of major elements Fe, Mn, and C (ASME 1995; ASTM 1997a).

This assumption is used in Section 6.7.4.2. No further justification of this assumption is required.

5.7.3 Humidity Threshold for Corrosion of Structural Steel

Steel corrosion is assumed to be insignificant to the EBS bulk chemical environment until the RH exceeds 70 percent. This is consistent with the approach developed to model the Viability Assessment waste-package corrosion allowance material (CRWMS M&O 1998b, Section 5.5.3.1, pp. 5-31).

This assumption is addressed in Sections 5.7.6 and 6.7.4.2. No further justification of this assumption is required.

5.7.4 Humidity Corrosion of Steel for Low-Water Conditions

When RH exceeds the critical threshold for steel corrosion (Assumption 5.7.3) but little or no water is calculated to be present, the aqueous-phase composition is set to the influent water composition. This occurs only in Zone 5/6 for Time Period 3, for which the Time Period 3B influent water composition is used. The result is a lower-bound estimate of the corrosion rate, and corresponding O_2 consumption rate.

This assumption is used in Section 6.7.4.2. No further justification of this assumption is required.

5.7.5 Effects from Corrosion-Resistant Materials

The drip shield, waste package, and pedestal are made from CRMs and stainless steel. Compared with corrosion of the structural steel used in ground support and the invert, corrosion of drip-shield, waste-package, and pedestal surfaces is slow to consume oxygen and slow to produce corrosion products. The corrosion products are also dominated by relatively inert metal oxides. Accordingly, corrosion of the CRMs and stainless steel is assumed to have no significant effect on the EBS bulk chemical environment during the 10,000-yr performance period.

This assumption is used in Section 6.7.4. Further justification is provided in Section 6.7.6.

6. ANALYSIS/MODEL

The overall objective is to evaluate the changes in the bulk environment that can affect drip-shield and waste-package degradation, and radionuclide migration. This includes changes in aqueous chemistry resulting from the interaction of heat and introduced materials with heat, and water seeping into the drift, taking into account water fluxes, thermal effects on chemical equilibria and rate processes, and physical processes such as evaporation and condensation.

The EBS P&CE model is developed as several models, integrated in a Chemical Reference Model, from which the conditions of the bulk chemical environment are estimated. The results support specification of environmental conditions for corrosion of the drip shield and waste package. Most aspects of the approach are bounding, for example, the selection of a reference TH model for chemical modeling. This set of models supports TSPA conceptually, but it is important to recognize that TSPA incorporates models and data which are beyond the scope of this report (e.g., UZ flow and drift seepage).

This section begins with a description of TH models representing conditions at the repository center and edge, for "lower" and "upper" infiltration conditions. Next, an analytical Gas Flux and Fugacity Model is developed to describe the transport of gases in the UZ under ambient and thermally perturbed conditions, and the dependence of fugacity on consumption of gaseous species by chemical reactions. This model is used to estimate CO_2 and O_2 fugacities for chemical modeling. The minerals and salts that could be deposited in the EBS because of seepage or dripping during the thermal period, are identified by the Normative Precipitates and Salts Model, based on laboratory test data. Finally, the TH Model, Gas Flux and Fugacity Model, and Normative Precipitates and Salts Model, are combined in the Chemical Reference Model to produce estimates of the bulk chemical environment.

The potential effects of cement used in rockbolts is evaluated in the Cementitious Materials Model, based on chemical equilibrium modeling of cement mineral phases. The potential effects of microbial activity, and the threshold environmental conditions required, are described in the Microbial Effects Model. The potential effects of ferric colloids produced from corrosion of structural steel used in the EBS, are evaluated in the EBS Colloids Model.

6.1 THERMAL HYDROLOGY MODEL

The purpose of the TH Model is to support modeling of the in-drift physical and chemical environment. It is intended to provide reasonable-bound estimates for temperature, liquid flux, humidity, and concentrations of gas-phase constituents in the EBS. It describes the evolution of these parameters with time during repository thermal evolution and analyzes the potential for evaporative concentration of solutes. This model generates abstracted results for use as input to reaction cell models. The objectives to be met by the TH Model include the following:

- Identify the processes and model inputs that control TH performance measures.
- Use the active-fracture model for nonequilibrium fracture–matrix interaction, consistent with the unsaturated-zone site-scale hydrologic model to perform TH calculations for representative locations within the repository layout.
- Evaluate calculated results and select reasonable-bound model output for further analysis of the EBS chemical environment.
- Develop reasonable-bound values of TH performance measures for the thermal period extending to 10,000 yr.

All NUFT calculations and postprocessed results described in this subsection pertain to the half-drift symmetry model, unless specified to be full-drift results. Thus, the calculated zone-to-zone fluxes and zone evaporation rates should be doubled to represent full-drift results. For other variables including temperature, saturation, air mass-fraction, and gas-phase vertical mass flux, the half-drift and full-drift results are identical.

6.1.1 Thermal Hydrology Calculations Using NUFT

The TH predictive model that forms the basis of these calculations is the NUFT V3.0s code (Nitao 1993). NUFT (Nonisothermal Unsaturated Flow and Transport) has been used to model a wide range of problems. It was the basis for simulating waste-package environment conditions for Total System Performance Assessment–Viability Assessment (TSPA-VA) (CRWMS M&O 1998a; Section 3.2) and has also been used for calculations in support of field-scale thermal testing (e.g., calculations reported in Buscheck et al. 1997). The implicit DKM version of NUFT that includes the AFC is used in these calculations. General descriptions of physical principles used in NUFT V3.0s, with references for additional information, are provided in Hardin et al. (1998, Sections 3.3.3, 3.3.4, and 3.3.5).

The DKM conceptualizes fractured rock as having two interacting continua, one representing the matrix and the other representing the fracture network. Fluxes of mass and heat between the fracture network and the matrix at each point in the model domain, are calculated from the local

temperature and pressure differences. These differences can be nonzero; thus, nonequilibrium conditions can exist at that point. This feature of the DKM allows for more realistic treatment of transient behavior when conditions such as saturation and temperature are changing with time.

The AFC is a scheme for dynamic modification of the contact area between the fracture network and the matrix (Liu et al. 1998). The underlying concept is that fracture flow occurs through some, not all, of the fractures at a given location and time. For transient conditions, this tends to produce stronger nonequilibrium response than does assuming that flux is uniformly distributed through all fractures. Flow through a fracture is greater when it has higher saturation, and focusing of flux through a limited population of active fractures tends to maximize the saturation, thereby enhancing fast pathways for flux through the mountain.

The hydrologic properties obtained from DTN LB990861233129.001 were developed for the unsaturated-zone site-scale model (herein called the unsaturated zone (UZ) model) using a procedure that assumes they will be applied in DKM employing AFC with the modified Brooks and Corey gas permeability function (Brooks and Corey 1966, Equation 33). That is how they are applied in this model.

The TH models developed for this report have the drift volume entirely filled with backfill, which promotes seepage into the drift. Liquid water flow is conducted from the host rock above the drift into the backfill, with little diversion around the drift opening. This condition has the following advantages for analysis:

- The magnitude of seepage flow into the drift is readily controlled in the simulations by varying the infiltration flux boundary condition.
- Conservative (greater) evaporation rates can be achieved with seepage, which tends to increase the proximity of percolating waters to the hottest parts of the EBS during the thermal period. Production of water vapor causes displacement of air, thus decreasing CO_2 fugacity (other factors can cause CO_2 fugacity to increase). Decreased CO_2 promotes high pH and is conservative with respect to corrosion of EBS components.

Specific TH performance measures calculated for the continuum representing the rock matrix are temperature, saturation, relative humidity, and the rate of evaporation. For the continuum representing the fracture network, these same measures and the air mass-fraction were calculated. These measures were reported by NUFT V3.0s as fields (values for each grid block) over the entire model domain for simulation times of 1, 2, 5, 10, 20, 50, 100, 200, 300, 400, 500, 700, 1000, 1500, 2000, 2500, 3000, 4000, 5000, 7000, and 10,000 yr as specified in a NUFT V3.0s input file (outputtime). In addition, reported at these same time steps was a vector field that describes the gas-phase total mass flux (air plus water vapor) in the matrix and fractures combined.

The two locations in the potential repository layout, for which TH calculations are performed for this report, are described in Section 4.1.1. The L4C1 location is along the eastern edge of the repository layout, and increased drift spacing is used to represent edge cooling effects in a 2-D model. Thus the drift spacing is increased by a factor of 60/36 or 167 percent of the nominal

value (1.67 × 81 m = 135 m). The model domain width is half the drift spacing because of symmetry.

Four NUFT cases are presented in this report, as described in Section 4.1.

6.1.2 Postprocessing NUFT Output

The postprocessing steps shown in Figure 1 are used to prepare and simplify NUFT V3.0s output for further analysis. Zone calculations describe the spatial subdomains and the temporal intervals for chemical modeling of reaction cells. Vertical profiles of key variables are used for 1-D modeling of CO_2 and O_2 gas fluxes. The conservative solute analysis is used to support selection of a location, areal mass loading, and infiltration flux distribution for chemical modeling.

6.1.2.1 Zone Fluxes

To capture evaporation and chemical alteration processes taking place in key areas, six zones are defined a priori for the NUFT V3.0s models (Figures 2 and 3). These zones are defined as follows:

Zone 0: Far-field host rock—Zone 0 is used as the chemical boundary condition for water composition entering Zone 1 from above. In Zone 0, the composition of percolating water is not significantly affected by evaporation or condensation, but it is affected by elevated temperature.

Zone 1: Host rock above the drift mid-plane—Zone 1 extends outward from the drift wall approximately 10 m, which is far enough to encompass the dryout zone. Zone 1 includes that region of the host rock in which boiling and evaporative concentration of waters can occur and through which water can flow into the drift. It also represents the region of the host rock where vapor generated within the drift is likely to condense. Zone 1 is above the drift midplane (the horizontal midplane passing through the drift center).

Zone 2: Host rock at the drift wall—Zone 2 comprises the grid blocks that represent the host rock and define the upper half of the drift opening above the springline (intersections of the horizontal midplane with the drift walls).

Zone 3: Backfill above the spring line

Zone 4: Backfill at the drip shield surface—Zone 4 comprises the grid blocks that represent backfill and define the drip-shield surface above the midplane.

Zone 5: Lower backfill—Zone 5 comprises the grid blocks that represent backfill outside the drip shield, below the mid-plane, and above the invert.

Zone 6: Invert below the backfill, drip shield, and waste package

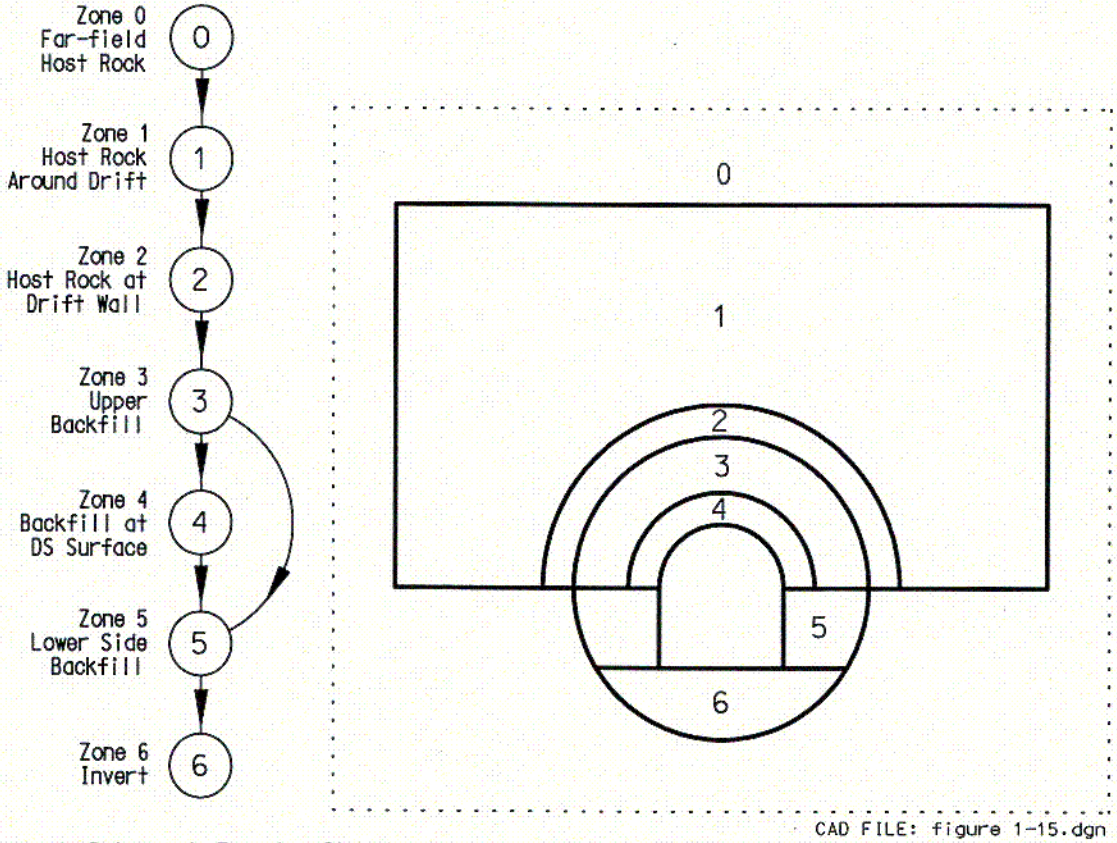

Figure 2. Schematic Drawing Showing the Zones Defined for Chemical Modeling and the Connectivity of the Zones

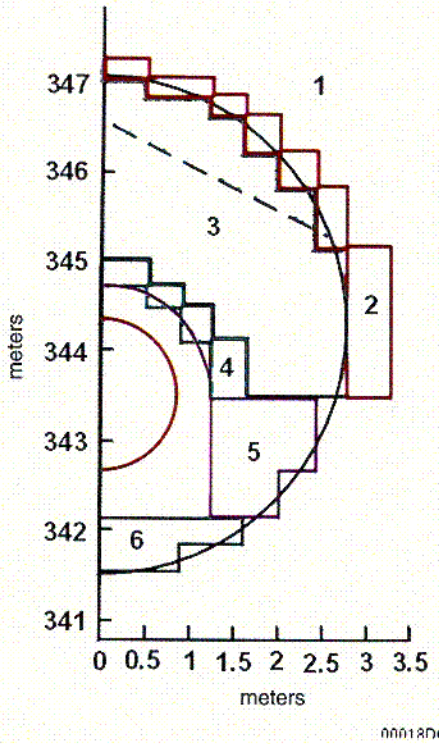

Figure 3. Representation of Zone Boundaries in the Model Grid, Showing Boundaries Between Zones 1 through 6

Zones are declared in the NUFT V3.0s input file (*.in) by assigning unique element names (or naming extensions) to each zone. The syntax used for these calculations is to include the string "*An*" in each element name ("n" is the zone number, and "*" signifies the remainder of the name, which may vary within each zone). A flux history command generates output consisting of the gas and liquid fluxes from one zone to another. The flux output is captured in a set of history files for each NUFT V3.0s model (*Gflux*.dat and *Lflux*.dat). These are used by software routine MYPLOT V1.1, which rearranges the information to produce a summary table of gas and liquid fluxes between zones as a function of time (*.exl). Figure 4 shows the liquid fluxes between zones, for the L4C4 location and "upper" infiltration distribution.

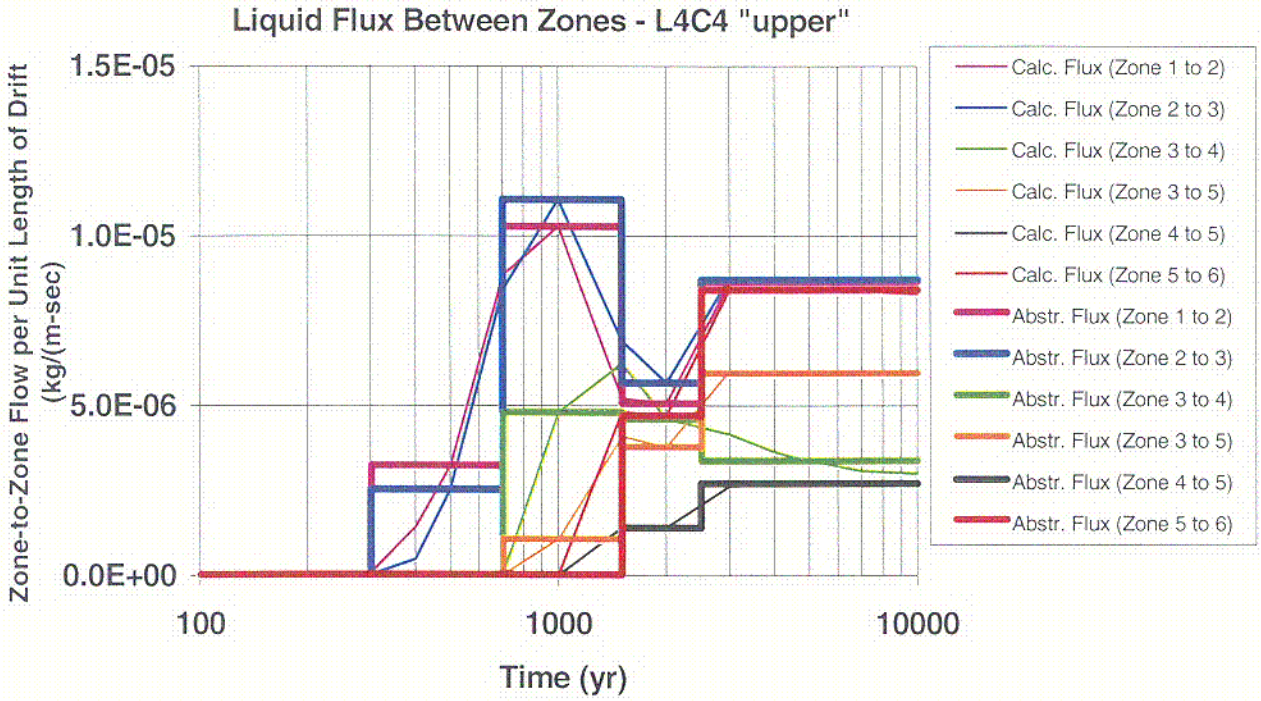

NOTE: The uniform time intervals, used to represent the thermal evolution in chemical reaction cell modeling, are also plotted.

Figure 4. Liquid Fluxes Between Zones for the L4C4 Location and the "Upper" Infiltration Distribution

The zone fluxes are used in conservative solute calculations and chemical modeling described in this report. They are transferred manually from the MYPLOT V1.1 output file (*.exl) to the TH+GASMODEL routine (file: "th+gasmodel_L4C*-*i-04.xls"; worksheet: Zone fluxes). The MYPLOT V1.1 output file (*.exl) is a table with rows corresponding to all the times evaluated in the NUFT run. Only those rows corresponding to the specific times identified in Section 6.1.1 are transferred.

6.1.2.2 Zone-Averaged State Variables

Zone-averaged scalar variables describe the state of each zone as a function of time. Within each zone, for each time step, the value for each grid block is weighted by its volume according to

$$\overline{x} = \frac{\sum_{\text{grid blocks}} v_i x_i}{\sum_{\text{grid blocks}} v_i}$$

(Eq. 12)

where

$\overline{x}$ = zone average of scalar field

v_i = grid block volume

x_i = scalar field value

This procedure and Equation 12 are implemented in software routine ZONEAVG V1.2, which reads the NUFT V3.0s output file (*.ext) and produces an output file (*.zavg) that contains a table of zone-averaged values for each zone and for each time step listed in Section 6.1.1 and in the NUFT input file (*.in by inclusion of file "outputtime"). Only those scalar variables identified in the NUFT V3.0s input file (*.in) are included in the zone-averaged output.

For each NUFT case run, the zone-averaged output for the matrix (*.m.ext.zavg) and the fractures (*.m.ext.zavg) is input to the TH+GASMODEL routine (file: "th+gasmodel_L4C*-*i-04.xls", worksheet: Matrix.zavg, and worksheet: Fracture.zavg). The entire contents of the zone-averaged output files (*.zavg) are transferred to the worksheets.

6.1.2.3 Vertical Mass-Flux Profiles

Software routine VFLUXPROF V1.1 sorts the NUFT output (*.ext) and produces an output file (*.vflux) containing the vertical component of the gas-phase total mass flux, along a vertical profile passing through the drift centerline. The structure of the output file is a table with columns corresponding to vertical position (z-index) and rows corresponding to the time steps at which NUFT V3.0s output was generated. A plot of the vertical component of the gas-phase total mass flux for the L4C4 location, "upper" infiltration, and simulation time of 1000 yr, along a vertical profile passing through the drift center, is shown in Figure 5.

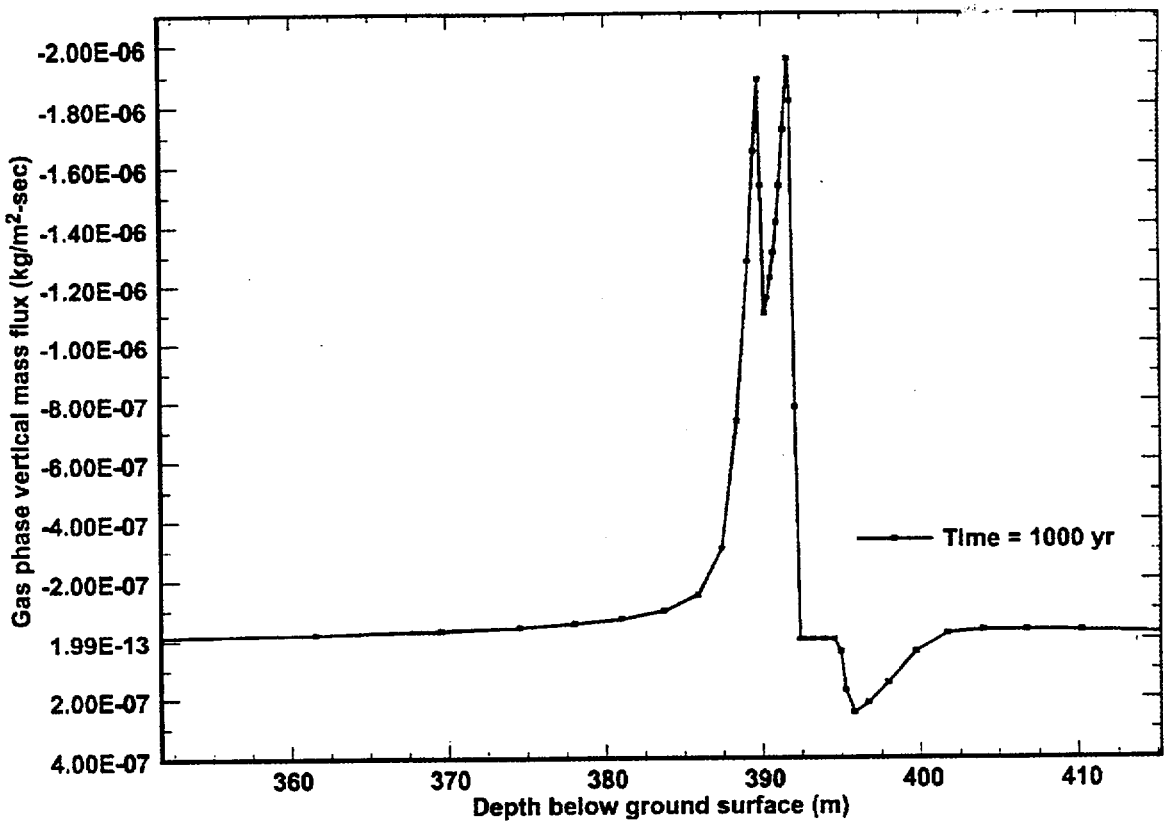

NOTES: Plotted along a vertical profile pass through the drift center for the L4C4 location and the "upper" infiltration distribution in units of kg/(m-sec)
Simulation time of 1000 yr
Plotted from file "L4C4-LDTH60-1Dds-ui-f.ext" using XTOOL 10.1

Figure 5. Vertical Component of the Gas-Phase Total Mass Flux (Air and Water Vapor) Along a Vertical Profile Passing Through the Drift Center

For each NUFT case run, the vertical profile of mass-flux for the matrix (*.m.ext.vflux) and the fractures (*.m.ext.vflux) is input to the TH+GASMODEL routine (file: "th+gasmodel_L4C*-*i-04.xls"; worksheet: Vertflux). The entire contents of the output files (*.vflux) are transferred to the worksheets.

6.1.3 Summary of NUFT Calculations and Postprocessing

6.1.3.1 Temperature, Saturation, and Air Mass-Fraction

Plots of temperature, saturation, and gas-phase air mass-fraction for Zone 4 at the drip-shield surface are shown in Figure 6 through Figure 8. These figures were generated by collecting columns of zone-averaged data values from the TH+GASMODEL routine (file: "th+gasmodel_L4C*-*i-04.xls"; worksheet: Matrix.zavg for saturation, and worksheet: Fracture.zavg for temperature and air mass-fraction).

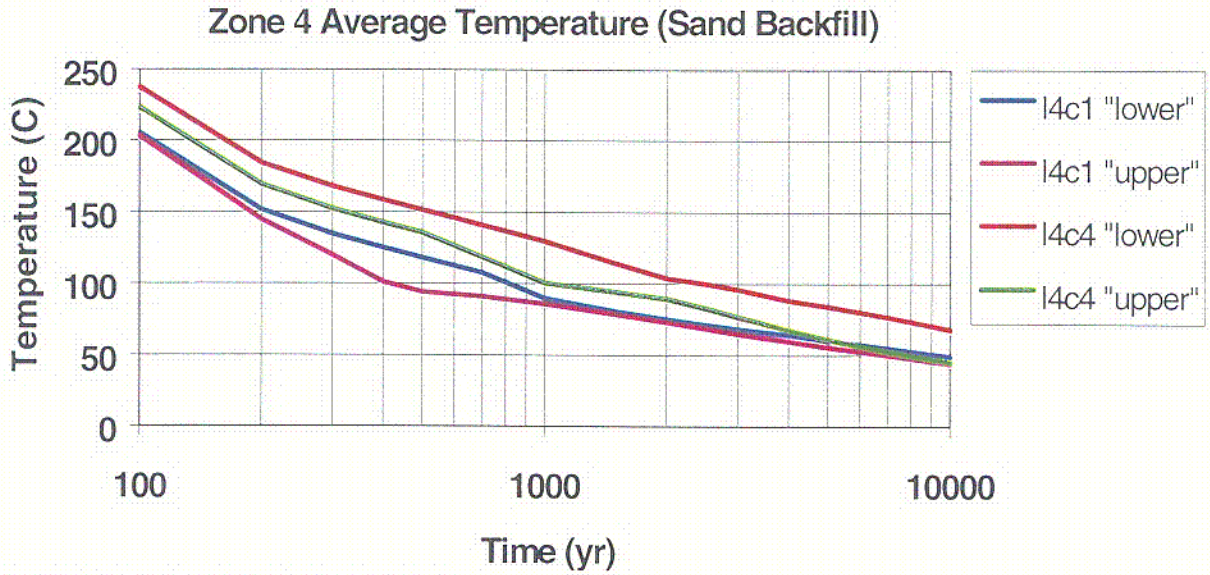

NOTES: Backfill at the drip-shield surface
Calculated for the L4C1 and L4C4 locations, using the "upper" and "lower" infiltration distributions

Figure 6. Average Temperature for Zone 4

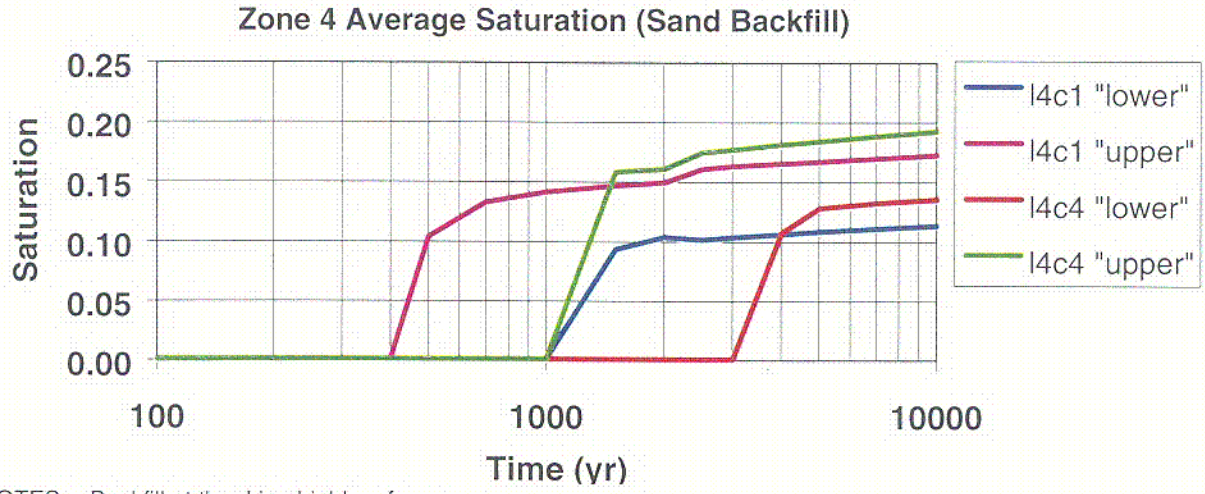

NOTES: Backfill at the drip-shield surface
Calculated for the L4C1 and L4C4 locations, using the "upper" and "lower" infiltration distributions

Figure 7. Average Saturation for Zone 4

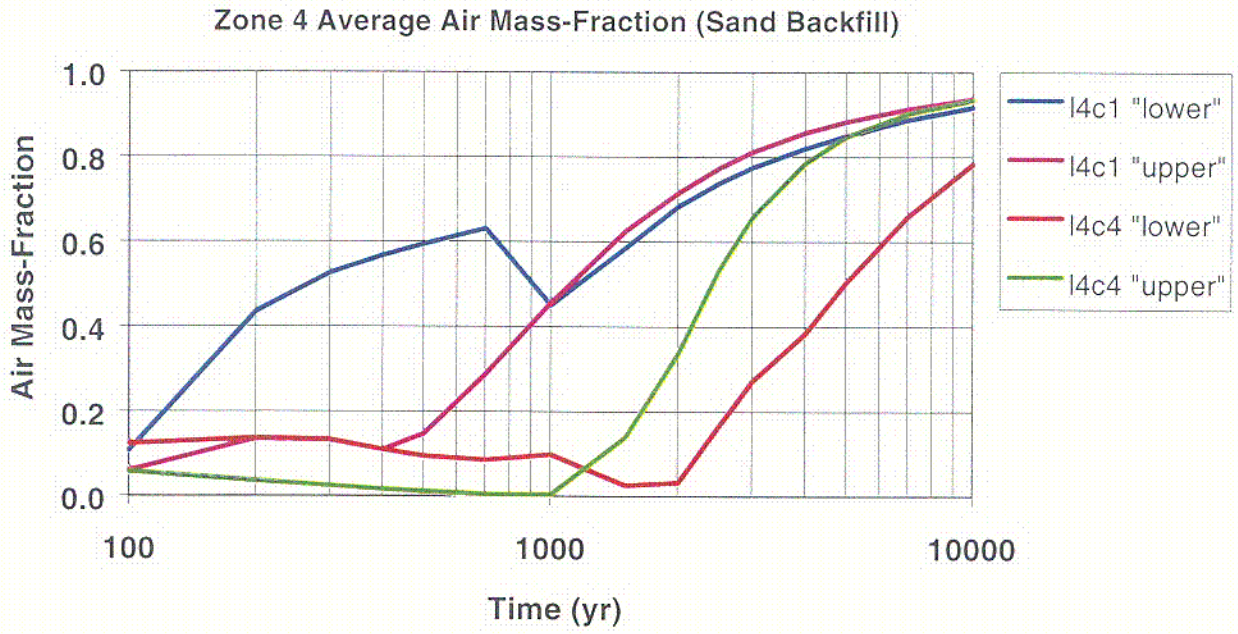

NOTES: Backfill at the drip-shield surface
This plot compares NUFT output for the L4C1 and L4C4 locations and the "upper" and "lower" infiltration distributions.

Figure 8. Average Air Mass-Fraction for Zone 4 as a Function of Time

The plots compare results from the four NUFT V3.0s runs generated for this report (i.e., data were taken from each of the four TH+GASMODEL routines). Examination of plots of zone-averaged data of this type has shown the following:

Temperature

- Matrix and fracture temperature fields are similar for these calculations and may be used interchangeably.
- Cooldown occurs sooner for conditions representing the repository edge.
- Low-flux conditions produce greater peak temperatures and slower cooldown because less liquid water is available to evaporate and transfer latent heat.

Saturation

- The spatial extent of dryout (zero or low liquid saturation) is greater for low-flux conditions.
- Water returns to the EBS environment sooner for high-flux conditions and for conditions representing the repository edge.

- After cooldown, the liquid water saturation in the upper part of the backfill is approximately 10 percent to 20 percent, depending on whether the infiltration distribution is "lower" or "upper."

Air Mass-Fraction

Air mass-fraction is calculated by NUFT V3.0s for matrix and fractures at each grid block for each time step (outputtime). The air mass-fraction represents the displacement of air by water vapor from evaporation. At high relative humidity, when the temperature is near the boiling point, the partial pressure of water approaches the total pressure, and the air mass-fraction approaches zero. Evaluation of air mass-fraction calculated data (*.zavg) has shown the following:

- Matrix air mass-fraction is smaller, and thus relative humidity is greater, than in the fracture network. This is because of vapor pressure lowering by the capillary potential at partial saturation, which tends to retain water in the matrix.

- The minimum air mass-fraction in the drift occurs when the rate of evaporation in the drift is maximal.

- The minimum air mass-fraction is approximately 10^{-3} when thermal output and infiltration (seepage) are maximized, as for the L4C4 location with the "upper" infiltration distribution.

6.1.3.2 Evaporation Rate

Evaporation rate is calculated by NUFT V3.0s, using a mass balance on liquid and gas-phase water fluxes, for each grid block at each time step for which output is directed (outputtime) for the matrix and the fractures. Evaporation rate is a scalar field, and a plot of the evaporation rate for the fracture continuum at the L4C4 location with the "upper" infiltration distribution at simulation time of 1000 yr is shown in Figure 9. This model and time step represent the maximum rate of evaporation calculated for the drip shield surface.

Total evaporation rate for all zones is computed from the zone-averaged results using

$$X_{total} = \sum_{zones} \max\{0, \overline{x}_j\} \sum_{\substack{\text{grid blocks} \\ \text{in jth zone}}} v_{i,j}$$

(Eq. 13)

where

X_{total} = total evaporation rate for all zones

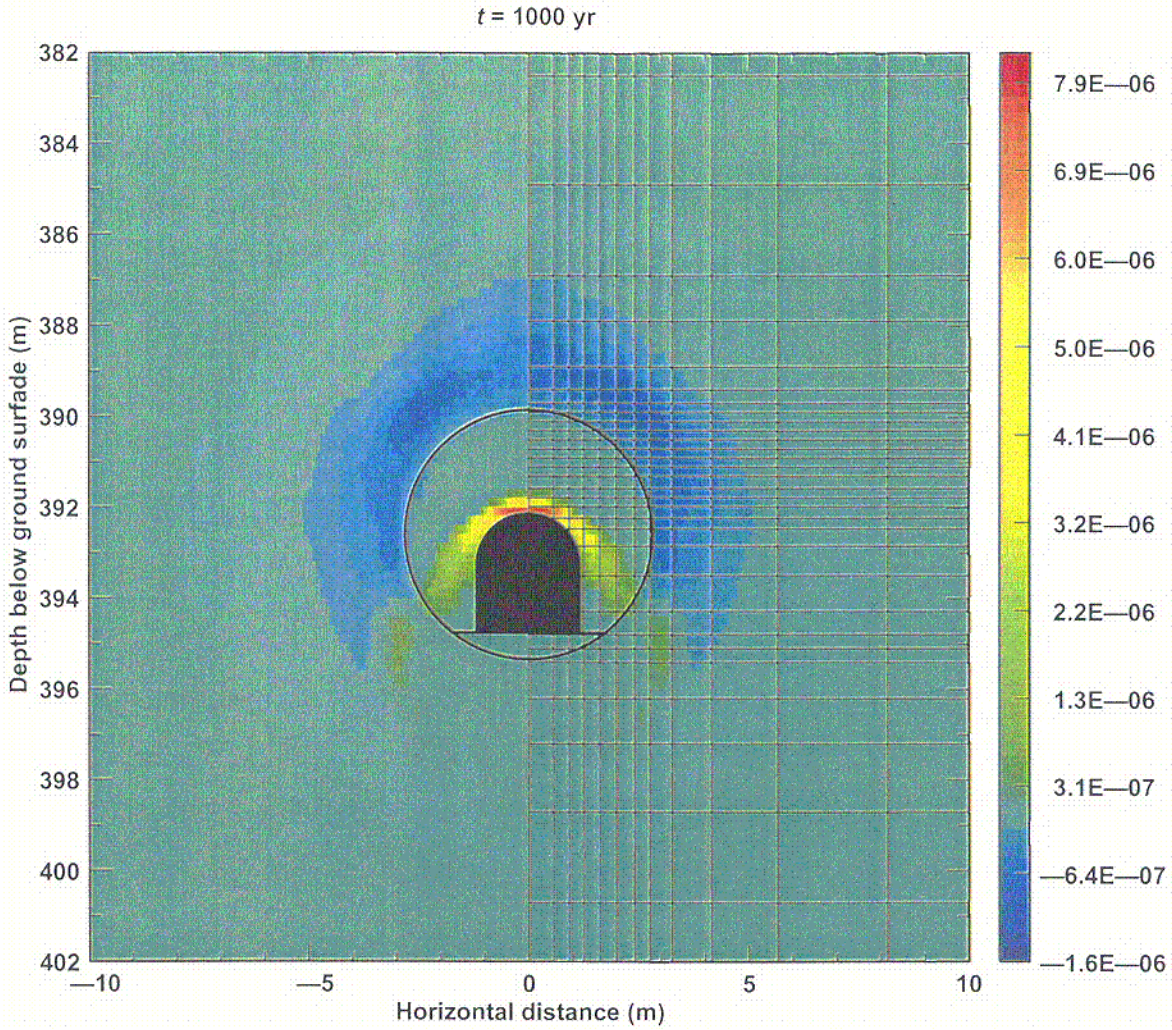

NOTES: The plotted variable is the evaporation rate from the fracture continuum. The color bar gives values for the mass rate of evaporation per unit volume (kg/m^3-sec). Positive values indicate evaporation; negative values indicate condensation. The model grid is plotted for reference.
Plotted from file "L4C4-LDTH60-1Dds-ui.f.ext" using XTOOL V10.1.

Figure 9. Fracture Evaporation Rate Field for the L4C4 Location with the "Upper" Infiltration Distribution at Simulation Time of 1000 yr

$\overline{X}_j$ = zone-averaged evaporation, j^{th} zone, for fractures and matrix combined (sign convention: positive is evaporation)

$v_{i,j}$ = volume of the ith grid block in the jth zone

Equation 13 is implemented in the TH+GASMODEL routine (file: "th+gasmodel_L4C*-*i-04.xls"; worksheet: Evap) using zone-averaged variable "qPhChg.water.gas" for both the matrix and fractures (data tabulated in worksheet: Matrix.zavg and worksheet: Fracture.zavg).

C5

The quantity

$$\sum_{\substack{\text{grid blocks} \\ \text{in jth zone}}} v_{i,j}$$

(Eq. 14)

is also calculated for each zone in the TH+GASMODEL routine (file: "th+gasmodel _L4C*-*i-04.xls"; worksheet: Zone.volume) using NUFT grid block information included in each output file from ZONEAVG V1.2 (*zavg). The total evaporation rates (all zones, fracture and matrix) vs. time are plotted in Figure 10 for all four NUFT models and compared with the repository thermal output vs. time (DTN SN9907T0872799.001; file: "heatTSPA-SR-99184-Ta.xls") (TBV-3599).

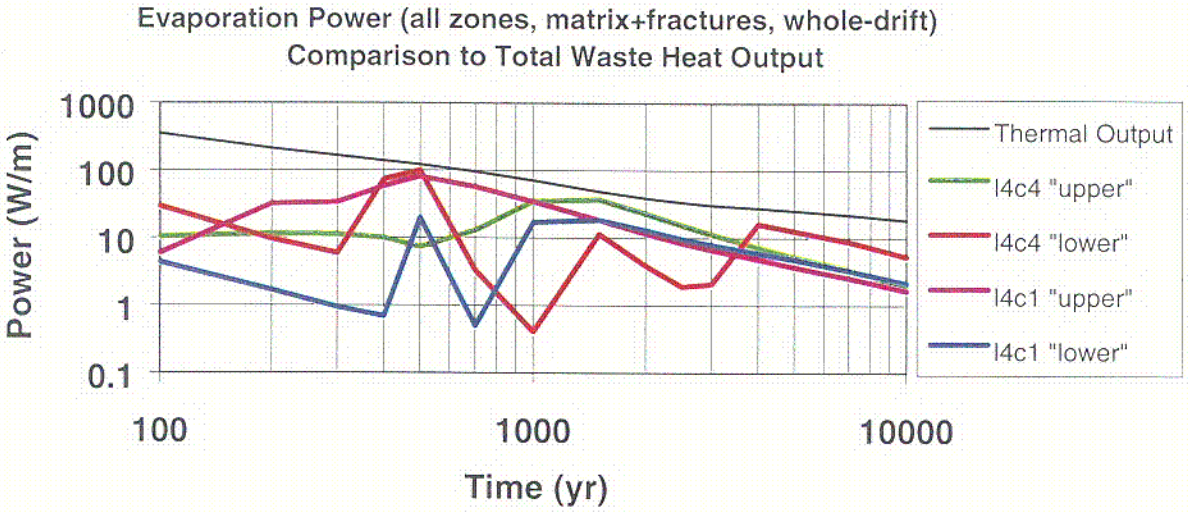

NOTES: Compares the L4C1 and L4C4 locations and the "upper" and "lower" infiltration distributions
The average thermal output (lineal power loading) is plotted for comparison.

Figure 10. Plot of Total Evaporation vs. Time for All Zones, Including Fractures + Matrix

Examination of evaporation rate calculations and plots shows the following:

- The rate of evaporation in the fracture continuum is greater than that in the matrix at the same locations, during the thermal period, because of vapor pressure lowering.
- Evaporation tends to be localized to a narrow zone above the dryout zone, where liquid water from condensation and ambient percolation flows toward the dryout zone under the influence of gravity. The zone of evaporation recedes toward the drip-shield surface as the heat source strength decays with time.

- For all cases, the rate of evaporation for all zones is much smaller than the total thermal output of the waste packages for the first few hundred years.
- For the "upper" infiltration distribution, there is more sustained evaporation (i.e., more total evaporation, with greater duration) that begins sooner for the L4C1 location (repository edge) than for the L4C4 location (center).
- The proportion of thermal output that causes evaporation, tends to decrease with time.

6.1.3.3 Gas-Phase Mass Flux

The vertical component of total mass flux (air + water vapor) in the gas phase, along a vertical profile passing through the drift center, is plotted in Figure 5 for the L4C4 location, "upper" infiltration distribution, and simulation time of 1000 yr. Mass-flux information is output by NUFT V3.0s (*.ext) and postprocessed by the VFLUXPROF software routine to extract the profile for the vertical component only (*.vlux). Mass flux is positive upward.

In addition, a horizontal profile of the vertical component of the gas-phase total mass flux for the L4C4 location and "upper" infiltration is shown in Figure 11, for simulation time of 1000 yr. This plot was produced using XTOOL V10.1 and the NUFT V3.0s output file (L4C4*.ext).

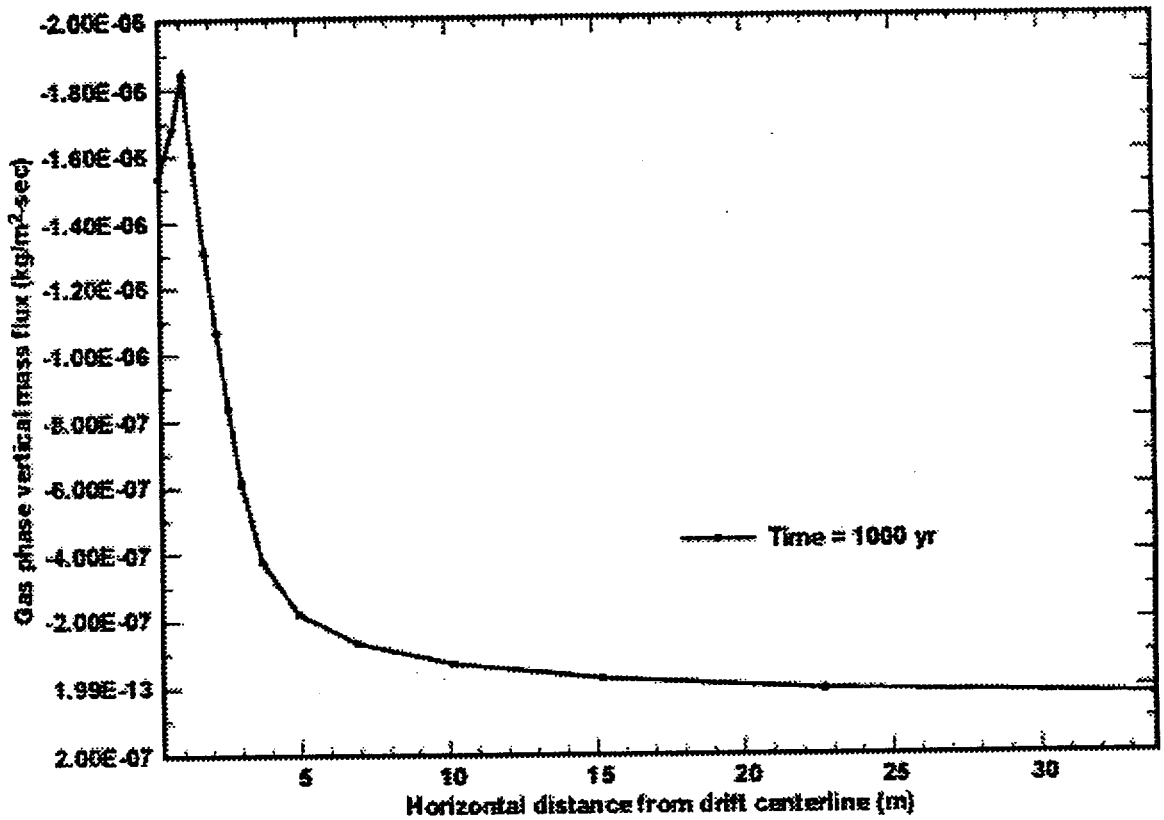

NOTES: For the L4C4 location and "upper" infiltration distribution
Simulation time of 1000 yr
The elevation of the profile represented in this plot, corresponds to approx. 392 m depth on Figure 5.
Plotted from file "L4C4-LDTH60-1Dds-ui.f.ext" using XTOOL V10.1

Figure 11. Vertical Component of the Gas-Phase Total Mass Flux (Air + Water Vapor) Along a Horizontal Profile Passing through the Drift Center

These calculated results and plots show the following:

- For the 2-D NUFT V3.0s models used in this report, the gas-phase mass flux is driven by evaporation of water. The excess pressure in the gas phase caused by evaporation causes mass to be expelled from the top of the model domain, where there is a constant pressure boundary.

- The maximum upward mass flux during the thermal period occurs in the host rock directly above the drift centerline (along the vertical profile). The maximum does not necessarily occur at the drift wall but may occur several meters within the host rock.

- There is a slight circulation, caused by thermally driven buoyant convection, whereby the mass flux is downward in the pillar and upward near the drift at the emplacement

elevation. The magnitude of the downward flux is much smaller than that of the upward flux.

6.1.4 Representing Thermal-Hydrologic Evolution by Uniform Time Intervals

To support chemical-reaction cell modeling, the repository thermal evolution is simplified to a series of intervals during which zone temperatures and fluxes are held constant, as shown in Table 30.

Table 30. Intervals During Which Zone Temperatures and Fluxes Are Held Constant

Nominal Time (yr)	Time Interval (yr)	
	From	To
100	50	300
500	300	700
1000	700	1,500
2000	1500	2,500
5000	2500	10,000

The values defining the time intervals are user-defined input in the TH+GASMODEL routine (file: "th+gasmodel _L4C*-*i-04.xls"; worksheet: THmodel). The values for the nominal time are assigned to the time interval without interpolation.

Using the TH+GASMODEL software routine (file: "th+gasmodel _L4C*-*i-04.xls"; worksheet: THmodel) values for liquid-phase water flux, the gas-phase water flux, fracture temperature, fracture air mass-fraction, fracture saturation, and matrix saturation are tabulated. The data are linked to other worksheets within the same routine.

The assigned time intervals bracket transitions in climate conditions at 600 and 2000 yr, so the effects of those transitions are incorporated at 700 and 2500 yr. Early-time thermal behavior, peak thermal behavior, and cooldown are represented in such a way that the interval values for temperatures and fluxes between zones lie reasonably close to the values calculated directly using NUFT V3.0s (Figure 4).

Preclosure (≤ 50 yr) TH conditions in the host rock and in the drift are not evaluated because they will be dominated by ventilation. The drying effects of ventilation are not explicitly simulated using the NUFT V3.0s formulation described in this report. The effects of preclosure processes on the composition of mobile waters and the accumulation of precipitates in the host rock fractures and matrix are assumed to be negligible for this report (Assumption 5.1.6).

6.1.5 Mass-Balance Calculation

Routine TH+GASMODEL (file: "th+gasmodel _L4C*-*i-04.xls"; worksheet: Thmodel) also includes a mass-balance analysis to verify that zone influxes and outfluxes sum to zero for each time interval. This is done as a check on data transcription and discretization errors. Also, there are small water fluxes in and out of Zones 5 and 6 during the thermal period that were not

specified to be included in NUFT output (because they could be calculated from the specified output). The routine calculates these small liquid fluxes and includes them in the mass balance. The need for these adjustments to the zone mass fluxes arises from temporal and spatial discretization of the calculated TH data.

Mass balance is calculated by adding together all the water liquid and vapor mass fluxes for each zone. The residual values are identified as being liquid fluxes back to the host rock (Zones 1 and 2) or gas fluxes (Zones 3 and 4). Evaporation in the backfill was maximized by assigning residual values to the gas-phase flux from Zones 3 and 4. For Zones 5 and 6, the residual values were assigned to the gas-phase flux for time intervals when the zones are dry and to the liquid-phase flux when they are not dry.

6.1.6 Conservative Solute Analysis Using Zone Fluxes

The zone-averaged saturations and fluxes between zones are analyzed to gain insight into requirements for chemical modeling. The four calculated TH cases are analyzed to support the basis for choosing one of them for more elaborate analysis of the Chemical Reference Model.

A fictive, conservative solute tracer is assumed to be present at a constant concentration ($C_0 = 1$) in water entering Zone 1 from Zone 0 above. The solute is then transported between zones at mass transfer rates that are determined by the liquid-phase concentrations and the liquid flow rates between zones. The approach is applied to the stepwise steady-state, finite-time-interval, zone-averaged descriptions of the liquid mass and to fluxes in and out of each zone. Both gas-phase and liquid-phase fluxes are considered so that the effects of evaporation and condensation are considered.

For linking solute fluxes between zones, it is necessary to consider the direction of fluxes so that the flux can be associated with the correct source concentration and destination zone. The following are needed for each zone, and each time interval:

- Positive liquid influx (or zero flux) from every other zone with a possible flow connection
- Total liquid water outflow rate from the zone
- Net gas-phase water-vapor flux (can be negative; positive values indicate mass increase)

Data preparation for the conservative solute analysis is handled in the TH+GASMODEL routine (file: "th+gasmodel _L4C*-*i-04.xls"; worksheet THmodel). For the liquid influxes to each zone, the algorithm tests the sign of each flux so that it can be assigned to the correct zone-to-zone connection. For the liquid outflux from each zone, the appropriate zone-to-zone fluxes are summed. The gas-phase fluxes are copied directly from the mass-balance analyses and include adjustments for discretization errors.

6.1.6.1 Derivation of Conservative Solute Analysis

In the conservative solute analysis for a given zone, when the influent concentration is greater than the outfluent concentrations, the concentration tends to increase; when the outfluent concentration is greater than the influent concentrations, the concentration tends to decrease. Also, in each cell, the concentration tends to be increased by evaporation and decreased by condensation.

For a single zone, the rate of change of the concentration is

$$\frac{\partial C_i}{\partial t} = \frac{1}{V_i}\sum_j q_{ji}C_j - \frac{C_i}{V_i}\sum_j q_{ik}$$

(Eq. 15)

where

C_i	=	concentration in the ith zone
q_{ji}	=	inflow rate from the jth zone into the ith zone
C_j	=	concentration in the jth zone
V_i	=	volume of the ith zone
q_{ik}	=	outflow rate from the ith zone to the kth zone

The summations imply that there can be more than one source of inflow or outflow. This formulation represents the change in concentration during a time interval during which the hydrologic conditions are constant but the solute concentration can vary. The fluxes (q_{ji}, q_{ik}) and volumes (V_i) are provided from the TH Model calculations for zone-average and zone-flux. The volume, or mass of solvent present in each cell, is invariant during each time interval; therefore, evaporation and condensation fluxes are not considered directly in the mass balance, but they are taken into account in the values used for liquid fluxes. Equation 15 is solved in the SOLUTERK routine (file: "SoluteRKV1.2_*L4C*-*i.mcd").

Equation 15 is written in terms of solute concentrations and volumetric flow rates, but a solution for the concentrations can easily be used to calculate the mass of solute in each zone as a function of time. The conversion is

$$m_i = C_i V_i$$

(Eq. 16)

which is used at the end of the routine (vector m) to calculate final solute mass m_i for use in analyzing the next time interval; it is also used to convert calculated concentrations to masses (matrix Mm). Volume V_i may be treated as solvent mass (in kg) instead of in volume (in liters) without consequence to the analysis.

Solution of Equation 15 requires initial concentrations that are based on the final masses from the previous time interval. For the first time interval, initial concentrations are set to zero, which is appropriate for initially dry materials. At the conclusion of each time interval, the solute mass is calculated using Equation 16. At the beginning of each time interval after the first, the initial concentration is calculated from the initial mass and the new volume for each zone.

When there is liquid inflow to a zone but the liquid mass or volume in the zone is zero (i.e., complete evaporation), a minimum value for V_i is used to facilitate the solute mass calculation (V_{min}). This is appropriate because there is no outflow, and the minimum value is canceled when the new solute mass values are calculated at the end of each time interval. The value for V_{min} is selected to be 1 L so that the computed solute concentrations may be interpreted as multiples of the reference concentration (C_0).

Expanding Equation 15 to represent all possible connections in Zones 1 through 6 (see Figure 3), a system of ordinary differential equations is developed:

$$
\begin{aligned}
\frac{\partial C_1}{\partial t} &= \frac{q_{01}C_0}{V_1} - \frac{(q_{12}+q_{10})C_1}{V_1} + \frac{q_{21}C_2}{V_1} \\
\frac{\partial C_2}{\partial t} &= \frac{q_{02}C_0}{V_2} + \frac{q_{32}C_3}{V_2} + \frac{q_{12}C_1}{V_2} - \frac{(q_{23}+q_{20}+q_{21})C_2}{V_2} \\
\frac{\partial C_3}{\partial t} &= \frac{q_{23}C_2}{V_3} - \frac{(q_{34}+q_{35}+q_{32})C_3}{V_3} + \frac{q_{43}C_4}{V_3} + \frac{q_{53}C_5}{V_3} \\
\frac{\partial C_4}{\partial t} &= \frac{q_{34}C_3}{V_4} - \frac{(q_{43}+q_{45})C_4}{V_4} + \frac{q_{54}C_5}{V_4} \\
\frac{\partial C_5}{\partial t} &= \frac{q_{05}C_0}{V_5} + \frac{q_{35}C_3}{V_5} + \frac{q_{45}C_4}{V_5} - \frac{(q_{53}+q_{54}+q_{56}+q_{50})C_5}{V_5} + \frac{q_{65}C_6}{V_5} \\
\frac{\partial C_6}{\partial t} &= \frac{q_{06}C_0}{V_6} + \frac{q_{56}C_5}{V_6} - \frac{(q_{60}+q_{65})C_6}{V_6}
\end{aligned}
$$

(Eq. 17)

where the notation is consistent with the C_i, q_{ij}, V_i notation used for Equation 15. This system is solved for each time interval by the Runge-Kutta method with adaptive step-size control, using the SOLUTERK routine. The Runge-Kutta algorithm is implemented in the intrinsic function "RKadapt" in Mathcad Pro V8. All units in this formulation follow the SI units convention.

For each time interval, the inputs are developed using the TH+GASMODEL routine (file: "th+gasmodel-L4C*-*i-04.xls"; worksheet: Thmodel). If liquid volume in a reaction cell is zero, a minimum value is assigned ($V_{min} = 1$).

The spreadsheet balances the fluxes and assigns values to liquid fluxes q_{10}, q_{05}, q_{50}, q_{06}, and q_{60}, which are not calculated by NUFT V3.0s. Where the destination zone has small or zero liquid volume, these balance fluxes are assigned to gas fluxes; otherwise they are liquid fluxes.

Annotations are provided in the spreadsheet files showing where these small adjustments are made.

The input data from routine TH+GASMODEL are transferred manually to routine SOLUTERK. As initial data for the first time interval (50 to 300 yr), the initial masses in all zones are set to zero. In this way, the final masses in each zone after the last time interval can be compared, as a check on the accuracy of the procedure, to the product of the reference concentration (C_0) and the final liquid volume for the zone.

6.1.6.2 Results from Conservative Solute Analysis

The procedure described in the foregoing section is repeated for each location and infiltration distribution calculated using NUFT V3.0s (locations L4C1 and L4C4; "upper" and "lower" infiltration). The results are plotted as normalized solute concentration vs. time for each zone for the TH cases (Figure 12 through Figure 15). Concentration is normalized to the reference concentration (C_0 = 1), except for when a zone is completely dry, when the equivalent concentration is plotted for 1 liter of solvent. All plotted concentrations may therefore be interpreted as multiples of the reference concentration.

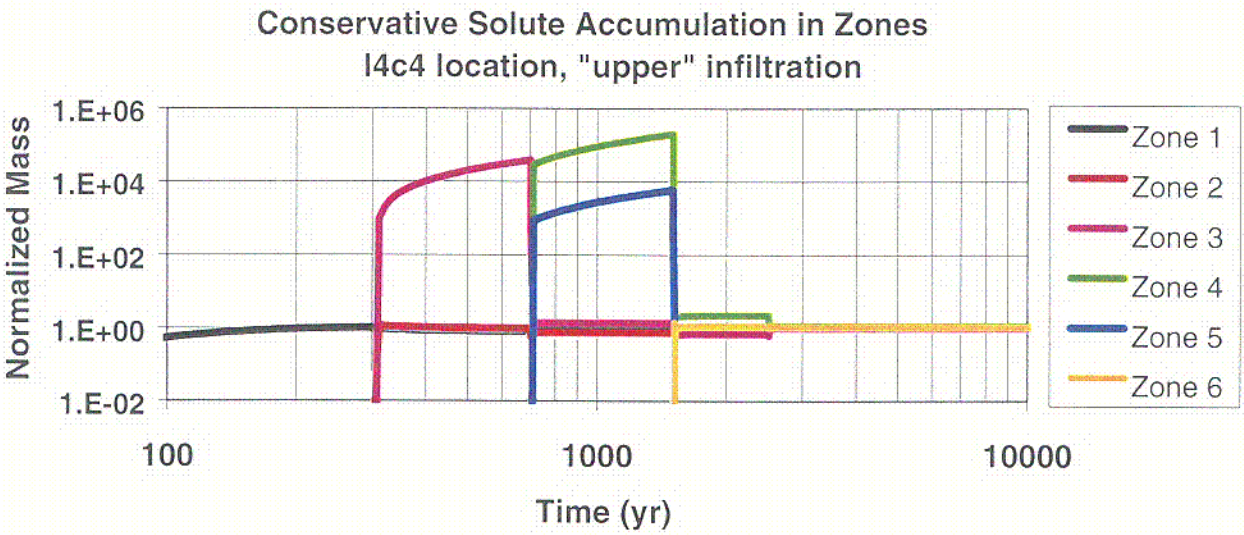

Figure 12. Normalized Mass of a Fictive Conservative Solute in Each Zone for Each of Five Time Intervals for the L4C4 Location with the Upper Infiltration Distribution

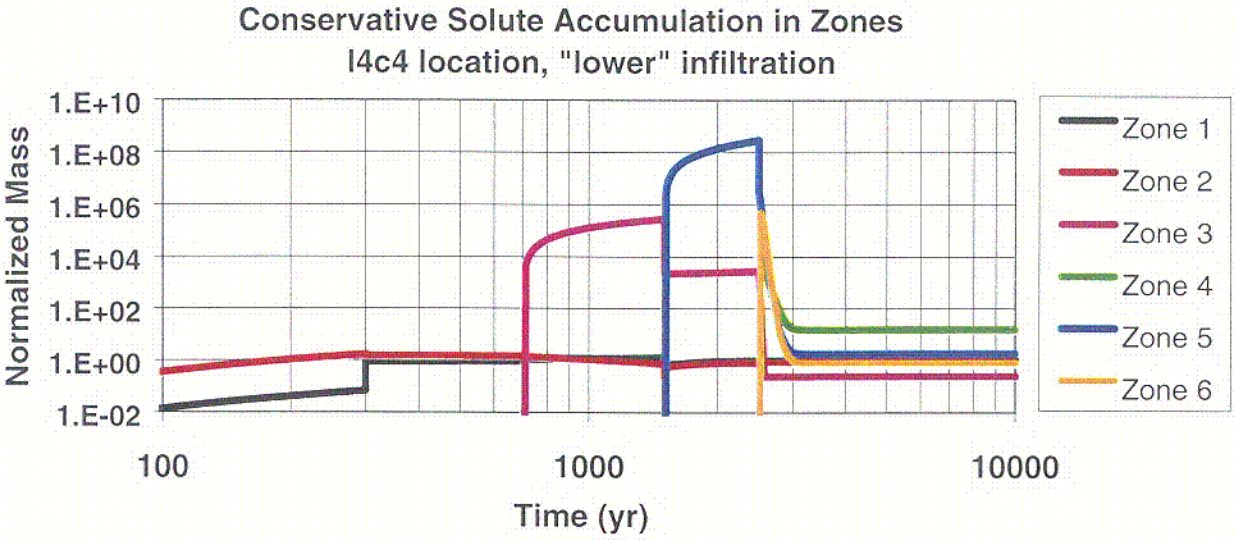

Figure 13. Normalized Mass of a Fictive Conservative Solute in Each Zone for Each of Five Time Intervals for the L4C4 Location with the Lower Infiltration Distribution

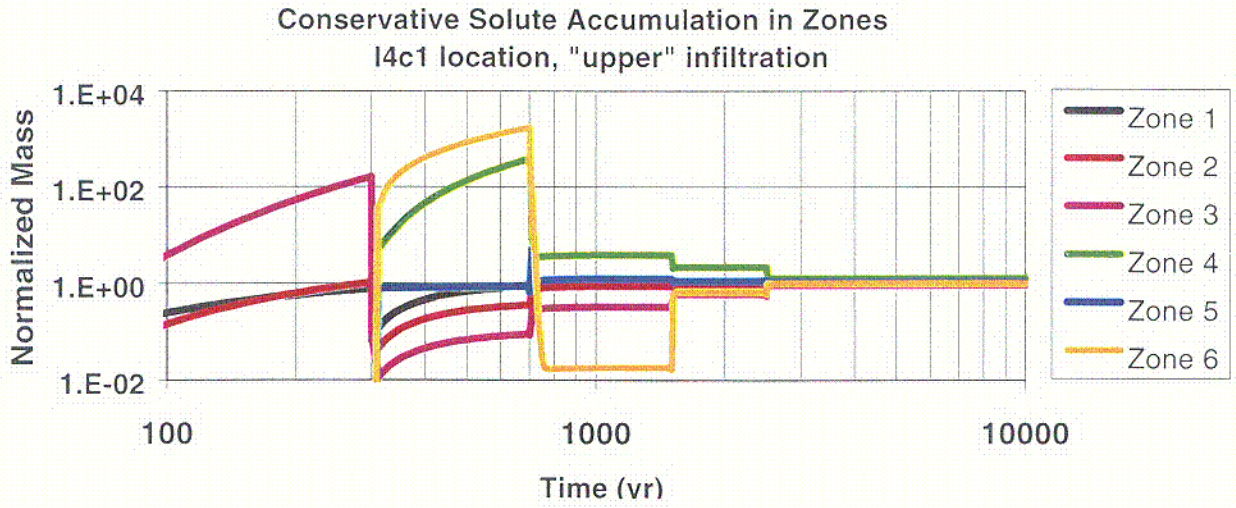

Figure 14. Normalized Mass of a Fictive Conservative Solute in Each Zone for Each of Five Time Intervals for the L4C1 Location with the Upper Infiltration Distribution

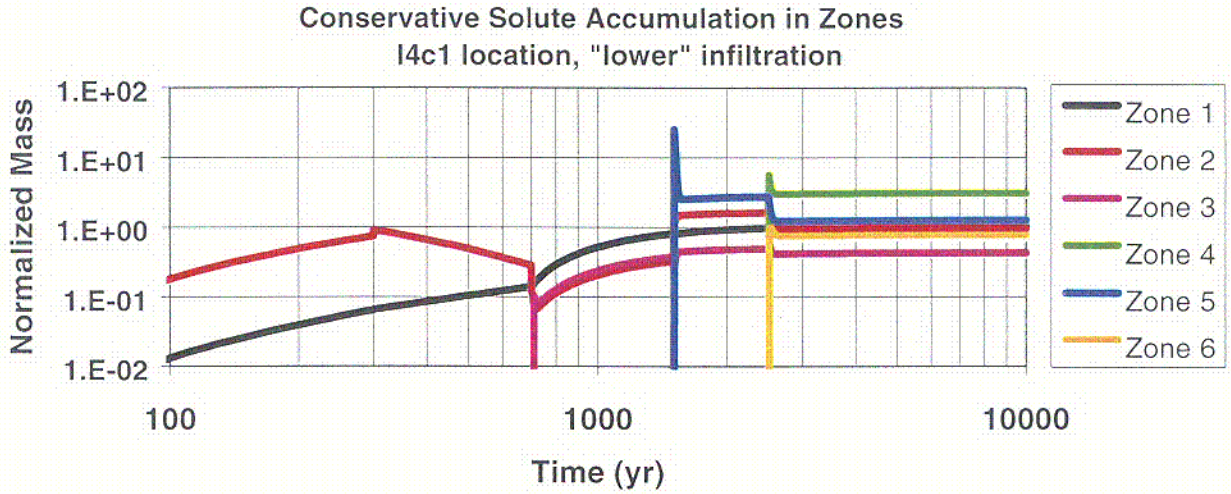

Figure 15. Normalized Mass of a Fictive Conservative Solute in Each Zone for Each of Five Time Intervals for the L4C1 Location with the Lower Infiltration Distribution

The maxima on these plots represent conditions for which liquid inflow occurred, but there was no liquid outflow (i.e., evaporation was complete); thus, all the solute transported to the zone was accumulated. In the calculation, when liquid returns to such a zone, the solute rapidly disperses; this is equivalent to infinite solubility. Accordingly, while these calculations provide reasonable estimates for potential solute accumulation from evaporation, they underestimate the time for which the accumulated solute mass remains in each zone. For solutes with limited solubility and prograde solubility variation with temperature (e.g., silica), the accumulation could remain for tens of thousands of years. The minima on these plots represent conditions where there is liquid outflow, but at least some of the liquid inflow occurs as condensation.

The conservative solute calculations and plots show the following:

- When zones have no liquid outflow, substantial accumulation of soluble salts may occur from evaporation (the zones need not be dry for this to occur).

- Solute mass on the order of 2×10^5 times the solute mass present in 1 kg of reference composition may accumulate in Zone 4 (drip-shield surface; see Figure 12). If chloride is present in the reference water at 7 mg/l (typical for J-13 water), the accumulated mass in the backfill could approach 1.5 kg per meter of drift.

- Comparing Figure 12 through Figure 15 with Figure 6, there is the potential for solute to accumulate in the backfill and at the drip-shield surface before these zones have cooled through boiling. Thus, there is the potential for aqueous conditions, caused by osmolality, at temperatures greater than 96°C.

- For location L4C1 (repository edge), the potential accumulation of soluble salts is less than at L4C4 (repository center) because there is less heat available for evaporation. The greater effective drift spacing enhances cooling; thus, drifts cool to less than 96°C within approximately 400 to 800 yr, depending on the infiltration flux. When the increased infiltration flux at 600 yr (i.e., representing future climate change) causes greater flux in the drifts, the temperature at the edge is less than or near boiling, whereas the repository center is hotter.

- For the L4C4 location with "lower" infiltration (Figure 13), less solute accumulates in Zone 4 because there is less evaporation there, even though temperatures are generally greater than for the "upper" infiltration (Figure 6). This may be an artifact of the solute calculation method and the selection of time intervals.

- For the "lower" infiltration results (Figure 13 and Fgure 15), solute concentrations are likely to stabilize at elevated levels (e.g., tenfold) in late-time, even if extreme evaporative solute accumulation does not occur previously.

- For the "lower" infiltration results, there is greater potential for solute accumulation in the invert (Zones 5 and 6). This may occur because, for an interval of time, the invert is cooler than the drip shield and receives liquid flux from the upper backfill (Zone 3) and the host rock (Zone 0).

The principal factors that limit solute accumulation on the drip shield are more rapid cooling (to less than 96°C) and less liquid flux into the drift (i.e., smaller infiltration). These factors are not well correlated because greater flux causes faster cooling, and greater percolation flux in the host rock is more likely to produce drift seepage.

It should be noted that NUFT V3.0s, as implemented for this report, does not simulate solute behavior and does not modify liquid boiling temperatures to account for osmotic effects (boiling-point elevation). Thus, there is the potential to underpredict solute accumulation by the method used here. However, the effect is probably small because the fluids in question are evaporated by 100- to 1000-fold; thus, their volume is small, and the associated saturation-dependent hydraulic conductivity in the backfill is small.

6.1.7 Selection of a Thermal-Hydrologic Model for Reasonable-Bound Chemical Modeling

The L4C4 location with the "upper" infiltration distribution is selected as a reasonable-bound case for chemical modeling of the in-drift environment. This is based on assessment of the TH calculation results, with respect to the assumed environmental conditions that promote corrosion (Assumption 5.1.7): duration of adverse conditions, temperature at which adverse conditions occur, precipitated salts, and alkaline (high-pH) conditions.

From discussion of the TH calculations described in this section, the following criteria are found to represent the environmental conditions that promote corrosion:

- Accumulation of conservative solute in Zone 4 (Figure 12 through Figure 15)
- Temperature at which aqueous conditions occur in Zone 4 (Figure 6)
- Duration for which adverse conditions occur at elevated temperature in Zone 4 (Figure 12 through Figure 15and Figure 6 through Figure 8)
- Proportion of thermal output that produces evaporation, especially during sustained periods when aqueous conditions occur in Zone 4 (Figure 10).

The L4C4 location with "upper" infiltration produces reasonable-bound conditions according to these criteria. The zone-averaged fluxes, temperatures, and liquid masses calculated by software routine TH+GASMODEL are shown in Table 31 (file: "th+gasmodel_L4C*-*i-04.xls"; worksheet: THmodel).

Table 31. Zone-Averaged Temperatures, Liquid and Water Vapor Influxes and Outfluxes, and Liquid Masses for Each Zone (L4C4 Location, "Upper" Infiltration)

Time (yr)		Liquid Fluxes Between Zones (kg/m-sec)						
From	To	Liquid 0 to 1	Liquid 1 to 2	Liquid 2 to 3	Liquid 3 to 4	Liquid 3 to 5	Liquid 4 to 5	Liquid 5 to 6
50	300	3.491E-05	5.493E-12	0.000E+00	0.000E+00	0.000E+00	0.000E+00	0.000E+00
300	700	3.353E-05	3.218E-06	2.510E-06	0.000E+00	0.000E+00	0.000E+00	0.000E+00
700	1500	6.165E-05	1.026E-05	1.105E-05	4.773E-06	1.039E-06	0.000E+00	0.000E+00
1500	2500	6.103E-05	5.034E-06	5.646E-06	4.575E-06	3.746E-06	1.410E-06	4.678E-06
2500	10000	1.049E-04	8.639E-06	8.684E-06	3.352E-06	5.930E-06	2.717E-06	8.376E-06
Time (yr)		Liquid Water Mass (kg/m)						
From	To	Zone 0	Zone 1	Zone 2	Zone 3	Zone 4	Zone 5	Zone 6
50	300		7.412E+04	5.612E+01	0.000E+00	0.000E+00	0.000E+00	0.000E+00
300	700		7.855E+04	1.221E+02	2.500E+00	0.000E+00	0.000E+00	0.000E+00
700	1500		8.220E+04	2.184E+02	2.553E+02	0.000E+00	7.242E+00	0.000E+00
1500	2500		8.255E+04	2.207E+02	3.548E+02	3.848E+01	1.479E+02	5.640E+01
2500	10000		8.212E+04	2.207E+02	3.972E+02	4.408E+01	1.617E+02	6.147E+01
Time (yr)		Temperature (C)						
From	To	Zone 0	Zone 1	Zone 2	Zone 3	Zone 4	Zone 5	Zone 6
50	300	7.364E+01	8.078E+01	1.223E+02	1.570E+02	2.225E+02	1.934E+02	2.076E+02
300	700	8.730E+01	9.003E+01	9.962E+01	1.112E+02	1.346E+02	1.248E+02	1.298E+02
700	1500	8.631E+01	8.840E+01	9.600E+01	9.605E+01	9.972E+01	9.913E+01	1.017E+02
1500	2500	7.821E+01	7.995E+01	8.479E+01	8.675E+01	8.881E+01	8.824E+01	8.905E+01
2500	10000	5.019E+01	5.168E+01	5.456E+01	5.659E+01	6.018E+01	5.869E+01	5.947E+01
Time (yr)		Liquid Water Outflux (kg/m-sec; >0 is mass decrease)						
From	To	Zone 0	Zone 1	Zone 2	Zone 3	Zone 4	Zone 5	Zone 6
50	300		3.209E-05	2.205E-09	0.000E+00	0.000E+00	0.000E+00	0.000E+00
300	700		3.500E-05	2.515E-06	0.000E+00	0.000E+00	0.000E+00	0.000E+00
700	1500		6.941E-05	1.105E-05	5.812E-06	0.000E+00	0.000E+00	0.000E+00
1500	2500		6.107E-05	5.646E-06	8.321E-06	1.410E-06	4.813E-06	4.796E-06
2500	10000		1.049E-04	8.684E-06	9.282E-06	2.717E-06	8.583E-06	8.418E-06
Time (yr)		Water Vapor Transfer (kg/m-sec; >0 is mass increase)						
From	To	Zone 0	Zone 1	Zone 2	Zone 3	Zone 4	Zone 5	Zone 6
50	300		-2.818E-06	2.200E-09	0.000E+00	0.000E+00	0.000E+00	0.000E+00
300	700		1.466E-06	-7.030E-07	-2.510E-06	0.000E+00	0.000E+00	0.000E+00
700	1500		7.762E-06	7.880E-07	-5.238E-06	-4.773E-06	-1.039E-06	0.000E+00
1500	2500		4.214E-08	6.062E-07	2.675E-06	-3.165E-06	-3.427E-07	1.175E-07
2500	10000		8.869E-09	4.402E-08	5.980E-07	-6.350E-07	-6.390E-08	4.208E-08

Source: file: "th+gasmodel_L4C4-ui-04.xls"; worksheet: THmodel (Attachment I)

Note : The fluxes between zones is reported in units of kg/(m-sec) and represent integrations of the mass flux across zone boundaries.

Table 32. Zone-Averaged Temperatures, Liquid and Water Vapor Influxes and Outfluxes, and Liquid Masses for Composite Zones (L4C4 Location, "Upper" Infiltration)

Time (yr) From	To	Liquid Influx (kg/m-sec)	Vapor Flux (kg/m-sec)	Liquid Mass (kg/m)	Liquid Outflux (kg/m-sec)	Concentration Factor	Temperature (°C)
Zone 0							
50	300	(This zone is a compositional boundary condition on Zone 1–2, and zone influx/outflux calculations are not performed.)					73.64
300	700						87.3
700	1500						86.31
1500	2500						78.21
2500	10000						50.19
Composite Zone 1–2							
50	300	3.491E-05	-2.816E-06	7.417E+04	-3.209E-05	1.088E+00	80.81
300	700	3.353E-05	7.630E-07	7.867E+04	-3.429E-05	9.778E-01	90.05
700	1500	6.165E-05	8.550E-06	8.241E+04	-7.020E-05	8.782E-01	88.42
1500	2500	6.103E-05	6.483E-07	8.277E+04	-6.168E-05	9.895E-01	79.96
2500	10000	1.049E-04	5.289E-08	8.234E+04	-1.050E-04	9.995E-01	51.69
Composite Zone 3–4							
50	300	0.000E+00	0.000E+00	0.000E+00	0.000E+00	NA	189.77
300	700	2.510E-06	-2.510E-06	2.500E+00	0.000E+00	NA	111.16
700	1500	1.105E-05	-1.001E-05	2.553E+02	-1.039E-06	1.064E+01	96.05
1500	2500	5.646E-06	-4.900E-07	3.933E+02	-5.156E-06	1.095E+00	86.95
2500	10000	8.684E-06	-3.700E-08	4.412E+02	-8.647E-06	1.004E+00	56.95
Composite Zone 5–6							
50	300	0.000E+00	0.000E+00	0.000E+00	0.000E+00	NA	200.53
300	700	0.000E+00	0.000E+00	0.000E+00	0.000E+00	NA	127.29
700	1500	1.039E-06	-1.039E-06	7.242E+00	0.000E+00	NA	99.13
1500	2500	5.156E-06	-2.252E-07	2.043E+02	-4.931E-06	1.046E+00	88.46
2500	10000	8.647E-06	-2.182E-08	2.232E+02	-8.625E-06	1.003E+00	58.90

NOTES: "NA" signifies not applicable, because there is no liquid inflow and/or outflow.
Source: file "th+gasmodel-L4C4-ui-04.xls"; worksheet: CHEMprobl4cL4C4upper (Attachment I)

These data are further processed in the same routine (worksheet: CHEMprobL4C4upper) to consolidate the zones to expedite the chemical calculations. Zones 1 and 2 represent the host rock above the drift (combined to become Zone 1–2); Zones 3 and 4 represent backfill above the drip shield (Zone 3–4); and Zones 5 and 6 represent backfill and invert materials in the lower part of the drift (Zone 5–6). The results are shown in Table 32.

For the consolidation step, fluxes and liquid masses were added, while composite temperatures were calculated using an average weighted by the water mass in each constituent zone. The concentration (or dilution) factor for each composite zone was computed from the ratio of composite vapor flux to composite liquid flux.

6.1.8 TH Model Validation

Validation requires review of model calibration parameters for reasonableness and consistency with all relevant data, the T-H model input parameters are grouped in the following categories:

- Hydrologic properties for natural and engineered materials
- Thermal properties for natural and engineered materials
- Thermal output of emplaced waste
- Temperature, total pressure, and infiltration flux boundary conditions
- Numerical gridding, convergence criteria, and other model settings

The hydrologic properties used for these models are taken directly from the Unsaturated Zone (UZ) Flow and Transport Model (CRWMS M&O 2000e). Thermal properties are based on laboratory-measured data (DTN: LB990861233129.001). It is noted that values for "wet" thermal conductivity are currently under review. Thermal output of the emplaced waste is based on best-available information for the characteristics of spent fuel and defense high-level waste (DTN: SN9908T0872799.004).

The temperature and pressure boundary conditions used for these models are based on averages for the ground surface and water table, constrained by measured data. Values for average infiltration flux are also taken directly from the UZ Model, for representative center and edge locations. Alternative infiltration flux boundary conditions are selected from both the "lower" and "upper" infiltration distributions developed for the UZ Model, to represent the range of uncertainty. These alternative values are used comparatively in several cases discussed in this section.

The above descriptions indicate that the model calibration parameters are reasonable since they are consistent with values in accepted model. From this discussion, and supporting information published elsewhere (CRWMS M&O 2000f) it is concluded that the TH models used for the TH Model are valid for their intended use. The level of confidence for the model is therefore relatively high. The models are based on appropriate inputs, including properties, boundary conditions, and thermal output. Gridding, convergence, and other model settings used for these models are consistent with past practice.

6.1.9 Alternative Models and Approaches

Changes in the TH models are possible to make representation of the waste package, drip shield, backfill, invert, and host rock more detailed and realistic. Possible changes include finer gridding, explicit simulation of the waste package and drip shield (instead of a single body with lumped properties), an air-filled space above the backfill, and spatial heterogeneity in the host rock. For this report, these potential enhancements would not be likely to produce more conservative bounds on TH responses (i.e., more potential for evaporative concentration, and accumulation of precipitates and salts, in the emplacement drifts).

6.1.10 Summary

The TH Model portion of the EBS P&CE Model has evaluated TH processes using four cases implemented with NUFT V3.0s. The TH environmental conditions needed for chemical modeling are evaluated for six zones representing the in-drift environment and the surrounding host rock. Zone-averaged conditions are calculated for five time intervals representing the postclosure period from 50 to 10,000 yr after waste emplacement. There are two primary categories of uncertainties for the TH model: those associated with the EBS and those associated with the natural system. Detail descriptions of the TH model uncertainties are provided in CRWMS M&O (2000f, Section 7.1)

Zone fluxes, evaporation, and analysis of the hypothetical migration of a conservative solute were used to choose one case as a reasonable-bound representation of TH conditions to carry forward in to a bounding analysis of the chemical environment. This case is the L4C4 location from the multiscale TH Model, with the "upper" infiltration distribution representing uncertainty on present-day hydrologic processes and future climate change.

The zone-averaged temperature, liquid masses, and gas- and liquid-phase influxes and outfluxes are specified for three composite zones representing the host rock, backfill, and the lower backfill and invert. Environmental conditions are prescribed for five time intervals spanning the postclosure period to 10,000 yr.

In general, it is shown that the model has an appropriate level of confidence suitable for its intended use. The observations and inferences developed from the TH calculations for this model are summarized as follows:

Temperature

- Cooldown occurs sooner for conditions representing the repository edge.
- Low-flux conditions produce greater peak temperatures and slower cooldown because less liquid water is available to evaporate and transfer latent heat.

Saturation

- The spatial extent of dryout (zero or low liquid saturation) is greater for low-flux conditions.
- Water returns to the EBS environment sooner for high-flux conditions and for repository-edge conditions.
- After cooldown the liquid water saturation in the upper part of the backfill is approximately 10 percent to 20 percent, depending on "lower" or "upper" infiltration conditions.

Air Mass-Fraction

- The minimum air mass-fraction in the drift occurs when the rate of evaporation in the drift is maximal.
- The minimum air mass-fraction is approximately 10^{-3} when thermal output and infiltration (seepage) are maximized for the reasonable-bound case.

Evaporation Rate

- Evaporation tends to be localized to a narrow zone above the dryout zone, which recedes toward the drip-shield surface as the heat-source strength decays with time.
- The rate of evaporation from all zones is much smaller than the total thermal output of the waste packages for the first few hundred years. At late-time, the proportion of thermal output that causes evaporation decreases for all cases.
- For the "upper" infiltration, there is more sustained evaporation than there is for the "lower" infiltration. The peak in evaporation rate occurs sooner for the repository-edge location than for the center.

Gas-Phase Mass Flux

- For the 2-D NUFT V3.0s models used in this report, the gas-phase mass flux is driven by evaporation of water vapor.
- The maximum upward mass flux during the thermal period occurs in the host rock directly above the drift centerline and does not necessarily occur at the drift wall, but may occur several meters within the host rock.
- There is a slight circulation whereby the mass flux is downward in the pillar and upward near the drift at the drift elevation. The magnitude of the downward flux is much smaller than the upward flux.

Potential for Salt Accumulation

- When zones have no liquid outflow, substantial accumulation of soluble salts may occur from evaporation (the zones need not be dry for this to occur).
- Solute mass on the order of 2×10^5 times the solute mass present in 1 kg of reference composition may accumulate in Zone 4 (drip-shield surface). For example, if chloride is present in the reference water at 7 mg/l (typical for J-13 water), the accumulated mass in the backfill could approach 1.5 kg per meter of drift.
- Because of the timing of salt accumulation, there is the potential for aqueous conditions, caused by osmolality, on the drip shield and waste package at temperatures greater than 96°C.

- For the repository-edge location, the potential accumulation of soluble salts is less than at the center because there is less heat available for evaporation.

- For the "lower" infiltration results, there is greater potential for solute accumulation in the invert.

6.2 GAS FLUX AND FUGACITY MODEL

This section develops an analytical model for fugacities of CO_2 and O_2 in the potential repository during the thermal period. The model provides lower-bound estimates of gas fugacities, using input from TH calculations (Section 3.1.2.1). It is calibrated by means of a unique application of ^{14}C abundance measurements from boreholes at Yucca Mountain. It describes an inverse relationship between fugacity and flux, which can be used to calculate the respective increase or decrease in fugacity that would be associated with a source or sink of CO_2 or O_2 in the EBS.

In the Chemical Reference Model (Section 3.1.2.7) the analytical model is used to constrain CO_2 and O_2 fugacities. The results are bounding for CO_2 in the sense that low CO_2 concentration contributes to higher pH, which can promote degradation of engineered materials such as steel or titanium. The approach allows comparison of the calculated rate of CO_2 consumption in the EBS, with the flux-fugacity relationship from the model, to evaluate whether in-drift processes are likely to strongly perturb the CO_2 fugacity in the host rock and EBS. A similar comparison is made for consumption of O_2 by corrosion of structural steel in the EBS.

The model development and discussion in this section includes the following elements:

- Identify the processes that control the flux and fugacity for CO_2 and O_2.

- Estimate the magnitude of gas-phase mass transfer, applicable to both CO_2 and O_2 gases, based on mass balance of $^{14}CO_2$ for ambient conditions. Develop a mass-transfer function that can represent gases other than CO_2, and modify the function to represent thermal effects.

- Develop reasonable lower-bound estimates for CO_2 and O_2 fugacities in the gas phase and the relationships between flux and fugacity for the thermal period extending to 10,000 years.

In addition to the analytical mass-transfer model, two alternative models are discussed: (a) the air mass-fraction approach and (b) reactive transport simulation. Each is shown to produce CO_2 fugacity values for the thermal period, which are comparable to results from the analytical mass-transfer model.

6.2.1 Conceptual Model

6.2.1.1 Background

Carbon dioxide can strongly affect pH for solutions present in the emplacement drifts during the thermal and post-thermal periods. The gas-phase CO_2 concentration can range over several orders of magnitude, and the associated solution compositions can range from sub-alkaline to

pH 11 or greater. Within this range, there are important differences in mineral solubility conditions and corrosion rates for engineered materials.

Carbon dioxide is present in the host rock under ambient conditions in three forms: CO_2 gas, dissolved carbonate species in fracture and matrix waters, and mineral carbonate solids. Gaseous and aqueous inorganic carbon in the unsaturated host rock are readily available for reactions of interest. Carbonate solids are common secondary minerals at Yucca Mountain and are common in fractures of the host rock. Calcite dissolution and precipitation can occur in response to repository heating and cooldown, but are not considered in this model (Assumption 5.2.4).

The following additional aspects of CO_2 transport and modeling are important to the Gas Flux and Fugacity Model:

- Ideal gas behavior is used to represent the behavior of all gases and mixtures of gases, including water vapor. This approach is common in physical chemistry applications because departures from ideal behavior are small.

- Quasi-steady conditions are used to represent repository thermal evolution, whereby the in-drift environment evolves in stages during which temperature and hydrologic conditions are steady. This approach simplifies the analyses and is justified because repository conditions will generally be slowly varying on a time scale of hundreds of years.

- Isotopic fractionation associated with dissolution or exsolution of $^{14}CO_2$ is a small effect, one that is twice the fractionation of $^{13}CO_2$, which is known to be approximately 1‰ (Fritz and Fontes, 1980, pp. 15 and 477). This corresponds to fractionation of approximately 2‰ for $^{14}CO_2$, which is a small fraction of the range of radiocarbon abundance in the host rock (typically 30 to 100 pmc). Accordingly, isotopic fractionation of $^{14}CO_2$ that is associated with dissolution, exsolution, and precipitation reactions is neglected in this discussion.

- Because diffusive-dispersive behavior for $^{12}CO_2$ and $^{14}CO_2$ is effectively the same, mass-transfer relations developed for $^{14}CO_2$ can be used to infer the availability of total CO_2 (which is made up of mostly $^{12}CO_2$). This is justified because the mass difference is small (46 vs. 44 g/mol), and the isotopes behave independently as minor constituents of the gas phase.

- The average ambient ^{14}C signature for CO_2 in recharge water or gas ($^{14}a_{in}$) is 100 pmc (modern, but not nuclear-age). This is based on the long half-life of ^{14}C relative to the nuclear age, such that the majority of ^{14}C in the UZ was naturally produced prior to the nuclear age.

In the Topopah Spring welded tuff and above, rapid recharge in fractures (that which exceeds the in situ matrix hydraulic conductivity) penetrates the host rock, with limited isotopic interaction between recharge and matrix porewater. This concept is supported by inspection of measured ^{14}C activity vs. depth for borehole SD-12 (Figure 16). The increase of ^{14}C activity near the bottom of the Topopah Spring welded tuff is associated with a transition from mostly fracture flow to mostly matrix flow in the underlying Calico Hills unit.

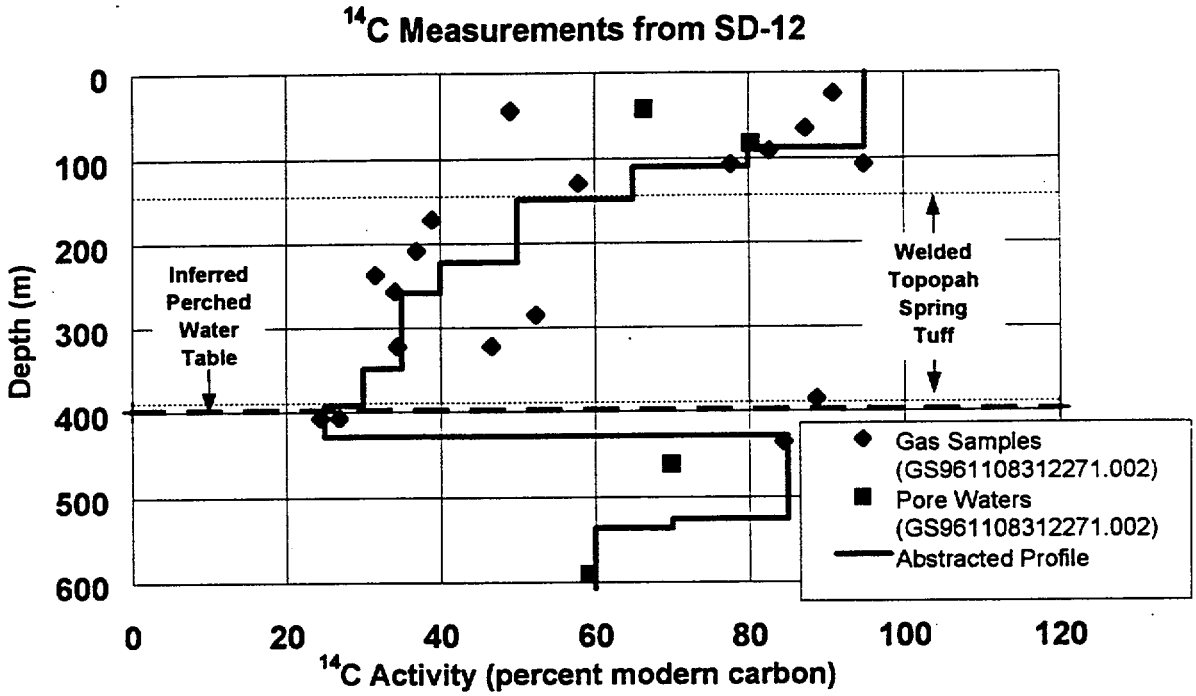

Source: file "gasC14-SD-12-1996dataV1.2.xls " (Attachment I)
Note: Abstracted Profile provided in Section 6.2.3 as User Defined Profile

Figure 16. Observed Distribution of ^{14}C Activity with Depth in Borehole SD-12

The model described subsequently separates the CO_2 flux transported in rapid vs. slow recharge and neglects any contribution from rapid recharge to the $^{14}CO_2$ inventory in the host rock. This approach is used to develop lower bounds on gas-phase transport because it minimizes the rapid recharge flux needed to replace ^{14}C decay deep in the UZ, thereby minimizing the need for gas-phase transport to penetrate there, thus minimizing the efficacy of the gas-phase transport mechanism predicted by the model.

6.2.1.2 CO_2 Transport Processes Under Ambient Conditions

The following discussion is based on observations of $^{14}CO_2$ for ambient (prerepository) conditions extended to CO_2 transport during the thermal period. Gas-phase CO_2 transport is produced by three transport processes:

- **Molecular diffusion**–Fickian diffusion along a concentration gradient
- **Advective-dispersive transport**–The gas column in the UZ undergoes volume reduction and expansion in response to episodic changes in barometric pressure at the ground surface. Gas molecules move back and forth essentially in 1-D and disperse in a manner similar to diffusion. Molecular diffusion and advective dispersion are mathematically analogous (Freeze and Cherry 1979, Equation 9.4) and are combined in one mass-transfer coefficient (D) developed for this model.

- **Convective circulation**–Ambient, multidimensional gas-phase convection is driven by long-term (e.g., seasonal) changes in gas density at the ground surface and is associated with variable topography. Convective circulation has been shown to readily displace air in the Tiva Canyon caprock, but the effect apparently does not extend into the Topopah Spring host rock (Thorstenson 1993). Ambient convective circulation is neglected in this bounding model.

CO_2 movement in the liquid phase can be produced by two transport processes:

- **Molecular diffusion**–Aqueous diffusion is approximately four orders of magnitude slower in liquids than in gases, and diffusive mobility is restricted because of path tortuosity. For this model, diffusive transport of solute in matrix porewater is limited conceptually to exchange with nearby fractures.

- **Advective transport**—Percolation can occur in the fractures and in the rock matrix. Where the percolation flux substantially exceeds the in situ, unsaturated matrix hydraulic conductivity, percolation flux is mostly through the fractures. Because flow velocity is small in the matrix, tens of thousands of years could be needed for penetration of porewater to repository depth. This is not consistent with borehole ^{14}C measurements that indicate rapid transport. To explain the ^{14}C variation with depth, aqueous and gas-phase transport must occur mostly in fractures.

In summary, the important processes for ambient transport of CO_2 to the host rock are gas-phase diffusion-dispersion and liquid-phase advective transport.

The ^{14}C activity for gas-phase and matrix porewater samples from the same or nearby locations are isotopically similar (comparing Table 12 and Table 13 for the host-rock units, and allowing for data scatter due to sampling uncertainty and spatial heterogeneity).

The gas-phase CO_2 inventory in the host rock is approximately an order of magnitude smaller than the aqueous-phase inventory dissolved in the matrix porewater; hence, the relatively immobile aqueous-phase inventory dominates the bulk, local isotopic signature. The average isotopic composition that is observed in boreholes represents long-term composition of matrix porewater, and the similarity of porewater and pore gas measurements indicates isotopic equilibrium with the gas phase.

6.2.1.3 CO_2 Transport Processes During the Thermal Period

Warming and evaporation of porewater causes exsolution of dissolved CO_2 and changes the partitioning of CO_2 between the gaseous and aqueous phases. Further evaporation can cause precipitation of carbonate solids. Changes in chemical conditions (e.g., pH increase associated with evaporative concentration) also affect the partitioning of CO_2 between the gas and liquid phases. These effects are limited to a region of the host rock around the drift and are greatly decreased outside the region of evaporation and condensation (Assumption 5.2.4).

Gas-phase fugacity is decreased proportionally to the air mass-fraction because of displacement of air by water vapor.

Convective circulation in the gas phase can occur because of buoyancy caused by density changes from thermal expansion and increased humidity. Through the combined effects of flow-field geometry, flow resistance from lower-permeability units above and below the host rock, and displacement of air by water vapor, convective activity will be maximal at the repository edges and minimal near the repository center. This type of large-scale convective circulation is neglected as a CO_2 transport process for this bounding model, which is consistent with its use for bounding approximations to gas flux and fugacity.

6.2.1.4 Ambient CO_2 Concentration in the Unsaturated Zone

The ambient concentration of the CO_2 in the gas phase of the UZ ($C_{CO2,amb}$) is 1000 ppm. This is a rough-average value consistent with surface-based borehole data (Table 12). Gas samples from the Exploratory Studies Facility (ESF), or from boreholes drilled from the ESF, are not included in Table 12 because of the potential for contamination by ventilation air.

6.2.2 Background—Oxygen

Oxygen gas is more abundant in air than is CO_2, but it is less soluble in water. Accordingly, the gas phase is the most important reservoir and transport pathway for O_2. Both gases exhibit decreased (retrograde) solubility with increasing temperature. For O_2, this is less potentially significant to performance.

Oxygen will react with metals such as steel in the repository environment. Tuff mineralogy is mostly oxidized, (e.g., the Fe content is represented by hematite and other oxides), and minerals containing reduced species tend to be armored by oxides and are not accessible. Thus, oxidation of the tuff is slow, and the oxygen concentration in the gas phase in the rock is close to atmospheric composition.

6.2.2.1 Ambient Gas-Phase O_2 Concentration in the Unsaturated Zone

Measured values for O_2 concentration in the UZ gas phase are in the range of 20 percent to 22 percent and are generally indistinguishable from atmospheric values (Drift-Scale Test gas samples, DTN LL980810004244.067).

6.2.3 Equilibrium Steady-State CO_2 Transport in the Unsaturated Zone

The CO_2 flux delivered to the host rock by natural (prerepository) processes is estimated using a steady-state radiocarbon mass balance from the ^{14}C activity of the carbon found there:

$$\frac{d^{14}M_{mat}}{dt} = 0 = \frac{{}^{14}C_{aq,in} q_{aq} \left({}^{14}a_{in} - {}^{14}a_{out}\right)}{{}^{14}a_{in}} + m_{gas,in} - l_{14}\,{}^{14}M_{mat}$$

(Eq. 18)

where

$^{14}M_{mat}$ = mass of $^{14}CO_2$ in the UZ, per square meter area, principally in the matrix porewater (kg/m^2)
$^{14}C_{aq,in}$ = concentration of $^{14}CO_2$ in recharge water (kg/m^3)
q_{aq} = flux of recharge water (m/sec)
$^{14}m_{gas,in}$ = mass flux of $^{14}CO_2$ transported in the gas phase (kg/m^2-sec^{-1})
λ_{14} = ^{14}C decay constant (3.84×10^{-12} sec^{-1})
$^{14}a_{in}$ = ^{14}C activity for recharge water (pmc)
$^{14}a_{out}$ = ^{14}C activity for effluent water (e.g., to the saturated zone) (pmc)

The mass variable $^{14}M_{mat}$ is summed over hydrostratigraphic intervals at the location considered

$$^{14}M_{mat} = \sum_{\substack{i=\text{hydro.}\\ \text{units}}} T_i \phi_{mat,i} S_{mat,i} C_{aq,in} \, ^{14}a_i$$

(Eq. 19)

where

T_i = thickness of ith unit
$\phi_{mat,i}$ = matrix porosity
$S_{mat,i}$ = matrix saturation
$C_{aq,i}$ = aqueous (porewater) CO_2 concentration
$^{14}a_i$ = porewater ^{14}C activity

Volumetric water content ($T_i\phi_{mat,i}S_{mat,i}$) is estimated for each interval. Porewater CO_2 concentration is estimated based on chemical analyses of porewater samples extracted from samples of drill core. The porewater ^{14}C activity is based on isotopic measurement of gas samples obtained from surface-based boreholes and of porewaters extracted from core samples.

For aqueous advection, the total CO_2 concentration is proportional to the $^{14}CO_2$ concentration

$$C_{aq,i} = \frac{^{14}C_{aq,i}}{^{14}a_i \gamma_{14}}$$

(Eq. 20)

where γ_{14} = ^{14}C:^{12}C abundance ratio at 100 pmc ($\gamma_{14} = 1.21\text{x}10^{-12}$; Fritz and Fontes 1980, pp. 51–53).

The steady-state aqueous CO_2 flux through a stratigraphic interval is determined from the decay rate of $^{14}CO_2$ in that interval:

$$^{14}M_{mat}\lambda_{14} = \frac{C_{aq,i}q_{aq}\gamma_{14}\left(^{14}a_{in} - ^{14}a_{out}\right)}{^{14}a_{in}}$$

(Eq. 21)

where q_{aq} = steady-state flux through the interval, and a_{in}, a_{out}= ^{14}C activities for influent and effluent water, respectively.

Equations 18 through 21 can be applied to the entire UZ or to any intervals of the UZ, such as above vs. below a hydrologic confining unit that acts as a barrier to gas flux but not to aqueous flux. Below such a confining unit, aqueous flux is the predominant source and mechanism for transport and storage, as dissolved inorganic carbon, of $^{14}CO_2$. Such confinement is inferred in borehole SD-12 immediately below a depth of 397 m (Figure 16) from barometric efficiency observations (Bodvarsson et al. 1997, p. 13-9).

The following discussion analyzes the $^{14}CO_2$ data from this borehole. Mass-balance calculations based on Equations 18 through 21 are implemented in the spreadsheet (file: "gasC14-SD-12-1996data.xls"). Input data for analysis of ^{14}C data from borehole SD-12 were identified previously, and sources of information are annotated in the associated spreadsheet routine (file: "gasC14-SD-12-1996data.xls").

Mass balance is performed for discrete, user-defined depth intervals, each of which represents one or more hydrostratigraphic units discretely (file: "gasC14-SD-12-1996data.xls"; worksheet: SD-12 stratigraphy). The ^{14}C activity of the gas phase and matrix porewater, and the porewater CO_2 concentration, are also represented as user-defined depth profiles for purposes of analysis (Figures 16 and 17, respectively). These are simplified representations of the plotted data (file: "gasC14-SD-12-1996data.xls"; worksheet: gas and porewater C-14).

The $^{14}CO_2$ flux to replace ^{14}C loss to radioactive decay and to maintain steady conditions is calculated using the porewater concentration and ^{14}C activity information (Figure 18; calculated in spreadsheet "gasC14-SD-12-1996dataV1.2.xls"; worksheet: gas and porewater C-14). The $^{14}CO_2$ flux is expressed in terms of the total mass flux of CO_2, given a ^{14}C activity of 100 pmc for the near-surface source.

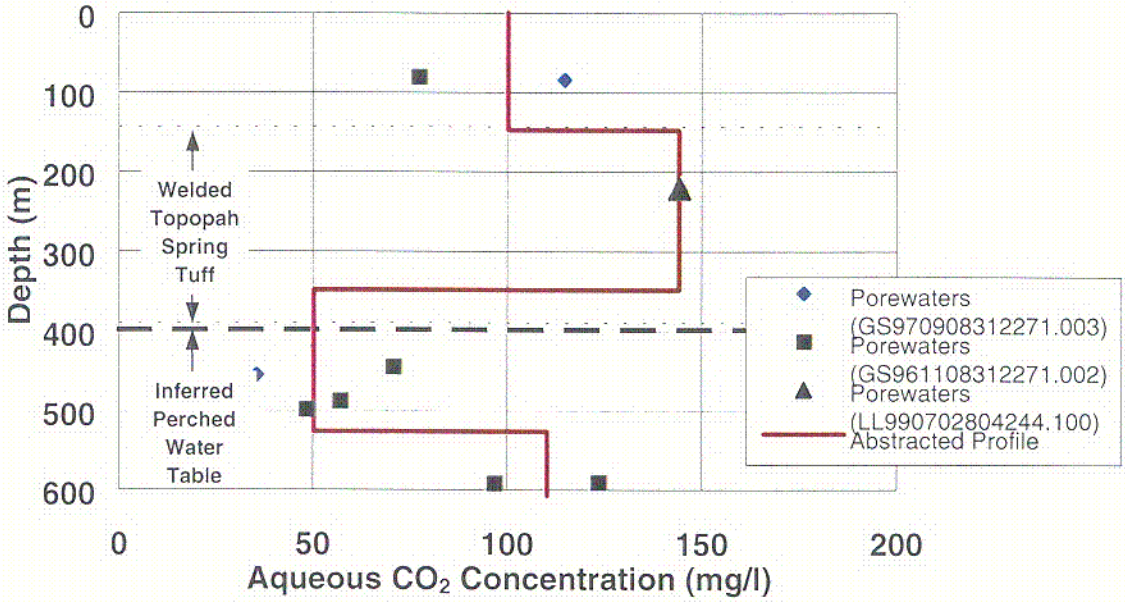

Source: file "gasC14-SD-12-1996dataV1.2.xls " (Attachment I)

NOTE: From borehole SD-12 and in core samples from the Drift-Scale Test heated drift

Figure 17. Observed Distribution of Porewater CO_2 Concentration in Core Samples

The ^{14}C mass balance for the entire UZ (Figure 18) shows that approximately 586 mg/m^2-yr of modern carbon (100 pmc) are required to replace ^{14}C decay and maintain the inventory of $^{14}CO_2$ at steady state (file: "gasC14-SD-12-1996dataV1.2.xls"; worksheet: gas and porewater C-14). This is the total flux of aqueous CO_2 that would be required, without considering the through-flux of $^{14}CO_2$ by recharge flow to the saturated zone (SZ).

For the interval below 397 m depth in borehole SD-12, the flux of modern CO_2 required to replace ^{14}C decay is approximately 287 mg/m^2-yr (file: "gasC14-SD-12-1996dataV1.2.xls"; worksheet: gas and porewater C-14). This flux is predominantly aqueous (i.e., dissolved in percolating waters and not gaseous) because of confining conditions present in the rock below this depth. In addition, the modern CO_2 flux must be increased to approximately 478 mg/m^2-yr so that the ^{14}C activity for effluent to the SZ is realistic (a value of 40 pmc corresponds to a an apparent groundwater age of approximately 7,000 yr, and is assigned, in the spreadsheet, to the ^{14}C activity of discharge to the SZ).

For the interval above 392 m depth in borehole SD-12, the flux of aqueous CO_2 required to replace ^{14}C decay is approximately 299 mg CO_2/m^2-yr (file: "gasC14-SD-12-1996dataV1.2.xls"; worksheet: gas and porewater C-14). Because the total recharge water flux is not enough to transfer this much aqueous CO_2 except under extreme infiltration conditions, gas-phase transfer is evident. The required gaseous flux of $^{14}CO_2$ is calculated using Equation 18, to be 6.9×10^{-10} mg $^{14}CO_2$/m^2-yr. Because this estimate does not include mixing with younger carbon, effluent from this interval has a realistic ^{14}C activity when it reaches the SZ.

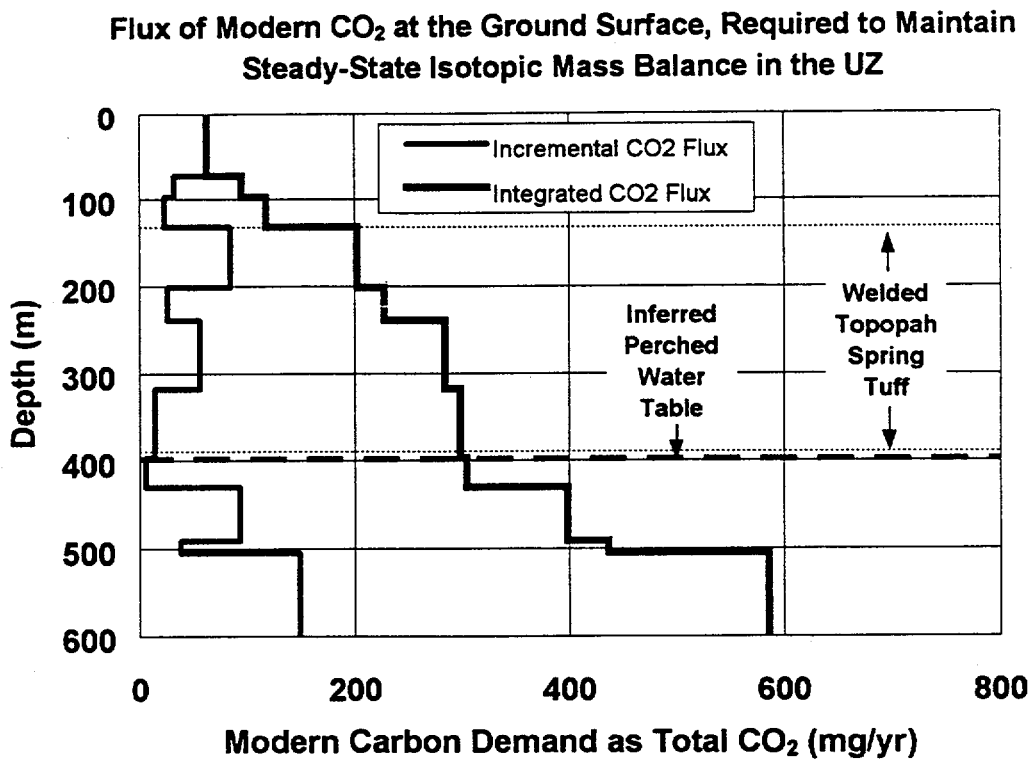

Source: file "gasC14-SD-12-1996dataV1.2.xls " (Attachment I)
NOTE: From borehole SD-12 and in core samples from the Drift-Scale Test heated drift
Expressed as the flux of aqueous total CO_2 containing modern carbon

Figure 18. Calculated Flux of $^{14}CO_2$ Required to Maintain Steady-State Isotopic Conditions in the Unsaturated Zone

6.2.3.1 Gas Transport for Ambient Conditions

Murphy (1995) derived an analytical expression for ambient CO_2 fugacity and fluxes that is based on the idea that transport occurs in the aqueous phase and the gas phase. The 1-D, steady-state diffusion model assumed that the UZ has uniform properties and that the surface boundary composition is constant. Diffusive behavior was assumed to include both molecular diffusion and advective-dispersive effects. The following discussion modifies this analytical model by addition of an advective term; it then evaluates gas-phase CO_2 transport in borehole SD-12. The

resulting mass transfer relation is used to represent transport of gases into the repository (Assumption 5.2.1 and Assumption 5.2.2).

In the discussion that follows, diffusive and analogous dispersive processes are assigned to the gas phase, while advection occurs in the liquid phase in response to percolation. A mass-balance equation taking into account transport and decay of ^{14}C is

$$\frac{\partial {}^{14}C_{bulk}}{\partial t} = \phi_{gas} D_{gas} \frac{\partial^2 {}^{14}C_{gas}}{\partial z^2} - u \frac{\partial {}^{14}C_{aq}}{\partial z} - \lambda_{14} {}^{14}C = 0$$
$${}^{14}C_{bulk} = \phi_{gas} {}^{14}C_{gas} + \phi_{aq} {}^{14}C_{aq}$$
$${}^{14}C_{aq} = K_d {}^{14}C_{gas}$$

(Eq. 22)

where

$^{14}C_{bulk}$	=	bulk concentration of $^{14}CO_2$ in the UZ (kg/m^3)
$^{14}C_{gas}$	=	$^{14}CO_2$ concentration in the gas phase (kg/m^3)
$^{14}C_{aq}$	=	$^{14}CO_2$ concentration in the aqueous phase (kg/m^3)
D_{gas}	=	diffusion-dispersion coefficient for gas-phase $^{14}CO_2$ transport (m^2/sec)
ϕ_{aq}	=	volume fraction liquid, predominantly in matrix porewater
ϕ_{gas}	=	volume fraction gas in which diffusive-dispersive transport occurs, predominantly fracture porosity
u	=	liquid flux that is isotopic equilibrium with gas (m/sec)
K_d	=	dimensionless distribution coefficient for CO_2 partitioning between gaseous and aqueous phases

Making the necessary substitutions, Equation 22 is linear with constant coefficients and has the characteristic equation

$$(r - r_1)(r - r_2) = 0$$

(Eq. 23)

and the roots that correspond to independent solutions of Equation 22 are

$$r_i = \frac{uK_d \pm \sqrt{u^2 K_d + 4\lambda_{14}\phi_{gas} D_{gas}\left(\phi_{gas} + \phi_{liquid} K_d\right)}}{2\phi_{gas} D_{gas}}$$

(Eq. 24)

Root r_1 is always positive, thus the exponential term proportional to $\exp(r_1 z)$ must be eliminated from the homogeneous solution to ensure that ${}^{14}C_{gas}(z)$ is finite. Root r_2 is always negative. Applying the boundary condition ${}^{14}C_{gas}(z \to 0) = \gamma_{14} a_{in} C_{gas,in}$ yields

$$
{}^{14}C_{gas} = g_{14} a_{in} C_{gas,in} \exp\left\{ z \left[\frac{uK_d - \sqrt{u^2 K_d + 4\lambda_{14}\phi_{gas} D_{gas}\left(\phi_{gas} + \phi_{liquid} K_d\right)}}{2\phi_{gas} D_{gas}} \right] \right\}
$$

$$
{}^{14}a = {}^{14}a_{in} \exp\left\{ z \left[\frac{uK_d - \sqrt{u^2 K_d + 4\lambda_{14}\phi_{gas} D_{gas}\left(\phi_{gas} + \phi_{liquid} K_d\right)}}{2\phi_{gas} D_{gas}} \right] \right\}
$$

(Eq. 25)

where $C_{gas,in}$ is the concentration of total carbon (all isotopes) representing the influent or recharge composition. Equation 25 is fit to measured data for ${}^{14}C$ activity vs. depth in borehole SD-12 (Figure 19; file: "gasC14-SD-12-1996data.xls"; worksheet: gas and porewater C-14). The spreadsheet routine contains several data manipulations which are necessary to implement Equation 25:

- CO_2 partitioning between the gas phase and matrix porewater is estimated using the 1000 ppmv CO_2 concentration for the gas phase (Section 4.1.2.1) and 94 mg/L CO_2 concentration for J-13 well water (Assumption 5.2.3). Converting concentrations to common units (kg/m^3) and taking the dimensionless ratio of aqueous to gaseous concentrations yields

$$
K_d = \frac{94\,\mathrm{mg\,L^{-1}}\,10^{-6}\,\mathrm{kg\cdot mg^{-1}}\,10^{3}\,\mathrm{L\,m^{-3}}}{1000\,\mathrm{ppmv}\,10^{-6}\,\mathrm{m^3\,m^{-3}}\,(P/RT)\,\mathrm{mol\,m^{-3}}\,0.044\,\mathrm{kg\,mol^{-1}}} = 53.1
$$

(Eq. 26)

where

P = total pressure (nominally 1 atm = 1.013×10^5 Pa)
R = gas constant (8.307 Pa m^3/K)
T = average UZ temperature (303 K) (Assumption 5.2.6)

- **Gas volume fraction (ϕ_{gas})**–The gas volume fraction in which diffusion occurs is dominated by the fracture porosity, which is estimated using hydrostratigraphic properties (file: "gasC14-SD-12-1996data.xls"; worksheet: SD-12 stratigraphy). Fracture porosity for each hydrostratigraphic unit is obtained from the 1-D drift-scale base-case property set (DTN LB990861233129.001, as implemented in the NUFT input file "dkm_afc-ds-NBS-m_inf"). Because it is small, fracture water saturation is neglected in computing the volume fraction for fracture gas.

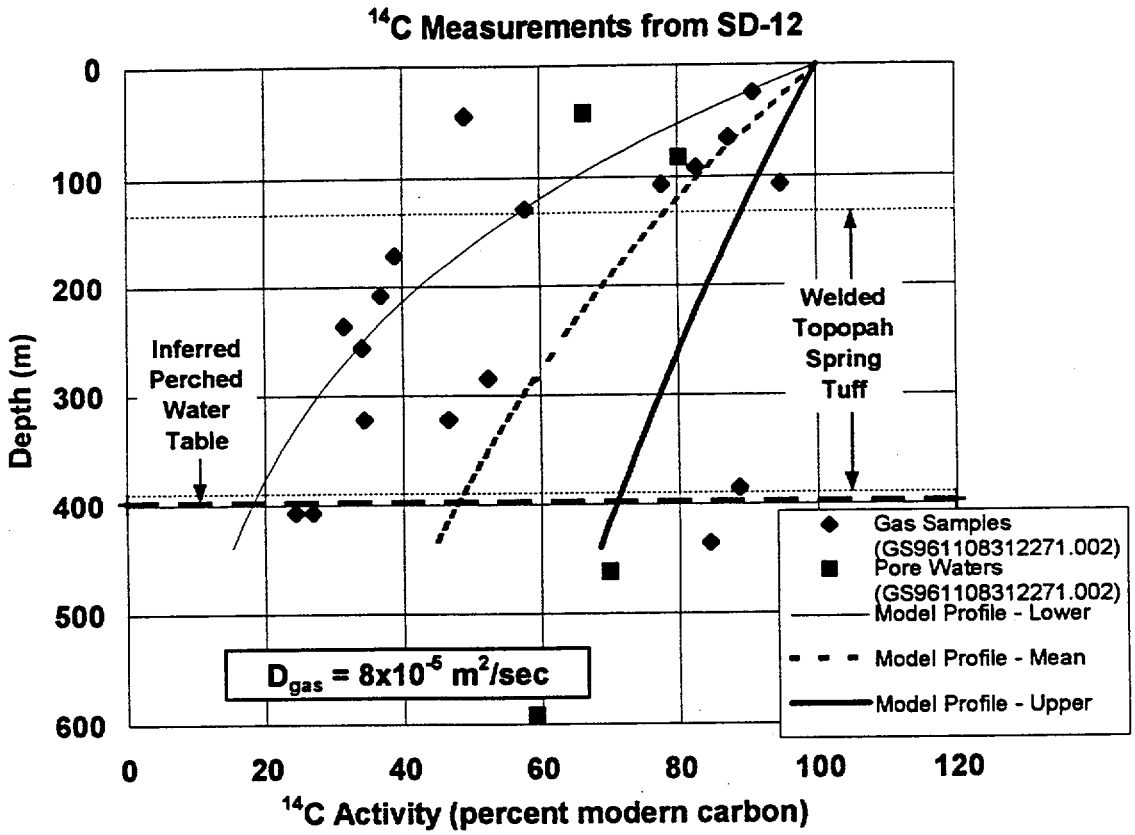

Source: file "gasC14-SD-12-1996dataV1.2.xls " (Attachment I)

Figure 19. Exponential Model Fit to ^{14}C Activity vs. Depth in Borehole SD-12

- **Liquid volume fraction (ϕ_{aq})**—The aqueous liquid volume is calculated using hydrostratigraphic properties and saturation (file: "gasC14-SD-12-1996data.xls"; worksheet: SD-12 stratigraphy). Matrix porosity for each hydrostratigraphic unit is obtained from the 1-D drift-scale base-case property set (DTN LB990861233129.001, as implemented in the NUFT input file "dkm_afc-ds-NBS-m_inf"). Matrix saturation is visually interpreted for borehole SD-12 from plotted laboratory data (Bodvarsson et al. 1997, Figure 6.4.10) and multiplied by matrix porosity to estimate volumetric water content in abstracted depth intervals.

- **Diffusion-dispersion coefficient (D_{gas})**—The diffusion-dispersion coefficient in Equation 25 is calculated from the molecular diffusion coefficient for CO_2 in air (Incropera and DeWitt 1996, Table A.8, p. 849). This calculation is implemented in the accompanying spreadsheet (file: "gasC14-SD-12-1996data.xls"; worksheet: gas and porewater C-14) as

$$D_{gas} = D_{CO2}\tau$$

(Eq. 27)

where

D_{CO2} = Diffusion coefficient for gas in air (1.60×10^{-5} m^2/sec for CO_2 and 2.1×10^{-5} m^2/sec for O_2; at 298 K (Incropera and DeWitt 1996, Table A.8, page 849)

τ = Tortuosity-dispersion multiplier ($\tau = 5$ for SD-12)

The use of diffusion coefficients for gases in dry air is consevative, for gas mixtures that will contain water vapor. Diffusion coefficients for CO_2 and O_2 in H_2O vapor (Cussler, 1997; Table 5.1-1) are greater than in air, therefore the values used in this model are conservative (i.e. smaller values, such that smaller gas flux and fugacity values result).

In Equation 27, the effect of gas-phase advective-dispersion is represented by a multiplier (τ) rather than by an additive term. This is justified because in the conceptual model, molecular diffusion works with oscillatory advection to enhance dispersion.

6.2.3.2 Ambient $^{14}CO_2$ Transport in Borehole SD-12

Values of $D_{gas} = 0.00008$ m^2/sec ($\tau = 5$) are used in Equation 25 to obtain the model plots shown in Figure 19, for borehole SD-12. The measured data are mostly bracketed by the curves for lower, mean, and upper average infiltration. This value (D_{gas}) represents the effects of dispersive processes as well as molecular diffusion. As discussed previously, gas-phase transport is required because the ambient percolation flux is insufficient to account for ^{14}C in the UZ by advection of water with composition equivalent to J-13 well water. In other words, if the value of D_{gas} is set to a small value or zero, the calculated ^{14}C activity throughout the UZ is too low.

6.2.3.3 Comparison with Data from Other Boreholes

Equation 25 is also fit to ^{14}C activity data from boreholes UZ-6/6S, UZ-1, NRG-5, and SD-7 in Figure 20, Figure 21, Figure 22, and Figure 23, respectively. The same input data are used, including the average volume fraction air in fractures and the volume fraction liquid (Assumption 5.2.6). For each figure, the value for D_{gas} is adjusted to improve agreement with the plotted ^{14}C activity data, and the selected value of D_{gas} is shown. For these other boreholes, the apparent diffusive-dispersive behavior is stronger than it is for SD-12. A value of $\tau = 13$ ($D_{gas} = 0.00021$ m^2/sec) is selected for developing lower-bound estimates of repository gas concentrations and fluxes.

Agreement between measured ^{14}C data from the UZ, and the exponential solution (Equation 25) is better at depth (e.g., in the welded host rock units) than closer to the surface. This is probably because the shallower data correspond to the fractured Tiva Canyon caprock at Yucca Mountain, and are more strongly affected by barometric pumping and other mechanisms of mass exchange with the atmosphere.

6.2.3.4 Gas Transport During the Thermal Period

Gas-phase flux of CO_2 or O_2 is estimated by combining diffusion and advection terms, which correspond to the first two terms on the right-hand side of Equation 22 (Assumption 5.2.1 and Assumption 5.2.2). The approach calculates gas-phase mass flux in response to a sink at the repository horizon, such as would be caused by chemical reactivity, analogous to the effect of radioactive decay in Equation 25. In other words, steady-state consumption by chemical reaction, is analogous to steady-state consumption by radioactive decay within a particular interval. Mass flux is calculated for constant concentration conditions at the ground surface and at the repository level as

$$m_{gas} = -\phi_{gas} D_{gas} \frac{\partial C_{gas}}{\partial z} - v \phi_{gas} C_{gas}$$

(Eq. 28)

where

m_{gas} = flux of gas-phase reactant ($kg/m^2 \cdot sec$)
D_{gas} = gas diffusion coefficient (m^2/sec, different for O_2 and CO_2)
v = velocity of gas phase (positive upward, m/sec)

and the other notation is similar to that of Equation 22. The gradient $\partial C_{gas}/\partial z$ is calculated from the difference between the gas concentration at the surface and that in the repository. Use of a single value of D_{gas} in Equation 28 instead of multiple values corresponding to the layered stratigraphy, is analogous to the effective 1-D hydraulic conductivity for a stack of layers with different conductivity values (Freeze and Cherry 1979, Equation 2-31, p. 34). A single, effective mass-transfer coefficient ($\phi_{gas} D_{gas}$) exists for which mass transfer is proportional to the overall average concentration gradient.

Temperature dependence of the binary gas-diffusion coefficients for CO_2 and O_2 is found from the relation $D_{gas} \propto T^{1.5}$ at constant pressure (Incropera and DeWitt 1996, Table A.8, p. 849). The concentrations of CO_2 and O_2 are important to performance because they affect aqueous reactions, particularly those in which evaporation occurs. Evaporation is maximized for temperatures near boiling; thus the temperature dependence of the gas-diffusion coefficients is calculated at 373°K. Taking $(373/298)^{1.5} = 1.4$ shows that diffusion coefficients increase with temperature. The effect will vary with the distribution of temperature in the host rock and is bounded in this model by using the values at 25°C (298°K). Coefficients of binary diffusion for CO_2 and O_2 gases in water vapor are assumed to be no less than the coefficients in air (Assumption 5.2.5).

Calculations show that gas-phase velocity (v) above the drifts tends to be negative during the thermal period because water vapor is convected upward (Section 6.1). Two-dimensional drift-scale TH simulations described in that section show that the gas-phase actually could

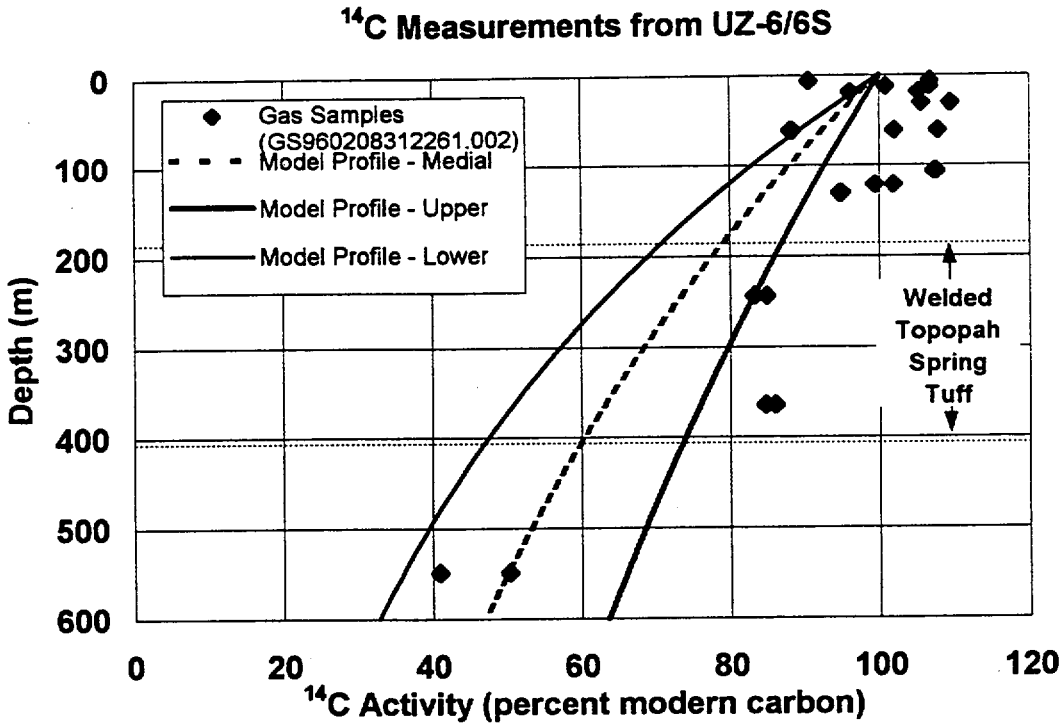

Source: file "gasC14-SD-12-1996dataV1.2.xls " (Attachment I)

Figure 20. Exponential Model Fit to ^{14}C Activity vs. Depth in Borehole UZ-6/6S

circulate in the host rock around the drift openings, which would tend to increase mixing and increase the availability of CO_2 and O_2 gases in the drifts.

Gas velocity varies with depth and location in the host rock; however, for lower-bound estimates of gas flux (m_{gas}), the maximum upward gas velocity in the host rock directly above the drift is used. This velocity is calculated as

$$v = \frac{q_{gas}}{\phi_{gas}\,\rho_{gas}}$$

(Eq. 29)

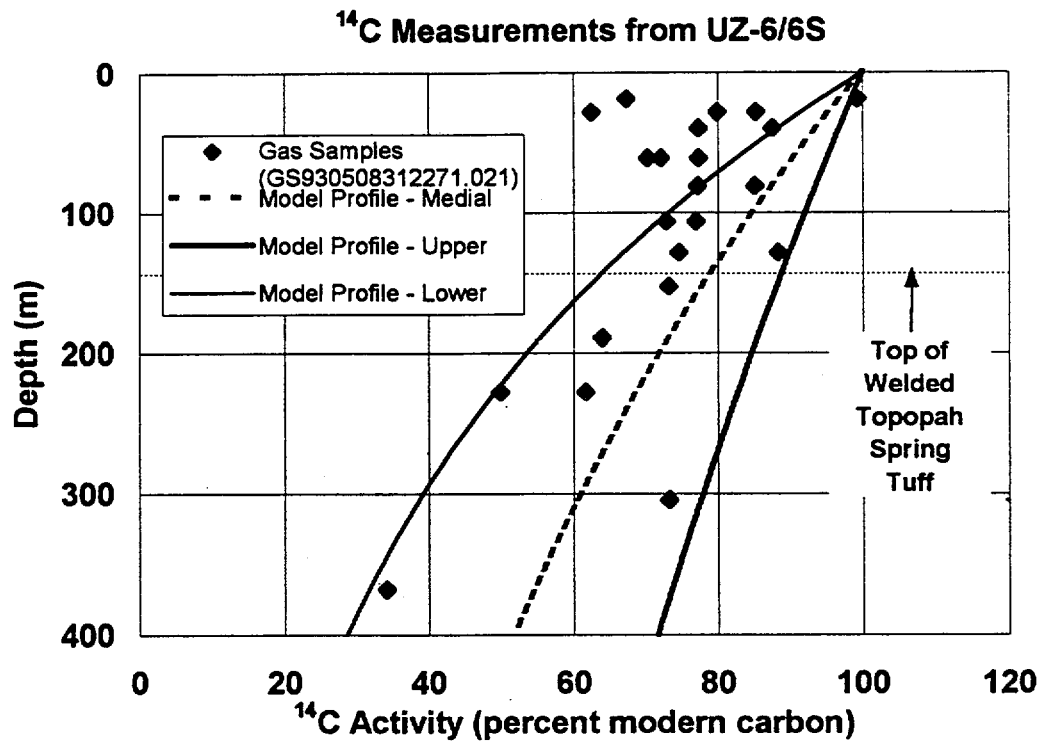

Source: file "gasC14-UZ-1-1985dataV1.2.xls " (Attachment I)

Figure 21. Exponential Model Fit to ^{14}C Activity vs. Depth in Borehole UZ-1

where q_{gas} is the fracture gas-phase total mass flux in the vertical direction (output from NUFT, positive upward) and ρ_{gas} is the gas density. The density depends on temperature and composition (output from NUFT) as

$$\rho_{gas} = \gamma_{air}\rho_{air} + (1-\gamma_{air})\rho_{H2O}$$

$$\gamma_{air} = \frac{\chi_{air} MW_{H2O}}{(1-\chi_{air})MW_{air} + \chi_{air} MW_{H2O}}$$

$$\rho_{air} = \frac{P\ MW_{air}}{RT}$$

$$\rho_{H2O} = \frac{P\ MW_{H2O}}{RT}$$

(Eq. 30)

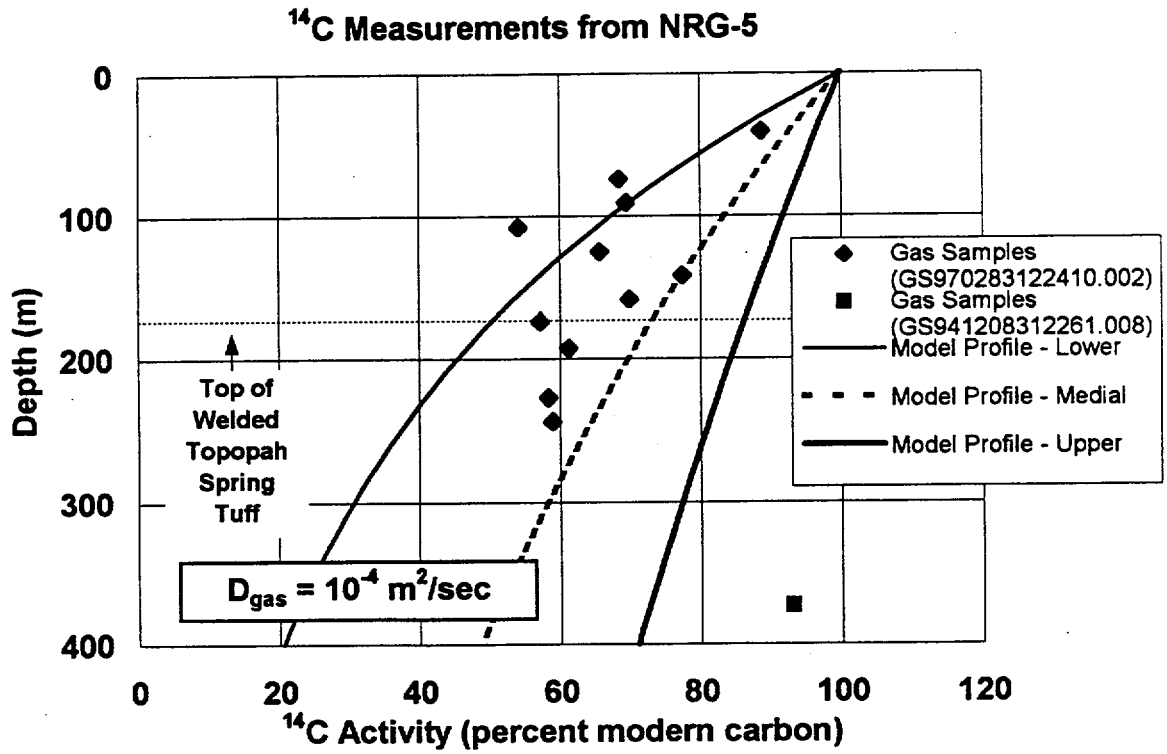

Source: file "gasC14-NRG-5-1996dataV1.2.xls " (Attachment I)

Figure 22. Exponential Model Fit to ^{14}C Activity vs. Depth in Borehole NRG-5

where

ρ_{air}, ρ_{H2O} = densities of dry air and water vapor (kg/m^3)
γ_{air}, γ_{H2O} = volume fractions for air and water vapor
χ_{air} = air mass-fraction
MW_{air} = equivalent molecular weight of air (kg/mol)
MW_{H2O} = molecular weight of water (kg/mol)

Concentration C_{gas} is independent from the air mass-fraction (i.e., absolute concentration is used to compute the gradient in Equation 28).

Equations 28 through 30 are combined to yield an expression directly relating the gas flux and concentration, using $(C_{gas,in} - C_{gas})/z$ to represent $\partial C_{gas}/\partial z$ as

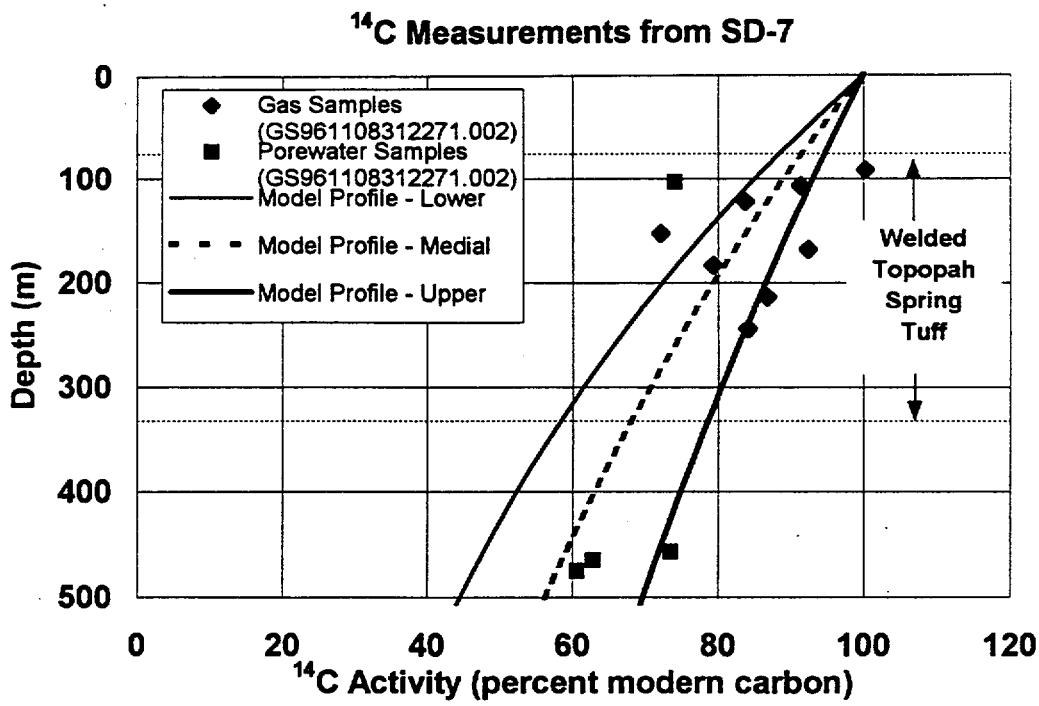

Source: file "gasC14-SD-7-1996dataV1.2.xls " (Attachment I)

Figure 23. Exponential Model Fit to ^{14}C Activity vs. Depth in Borehole SD-7

$$m_{gas} = \frac{\phi_{gas} D_{gas} C_{gas,in}}{z} - C_{gas}\left(\frac{q_{gas}}{\rho_{gas}} + \frac{\phi_{gas} D_{gas}}{z}\right) = aC_{gas,in} + bC_{gas}$$

(Eq. 31)

For a given concentration (C_{gas}) Equation 31 gives the associated mass flux (m_{gas}). Where this value is calculated to be less than zero, an upward mass flux would be indicated. For conditions of zero consumption and zero loss from gas-phase advection ($m_{gas} = q_{gas} = 0$), the concentration at depth equals that at the surface ($C_{gas} = C_{gas,in}$).

Equations 28 through 31 are implemented for the L4C4 location with the upper infiltration flux. The L4C4 location is near the geographic center of the potential repository where large-scale bouyant convection in the gas phase is likely to be minimal as discussed in Section 6.2.1.3, and gas-phase composition in the drifts is more likely to be determined by local processes. The upper-range infiltration maximizes the flux of water into the drift and the ensuing evaporation

and decrease of the air mass-fraction. The selection L4C4 with upper infiltration is discussed in Section 6.1.

NUFT output for the L4C4 location with 60 MTU/acre mass loading and upper infiltration is summarized in ".ext" files for fractures (file: "L4C4-LDTH60-li.m.f.ext") and for the matrix (file: "L4C4-LDTH60-li.m.ext").

The gas-phase mass flux (q_{gas}) in Equation 29 is taken directly from NUFT ".ext" output postprocessed using the VFLUXPROF V1.1 software routine; ρ_{gas} is calculated from the air mass-fraction (χ_{air}) and temperature (T) postprocessed using the ZONEAVG V1.2 software routine. These routines are discussed in Section 3.1.2. For bounding calculations, the maximum values for the gas-phase mass flux (q_{gas}) and temperature (T) are selected along the vertical profile above the drift and passing through the drift center. The minimum value of the air mass-fraction (χ_{air}) is taken along this same profile.

6.2.4 Results—Lower-Bound Estimates for CO_2 Concentration and Flux

Equations 28 through 31 are implemented in the TH+GASMODEL routine (file: "th+gas_model-L4C4-ui-04.xls"; worksheet: Gasmodel) with the results depicted in Figure 24. The maximum value for C_{gas}, expressed as the ratio $C_{gas}/C_{gas,in}$, is computed by setting $m_{gas} = 0$. The maximum mass flux is computed by setting $C_{gas} = 0$ and $q_{gas} = 0$ in Equation 31. The CO_2 concentration (C_{gas}) is calculated at different time steps, for various values of the mass flux, expressed as a proportion of the maximum mass flux.

The mass-transfer model shows that lower-bound values for CO_2 fugacity are in the range of 1 ppmv to 10 ppmv over a wide range of flux (Figure 24). The figure shows that further decrease of CO_2 fugacity by consumption in the repository environment would not be substantial until the mass flux ratio (mass flux from consumption, normalized to the maximum flux) exceeds 99 percent. This is a consequence of the functional form of Equation 31.

Comparison of the mass-transfer model represented by Equation 31 with the air mass-fraction (χ_{air}) estimation approach shows that the mass-transfer model predicts greater minimum fugacities, but is slower to recover during cooldown. The χ_{air} estimation approach is most similar to the mass-transfer model with low flux (i.e., low consumption of CO_2 in the repository environment). This is expected because the χ_{air} approach does not relate fugacity with flux.

6.2.5 Results–Lower-Bound Estimates for O_2 Concentration and Flux

Estimates for O_2 fugacity are also implemented in the TH+GASMODEL routine (file: "th+gas_model-L4C4-ui-04.xls"; worksheet: Gasmodel) and are depicted in Figure 25. The maximum value for C_{gas}, is expressed as the ratio $C_{gas}/C_{gas,in}$. The O_2 concentration (C_{gas}) is calculated at different time steps, for various values of the mass flux, expressed as a proportion of the maximum mass flux.

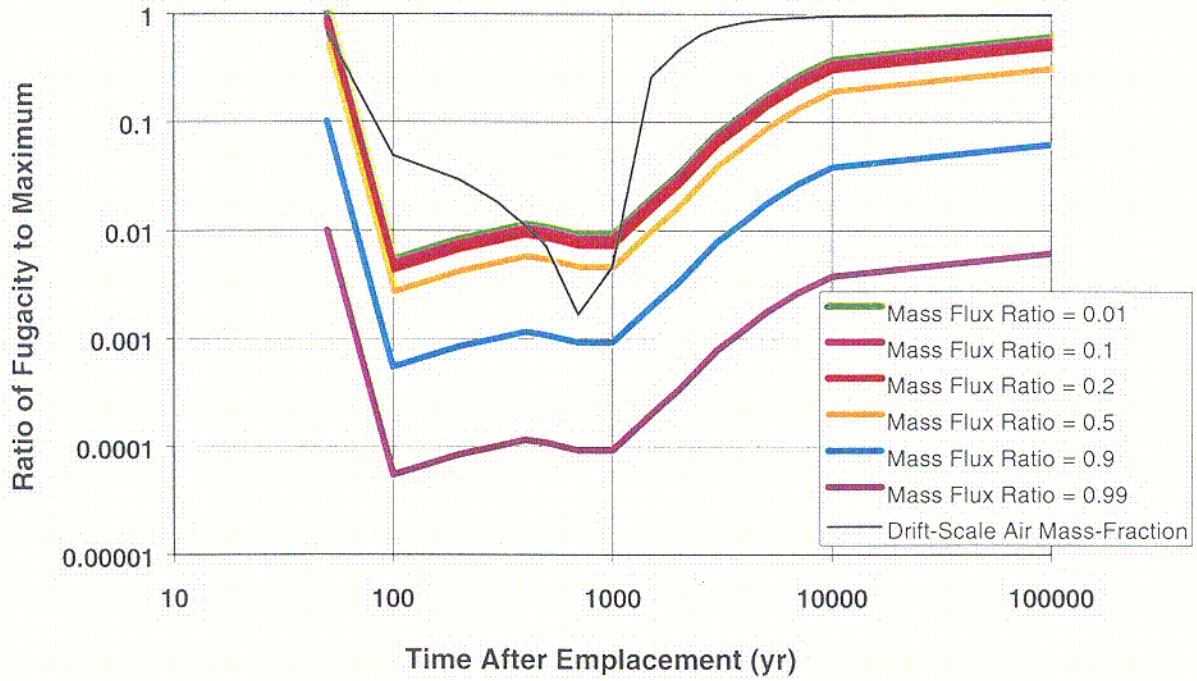

Source: file "th+gas_model-l4c4-ui-04.xls " (Attachment I)

NOTE: Fugacity ratios are normalized to the maximum value at the ground surface.

Figure 24. Lower-Bound Ratios of the CO_2 Concentration (Fugacity) at Repository Depth

The mass-transfer model shows that lower-bound values for O_2 fugacity are in the range of 200 ppmv to 2000 ppmv over a wide range of flux (Figure 25). The figure shows that further decrease of CO_2 fugacity by consumption in the repository environment would not be substantial until the mass flux ratio (mass flux from consumption, normalized to the maximum flux) exceeds 99 percent. This is a consequence of the functional form of Equation 31.

Comparison of the mass-transfer model with the χ_{air} estimation approach shows similar behavior to that discussed previously for CO_2. The mass-transfer model predicts greater minimum fugacities, but is slower to recover during cooldown.

C10

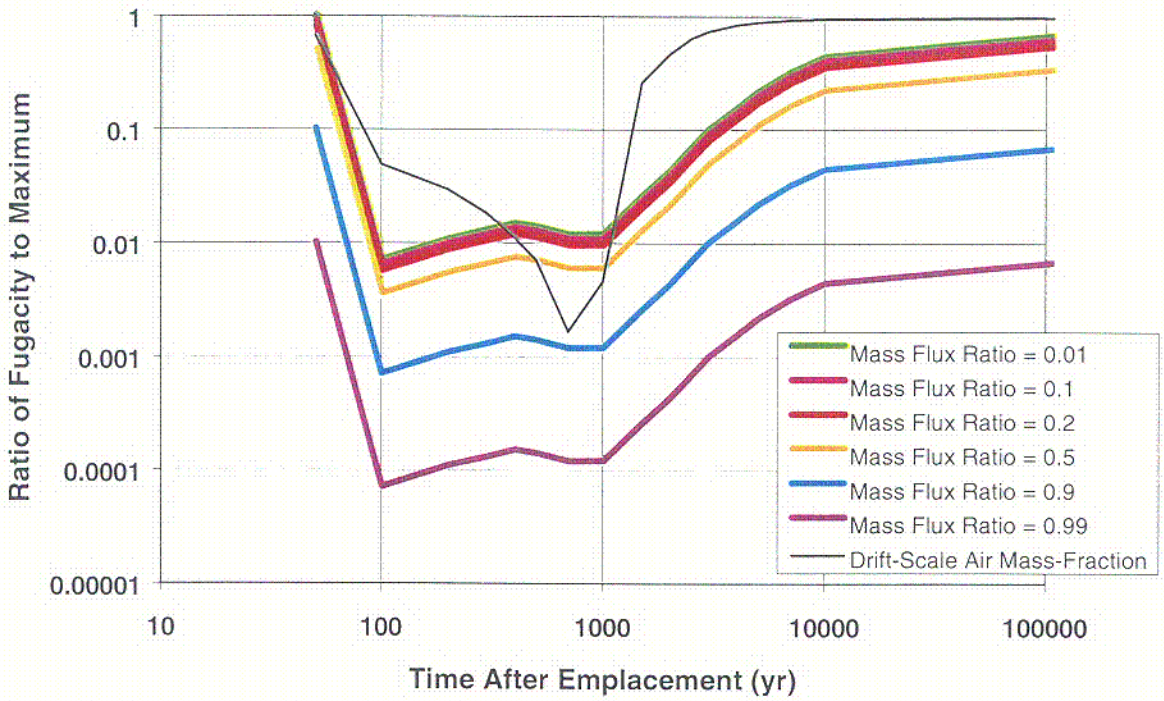

Source: file "th+gas_model-l4c4-ui-04.xls " (Attachment I)

NOTE: Fugacity ratios are normalized to the maximum value at the ground surface.

Figure 25. Lower-Bound Ratios of the O_2 Concentration (Fugacity) at Repository Depth

6.2.6 Summary

The flux and fugacity information calculated using the mass-transfer model for the L4C4 multiscale location, and the "upper" infiltration condition, are plotted in Figure 24 and Figure 25 for CO_2 and O_2 gas, respectively. The results are similar to the air mass-fraction approach (also plotted). The mass-transfer model predicts greater minimum fugacities, but the fugacities are slower to recover during cooldown than they are with the air mass-fraction. This is an approximate model, and the assumptions and limitations are discussed in Section 5.2.

In general, it is shown that the model has an appropriate level of confidence suitable for its intended use. This model has associated uncertainties which derive from consideration of alternative models, and from assumptions related to input data and from selections made in model development. Uncertainty is mitigated because this is a bounding model. The greatest uncertainty is probably associated with the assumption of limited CO_2 interaction with solid phases during the thermal period. Uncertainties are addressed in the following sections, which include comparison to similar results obtained using alternative methods.

The results documented in this report (Figure 24 and Figure 25) show that the advective-dispersive oscillatory barometric pumping process represented by the D_{gas} parameter in

Equation 27 is a potentially important mechanism for gas transport in the UZ. Increasing diffusion coefficient values to account for this effect has not been applied in any other models of Yucca Mountain. The effect can disperse heat and water vapor as well as transport gas from the surface, as calculated here. The use of enhanced diffusion coefficients (relative to the molecular diffusion coefficient modified for porosity and tortuosity) can be incorporated in other models (e.g., NUFT V3.0s for thermal-hydrologic-chemical simulations) and tested for ambient (prerepository) conditions by comparison to radiocarbon and other data.

6.2.6.1 Discussion of Conservatism in the Bounding Model

The gas-phase CO_2 and O_2 fugacities and their variation with postulated mass flux (i.e., consumption at depth) as shown in Figures 24 and 25, represent reasonable lower-bound availability for chemical reactivity in the drifts for the following reasons:

- Aqueous flux of CO_2 as implied by the nonequilibrium nature of $^{14}CO_2$ transport interpreted for borehole SD-12, is neglected in the model.
- One-dimensional transport is assumed, but there are indications from the TH models (Section 6.1) that multidimensional gas-phase occurs even in 2-D "chimney" models. The wider drift spacing associated with the Enhanced Design Alternative (EDA) II design concept (Wilkins and Heath 1999) allows for cooler temperatures in the pillars, which promotes convective circulation. The effects of circulation would include mixing; thus, mass transfer over the entire repository footprint could have a role in controlling gas fugacities in the emplacement drifts.
- Retrograde solubility is neglected in the model; hence, the gas-liquid phase partitioning does not change as a function of temperature. With higher temperature, the distribution coefficient K_d decreases, which decreases the effective retardation of gas-phase diffusive-dispersive CO_2 transport.
- Increase of molecular diffusion coefficients with temperature is neglected in the model.

6.2.6.2 Comparison with Alternative Models and Approaches

Simulation of Gas-Phase Fluxes for the Viability Assessment

Previous mountain-scale TH modeling of the air mass-fraction and the cumulative mass flux of air at the repository horizon showed that gas-phase convective circulation may be limited in the thermal period (CRWMS M&O 1998c). Two demonstrative figures from the TSPA-VA Technical Basis Document are reproduced here as Figure 26 and Figure 27 (CRWMS M&O 1998c, Figure 4-16 and Figure 4-18). These figures summarize model calculations using a 2-D, repository-scale NUFT simulation to represent gas-phase composition and flux for the Viability Assessment (VA) repository design. They are presented here for comparison only; for documentation of these results, the reader is referred to the source document.

It should be noted that the VA design was intended to have higher peak temperatures and a longer-lasting thermal period than the current conceptual design basis (the "EDA-II" design; see Wilkins and Heath 1999).

Ambient CO_2 and O_2 concentrations (1000 ppmv and 20 percent v/v, respectively) were assumed for the air fraction of the gas-phase (air mass-fraction estimation approach). Thus CO_2 fugacity is obtained by multiplying the air mass-fraction (Figure 26) by 1000 ppmv. With this air mass-fraction approach, the minimum CO_2 and O_2 fugacity values, which depend directly on the air mass-fraction, can be very small at the repository center (Figure 26). Limited mass flux through the repository center is evident for the time period from approximately 300 to 1000 yr, when the cumulative mass-flux curve for the repository center is flat. Important differences between this air mass-fraction approach and the mass-transfer model previously described (e.g., Equation 31) include:

- Natural advective-dispersive mass-transfer processes that operate in the UZ were not taken into account in the TSPA-VA approach
- Large-scale, thermally driven gas-phase convection is not taken into account in this report

For both approaches, there is a time period during which evaporation is active and CO_2 and O_2 fugacity values are predicted to be small (e.g., less than 1 percent of ambient values).

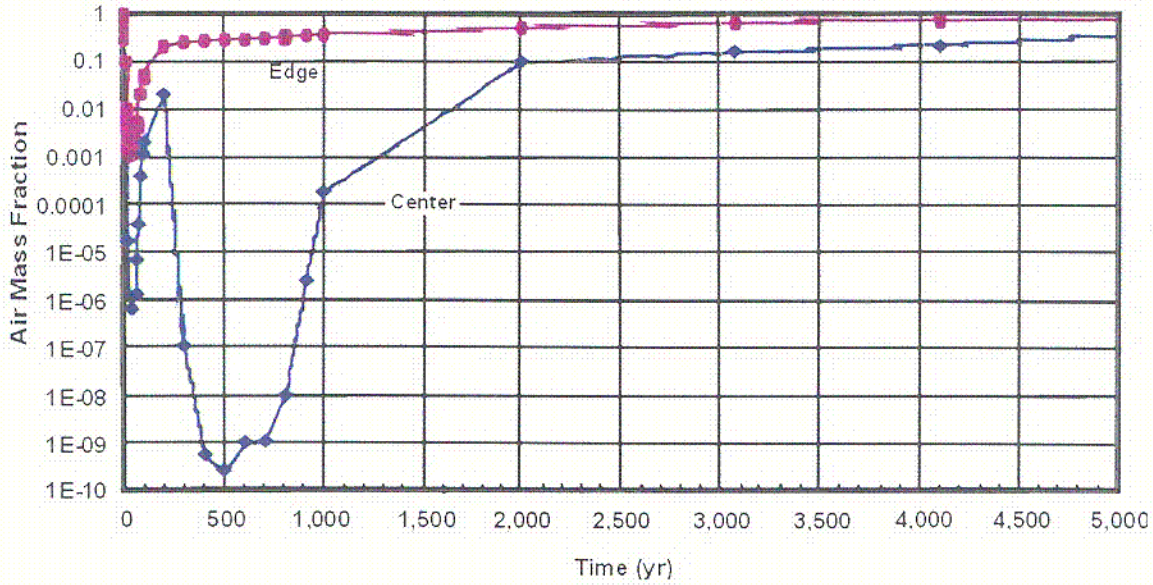

00018DC EBS-PMP-20.cdr

Source: CRWMS M&O 1998b, Figure 4-16

Figure 26. Evolution of Air Mass-Fraction Calculated for Repository Center and Edge Locations, for the Viability Assessment Repository Design

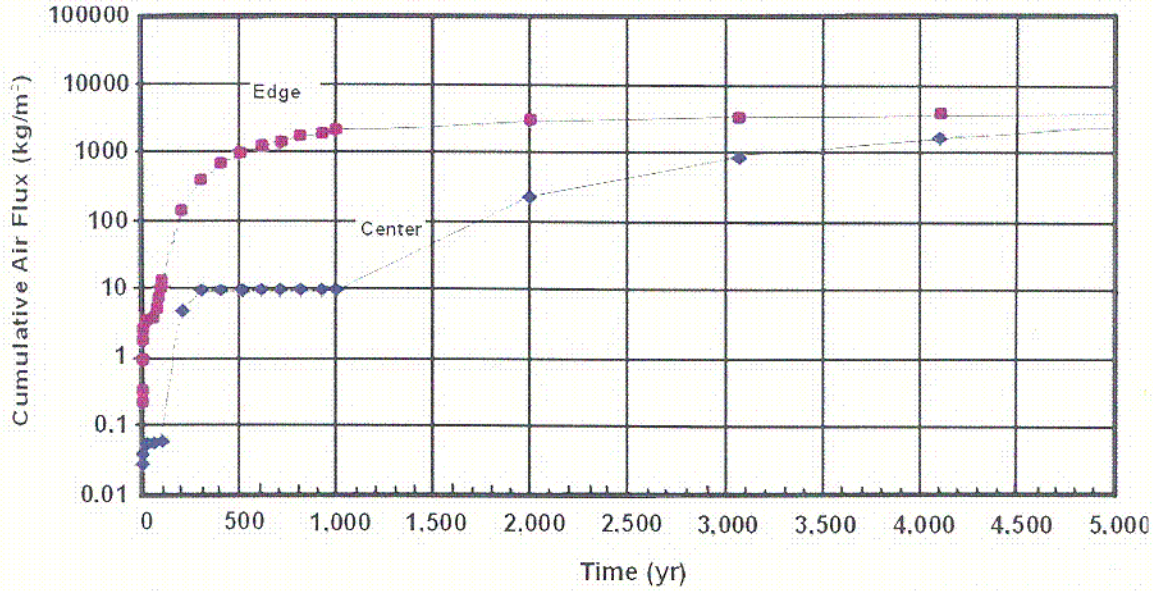

00018DC EBS-PMP-21.cdr

Source: CRWMS M&O 1998b, Figure 4-18

Figure 27. Cumulative Air Flux Flowing Through the Repository Horizon, Calculated for Repository Center and Edge Locations for the Viability Assessment Repository Design

C12

Air Mass-Fraction Analysis of TH Models

The approach used for TSPA-VA can be applied to the TH results calculated using the model described in Section 6.1. This is accomplished by determining the flux of gas through the drift, multiplying the gas-phase mass flux by the drift diameter (5.5 m). The result is multiplied by the air mass-fraction in the drift, and the reference concentration of CO_2 or O_2 in the air fraction (1000 ppmv and 0.2, respectively).

The results for both CO_2 and O_2 are plotted in Figure 28. The figure shows that the air mass-fraction approach (based on the 2-D models described in Section 6.1) is comparable to the mass-transfer model (e.g., Equation 31). One potentially important difference is that the air mass-fraction approach causes transport to diminish as cooldown progresses, whereas the mass transfer model indicates that gas flux can continue beyond the thermal period.

Multicomponent Reactive-Transport Simulation

Coupled reactive transport simulations couple TH with transport of chemical components, mass balance of components, chemical speciation and heterogeneous reactions, and rate-dependent reactions. Two simulations of this type for the potential repository host rock, including the emplacement drifts, are discussed here (CRWMS M&O 2000d). Gas-phase chemistry is an appropriate measure for comparison of chemical models because the pH and mineral precipitation depend strongly on the CO_2 fugacity.

Host-rock water composition and CO_2 fugacity values were calculated, for several different assumptions on the infiltration flux magnitude, in this series of drift-scale reactive transport simulations. Results for the "upper" infiltration distribution (CRWMS M&O 2000d) are shown in Figure 29. Two cases are discussed here: Case 1 includes representative clay and zeolite minerals in addition to silica and calcite, and Case 2 includes only silica and calcite.

The CO_2 fugacity at the drift wall as a function of time, calculated from reactive transport, the air mass-fraction approach, and the 1-D mass-transfer approach, is shown in Figure 29. The air mass-fraction and mass-transfer approaches are discussed in more detail in later sections of this report. The CO_2 fugacity from reactive transport simulations is reported at the drift crown, which is the highest point on the drift wall directly above the DS. For all three modeling approaches considered, the values are generally within a factor of approximately 30 during the thermal period. At late time, the reactive transport simulations show increased CO_2 fugacity as the air mass-fraction increases and as the gaseous CO_2 liberated during heating returns to the drift environment. The other approaches effectively require that the CO_2 released by heating, is dissipated before cooldown.

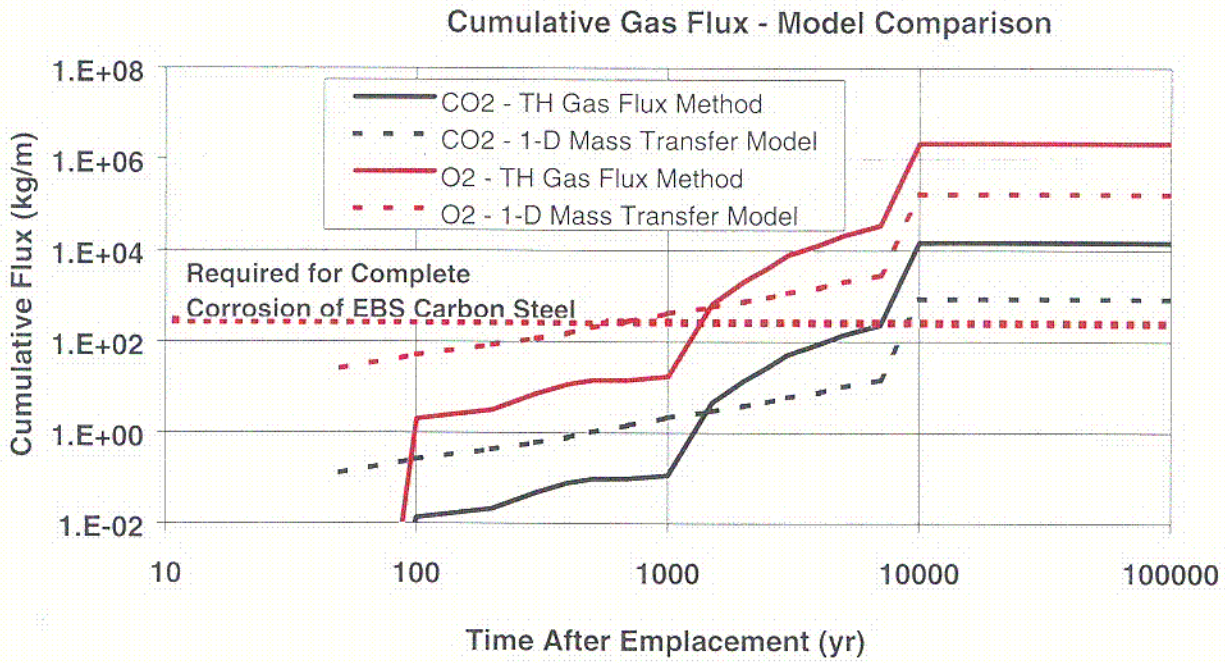

Figure 28. Comparison of the 2-D Air Mass-Fraction Approach to Estimating the Available Fluxes of CO_2 and O_2, With the Mass Transfer Model (L4C4 Location; "Upper" Infiltration)

The reactive transport simulations are subject to ionic strength limitations that also exist for other approaches to chemical modeling. The chemical activity models (e.g., B-dot model; Section 6.7) can be used for ionic strength values up to approximately 1 molal. When evaporative concentration causes solution ionic strength to exceed this limit, approximations are used to represent chemical conditions. In the reactive transport simulations, chemical speciation and dissolution/precipitation reactions are suspended when the ionic strength limit is reached and until dilution by water returning during cooldown. The extreme values for CO_2 fugacity occur during this period of approximation.

An advantage of the reactive transport approach is the integration of chemical processes, with spatial and temporal resolution limited only by the model design. Disadvantages include computational effort, the representation of the host rock and simulation of engineered barriers using only a few chemical species and precipitates, and restricted flexibility in handling ionic-strength limitations. Simulations of this type will be incorporated in this model as applicable calculations become available.

6.2.6.3 Gas Flux and Fugacity Model Validation

Analytical solutions are developed to describe the variation of ^{14}C activity with depth in the gas phase. These models are extended, to describe the transport of CO_2 and O_2 gases in the UZ during the thermal period in response to chemical sources or sinks at depth. Bounding values are used for most parameters of these models, in the sense that the values tend to minimize the

C13

fugacity of CO_2 and O_2 gases during the thermal period, or any other time when these constituents are being consumed in the drift environment. One parameter, the diffusion-dispersion parameter that controls gas-phase transport, is calibrated to field data from borehole SD-12. The results show that ^{14}C observations can be represented by an envelope of curves corresponding to uncertainty in the infiltration flux (Figures 19 through 23).

The model is also applied to four other boreholes in the same manner. The same bounding parameter values are used to approximate the other boreholes, and the diffusion-dispersion parameter is fitted for each borehole. The results show that the fitted parameter has a greater value (more transport) in the other boreholes. A representative value of the diffusion-dispersion parameter is selected for use in gas flux and fugacity calculations.

The 1-D analytical solution includes multiple bounding approximations. It is based on bounding inputs as shown by checking against ^{14}C data from four other boreholes in addition to SD-12. The bounding nature of the model results for gas flux and fugacity is also shown by comparison to the air mass-fraction method, and comparison to results from reactive transport simulations.

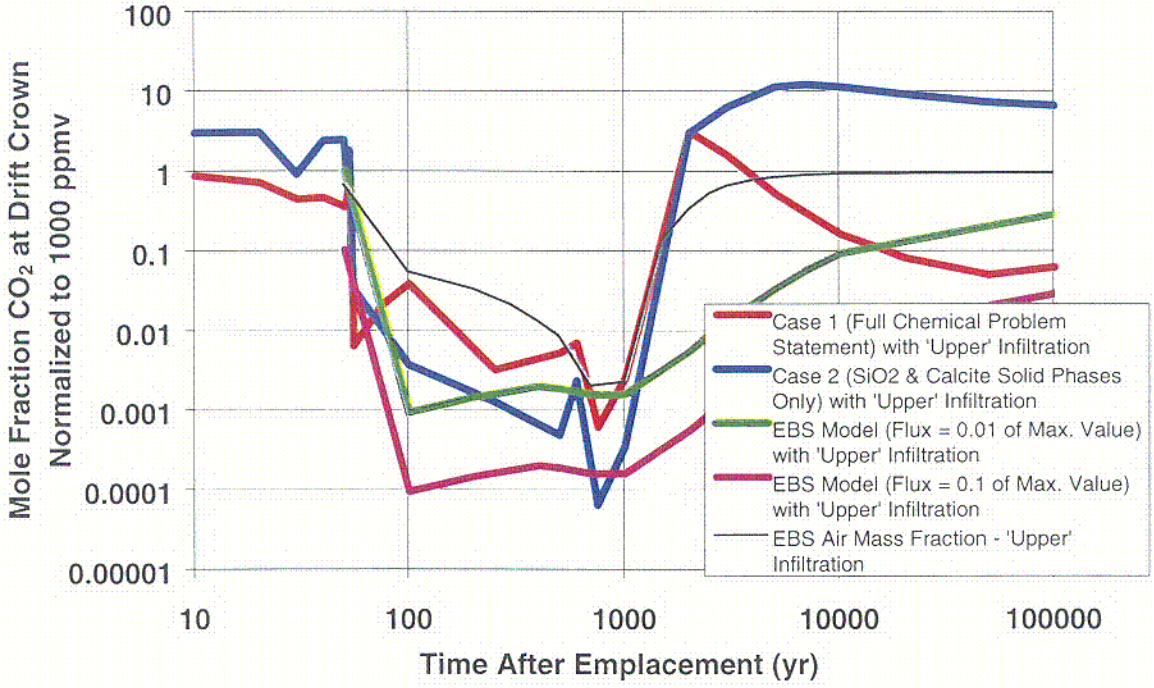

Notes: Reactive transport calculations are taken from files: "case1_15.xls" and "case2_15.xls" of reference: CRWMS M&O (2000d).

Results from the Gas Flux and Fugacity Model are those described in this report.

Figure 29. Comparison of Reactive Transport Simulation of CO_2 Fugacity, with Results from the Gas Flux and Fugacity Model

6.3 CEMENTITIOUS MATERIALS MODEL

The Cementitious Materials Model is used to develop bounding estimates for potential chemical effects from percolating water that contacts grouted rockbolts in the repository and for interaction of that water with quartz-sand backfill and gas-phase CO_2. Interaction with quartz is modeled instead of interaction with tuff, because the tuff contains more soluble and reactive silica polymorphs (e.g. cristobalite), and would be likely to buffer the leachate composition more readily than quartz. Therefore the model approach is conservative with respect to silica buffering. Interaction with quartz is modeled as an equilibrium process, the basis for which is documented in Section 6.7.2.3.

Grouted rockbolts are planned for use in the portion of the potential repository that is constructed in the middle nonlithophysal tuff (CRWMS M&O 2000a) (TBV-3902). No other use of cementitious material in the repository is addressed by this model.

When contacted by water, cement can yield high pH and anions such as sulfate. However, only a portion of the potential seepage flow into repository drifts would be affected by cement, and the effects will be moderated and diluted downstream. This model provides the source function representing the volume of affected water, and the inventory of chemical constituents, from cement-water interaction. Following are the specific objectives for this model:

- Describe the mineralogy of the specified cementitious grout and its evolution over time.
- Describe the composition of water before contacting the grout.
- Develop reasonable upper-bound estimates for the composition of water contacting grout, emphasizing pH and concentrations for anions such as sulfate.
- Evaluate equilibration of cement-influenced water with backfill and gas-phase CO_2.
- Develop reasonable-bound estimates for flow rate of affected water into the drift.

The Cementitious Materials Model does not address mixing of cement-affected waters with seepage in the drift, nor does it address the effects of heating on flow in the host rock. Mixing is ignored because the composition of equilibrated leachate is similar to water composition calculated for the Chemical Reference Model. The effects of heating on flow are considered in Section 6.1, and the resulting fluxes are used in the Cementitious Materials Model to estimate the flux of water that could interact with cement.

6.3.1 Grout Description and Evolution

The mineralogy of the grout determines how it reacts with groundwater. The mineralogy of cement grout (Table 29) is represented by portlandite, ettringite, tobermorite, and brucite (Assumption 5.3.1 and Assumption 5.3.3). Portlandite and brucite are represented in the PHREEQC chemical database (file: "wateqcem.txt"; Attachment I). Chemical data for ettringite and tobermorite were obtained from other sources and combined with the PHREEQC database (Assumption 5.3.6).

To simulate the effects of partial carbonation, calcite is included in the mineral assemblage as an equilibrium phase in the PHREEQC calculations (Assumption 5.3.2). Only the presence, not the amount, of calcite is specified. Carbonation does not proceed to completion in this model (i.e., not all portlandite is converted to calcite, and both phases are present) (Assumption 5.3.2). Precipitation of calcite occurs when the leachate is exposed to fixed CO_2 fugactiy, representing the drift atmosphere.

The aging of cement grout is simulated by progressive leaching or dissolution of mineral phases in proportion to their equilibrium solubilities (Assumption 5.3.5). Accordingly, the calculations described subsequently show that for the mineral assemblage and environmental conditions considered, the solubilities of portlandite and ettringite cause them to be leached before tobermorite, brucite, and calcite and to be completely leached. These phases (particularly ettringite) are assumed to be stable for the temperatures, moisture conditions, and time periods considered in this model (Assumption 5.3.4).

6.3.2 Temperature and P_{CO2} Sensitivity

Calculations performed for this report and described in the following sections show that leachate composition will differ strongly from the influent fracture-water composition for at least several thousand years. Leachate composition will be affected until the dissolving phases are exhausted; therefore, changes in solution composition during this period will be caused primarily by temperature and P_{CO2} effects rather than by mineralogical changes. Accordingly, a sensitivity study was undertaken to characterize the effects of temperature and P_{CO2} on the mineral assemblage. These calculations are limited to thermodynamic modeling of inorganic, abiotic processes (Assumption 5.3.7).

6.3.2.1 The PHREEQC code

Required PHREEQC input includes parameters that control the availability of CO_2. Different CO_2 conditions were used to represent formation of leachate within the grout column and reaction of the leachate with the environment outside the grout column:

- Grout system closed with respect to CO_2 (i.e., the CO_2 available within the grout column is that dissolved in the influent water) to represent the maximum leachate pH from contact with cement
- Leachate and quartz-sand system open with respect to CO_2 (i.e., fugacity is held constant so that no reaction extent is limited by the availability of CO_2) to represent interactions in the drift

In the closed-system calculation, CO_2 is restricted from diffusing into the grout either as aqueous or gas-phase diffusion (Assumption 5.3.5), and carbonation reactions are reactant-limited. As the closed system is reacted in the model, fugacity decreases with reaction progress; in the open calculation, the CO_2 fugacity is constant.

To determine the sensitivity of solution chemistry to variable temperature and P_{CO2}, PHREEQC simulations were performed for temperatures of 30, 50, 70, and 90°C using the closed-system CO_2 condition with initial P_{CO2} values of 9.52, 952, and 9520 ppmv. These P_{CO2} values represent

a range of conditions that could occur in the host rock; they are arbitrary values generated by selecting values of 10, 1,000, and 10,000 ppmv and correcting them for the air mass-fraction at ambient RH conditions. The results are summarized in Table 33 through Table 36.

Table 33. Calculated Composition of Leachate from Partially Carbonated Grout Assemblage at T = 30°C and Several Values of P_{CO2}

Element or Species	Initial J-13 Groundwater (mol/kg)	J-13 Water Equilibrated with Grout (mol/kg)	Grout Leachate Equilibrated with Backfill for Several Values of P_{CO2}		
			9.5 ppmv [A] (Values in mol/kg)	952 ppmv [B] (Values in mol/kg)	9520 ppmv [C] (Values in mol/kg)
Al	0.0	2.134E-04	2.133E-04	2.133E-04	2.133E-04
C (as HCO_3)	2.11E-03	6.660E-06	3.892E-04	1.525E-03	3.485E-03
Ca	3.24E-04	1.830E-02	1.154E-04	6.060E-04	1.448E-03
Cl	2.02E-04	2.014E-04	2.014E-04	2.014E-04	2.014E-04
F	1.15E-04	1.148E-04	1.147E-04	1.147E-04	1.147E-04
K	1.29E-04	1.289E-04	1.289E-04	1.289E-04	1.289E-04
Mg	8.27E-05	1.352E-07	1.351E-07	1.351E-07	1.351E-07
NO_3	3.19E-05	3.194E-05	3.193E-05	3.193E-05	3.193E-05
Na	1.99E-03	1.993E-03	1.992E-03	1.992E-03	1.992E-03
SO_4	1.92E-04	5.117E-04	5.115E-04	5.115E-04	5.115E-04
Si	1.02E-03	3.954E-15	1.773E-04	1.258E-04	1.239E-04
pH	7.41	12.286	9.371	8.012	7.336
Portlandite dissolved (mol/kg solvent)		2.029E-02			
Ettringite dissolved (mol/kg solvent)		1.067E-04			
Quartz dissolved (mol/kg solvent)		0.0	1.773E-04	1.259E-04	1.239E-04
Calcite precipitated (mol/kg solvent)		2.106E-03	1.819E-02	1.770E-02	1.685E-02

NOTES: A Input file "grout301.txt "; output file "grout301.out" (Attachment I)
B Input file "grout302.txt"; output file "grout302.out" (Attachment I)
C Input file "grout303.txt"; output file "grout303.out" (Attachment I)

Table 34. Calculated Composition of Leachate from Young, Partially Carbonated Grout Assemblage at T = 50°C and Several Values of P_{CO2}

Element or Species	Initial J-13 Groundwater (mol/kg)	J-13 Water Equilibrated with Grout (mol/kg)	Grout Leachate Equilibrated with Backfill for Several Values of P_{CO2}		
			9.5 ppmv [A] (Values in mol/kg)	952 ppmv [B] (Values in mol/kg)	9520 ppmv [C] (Values in mol/kg)
Al	0.0	9.587E-04	9.584E-04	9.584E-04	9.584E-04
HCO_3	2.11E-03	7.764E-06	7.886E-05	6.611E-04	1.966E-03
Ca	3.24E-04	1.496E-02	1.416E-03	1.656E-03	2.214E-03
Cl	2.02E-04	2.014E-04	2.013E-04	2.013E-04	2.013E-04
F	1.15E-04	1.147E-04	1.147E-04	1.147E-04	1.147E-04
K	1.29E-04	1.289E-04	1.289E-04	1.289E-04	1.289E-04
Mg	8.27E-05	1.998E-07	1.997E-07	1.997E-07	1.997E-07
$N0_3$	3.19E-05	3.193E-05	3.192E-05	3.192E-05	3.193E-05
Na	1.99E-03	1.992E-03	1.992E-03	1.992E-03	1.992E-03
SO_4	1.92E-04	1.630E-03	1.629E-03	1.629E-03	1.629E-03
Si	1.02E-03	5.849E-15	2.777E-04	2.328E-04	2.294E-04
pH	7.41	11.616	8.803	7.771	7.214
Portlandite dissolved (mol/kg solvent)		1.472E-02			
Ettringite dissolved (mol/kg solvent)		4.795E-04			
Quartz dissolved (mol/kg solvent)		0.0	2.779E-04	2.330E-04	2.295E-04
Calcite precipitated (mol/kg solvent)		2.105E-03	1.355E-02	1.331E-02	1.275E-02

NOTES: A Input file "grout501.txt"; output file "grout501.out" (Attachment I)
B Input file "grout502.txt"; output file "grout502.out" (Attachment I)
C Input file "grout503.txt"; output file "grout503.out" (Attachment I)
C Input file "grout503.txt"; output file "grout503.out" (Attachment I)

Table 35. Calculated Composition of Leachate from Young, Partially Carbonated Grout Assemblage at T = 70°C and Several Values of P_{CO2}

Element or Species	Initial J-13 Groundwater (mol/kg)	J-13 Water Equilibrated with Grout (mol/kg)	Grout Leachate Equilibrated with Backfill for Several Values of P_{CO2}		
			9.5 ppmv [A] (Values in mol/kg)	952 ppmv [B] (Values in mol/kg)	9520 ppmv [C] (Values in mol/kg)
Al	0.0	3.118E-03	3.117E-03	3.117E-03	3.118E-03
HCO_3	2.11E-03	8.829E-06	3.618E-05	2.886E-04	9.718E-04
Ca	3.24E-04	1.561E-02	5.732E-03	5.785E-03	6.042E-03
Cl	2.02E-04	2.013E-04	2.013E-04	2.013E-04	2.013E-04
F	1.15E-04	1.147E-04	1.147E-04	1.147E-04	1.147E-04
K	1.29E-04	1.288E-04	1.288E-04	1.288E-04	1.288E-04
Mg	8.27E-05	2.977E-07	2.977E-07	2.977E-07	2.977E-07
$N0_3$	3.19E-05	3.192E-05	3.191E-05	3.191E-05	3.191E-05
Na	1.99E-03	1.991E-03	1.991E-03	1.991E-03	1.991E-03
SO_4	1.92E-04	4.868E-03	4.868E-03	4.868E-03	4.868E-03
Si	1.02E-03	7.912E-15	4.657E-004	3.993E-04	3.942E-04
pH	7.41	11.019	8.522	7.520	7.012
Portlandite dissolved (mol/kg solvent)		8.886E-03			
Ettringite dissolved (mol/kg solvent)		1.560E-03			
Quartz dissolved (mol/kg solvent)		0.0	4.661E-04	3.997E-04	3.946E-04
Calcite precipitated (mol/kg solvent)		2.104E-03	9.884E-03	9.831E-03	9.574E-03

NOTES: A Input file "grout701.txt"; output file "grout701.out" (Attachment I)
B Input file "grout702.txt"; output file "grout702.out" (Attachment I)
C Input file "grout703.txt"; output file "grout703.out" (Attachment I)

Table 36. Calculated Composition of Leachate from Young, Partially Carbonated Grout Assemblage at T = 90°C and Several Values of P_{CO2}

Element or Species	Initial J-13 Groundwater (mol/kg)	J-13 Water Equilibrated with Grout (mol/kg)	Grout Leachate Equilibrated with Backfill for Several Values of P_{CO2}		
			9.5 ppmv [A] (Values in mol/kg)	952 ppmv [B] (Values in mol/kg)	9520 ppmv [C] (Values in mol/kg)
Al	0.0	8.115E-03	8.114E-03	8.114E-03	8.114E-03
HCO_3	2.11E-03	8.811E-06	2.222E-05	1.524E-04	5.355E-04
Ca	3.24E-04	2.235E-02	1.576E-02	1.571E-02	1.582E-02
Cl	2.02E-04	2.011E-04	2.010E-04	2.010E-04	2.010E-04
F	1.15E-04	1.146E-04	1.145E-04	1.145E-04	1.145E-04
K	1.29E-04	1.287E-04	1.287E-04	1.287E-04	1.287E-04
Mg	8.27E-05	5.029E-07	5.028E-07	5.028E-07	5.028E-07
$N0_3$	3.19E-05	3.188E-05	3.188E-05	3.188E-05	3.188E-05
Na	1.99E-03	1.989E-03	1.989E-03	1.989E-03	1.989E-03
SO_4	1.92E-04	1.236E-02	1.236E-02	1.236E-02	1.236E-02
Si	1.02E-03	9.574E-15	7.499E-04	6.439E-04	6.358E-04
pH	7.41	10.453	8.337	7.337	6.836
Portlandite dissolved (mol/kg solvent)		6.290E-04			
Ettringite dissolved (mol/kg solvent)		4.065E-03			
Quartz dissolved (mol/kg solvent)		0.0	7.515E-04	6.452E-04	6.371E-04
Calcite precipitated (mol/kg solvent)		2.104E-03	6.600E-03	6.651E-03	6.548E-03

NOTES: A Input file "grout901.txt"; output file "grout901.out" (Attachment I)
B Input file "grout902.txt"; output file "grout902.out" (Attachment I)
C Input file "grout903.txt"; output file "grout903.out" (Attachment I)

6.3.2.2 Grout-Leachate Equilibrium

The calculations show that, prior to contact with atmospheric CO_2 and backfill, the grout-equilibrated leachate is highly alkaline (pH 12.286; Table 33) with a high concentration of dissolved calcium.

The composition of the grout-equilibrated leachate is controlled by dissolution of portlandite and ettringite. The solubilities of portlandite and ettringite are temperature-dependent. As temperature increases, portlandite solubility decreases, and ettringite solubility increases. Solubilities calculated using PHREEQC for temperatures from 30 to 90°C are shown in Table 37. These are closed-system solubility values whereby CO_2 input is fixed and limited to that initially present in groundwater.

Table 37. Solubilities (kg/m^3) of Portlandite and Ettringite at Several Temperatures, with Closed-System CO_2 Conditions Limited to the Influent Dissolved Inorganic Carbon

Solubility (mol/kg solvent)	Temperature			
	30°C	50°C	70°C	90°C
Portlandite	2.029E-002	1.472E-002	8.886E-003	6.290E-004
Ettringite	1.067E-004	4.795E-004	1.560E-003	4.065E-003

6.3.2.3 Leachate Composition Outside the Grout

Upon equilibrium with atmospheric CO_2 and quartz-sand backfill, quartz dissolves, pH decreases, and calcite precipitates.

Upon reaction of the grout-equilibrated leachate with quartz sand, the resulting calcite precipitation and quartz dissolution are also sensitive to temperature, but are relatively insensitive to P_{CO2} for the range considered.

At 30°C, calcite precipitates at rates from 1.819×10^{-2} mol/kg at low P_{CO2} down to 1.685×10^{-2} mol/kg as P_{CO2} approaches 10,000 ppmv (Table 33). At 90°C, calcite precipitates at 6.600×10^{-3} mol/kg at low P_{CO2}, and precipitation increases slightly with increasing P_{CO2}. These estimates of calcite precipitation are upper-bound equilibrium values that do not take into account supersaturation that is known to occur with calcite.

Quartz dissolution at 30°C decreases from about 1.773×10^{-4} mol/kg at low P_{CO2}, to 1.239×10^{-4} mol/kg as P_{CO2} increases toward 10,000 ppmv (Table 33). At 90°C, quartz dissolution decreases from about 7.515×10^{-4} mol/kg at low P_{CO2}, to 6.371×10^{-4} mol/kg at high P_{CO2} (Table 36).

The pH is controlled by the solubility of gaseous CO_2, which decreases with increasing temperature. At 30°C, the leachate is initially at pH 12.286 (Table 33), but equilibrates to pH 9.371 at P_{CO2} = 9.5 ppmv, and decreases further to pH 7.336 at P_{CO2} = 9520 ppmv. At 90°C, the

leachate is initially at pH 10.453 (Table 36), but equilibrates to pH 8.337 at P_{CO2} = 9.5 ppmv, and decreases further to pH 6.836 at P_{CO2} = 9520 ppmv.

As the grout is leached by low-temperature groundwater, the resulting solution chemistry is determined by portlandite dissolution; at higher temperatures, solution chemistry is controlled by ettringite dissolution. In both cases, the leachate is alkaline, supersaturated with respect to calcite, and aggressive with respect to potential dissolution of quartz backfill. However, at high temperatures, the solution is calculated to contain more dissolved sulfate (up to approximately 1,200 mg/L; see Table 36) from dissolution of ettringite, with moderate increases in dissolved aluminum and calcium. As a consequence, at high temperatures, the leachate is supersaturated with respect to gypsum and anhydrite.

Any grout leachate, the composition of which is described in Table 33 through Table 36, that contacts the quartz-sand backfill and gas-phase CO_2 will dissolve relatively small amounts of sand while precipitating larger amounts of calcite. As temperature increases, however, the amount of silica dissolved increases while the amount of calcite precipitated decreases.

6.3.3 Grout Dissolution Rate

The composition variation of the initial grout leachate solution as a function of time will be determined by dissolution and leaching of the grout mineral phases, which are determined by temperature and, to a lesser extent, by P_{CO2}. As the mineral phases are successively dissolved, the solution composition will change. Table 38 summarizes leaching conditions for rockbolt grout.

Table 38. Summary of Leaching Conditions for Rockbolt Grout

	Time Period 2 [A]	Time Period 3 [B]	Time Period 4 [C]	Time Period 5 [D]
Time Period from (yr)	300	700	1500	2500
To (yr)	700	1500	2500	10000
Temperature (Zone 1/2; °C)	90.05	88.42	79.96	51.69
P_{CO2} (atm)	1.06E–05	9.07E–06	3.31E–05	1.72E–04
Ettringite Solubility (mol/kg solvent)	4.074E-003	3.795E-003	2.576E-003	5.351E-004
Portlandite Solubility (mol/kg solvent)	6.041E-004	1.404E-003	5.170E-003	1.428E-002
Water Density (kg/m^3)	965.254	966.390	971.799	987.259
Zones 3 and 4 Inflow Rate (kg/m-sec)	2.51E–06	1.11E–05	5.65E–06	8.67E-06
Seepage Flux (m/sec)	9.46E–10	4.16E–09	2.11E–09	3.19E–09
Seepage Flux (m/yr)	2.98E–02	1.31E–01	6.67E–02	1.01E–01
Scaled Flow per Rockbolt (m^3/yr)	7.52E–05	3.31E–04	1.68E–04	2.54E-04
Potential Ettringite Dissolution Rate (kg per year per rockbolt) [E]	3.82E-04	1.57E-03	5.39E-04	1.69E-04
Potential Portlandite Dissolution Rate (kg per year per rockbolt) [E]	3.36E-06	3.44E-05	6.43E-05	2.68E-04
Potential Portion of Ettringite Leached [F]	11%	92%	40%	93%
PotentialPortion of Portlandite Leached [F]	0.08%	1.7%	4.0%	124%

NOTES: Rockbolt diameter = 6.35E–02 m, Rockbolt steel diameter = 2.87E–02 m
Rockbolt grout flow area = 2.53E–03 m^2, Rockbolt length = 2.15 m
Drift diameter = 5.5 m,
A. Solubilities from file: "grout90.out" (Attachment I), B. Solubilities from file: "grout88.out" (Attachment I)
C. Solubilities from file: "grout79e.out" (Attachment I), D. Solubilities from file: "grout51e.out" (Attachment I)
E. Product of solubility and scaled flow. Use 1.246 kg/mole for ettringite; 0.074 kg/mole for portlandite.
F. Use total mineral mass per rockbolt from Table 29, divided by 3 to ignore excess grout.

Groundwater flux for the preclosure period (the first 50 yr after waste emplacement) is not considered because moisture movement in the host rock will be dominated by ventilation. The Thermal Hydrology Model described in this report predicts that there will be no water flux into the drift for the Time Period 1 (from 50 to 300 yr); thus, grout dissolution is negligible during this period. For Time Period 2 (from 300 through 700 yr), the liquid influx to the backfill in the upper part of the drift, for half of the drift cross-section, is predicted to be 2.510×10^{-6} kg/sec (file: "th+gas_model-L4C4-ui-04.xls"; worksheet: CHEMprobL4C4upper). A small proportion of this influx will be intercepted by the grouted rockbolt holes; thus, grout dissolution is projected to begin at 300 yr.

The dissolution rates for the most soluble phases of the grout are calculated for two bounding cases:

- Groundwater saturates the grout cylinder, and the fluid transfer is limited by the saturated hydraulic conductivity.

- Groundwater flows along rockbolt holes, in proportion to the ratio of the rockbolt hole cross-sectional area to the total plan area of the drift.

The hydraulically saturated cylinder represents a minimum flow condition and therefore a maximum leaching time; geometric scaling of rockbolt flow to the total drift seepage inflow yields flow rates that are approximately three orders of magnitude greater and therefore yields a lesser leaching time. Use of the rockbolt borehole cross-sectional area for both types of flow calculations is based on the assumption that geometrical integrity is maintained the alkaline components of the cement (Assumption 5.3.7). In the following sections, degradation of the geometry is addressed by modifying the flow area.

Temperature values representing the host rock where rockbolts will be installed are obtained from the TH Model, Zone 1/2 (Section 6.1; file: "th+gas_model-L4C4-ui-04.xls"; worksheet: CHEMprobL4C4upper). The reference location for TH calculations (L4C4 location) is in the lower lithophysal unit of the Topopah Springs tuff, whereas rockbolts would be installed only in the middle nonlithophysal unit (CRWMS M&O 2000a) (TBV-3902). However, thermal properties for the two units are similar, and temperature differences are small (all other aspects of the simulation being held constant). The timing of temperature changes, such as cooling through the boiling point when liquid inflow and outflow conditions return, is more strongly affected by location (center vs. edge) and the spatial variation of infiltration flux than by variability in thermal and hydrologic properties. Average temperature values for Zone 1/2 in each of four time periods are shown in Table 38.

The dissolution rate of an individual mineral phase is estimated by multiplying the flow of water infiltrating a grout cylinder by the calculated solubility of the given phase for specific chemical conditions (Table 37):

$$r = QS \qquad \text{(Eq. 32)}$$

where

r	=	dissolution rate (kg/sec)
S	=	solubility for specific chemical conditions (kg/m^3)
Q	=	flow rate (m^3/sec)

The PHREEQC model results show that for temperatures greater than approximately 50°C, ettringite is the most soluble constituent phase and will dominate leaching response for several thousand years.

6.3.4 Flux Through Saturated Grout Cylinder

Flow through a saturated vertical grout cylinder can be estimated using Darcy's Law (Freeze and Cherry 1979, Equation 2.2) which yields the following:

$$Q_{grout} = A\frac{\rho g k}{\mu}\frac{dh}{dz}$$

(Eq. 33)

where

Q_{grout}	=	Flow rate through grout (m^3/sec)
A	=	Cross-sectional area of the grout column (m^2)
k	=	Intrinsic permeability (0.1 μdarcy = $10^{-19}m^2$; Assumption 5.3.8)
ρ	=	Density (958.38 kg/m^3 at 100°C; 964.8 kg/m^3 at 90°C; Incropera and DeWitt 1996, interpolated from Table A.6, p. 846)
g	=	Gravitational constant (9.81m/sec^2)
dh/dz	=	Hydraulic gradient (dimensionless value of unity)
μ	=	Dynamic viscosity (μ = 3.13×10^{-4} Pa-sec at 90°C; Incropera and DeWitt 1996, interpolated from Table A.6, p. 846)

The grout occupies a hollow cylinder with 2.5-in. outside diameter, 1.125-in. inside diameter, and 2.15-m length (Section 4.1.3.4). Geometrical integrity of the grout column is assumed (Assumption 5.3.9). Vertical orientation of the bolt maximizes the hydraulic gradient. Substituting the listed values yields a flow rate through one vertical grout cylinder of 8.68×10^{-12} m^3/sec, or less than 1 mL/yr.

The time to completely dissolve a mineral phase, for the stepwise, steady-state conditions developed for chemical modeling (Section 6.1), is

$$t = \frac{m}{SQ}$$

(Eq. 34)

where

t	=	Time to exhaust mineral phase (sec)
m	=	Mass of mineral present (kg)

Using the ettringite solubility of 4.065×10^{-3} mol/kg solvent at 90°C, a mass of 4.08 kg ettringite per rockbolt, and a molecular weight of 1.246 kg/mole, the time to dissolve the ettringite with a flow rate of 8.68×10^{-12} kg/sec is more than one million years for saturated conditions. This may be unrealistic, but the implication is that ettringite may be present for thousands of years.

In the event that the grout is fractured or degraded, its hydraulic conductivity will increase so that the flux-scaling approach may be more appropriate.

6.3.5 Flux-Scaling

The TH Model predicts that, from 300 to 700 yr, there will be a small inflow of water to the drift for half of the drift cross-sectional area (file: "th+gas_model-L4C4-ui-04.xls"; worksheet: CHEMprobL4C4upper). Multiplying by two to represent the full cross-section and dividing by the drift diameter gives the seepage flux:

$$q_{seep} = \frac{2Q_{inflow}}{D\rho\,(1\text{ m})}$$

(Eq. 35)

where

q_{seep} = Seepage flux (m^2/m-sec)
Q_{inflow} = Seepage mass-flow entering the half-drift in the TH Model (kg/m-sec)
D = Drift diameter (5.5 m)

For the 300- to 700-yr time period, $Q_{inflow} = 2.510 \times 10^{-6}$ kg/sec per meter of drift. Using Equation 35 and converting units, this gives a seepage flux of $q_{seep} = 0.0287$ m^3/m^2-yr.

Taking the interception area for one rockbolt as its cross-sectional area (Assumption 5.3.9), the flow of water that could interact with the grout is

$$Q_{grout} = \frac{\pi d^2}{4bD} q_{seep} bD = \frac{\pi}{4} d^2 q_{seep}$$

(Eq. 36)

where

Q_{grout} = Flow of water interacting with one rockbolt (m^3/sec)
d = Rockbolt diameter (2.5 inch)
q_{seep} = Seepage flux (0.0287 m^2/m-yr for the 300- to 700-yr time period; see above)
D = Drift diameter (5.5 m)
b = Spacing between rockbolt patterns, along the drift axis (1.5 m)

Substituting input values in Equation 36 and converting units gives a flow rate of 75 mL/yr per rockbolt for Time Period 2 (300–700 yr). Flow-rate calculations implementing Equation 36 for all of the time periods used for chemical modeling (except Time Period 1, for which there is no seepage flow into the drift) are shown in Table 38.

For all time periods, the potential dissolution of ettringite and portlandite in each time period is calculated by solving Equation 34 for mass (Table 38). The tabulated values do not account for

excess grout. Comparing the potential dissolution values in Table 38 with the available masses of ettringite and portlandite in Table 29 shows that the ettringite will be depleted in approximately 1500 yr (L4C4 location; "upper" infiltration distribution, as discussed in Section 6.1), and dissolution of the portlandite could require 10,000 yr or more.

6.3.6 Evolution of Leachate Composition

The calculations presented in the preceding sections are integrated to model the evolution of solution chemistry for the grout leachate and for the leachate equilibrated with quartz-sand backfill (Assumption 5.3.10). The model is based on the time steps used in the TH Model, with corresponding temperatures and P_{CO2} values (file: "th+gas_model-L4C4-ui-04.xls"; worksheet CHEMprobL4C4upper). As discussed previously, the grout-water equilibration is assumed to be closed to gas-phase CO_2, while the leachate-sand equilibration is assumed to be open (Assumption 5.3.2). The water compositions predicted to result from grout-leachate and leachate-sand equilibria are presented in Table 39.

6.3.7 Cementitious Materials Model Validation

This model calculates the composition and flow rate of leachate that has interacted with fully-grouted rockbolts. (Such bolts would be used only in the portion of the potential repository that is constructed in the Tptpmn unit, in the current design concept.)

A mineral assemblage is selected based on "young" cement (Hardin et al., 1998) with the exception that the gel phase is replaced by tobermorite, a compositionally similar crystalline phase. Use of a modified "young" is a bounding approximation because the labile, alkaline solids present in cement tend to produce less alkaline, carbonate minerals over tens or hundreds of years, on exposure to atmospheric CO_2. The result of the approximation is that alkaline leachate is produced for thousands of years from dissolution of portlandite. Other bounding approximations include equilibration of the leachate with cement minerals, and closed-system conditions whereby gas-phase CO_2 does not interact directly with leachate in the grout. Interaction of the leachate with gas-phase CO_2, and quartz sand backfill, is calculated for conditions outside the grout.

The flow rate of leachate associated with a rockbolt is calculated from seepage estimates, which are taken from the conservative TH models described in Section 6.1. Interaction of seepage with cement grout is calculated from the ratio of the grout annulus area of the rockbolt, to the plan area of the drift. This is a bounding approximation because the saturated hydraulic conductivity of the grout will be very small. If saturated permeability were used to limit the flow rate of leachate, the result would be orders of magnitude less than the area ratio result.

The cementitious materials model is a valid bounding model for leachate chemistry and flow rate. The model does not consider diffusive transport of alkaline species from the interior of the grout to the surface (nor transport of gas-phase CO_2 to the interior).

6.3.8 Summary

This model provides estimates for flow rate and major-species chemistry of grout leachate. Leachate pH values of 10.4 to 11.6 are predicted during cooldown (Table 39) and depend primarily on the solubility of portlandite, which increases at lower temperature. These elevated

pH values for leachate will probably not occur at the drip shield or the waste package because of mixing with other water in the EBS and because of reaction with quartz-sand backfill and gas-phase CO_2. After the leachate reacts with CO_2 and quartz-sand backfill, pH in the range 8.5 to 9.0 is predicted.

Depending on the solubility of ettringite, sulfate concentrations as great as 1.24×10^{-2} mol/kg (1200 mg/L) are predicted at the highest temperatures. The total mass of sulfate delivered to the drifts from the cement by seepage depends on the flow rate, which may vary from less than one to several hundred mL/yr per rockbolt. Because of the relatively high sulfate concentration in leachate, particularly at elevated temperatures, the effect of mixing with other water in the EBS could be to moderate the pH obtained as the mixture is evaporated. However, the mass of sulfate and the associated products of evaporation will be increased.

The grout permeability is small (Assumption 5.3.8), which substantially limits chemical interaction of the grout with the EBS environment and increases the longevity of the grout to dissolution. Flux scaling produces greater flow rates, and thus greater potential effect on the bulk chemical environment, than does limiting leachate flow by the saturated permeability of the grout. Even with flux scaling, the composition and quantity of leachate after equilibration to quartz and CO_2, are of minor importance compared to the composition of water in the bulk environment (Section 6.7.2).

Neither ettringite nor portlandite completely dissolves until at least 1500 yr, depending on the water flow rate. Other phases (e.g., brucite, tobermorite) are more stable to dissolution and tend to alter to more thermodynamically stable minerals. These results are based on the selected TH Model (Section 6.1; L4C4 location, "upper" infiltration distribution), which provides a reasonable-upper bound on infiltration and seepage rates and therefore tends to maximize the rate of dissolution of ettringite and other cement phases.

Potentially important uncertainties associated with this model include the transient effects of rockfall, which could cause rapid rockbolt failure and comminution of the grout. Conversely, the model does not consider cement carbonation from diffusion of gas-phase CO_2 directly into the grout, which could completely neutralize the alkaline constituents well within the 10,000-yr performance period. Consumption of CO_2 by reaction with cement leachate is discussed in Section 6.7.7.1. In general, it is shown that the model has an appropriate level of confidence suitable for its intended use.

Table 39. Evolution of Leachate Composition with Time

	Time Period 2 300–700 yr T = 90.05°C P_{CO2} = 10 ppmv [A]		Time Period 3 700–1500 yr T = 88.42°C P_{CO2} = 9 ppmv [B]		Time Period 4 1500–2500 yr T = 79.96°C P_{CO2} = 20 ppmv [C]		Time Period 5 2500-5000 yr T = 51.69°C P_{CO2} = 53 ppmv [D,E]	
	Grout Equil.	Quartz Equil.	Grout Equil.	Quartz Equil.	Grout Equil.	Quartz Equil.	Grout Equil.	Quartz Equil.
Al (mol/kg)	8.13E-03	8.13E-03	7.58E-03	7.58-03	0.0	0.0	0.0	0.0
CO_2 (total) (mol/kg)	8.81E-06	1.46E-05	8.87E-06	1.45E-05	9.17E-06	1.04E-04	7.90E-06	8.29E-04
Ca (mol/kg)	2.24E-02	1.59E-02	2.15E-02	1.48E-02	8.85E-03	1.23E-04	1.30E-02	3.73E-05
Cl (mol/kg)	2.01E-04	2.01E-04	2.01E-04	2.01E-04	2.01E-04	2.01E-04	2.01E-04	2.01E-04
F (mol/kg)	1.15E-04	1.15E-04	1.15E-04	1.15-04	1.15E-04	1.15E-04	1.15E-04	1.15E-04
K (mol/kg)	1.29E-04	1.29-04	1.29E-04	1.29-04	1.29E-04	1.29E-04	1.29E-04	1.29E-04
Mg (mol/kg)	5.04E-07	5.04-07	4.80E-07	4.80E-07	2.76E-07	2.76E-07	1.95E-07	1.95E-07
NO_3 (mol/kg)	3.19E-05	3.19-05	3.19E-05	3.19E-05	3.19E-05	3.19E-05	3.19E-05	3.19E-05
Na (mol/kg)	1.99E-03	1.99E-03	1.99E-03	1.99E-03	1.99E-03	1.99E-03	1.99E-03	1.99E-03
SO_4 (mol/kg)	1.24E-02	1.24-02	1.16E-02	1.16E-02	1.92E-04	1.92E-04	1.92E-04	1.92E-04
Si (mol/kg)	9.58E-15	9.03-04	9.46E-15	8.92E-04	1.01E-14	1.21E-03	6.17E-15	4.07E-04
pH	10.45	8.70	10.50	8.74	10.81	9.35	11.58	9.31
Portlandite dissolved (mol/kg solvent)	6.04E-04		1.40E-03		1.15E-02		1.56E-02	
Ettringite dissolved (mol/kg solvent)	4.07E-03		3.80E-03		Note E		Note E	
Quartz dissolved (mol/kg solvent)	0.0	9.05-04	0.0	8.93E-04	0.0	1.21E-03	0.0	4.07E-04
Calcite precipitated (mol/kg solvent)	2.10E-03	6.46E-03	2.10E-03	6.69E-03	2.10E-03	8.72E-03	2.11E-03	1.30E-02

NOTES:
- A Input file "grout90.txt "; output file "grout90.out" (Attachment I)
- B Input file "grout88.txt "; output file "grout88.out" (Attachment I)
- C Input file "grout79.txt "; output file "grout79.out" (Attachment I)
- D Input file "grout51.txt "; output file "grout51.out" (Attachment I)
- E Ettringite is totally leached from the grout for Time Periods 4 and 5, based on results in Table 38.

6.4 MICROBIAL EFFECTS MODEL

6.4.1 Introduction

The Microbial Effects Model is intended to support modeling of the in-drift chemical environment and to identify the most important ways that microbial activity could affect the bulk chemical environment. Its purpose is also to implement these mechanisms as sensitivity studies in the in-drift chemical models. This model provides a framework for including microbial effects in performance assessment and for establishing confidence that repository construction and the use of introduced materials will not promote unacceptable rates of waste-package and drip-shield corrosion from microbial causes.

The objectives of the microbial portion of this report include the following:

- Develop a conceptual model for the consequences of microbial activity to repository performance.
- Summarize available laboratory data on microbial effects associated with engineered materials and Yucca Mountain tuff.
- Specify factors that limit microbial activity and the extent of such limitation expected in the repository environment.
- Develop a model framework for including microbial effects in predictive models of the bulk chemical environment.

There are approximately 10^4 to 10^5 total bacteria per gram of Yucca Mountain tuff at the repository horizon (Horn et al. 1998a, pp. 4–5). This is a low density compared to microbially rich environments (e.g., marine sediments, agricultural soils), which can contain as much as 10^9 bacteria per gram.

In the long run, the microbiological community in a potential Yucca Mountain repository may accelerate degradation of engineered materials (e.g., steel used in ground support or the CRM used in waste packages). Bacteria can cause pH changes and oxidize or reduce various chemical species, thereby solubilizing metals. End products of some metabolic activities, such as the generation of sulfide, can also be corrosive to metals. Bacteria may also dissolve metals by means of chelation or by interaction with polysaccharide compounds excreted externally to the organisms. Deposition of polysaccharides also creates differential aeration gradients that accelerate corrosion.

Microorganisms isolated from Yucca Mountain have been shown to possess activities associated with alteration of construction materials, including exopolysaccharide production, acid generation, sulfide production, and iron oxidation; this demonstrates the potential for these activities during repository evolution (Horn et al. 1998a, pp. 4–5). However, the actual occurrence of microbial effects on EBS and waste package materials will depend on the capacity of microbes to remain active and grow in the repository environment. Accumulation of microbial effects over time will depend on the microbial population densities and on the metabolic strategies they employ.

6.4.2 Conceptual Models for Factors Limiting Microbial Activity

Bacteria are ubiquitous in nature, but they require the following for growth and metabolic activity:

- Environmental conditions including temperature and availability of water. (Some strains of bacteria are also inhibited by nuclear radiation at intensities anticipated to occur in immediate proximity to waste packages.)
- Nutrient availability for building the molecules that make up the organisms plus extracellular organic material. (Required nutrients include a carbon source and trace species such as phosphate, sulfur, and nitrogen.)
- Energy sources in the form of thermodynamically favored reactions between accessible elements and compounds in the environment, which may also include carbon sources.

The nature of environmental conditions, the availability of nutrients, and the availability of energy sources have been observed to limit microbial growth and metabolic activity in Yucca Mountain welded tuff or in analogous settings in other geologic media, as discussed below.

6.4.2.1 Environmental Conditions

Water Availability

Experiments have determined that the primary environmental factor limiting microbial growth in the Yucca Mountain welded tuff host rock is lack of water (Kieft et al. 1997, p. 3131; Horn et al. 1999b, p. 565).

Water inside microbial cells is needed to do the following:

- Maintain intracellular metabolic functions
- Maintain turgor of cells (i.e., the internal hydrostatic pressure)
- Allow movement of molecules through the environment and through the cell membranes
- Maintain stability of hydrated cellular components

Based on observed microbial growth from Yucca Mountain rock in synthetic Yucca Mountain groundwater under saturated conditions in the absence of a reduced carbon source, the availability of water was determined to be the primary factor limiting microbial growth. These experiments duplicated the in situ environmental conditions at Yucca Mountain except for the presence of 100 percent saturation of the rock with tuffaceous groundwater. Under these saturated conditions, microbial growth rose to 10^6 to 10^7 aerobic carbon-degrading cells per milliliter groundwater. The fact that microbial growth was observed only when the degree of

saturation was altered indicated that water availability was the primary factor preventing microbial growth beyond 10^4 to 10^5 cells/gm Yucca Mountain rock (Horn et al. 1999b, p. 565).

Many types of microorganisms can survive long periods of desiccation because of specialized dormant structures such as spores, cysts, and resting stages. However, free water is required for resumption of active metabolism and growth.

Elevated Temperature

Elevated temperature can also limit microbial activity and growth. Temperature ranges in which activity and growth can occur vary widely among different types of organisms. Mesophiles that inhabit temperate environments such as the potential repository host rock (before or after heating) typically have growth optima in the range of 25–40°C, although special adaptations can allow activity beyond the upper limit (Straus et al. 1987, pp. 348–351). Organisms in resting stages can survive temperatures well beyond the limit but do not permit metabolic activity because encysted cells remain dormant until the return of conditions that allow growth.

Microorganisms that are found in extreme environments can exhibit higher optimal growth temperatures. Organisms are known that are capable of growth at temperatures exceeding 60°C (thermophiles), including some that grow at 90° to 100°C (hyperthermophiles) and are typically found in habitats such as mudpots and hot springs (Kristjánsson and Hreggvidsson 1995, pp. 18-19). The consensus among workers in this field is that the upper limit to any bacterial growth is approximately 120°C. Such organisms are encountered in deep-sea hydrothermal vents (Reeve 1994, p. 541).

Whether hyperthermophilic organisms are present at Yucca Mountain or will be introduced into repository drifts by repository construction is not determined, although bacterial growth has been detected from Yucca Mountain rock at 50°C (Horn et al. 1998a, p. 8). Where temperatures in the repository exceed 120°C, no bacterial activity will be possible (although sporulated bacteria could survive through such conditions). At temperatures less than 120°C hyperthermophiles can become active if they are present and if water availability and other environmental conditions permit.

Gamma Irradiation

Another factor that will limit bacterial growth in the potential repository is ionizing radiation generated by decaying radioactive waste. Because radiation must penetrate the waste package wall to affect the EBS environment, only gamma radiation is considered. Resistance of microbes to gamma irradiation varies depending on the species. Bacterial spores are relatively radiation-resistant; a dose of 0.3–0.4 Mrad is required to effect 90 percnent kill. Most vegetative cells (active, nonsporulated) require only a tenth of this dose to effect the same rate of kill (Atlas and Bartha 1981, pp. 142–143). However, there are species that display higher radiation resistance even in the vegetative state; these include Micrococcus radiodurans, which can tolerate 1.0 Mrad of irradiation without decrease of the viable cell count (Mattimore and Battista 1996, p. 633). Generally, a gamma dose of 3 Mrad is used to sterilize food and medical instruments (McLaren 1969, p.63). Gamma radiation doses will be on the order of 100 rad/hr immediately following

emplacement of waste packages containing nuclear fuel assemblies. Thus, within a period of just more than a year, a total dose of 1 Mrad would be achieved on the surface of waste packages.

Gamma radiation fields will be most intense when waste-package heat output is highest; thus, radiation effects will be coupled with elevated temperature and dry conditions. It is not known whether radiation-resistant organisms inhabit Yucca Mountain or will be introduced by repository construction, and whether such organisms, if present, can survive elevated temperatures and dry conditions. However, the naturally occurring radioactive environments in which radioresistant organisms evolved often include multiple environmental stressors such as the occurrence of elevated temperatures. Therefore, radioresistance might be coupled to other types of resistance in these types of organisms. Further, physiological response to a single stressor has been shown to cause induction of resistance to other stressors in bacteria (McCann et al. 1991, p.4193).

When considering the effects of irradiation on activity and growth, it is important to consider shielding provided by backfill, ground support materials, and rock. These are effective shielding materials; thus, organisms located a few meters from the waste packages will receive a much smaller gamma dose than will those at the waste-package surface. These organisms could readily re-enter the EBS during cooldown when liquid flux resumes; therefore, even if much of the EBS is sterilized by high radiation, later recolonization will occur. It can occur rapidly (relative to the 10,000-yr performance period) when liquid flux conditions are conducive to transport and environmental conditions (water, heat, radiation) are within ranges that permit growth.

6.4.2.2 Nutrient Availability

Phosphate

Testing has shown that when sufficient water is available, and temperatures and radiation are within ranges conducive to growth, phosphate availability is the primary factor that limits bacterial growth (Horn et al. 1999b, p. 565; McCright et al. 1998, pp. 191–193, 209). Phosphate is a principal component of both nucleic acids (DNA and RNA) and phospholipids, which are major components of biological membranes. Phosphate is therefore an essential nutrient for activity and growth of all biological organisms.

Phosphate is the predominant phosphorous species in groundwaters, and UZ waters contain low concentrations of phosphate. J-13 water is an analogue to fracture waters in the host rock; using standard methods of analysis for groundwater, the phosphate concentration has been found to be approximately 120 μg/L (DTN LL980711104242.054; see discussion of J-13 water in Section 4.1.5). Phosphate concentration has not been reported for matrix porewater extracted from drillcore. However, when comparing other rock-derived anionic species such as chloride and sulfate in matrix porewaters vs. J-13 water (DTN GS970908312271.003, DTN GS961108312271.002 (TBV-3610), and DTN LL980711104242.054) (TBV-3588), the matrix porewaters are more concentrated. By analogy, the phosphate concentration in matrix porewaters may be greater than in J-13 water.

Experimental studies have shown that under saturated conditions, when Yucca Mountain tuff is used as a source of microbial inoculum and incubated in synthetic Yucca Mountain groundwater,

microorganisms mobilize the phosphate contained in the tuff to support growth to densities of at least 10^6 bacteria per milliliter of water (Horn et al. 1999b, p. 565; McCright et al. 1998, pp. 191–193, 209). When synthetic groundwater is amended with exogenously added phosphate, bacterial densities increase well beyond 10^6 to 10^7 bacteria per milliliter (Horn et al. 1999b, p. 565; McCright et al. 1998, pp. 191–193, 209). Thus, it is likely that any EBS material that contains biologically labile phosphate will stimulate microbial growth beyond bacterial densities that are achieved with tuff only (other environmental conditions permitting).

It is important to note that phosphate is cycled in microbial communities. This means that the same phosphate mass inventory can continue to sustain the activity of a microbial population even as the abundance of other nutrients fluctuates and despite the fact that individual organisms undergo birth and death. The total population of organisms is limited by the total availability of phosphate, but a continuous supply is not required to sustain metabolic activity. For limiting microbial activity on the waste-package surface, this fact essentially lowers the threshold for allowable phosphate transport to the waste package, relative to species that are primarily consumed by metabolic activity such as energy sources.

Investigation of phosphate limitation for Yucca Mountain organisms has focused exclusively on those types that degrade organic carbon (as a carbon source) and utilize oxygen (as a terminal electron acceptor). Investigations in progress are examining the growth of Yucca Mountain anaerobes (which use alternative electron acceptors such as sulfate) and are capable of using CO_2 as a carbon source for growth. It is expected that these organisms will also be phosphate-limited because phosphate is utilized by all biological organisms, and concentrations of phosphate in Yucca Mountain groundwater are relatively low.

Other "macronutrients" (those used at high levels)—carbon, sulfur, and nitrogen—were not found to limit, in synthetic J-13 water, the support of growth to levels of 10^9 cells per milliliter (McCright et al. 1998, pp. 191–193, 209).

Carbon Source

The cited investigations using Yucca Mountain tuff have examined only the growth of aerobic carbon-degrading organisms. These include organisms capable of obtaining carbon from the CO_2 in air or equivalently from dissolved inorganic carbon. This selection is justified because there are no significant natural sources of organic carbon in the host rock nor sources of organic carbon in the EBS (Assumption 5.4.1, Assumption 5.4.2, and Assumption 5.4.3).

Like phosphate, the carbon contained in biomass is cycled in microbial communities; thus, organic carbon may become available for supporting increasingly diverse types of organisms once a microbial community becomes established. Based on information presented in this discussion and because of the availability of CO_2 in the gas phase, it is currently unfeasible to show that a carbon source is limiting for any type of microbial activity for any location in the potential repository where conditions favor growth of carbon-reducing bacteria.

6.4.2.3 Energy Sources

Bacteria generally extract energy from the environment by mediating thermodynamically favored oxidation-reduction reactions. As part of a subsistence strategy, the organisms may alter

their environment, and the alteration often has the effect of promoting solubilization of reactants. This is one important basis for microbially induced corrosion (MIC) in which bacteria on metal surfaces change the local environment.

Energy sources for bacteria exist in the host rock, as is evident from the existing population of viable organisms. The host rock contains reduced iron, manganese, and traces of other redox-sensitive metals (Broxton et al. 1989, Tables 3 and 4) that can act as electron donors. For potential electron acceptors, the environment has abundant oxygen in the gas phase, and UZ waters contain available sulfate and nitrate.

The repository environment will therefore be associated with a some level of microbial activity after return of moisture during cooldown. If the potential repository is constructed without adding electron donors or acceptors other than those already qualitatively present in the host rock, the types of energy sources will not change. The changes that will occur include the distribution of water, the effects of heat, the composition of the aqueous phase, and the relative amounts and spatial distribution of potential nutrients represented by introduced materials. These changes may constitute a significant perturbation of the environment for microbial growth and activity. The overall rate of microbial activity, and the balance between different energy sources used, may vary from background conditions (pre–waste-emplacement and/or far-field) depending on the concentration and distribution of introduced materials. It is important to note that the microbial population in the host rock may be capable of alternative exploitation strategies if environmental and nutrient conditions are substantially modified. For example, other classes of organisms that are present in the host rock, particularly sulfate-reducing forms, are under investigation. Also, the in situ population will be augmented by exogenous organisms during construction and operation. The combined types must be considered capable of metabolizing any energy sources present in the repository.

6.4.3 Conceptual Models for Microbially Induced Corrosion of Corrosion-Resistant Materials

MIC can be important to waste isolation without significantly altering the bulk chemical environment. The hallmark of MIC is the establishment of a biofilm or accretion of a consortium of bacteria on a metal surface. Concentrations of various chemical species are greater within the biofilm than in the bulk environment. The effects of collective microbial activity in the biofilm are localized and impinge directly on the metal surface and on the immediate surrounding areas.

As energy sources, the CRMs are electron donors similar to steel, but are less available for biological use because of their greater resistance to attack. Also, some alloy components are spontaneously and abiotically oxidized in aerobic environments, thus forming products with low solubility and minimal availability to microorganisms. For example, the chromium in A-22 can be solubilized to Cr(II), but it then oxidizes abiotically to Cr(III), which then precipitates as Cr-oxide or Cr-hydroxide at near-neutral pH. The precipitated phases have low solubility and minimal availability to microorganisms. Of the alloying elements contained in the CRMs, manganese, iron, and sulfur are the components most potentially labile and likely to be used as energy sources.

6.4.4 Conceptual Models for Potential Interaction of Yucca Mountain Bacteria with Engineered Barrier System Materials

The following discussion is included as background information and shows that under certain environmental conditions, microbial activity can degrade the materials present in the EBS. These potential interactions are limited by factors discussed previously: elevated temperature, limited water availability, and nutrient limitation. The discussion in the following sections is summarized in Table 40. The table also indicates, for each potential interaction in which EBS materials could be affected, possible causes and the priority for consideration in ongoing laboratory investigation of microbial effects.

Table 40. Summary of Potential Microbial Interactions with EBS Materials, Possible Causes, and Priority for Inclusion in a Model of Microbial Effects

EBS Material	Potential Interaction	Possible Causes	Priority	Information Source	Comments
Carbon steel	Cathodic corrosion	Carbon-reducing bacteria	High	YMP testing	Can use inorganic carbon as C source; produces acids, solubilizes Fe, Mn; ferric precipitates
		Sulfate-reducing bacteria	High	YMP testing	May couple with sulfur-oxidizing bacteria and produce corrosive sulfides
		Iron-oxidizing bacteria	High	YMP testing	May produce protons, hydrogen, $FeCl_3$, and biogenic mineral acids
		Sulfur-oxidizing bacteria	Low	YMP testing	Produces biogenic acids and hydrogen; may couple with sulfate-reducing bacteria
Host rock	Source of aqueous phosphate	Yucca Mountain bacteria	High	YMP testing	Also a source of solubilized Fe, Mn, Al, Ca, Mg, Na, K, and Si
		Sulfur-oxidizing bacteria	Low	YMP testing	Release phosphate probably associated with biogenic acids
Dolomite and limestone	Dissolution	Biogenic acids	Low	Literature	
	Precipitation	$CaSO_4$ decomposition; methanogenesis	Low	Literature	Methanogenesis requires anoxic conditions
Cement	Dissolution	Sulfur-oxidizing bacteria; nitrifying bacteria; fungi	Low	Literature	May couple with sulfate-reducing or denitrifying bacteria
Quartz-sand backfill	Dissolution	Biogenic acids; exopolysaccharides	Low	Literature	Unknown metabolic advantage at the expense of synthesized chelates

6.4.4.1 Carbon Steel

Historically, MIC of metals was attributed to a single class of organisms: the sulfate-reducing bacteria (SRB). These microbes carry out an anoxic (anaerobic) metabolism whereby sulfate is a terminal electron acceptor instead of oxygen. Sulfide is produced and can occur as H_2S. Metal corrosion occurs in part because hydrogen is used as an electron source for sulfate reduction. Stripping of hydrogen from metal surfaces decreases cathode polarization and accelerates corrosion. Additionally, FeS can be produced as the product of sulfides reacting with ferrous ions and can be corrosive.

Currently, MIC is recognized as a group of interacting processes carried out by multiple classes of bacteria (as reviewed by Borenstein 1994, pp. 4–5, and Little et al. 1991, pp. 256–259). Bacteria that secrete exopolysaccharides (EPS) into the extracellular environment form slime capsules that obstruct free diffusion of oxygen to the metal surface, thus creating a reducing environment. This condition is accentuated by aerobes within the slime layer that consume oxygen. The creation of anoxic regions within the slime layer facilitates the growth of anaerobic sulfate reducers. Differential oxygen gradients within the slime film contribute further toward the creation of anodes, which is where metal dissolution occurs. The acidic end products of fermentation, another anaerobic metabolic process, also can contribute to metal attack. In the aerobic regions of the film, iron and sulfur oxidizers may oxidize dissolved metal components and generate mineral acids. These conditions degrade the protective metal oxide film and produce pitting. These processes require the formation of biofilms and sufficient water availability to prevent desiccation.

Electrochemical studies have shown that, for the experimental conditions employed, Yucca Mountain bacteria can increase corrosion rates of carbon steel alloy C1020 by a factor of six to seven (Horn et al. 1998b, pp. 3–4; Lian et al. 1999, pp. 3, 12; Horn 1999). Electrochemical studies may have produced lower-bound corrosion rates; thus, a tenfold increase is assumed for this model (Assumption 5.4.5) (Horn 1999). This may be a lower-bound rate estimate because the test cells employed probably became anaerobic during the five-month duration of the test and because the bacterial growth medium employed was not replenished.

Continual-flow (i.e., replenished) experiments using synthetic J-13 groundwaters and nonsterile Yucca Mountain tuff were also conducted. Chemical analyses of the surfaces of corroded carbon steel alloy C1020 coupons showed accretion of calcite, greenalite (a reduced-iron silicate oxyhydroxide), rancieite (a calcium-manganese oxide), and an unidentified iron-silicate phase. A particulate phase detached from the coupons during the tests and contained the Fe(III) oxyhydroxide iron phases lepidocrocite and goethite as well as smectite silicates, cristobalite, and feldspars. These particles consisted of spalled corrosion products and tuff fines as well as precipitated minerals from the aqueous phase. Both solubilized iron and manganese were found in the aqueous phase, and the concentrations were greater than in the absence of C1020 steel. Manganese concentrations rose to 0.700 ppm in the presence of C1020 and to 0.540 ppm in its absence; iron concentrations increased to 0.700 ppm when C1020 was present but only to 0.030 ppm or less in its absence (Horn et al. 1999a, pp. 4, 11). In ongoing work, these results are being compared to identical systems containing sterilized tuff (i.e., not containing Yucca Mountain or other bacteria) to determine the contribution of microbial activity to these results.

Other Potential Corrosion Mechanisms

Iron-oxidizing bacteria use ferrous iron as an electron source and generate ferric iron, which precipitates as an oxide. Other organisms are also capable of oxidizing manganese, a component of carbon steel. Metal cations react with water to generate protons, resulting in decreased pH. Colonies of organisms can create anoxic conditions and anodic and cathodic regions, as described previously. Additionally, ferric cations attract and combine with free chloride anions and produce ferric chloride, which is aggressive toward metal surfaces (Borenstein 1994, pp. 27-31; Lian et al. 1999, pp. 5–6, 10).

Many microorganisms secrete organic and inorganic acid metabolites. Oxidizing acids (such as sulfuric acid produced by sulfur-oxidizing bacteria) are directly corrosive and disrupt surface-passivating oxide films. The presence of acids also contributes to hydrogen generation for consumption by sulfate reducers and can dissolve protective calcium scale.

Bacteria may promote hydrogen embrittlement of metals by direct production of hydrogen, by generation of protons that can be reduced to hydrogen at cathodic sites, and by production of hydrogen sulfide, which promotes the adsorption of hydrogen into metal matrices.

Not all of these microbial processes occur in every instance of MIC. Rather, each of the different types of microbes contributes different corrosive properties and can occur in various combinations, depending on the nature of the metal surface and environmental conditions. For example, MIC failures of carbon steel are most often associated with acid production and sulfate reduction (Little and Wagner 1997, pp. 40–44).

6.4.4.2 Host Rock

As discussed previously, tuff can serve as a source of phosphate for growth of Yucca Mountain organisms. Microbial growth was observed in response to increased water availability, and the phosphate needed for growth must have been mobilized from Topopah Spring welded host rock, which contains approximately 0.007 percent phosphate (Broxton et al. 1989, Table 3, 0.01 percent P_2O_5 in Topopah Spring rhyolite). Addition of exogenous phosphate further increased growth, resulting in greater cell densities.

Also, manganese has been shown to solubilize from Yucca Mountain tuff in the presence of Yucca Mountain microorganisms, while iron contained in tuff is not mobilized to the same extent (Horn et al. 1999a, pp. 4, 11). Further, these results show that silicon and calcium are also solubilized from tuff when bacteria are present because these elements are found in precipitates observed as mineral phases associated with corrosion products. It is also evident that aluminum, magnesium, sodium, and potassium are solubilized from tuff because these are present in the particulate fraction from these tests (Horn et al. 1999a, pp. 4–7). In ongoing work, these results are being compared to identical systems containing sterilized tuff (i.e., not containing Yucca Mountain or other bacteria) to distinguish the effects that are attributable to microbial activity.

Microbial dissolution of phosphate from rock is directly related to acidity (He et al. 1997, pp. 329–331). Ghani and coworkers (1994, pp. 127–130) reported release of phosphate from rock by a species of sulfur-oxidizing bacteria and attributed observations to biogenic acid production.

6.4.4.3 Dolomite and Limestone

The primary effect of bacteria on carbonate minerals is dissolution by biogenic acids. Bacterial processes may lead to production of carbonates, by means of SRB, through utilization of sulfate contained in gypsum ($CaSO_4$) and other sulfate-containing minerals. Conversion of dissolved carbonate by methane-producing bacteria may also lead to carbonate precipitation.

It has been reported that carbon-reducing organisms, which are present in the host rock and may be active in the potential repository, can produce carbonate precipitates by possibly unknown mechanisms (Fenchel and Blackburn 1979, pp. 98–99). Calcite crystals were observed on the surface of exposed C1020 coupons incubated in the presence of synthetic J-13 water and Yucca Mountain tuff. The contribution of bacteria to this process will be established when sterile control experiments are analyzed (Horn et al. 1999a, pp. 4–7).

6.4.4.4 Cement

A number of types of microorganisms are capable of degrading cementitious materials by producing acids that leach calcium and other alkaline binding agents. Such organisms are known to degrade sewer lines and surface concrete structures. In environments where reduced sulfur compounds are present (e.g., sewers), the production of sulfuric acid by sulfur-oxidizing bacteria causes extensive cement degradation. Sulfur-oxidizing bacteria have been found in every sample of Yucca Mountain tuff tested for their presence (Horn et al. 1998a, p. 4). In environments where reduced sulfur compounds have limited abundance (e.g., at the ground surface) nitric-acid–producing bacteria have been found to play a role in cement degradation (Diercks et al. 1991, p. 515). Reduced sulfur compounds and reduced nitrogen compounds both can concentrate in slime layers in biofilms. Concrete can also be corroded by organic acids produced by fermentative bacteria under reducing conditions (Sand and Bock 1991, pp. 175–181). Fungi have also been implicated in these processes and are present in Yucca Mountain tuff (Perfettini et al. 1991, pp. 528–529; McCright et al. 1998, pp. 194–195).

6.4.4.5 Quartz Sand

Bacteria and fungi can have a role in cycling of silica in the geosphere. Biomobilization of silica occurs through a number of different mechanisms, as reviewed by Ehrlich (1996, pp. 226–232). Dissolution of quartz by biogenic acids has been reported, a situation whereby microbial colonization of quartzose rock in a polluted aquifer resulted in etching of the mineral phase (Hiebert and Bennett 1992, pp. 279–281). Silicate minerals containing polyvalent cations such as aluminum or calcium are solubilized by biogenic production of organic acids, which chelate the mineral cation component and thereby release soluble silica.

Microbially produced EPS can have a role in silicon release from quartz. Such charged polymeric sugars apparently react with siloxanes to produce organo-siloxanes (; Heinen and Lauwers 1988, p. 146). Because it occurs even in EPS extracts from which cells have been removed, the reaction is not enzymatically mediated, which lends support to the direct reaction of siloxanes with EPS.

6.4.5 Threshold-Modeling Approach Based on Growth-Limiting Factors

This approach uses available data defining limiting factors to growth. Limiting factors determine the timing of bacterial activity when bulk environmental conditions permit growth and metabolic activity. This approach takes advantage of TH Model results and makes possible superposition of other factors such as radiation dose.

Microbiologists commonly use the term "water activity" (a_w) to describe microbial water relationships in complex environments. It is an index of water availability for use by organisms and encompasses osmolality, adsorption, and capillarity. The a_w for dilute free water is defined as unity; solute and solid surface interactions lower a_w to some fraction (Potts 1994, pp. 757-758). The a_w has also been defined as the ratio of the vapor pressure of a solution to that of pure water at a given temperature, which is equivalent to relative humidity (Stotzky and Pramer 1973, pp. 64–65).

Most bacteria require $a_w > 0.9$ for active metabolism; a specialized group of salt-tolerant bacteria (halophiles) can remain active at a_w values of 0.75 or less. Fungi are generally more tolerant of desiccation and remain active to a_w as low as 0.55 (Brown 1976, pp. 806–807). These values define bounding values for the relative humidity, and thus the time, at which microbial activity in the potential repository can resume during cooldown. The principle applies to geologic materials such as backfill. Water activity tends to be uniform in the EBS because of liquid- and gas-phase migration of water in air and porous media; thus, isolated pockets of high water activity are not likely to occur.

Water-activity, temperature, and radiation-dose conditions can be combined to formulate limits for microbial activity. Published results based on extreme behaviors of known organisms can be used as a guide for establishing limits where site-specific data are unavailable. More precise estimates based on comprehensive characterization of organisms at Yucca Mountain are unwarranted because of uncertainty about which types of organisms will be present during the postclosure period and because of the potential for biological adaptation in response to environmental stresses.

The threshold model for microbial growth and activity on the waste package surface is described as follows.

6.4.5.1 Threshold Conditions for Microbially Induced Corrosion of the Waste Package

- Growth and activity are nil until the waste-package surface temperature drops to less than 120°C for all environmental conditions.

- Growth and activity on the waste-package surface are nil, even after RH increases above 90 percent, as long as the following conditions apply (Assumption 5.4.4):

  Water has not leaked through the drip shield onto the waste package.

  The waste package has not directly contacted the backfill, invert, or corrosion products of steel ground support during the postclosure period, nor are there sufficient tuff particulates on the waste package to support growth.

- If water leaks onto the waste package during the thermal period before the relative humidity has returned to 90 percent, microbial growth and activity are nil as long as the time-averaged relative humidity is less than the threshold at which aqueous conditions occur in the presence of evaporated salts.

6.4.5.2 Threshold Conditions for Microbially Induced Corrosion of the Drip Shield

- Growth and activity are nil until the drip-shield surface temperature drops to less than 120°C for all environmental conditions.

- For water contacting the drip shield during the thermal period before the relative humidity has returned to 90 percent, microbial growth and activity are nil as long as the time-averaged relative humidity is less than the threshold at which aqueous conditions occur in the presence of evaporated salts.

Biofilms are complex consortia of organisms that form on a solid substrate. Biofilm formation has been closely associated with microbially influenced corrosion of metals (Little et al. 1991, pp. 235–255). Experimental investigation would be needed to determine the minimum relative humidity that supports formation of biofilms on candidate waste-package materials, for humidity conditions (Assumption 5.4.4).

6.4.6 Effects of Microbial Activity on the Bulk Physical and Chemical Environment

The foregoing discussion has shown that microbial growth and activity will return to the EBS when environmental conditions permit. The rate of that activity will determine the overall magnitude of the potential effects on the bulk chemical environment. The principal effects will consist of the following:

Interaction with Quartz Sand–The specific surface area of quartz-sand backfill may be large relative to accessible quartz surfaces in the host rock, and conditions may be warm and moist at times during the repository evolution, which could be favorable to microbial growth. However, silica polymorphs are common in the host rock, which is 75 to 77 percent SiO_2 (Broxton et al. 1989, p. 5973), yet there has been no reported interpretation of silica interaction with microbes in situ from mineral textures, aqueous silica concentration, or the presence of complexing agents for Si. By themselves, silica polymorphs, including quartz, do not offer an energy source nor the chemical constituents needed for growth. Accordingly, it is unlikely that the rate of microbial interaction with quartz would be sufficient to alter the bulk chemical environment.

Interaction with Crushed Tuff–The crushed tuff that will be used as invert ballast material will differ from the local host rock only with regard to comminution and the source of the rock within the repository excavation. Prior to use in the invert, the crushed tuff will be treated to limit surface-derived organic contamination (Assumption 5.4.2). Broken surfaces may expose grains of minerals bearing biologically important constituents while increasing access to water. However, extensive laboratory testing experience with crushed tuff has shown that microbial growth is limited even when tests are liquid-saturated (without carbon or phosphate augmentation).

Microbially Induced Corrosion of CRMs—MIC will oxidize metallic barriers and likely consume oxygen as an energy source while obtaining carbon from an inorganic source such as dissolved or gaseous CO_2. Sulfur reduction, with associated oxidation and possible production of H_2S and mineral acids, may occur. The rates of these processes will be negligible because of inherent resistance of CRMs to microbial attack and because of slow rates of corrosion.

Microbially Mediated Corrosion of Structural Steel—The corrosion rate for steel ground support and invert support steel may be greater because of MIC and is the only potentially significant effect of microbial activity on the bulk chemical environment. Steel corrosion will consume oxygen and lower the O_2 fugacity in the drift environment. As a sensitivity study reported in Section 6.7 of this report, abiotic measured rates for corrosion of steel are multiplied by a factor of 6 to represent accelerated corrosion from MIC (Assumption 5.4.5 and Table 17).

6.4.7 Microbial Effects Model Validation

The Microbial Effects threshold model is based on information from the literature, describing the environmental conditions for which microbial growth and activity are observed. The model is bounding in the sense that extreme microbial observations (e.g. halophiles and hyperthermophiles) are included, but these types of organisms will not necessarily be important in the potential repository. The basic threshold conditions for growth and activity are relative humidity (> 90 percent, or lower if halophiles are active) and temperature (< 120°C). No distinction is made between environmental conditions necessary for microbial activity, and for biofilm development, which is conservative. Use of these conditions constitutes a valid model that is based on accepted information.

6.4.8 Summary

Investigations over the past 10 yr at Yucca Mountain and elsewhere have demonstrated that bacteria and fungi are important components of what was previously regarded as abiotic chemistry of deep subsurface environments. Bacteria are present in the host rock at Yucca Mountain, and laboratory testing has shown that when moisture and tuff or other sources of nutrients are available, these bacteria can produce MIC of carbon steel and waste-package materials.

Microbial growth and activity in the host rock are limited by the availability of water and nutrients such as phosphate. Dryout of the EBS during the repository thermal period will further limit water, arresting microbial growth and activity. The threshold model addresses the time until the return of microbial growth and activity based on environmental factors. Observations of temperature dependence reported in the published literature show that no microbial activity will occur at temperatures greater than 120°C in aqueous environments. Reported dependence on humidity shows that growth and activity do not generally occur at less than approximately 90% relative humidity. When salts are present, the threshold humidity will decrease, depending on the deliquescence behavior of the salts.

In principle, bacteria are capable of degrading all EBS materials. The primary electron donors in the EBS will be metals (such as steel) or metal ions in reduced form (such as the ferrous ion).

The primary electron acceptors will be sulfate, nitrate, and gas-phase oxygen. The backfill will consist of clean, washed quartz sand, which is not an energy source.

No microbial growth or activity will occur in the EBS where the temperature exceeds 120°C. Below a humidity threshold of approximately 90%, or less in the presence of salts, MIC is not expected to occur. EBS water-diversion features (including the drip shield) will protect the waste package during the thermal period and beyond. No salts or necessary nutrients such as phosphate will be deposited on the waste package as long as the drip shield is intact and functions as intended. Unless there is sufficient tuff dust on the package, even if relative humidity is greater than 90% under the drip shield, MIC of the waste package may be negligible until drip-shield failure occurs. If liquid water penetrates the drip shield, or the waste package comes into direct contact with backfill or invert materials, MIC of the waste package can occur.

The Microbial Effects Model is used to develop a set of threshold conditions for microbial growth and activity, based on information from the literature, describing the environmental conditions for which microbial growth and activity are observed. The model is bounding in the sense that extreme microbial observations (e.g. halophiles and hyperthermophiles) are included, but these types of organisms will not necessarily be important in the potential repository. No distinction is made between environmental conditions necessary for microbial activity, and for biofilm development, which is conservative. Use of these conditions constitutes a valid model that is based on accepted information. In general, it is shown that the model has an appropriate level of confidence suitable for its intended use.

6.5 NORMATIVE PRECIPITATES AND SALTS MODEL

Water that enters the drift during the thermal period (as seepage or unsaturated flow) will tend to evaporate, leading to increased solution concentration and eventually complete dryness. As solution ionic strength exceeds approximately 1 molal, extended Debye-Huckel theory for solute activity at elevated temperature does not apply (Wolery and Daveler 1992; pp. 25-26). Rather than rely on the Pitzer approach for activity modeling, which has data support for a limited variety of chemical species at 25°C only, this model presents an alternative approach based on experimental observations. Given water composition that is close to chemical equilibrium with Topopah Spring tuff, a "normative" set of mineral precipitates is developed that represents the products of evaporating the water to dryness. In the Chemical Reference Model, for zones and time periods in which evaporation in the EBS is complete or nearly so, the mineral precipitate and salt species that form are predicted using the insights that underlie the normative approach.

6.5.1 Conceptual Model

The chemical composition of waters that could contact the drip shield or waste package is an important factor in assessing corrosion rates. The composition of such waters is dominated by interaction with precipitates formed by previous evaporation. For example, for corrosion modeling, if chloride and sulfate salts form because of evaporation, the water composition during evaporation and during redissolution of those salts during cooldown will be a saturated brine; if carbonate or hydroxide precipitates form instead, the different chemical conditions will prevail. Of particular interest, therefore, is the nature of salts that precipitate.

6.5.2 Evaporation Tests with Synthetic J-13 Water and Synthetic Porewater

Laboratory batch tests were conducted at Lawrence Livermore National Laboratory in 1998 and 1999 (DTN LL991008004241.041 and DTN LL991008104241.042). In the first two tests, 30 L of synthetic J-13 well water was evaporated down to 30 mL, resulting in an evaporative concentration factor of approximately 1000×. In all tests, the actual concentration factors were estimated by total mass measurements and are accurate to approximately 10%. Synthetic J-13 water was pumped into a 1-L Pyrex™ beaker at a constant rate using a peristaltic pump while the sample evaporated at 85°C; a hot plate was used as the heat source. The fluid-delivery rate and heat flux were balanced to maintain constant temperature in the fluid contained within the beaker.

The tests were performed at sub-boiling conditions to represent evaporation of slowly migrating waters in the EBS, such as would occur in an engineered backfill material with porous medium characteristics. The 85°C temperature is similar to predicted conditions for inflow to the potential repository during the thermal period, should it occur, while maintaining subboiling conditions for the test. The assemblage of mineral phases resulting from the evaporation is controlled predominantly by precipitation kinetics at these temperatures, and it is thought that the assemblages observed are representative of repository conditions.

In the first test (evap1), detailed chemical analysis was performed on the initial starting water composition and on a sample collected after approximately 1000× concentration. A small split of the solids that had precipitated at the 1000× stage (not yet dry) was collected for mineralogic analysis. The solution was then evaporated to complete dryness, and another small split of the solids was collected. The remaining solids were then rewet with 200 mL of deionized water and evaporatively concentrated to 100 mL at 75°C; the resulting solution was collected for detailed water-chemistry analysis. The rewetting step was incorporated to evaluate the reproducibility of precipitate formation at supersaturated conditions. Three water compositions (including the initial solution) and two solid samples were analyzed for this test.

In a second test (evap2), the protocol was the same as for the first test except that the beaker contained 10 g of crushed Topopah Spring welded tuff (Yucca Mountain Site Characterization Project Sample Management Facility Specimen ID #00521699). The tuff was prepared by sieving the original material (<2 mm grain size) to >0.5 mm to remove the fine fraction. The sized material was washed three times in isopropanol. The grains were allowed to settle, before decanting, to remove adhering fine particles and were then allowed to air dry. The test was taken to complete dryness, and a rewetting step was incorporated as described previously. Three water compositions (including the initial solution) and two solid samples were analyzed for this test.

The pH of the rewet samples for both the evap1 and evap2 tests was measured. A third test (evap4) was conducted to further investigate the evolution of pH during a relatively short-term evaporative concentration to approximately 100×. The initial and final solutions were sampled for complete chemical analysis. Note that in this experiment, two data sets were combined: one from a four-day run with pH measured at time intervals of approximately 2 hr, and another from a run lasting only 3 hr with pH measured at intervals of approximately 20 minutes. In the description of results that follows, the two runs are combined in order of concentration factor and

presented as one test. The same starting solution composition was used for both tests. The results of these tests (evap1, evap2, and evap4) are summarized in Table 41 through Table 47.

Table 41. Evolution of Water Composition in Test with Synthetic J-13 Water (evap1)

Species (mg/kg)	Synthetic J-13 (mg/kg)	Species Conc. (mg/kg) w/ Evap. Factor: 956× [A]	Concentration Ratio	Rewet [B] (mg/kg)	Concentration Ratio
Ca	6.4	29.86	4.7	3.48	0.54
Cl^-	6.9	4,835	701	1,773	257
F^-	2.2	1,550	705	530	241
HCO_3^-	108	24,878	231	9,539	88.3
K	5.3	4,792	904	1,364	257
Mg	2.2	0.14	0.06	0.09	0.04
Na	46	44,082	958	12,512	272
NO_3^-	8.0	5,532	694	2,016	252
SO_4^{2-}	18.1	12,926	714	4,631	256
SiO_2(aq)	11.3	18,008	1,594 [C]	3,606	319
pH	7.84	[D]		10.59	

DTN: LL991008104241.042

NOTES:
- A 30 L of synthetic J-13 well water was evaporated to 30 mL, resulting in a concentration factor of approximately 1000×.
- B After evaporation to complete dryness, the solids were rewet with 200 mL of deionized water and evaporatively concentrated to 100 mL.
- C The apparent concentration ratio for SiO_2 is greater than that estimated from total mass measurements and the concentration ratios for other ions, possibly because of analytical errors associated with the high ionic strength.
- D Not analyzed

Table 42. Evolution of Water Composition in Test with Synthetic J-13 Water and Tuff (evap2)

Species (mg/kg)	Avg. Synthetic J-13 (mg/kg)	Species Conc. (mg/kg) w/ Evap. Factor: 1114x [A]	Concentration Ratio	Rewet [B] (mg/kg)	Concentration Ratio
Ca	5.6	6.9	1.2	3	0.5
Cl^-	7.2	6123	850	2,349	326
F^-	2.2	1,522	691	605	275
HCO_3^-	104	31,434	303	13,434	129
K	5.3	3,716	702	1,553	292
Mg	2.1	< 0.28	C	< 0.08	C
Na	44.3	37,713	851	14,520	327
NO_3^-	7.8	6,729	863	2,598	333
SO_4^{2-}	18.3	15,711	858	6,138	336
SiO_2(aq)	9.4	7,118	758	2,691	287
pH	8.03	C		9.99	

DTN: LL991008104241.042

NOTES: A 30 L of synthetic J-13 well water was evaporated to 30 ml, resulting in a concentration factor of approximately 1000x.

B After evaporation to complete dryness, the solids were rewet with 200 mL of deionized water and evaporatively concentrated to 100 mL.

C Not analyzed

Table 43. Evolution of pH in Short-Term Test with Synthetic J-13 Water (evap4)

Concentration Factor	pH
1.00	8.46
1.00	8.65
1.05	9.04
1.29	9.43
1.60	9.58
2.41	9.67
6.08	9.67
6.37	9.77
7.59	9.79
11.6	9.95
12.6	10.00
15.3	10.03
20.9	10.08
25.2	10.09
34.4	10.12
52.1	10.18
104	10.18
157	10.18

DTN: LL991008104241.042

NOTE: This table represents the combined results of a four-day run with pH measured approximately every 2 hr and a shorter run lasting only 3 hr, during which pH was measured approximately every20 minutes.

Table 44. Evolution of Water Composition in Short-Term Test with Synthetic J-13 Water (evap4)

Species (mg/kg)	Synthetic J-13 (mg/kg)	Species Conc. (mg/kg) w/ Evap. Factor: 157×	Concentration Factor
Ca	6.4	1.2	0.01
Cl^-	6.9	849	113
F^-	2.2	247	103
HCO_3^-	108	4,295	42
K	5.3	560	114
Mg	2.2	0.05	0.57
Na	46	5,298	117
NO_3^-	8.0	1,050	131
SO_4^{2-}	18.1	2,162	114
SiO_2(aq)	11.3	999	100
pH	7.84	10.18	

DTN: LL991008104241.042

Table 45. Mineralogical Results from Test with Synthetic J-13 Water (evap1)

evap1—956×	evap1—Complete Evaporation
SiO_2 (amorphous) aragonite ($CaCO_3$) calcite ($CaCO_3$)	SiO_2 (amorphous) aragonite ($CaCO_3$) calcite($CaCO_3$) halite (NaCl) niter (KNO_3) thermonatrite ($Na_2CO_3{:}H_2O$) gypsum ($CaSO_4{:}2H_2O$) [A] anhydrite ($CaSO_4$) [A] hectorite ($Na_{0.33}Mg_3Si_4O_{10}(F,OH)_2$) [A]

DTN: LL991008104241.042

NOTE: A Species is a minor constituent, and identification is uncertain.

Table 46. Mineralogic Results from Test with Synthetic J-13 Water and Tuff (evap2)

Evap2—1114× [a]	evap2—Complete Evaporation [A]
SiO_2 (amorphous) trona ($Na_3H(CO_3)_2{:}2H_2O$) Thermonatrite ($Na_2CO_3{:}H_2O$) halite (NaCl) calcite ($CaCO_3$) Aragonite ($CaCO_3$) Anhydrite ($CaSO_4$) smectite ($Na_{.3}(Al,Mg)_2Si_4O_{10}(OH)_2$) niter ($KNO_3$)	SiO_2 (amorphous) trona ($Na_3H(CO_3)_2{:}2H_2O$) thermonatrite ($Na_2CO_3{:}H_2O$) halite (NaCl) calcite ($CaCO_3$) aragonite ($CaCO_3$) anhydrite ($CaSO_4$) smectite ($Na_{.3}(Al,Mg)_2Si_4O_{10}(OH)_2$) niter (not detected by XRD)

DTN: LL991008104241.042

NOTE: A Only the minerals produced by evaporation and not present in the starting tuff are reported here. The major minerals constituting the tuff are probably crystobalite (α), K-feldspar, albite, anorthite, and quartz.

Table 47. Mass of Minerals Formed in Tests with Synthetic J-13 Water (evap1 and evap2)

Synthetic J-13 well water (evap1)	5.636 g
Synthetic J-13 well water with tuff (evap2)	6.468 g

DTN: LL991008104241.042

The laboratory batch experiments with SPW conducted at LLNL in 1998 and 1999 were completely analogous to those done with synthetic J-13 well water. An initial test investigated the evaporation of water to dryness (evap3) and a subsequent test added 10 g of Topopah Spring welded tuff (Sample Management Facility Specimen ID #00521699). A third test (evap5) was conducted to investigate the evolution of pH during a relatively short-term evaporative concentration to approximately 100× and was conducted in exactly the manner described previously (evap4). The results of these experiments are summarized in Table 48 through Table 54.

Table 48. Evolution of Water Composition in Test with Synthetic Porewater (evap3)

Species (mg/kg)	SPW (mg/kg)	Species Conc. (mg/kg) w/ Evap. Factor: 1243×	Concentration Ratio	Rewet (mg/kg)	Concentration Ratio
Ca	57.2	15,629	273	6,010	105
Cl–	78.0	53,084	681	19,248	247
F^-	2.30	< 577	B	< 301	B
HCO_3^-	16.2	< 35	B	< 37	B
K	4.20	2,779	661	973	232
Mg	11.7	5,478	470	1,949	167
Na	8.20	5,961	727	2,077	253
NO_3^-	11.0	B	B	2,647	241
SO_4^{2-}	81.7	2,077	25	1,564	19
$SiO_2(aq)$	9.80	513	52	340	35
pH	7.68	6–6.5 [A]		5.56	

DTN: LL991008004241.041

NOTES: A Semiquantitative measurement using pH paper
B Not analyzed or determined

Table 49. Evolution of Water Composition in Test with Synthetic Porewater and Tuff (evap6)

Species (mg/kg)	SPW (mg/kg)	Species Conc. with Evap. Factor: 564x	Concentration Ratio	Rewet	Concentration Ratio
Ca	59.2	12,553	212	10,249	173
Cl^-	76.1	37,198	489	30,359	399
F^-	2.10	< 248	A	< 284	A
HCO_3^-	20.2	< 60	A	< 36	A
K	4.10	2,006	488	1,622	395
Mg	12.0	3,615	300	2,889	240
Na	8.70	4,420	508	3,574	411
NO_3^-	10.5	5,267	501	4,344	413
SO_4^{2-}	85.2	1,316	15.4	1,516	17.8
SiO_2(aq)	11.5	696	60.6	355	30.9
pH	7.52	5.14		5.43	

DTN: LL991008004241.041

NOTE: A Not analyzed

Table 50. pH and Carbonate Evolution from Short-Term Test with Synthetic Porewater (evap5)

Concentration Factor	pH	HCO_3^- (mg/L)
1.00	7.45	24.7
1.06	8.69	A
1.38	9.01	A
1.76	8.99	A
2.31	8.86	A
4.19	8.57	A
6.09	A	20.1
6.36	8.55	A
8.16	8.51	A
8.19	A	19.5
12.0	8.45	19.4
29.9	8.29	14.0

DTN: LL991008004241.041

NOTE: A Not analyzed

Table 51. Evolution of Water Composition in Short-Term Test with Synthetic Porewater (evap5)

Species (mg/kg)	SPW (mg/kg)	Species Conc. (mg/kg) w/ Evap. Factor: 62x	Concentration Ratio
Ca	57.3	1661	29.9
Cl^-	76.6	4202	55.6
F^-	2.2	37.2	17.7
HCO_3^-	20.3	12.1	0.49
K	4.0	248	67.1
Mg	11.8	546	46.6
Na	8.6	490	55.7
NO_3^-	10.7	580	55.3
SO_4^{2-}	83.9	1557	18.4
SiO_2(aq)	22.2	476	48.4
pH	7.55	7.65	

DTN: LL991008004241.041

Table 52. Mineralogical Results from Test with Synthetic Porewater (evap3)

evap3—1243x	evap3—Complete Evaporation
gypsum ($CaSO_4$:$2H_2O$)	gypsum ($CaSO_4$:$2H_2O$) tachyhydrite ($CaMg_2Cl_6O_{10}$:$12H_2O$)

DTN: LL991008004241.041

Table 53. Mineralogic Results from Test with Synthetic Porewater and Tuff (evap5)

evap6—564x	evap6—Complete Evaporation [A]
gypsum ($CaSO_4$:$2H_2O$) halite (NaCl)	gypsum ($CaSO_4$:$2H_2O$) halite (NaCl) Mg-smectite ($Na_{.3}(Al,Mg)_2Si_4O_{10}(OH)_2$) Kenyaite ($NaSi_{11}O_{20.5}(OH)_4$:$3\ H_2O$)[B]

DTN: LL991008004241.041

NOTES: A Only the minerals produced by evaporation and not present in the starting tuff are reported here. The major minerals constituting the tuff are probably crystobalite (α), K-feldspar, albite, anorthite, and quartz.

B Species is a minor constituent and identification is uncertain.

Table 54. Mass of Minerals Formed in Tests with Synthetic Porewater

Synthetic porewater (evap3) [A]	11 g
Synthetic porewater with tuff (evap6) [A]	15 g

DTN: LL991008004241.041

NOTE: A Some of the minerals formed in these experiments were hygroscopic, making it difficult to obtain accurate mass measurements.

6.5.2.1 Collection and Analysis of Aqueous Samples

The aqueous samples for cation and anion analyses were collected in plastic syringes. Aliquots were filtered through a 0.45-µm filter that had been prerinsed with one syringe of deionized water. Aliquots for cation analysis were delivered to a plastic sample vial, further diluted with water, and spiked with a concentrated acid solution. Total dilution was determined and ranged from 10- to 15-fold. Aliquots for anion analysis were collected in a similar manner (i.e., prefiltered and diluted with deionized water) using glass sample vials.

For analysis of total dissolved inorganic carbon (DIC), a small split of each anion sample was injected directly into an infrared CO_2 analyzer in the Geochemistry Laboratory, Building 281, Lawrence Livermore National Laboratory. Speciation of DIC as bicarbonate or carbonate was determined from the measured pH.

The anions fluoride, chloride, nitrate, and sulfate were determined using ion chromatography (IC). The analytical protocol supports detection of several other anion analytes, but these four were the only ones (other than the carbonate species) detected in these solutions. Samples were diluted considerably for this method.

Cation (Na, K, Ca, Mg, and Si) concentrations were determined using inductively coupled plasma (ICP) emission spectrometry. These sample aliquots were also diluted considerably.

The pH measurements were accomplished by sampling the fluid into a plastic syringe and delivering it, at approximately room temperature, gently into a plastic tube containing a calibrated combination pH electrode. (The reported pH data are for ambient temperature; elevated temperature values would be slightly lower because of the temperature effect on H_2O ionization.) The solution pH was determined using a method recommended by the National Bureau of Standards (NBS); this is a reproducible potentiometric measurement using a cell consisting of a glass H^+ electrode and a reference electrode with a liquid junction. The method is best suited for low ionic strength solutions (i.e., solutions with less than 0.1 molal ionic strength), although useful measurement can be made up to ionic strength as great as that of seawater (approximately 0.7 molal). For J-13 water and similar compositions, measurement is limited to less than 200× evaporative concentration. Accordingly, pH measurements for the starting solutions and the evap4 test are accurate, but those made for the rewet samples of the evap1 and evap2 runs are approximate. No attempt was made to measure the pH of the batches concentrated to 1000× or greater.

6.5.2.2 Minerals Present in Solids

Solids samples (tests evap1 and evap2) were dried, weighed, and analyzed using x-ray diffraction (XRD). The purpose of the XRD analysis was to identify the phases produced, and quantification was not attempted.

6.5.3 Test Results for Synthetic J-13 Water

Test results from water composition, pH, and solid-phase observations are summarized in Tables 41 through 47. It is important to note that these results were obtained from an open system (free exchange with gas-phase CO_2) under ambient atmospheric composition conditions. Following are some major findings from these tests:

- Divalent cations (Ca^{2+}, Mg^{2+}) tend to precipitate early in evaporative evolution, both with and without tuff present (evap1 and evap2), from precipitation of carbonate (probably calcite and low-Mg calcite).
- Halite and niter apparently contain the chloride and nitrate from the starting solution. Niter is among the last solids to precipitate.
- Polymorphic phases (e.g., aragonite and calcite; anhydrite and gypsum) indicate that solubility constraints changed substantially during the final stages of evaporation.
- Test results provided no indication of hydroxides (portlandite, NaOH) for evaporation under ambient atmospheric composition conditions.
- The pH of the rewet solution without tuff present (evap1) was 10.59, which probably represents carbonate buffering.
- The measured pH of the rewet solution with tuff present (evap2) was 9.99, compared to pH 10.59 without tuff (evap1), probably from buffering associated with dissolution of SiO_2 and silicates.
- pH is approximately 10 to 11 for concentrated J-13 waters up to approximately 150×, with and without tuff present, under ambient atmospheric conditions (pH value measured at ambient temperature).
- The Si concentration was lower in the concentrated evap2 solutions than in the evap1 solutions, which suggests that the presence of the silicate and aluminosilicate minerals in the tuff enhances precipitation.
- The presence of tuff appears to have little effect on relative concentrations of the anions, except for fluorides; this indicates that fluorite precipitation may be enhanced by increased Ca concentration derived from tuff. (Flourite was not detected, probably because it was a minor species.)

- With tuff present in the ~1000× solution (evap2), the absolute amounts of Na and K are lower relative to the test with no crushed tuff present (evap1), even though the concentration factor is estimated to be greater in this case (1114× vs. 956×).

- The clays found in the 1000× sample were separated and found to be a mixture of dioctohedral smectite (probably montmorillonite) and trioctohedral smectite (hectorite, stevensite, or saponite).

6.5.4 Test Results for Synthetic Porewater

Test results from water composition, pH, and solid-phase observations are summarized in Tables 48 through 54. It is important to note that these results were obtained from an open system (free exchange with gas-phase CO_2) under ambient atmospheric composition conditions. Following are some major findings from these tests:

- Sulfate is the predominant anion; therefore, the effects of carbonate species are substantially less important in the synthetic porewater tests.

- The pH decreases to approximately 5.5 to 6.0, with evaporative evolution of the Ca-sulfate porewater, instead of increasing to pH ~10 as was observed for the J-13 water.

- Larger discrepancies between the concentration factors computed from measured species concentrations and the total mass concentration factor are noted for the porewater tests when compared to the J-13 water tests. For species such as chloride (Table 48), the apparent concentration factor for dissolved species was substantially less than the total mass concentration factor. This probably occurred because the greater dissolved-solids content of the starting porewater solution caused the system to approach or exceed solubility equilibrium during evaporation, so that more precipitates formed, and there was greater potential for suspended, precipitated solids to contribute to the chemical analyses.

Comparison of results from analogous tests using synthetic J-13 and porewater (e.g., Table 41 and Table 48) shows that bicarbonate waters such as J-13 are more sensitive to CO_2 fugacity, particularly during evaporation, and more likely to produce high-pH conditions than are sulfate-type waters such as the synthetic porewater. Selection of J-13 water composition for investigating the EBS chemical environment is therefore bounding with respect to alkaline pH. The J-13 composition is used for the Chemical Reference Model in Section 6.7.

The foregoing conclusion is insensitive to differences between the compositions of synthetic waters, and natural waters, as represented in Table 19 and Table 20. This is because the important aspect of solution composition that determines pH on evaporation, is the proportion of bicarbonate to other anions. The exact proportion of bicarbonate is not critical, if a significant amount of CO_2 is present, and it is the only species controlled by a fixed-fugacity boundary condition.

6.5.5 Normative Concept and Predictive Model

For waters having composition similar to the synthetic J-13 and synthetic porewater, a set of precipitates is identified that is consistent with the observations reported in Table 45 and Table 52 for total evaporation.

Nitrate, Fluoride, and Chloride Salts

The first precipitates treated in the model are the noncarbonate and nonsulfate salts which are most likely to form. For example, nitrate is most likely to precipitate as niter (KNO_3), which is the likely disposition for all nitrate (Table 55). The amount of KNO_3 that forms is determined by the molality of K or NO_3, whichever is smaller. This calculation can be written

$$KNO_3(s) = \min(K, NO_3)$$
$$C_{NO3,remain} = C_{NO3,initial} - C_{KNO3(s)}$$
$$C_{K,remain} = C_{K,initial} - C_{KNO3(s)}$$

(Eq. 37)

where

$C_{KNO3(s)}$	=	Moles of niter precipitated
$C_{NO3,initial}$	=	Initial concentration of nitrate (mol/kg)
$C_{NO3,remain}$	=	Concentration of nitrate remaining in solution (mol/kg)
$C_{K,initial}$	=	Initial concentration of potassium (mol/kg)
$C_{K,remain}$	=	Concentration of potassium remaining in solution (mol/kg)

If there is insufficient potassium to precipitate all the nitrate, sodium is used to form Na-niter ($NaNO_3$). Next, fluorite (CaF_2) is formed from Ca and fluoride, which is reasonable because of its relative insolubility. Any remaining fluoride is precipitated as villiaumite (NaF), which is reasonable because sodium is abundant and NaF is also relatively insoluble. Next, any excess potassium is precipitated as sylvite (KCl); then halite (NaCl) is precipitated, limited by the available sodium or chloride, whichever is less. For J-13 water, these steps will eliminate nitrate, chloride, fluoride, and potassium from the solution. For the synthetic porewater, some chloride may remain as discussed below.

Table 55. Normative Mineral Assemblage Algorithm for Evaporation of Waters Similar to J-13 Under Near-Atmospheric CO_2 Conditions

Minerals in Assemblage	Remarks [a]
Niter (KNO_3)	Use all nitrate or all potassium
Na-niter ($NaNO_3$)	Use all remaining nitrate
Fluorite (CaF_2)	Use all fluoride
Villiaumite (NaF)	Use all remaining fluoride
Sylvite (KCl)	Use all remaining potassium
Halite (NaCl)	Use all sodium or chloride
Mg-smectite ($Mg_{0.165}Al_{2.33}Si_{3.67}O_{10}(OH)_2$)	Use all magnesium or aluminum
Ca-smectite ($Ca_{0.165}Al_{2.33}Si_{3.67}O_{10}(OH)_2$)	Use all calcium or aluminum
Na-smectite ($Na_{0.33}Al_{2.33}Si_{3.67}O_{10}(OH)_2$)	Use all remaining aluminum
Thenardite (Na_2SO_4)	Use all sodium or all sulfate
Anhydrite ($CaSO_4$)	Use all remaining sulfate
Calcite ($CaCO_3$)	Use all remaining calcium (CO_2 is from open-system)
Thermonatrite ($Na_2CO_3{:}H_2O$)	Use all remaining sodium (CO_2 is from open-system)
Amorphous silica (SiO_2)	Use all remaining silica

Clays

The next species considered in the normative approach are smectites (e.g., beidellite compositions). For waters similar to J-13, clays can form in relatively small amounts, limited by the available Al in solution. Mg-smectite, Ca-smectite, and ultimately Na-smectite composition are used as needed to precipitate the Al. The approach does not include precipitates that could accommodate Mg in excess of the Al or instead of Mg-smectite. However, calcite is included in the model, and a low-Mg calcite would be plausible in this case. With an open-system, constant-fugacity condition placed on CO_2, the choice of clay or calcite as the endpoint for a minor amount of Mg is not critical.

Sulfates and Carbonates

Thernardite is then used to precipitate sulfate, although gypsum and anhydrite were suspected or detected in the laboratory tests (Table 45 and Table 46). This selection is based on thermodynamic arguments presented below, which show that:

- Anhydrite ($CaSO_4$) is thermodynamically favored over gypsum ($CaSO_4{:}2H_2O$) for the humidity conditions calculated for the EBS.
- Calcite ($CaCO_3$) is thermodynamically favored over portlandite ($Ca(OH)_2$) for the CO_2 fugacity conditions calculated for the EBS.
- Thenardite (Na_2SO_4) and calcite ($CaCO_3$) are a more stable assemblage than thermonatrite ($Na_2CO_3{:}H_2O$) and anhydrite ($CaSO_4$), therefore thenardite is the more likely sulfate precipitate.

Accordingly, thenardite is used to precipitate all the sulfate. If there is insufficient Na to precipitate all of the sulfate (e.g., as in synthetic porewater), anhydrite could form at the expense of calcite. This could happen sequentially so that anhydrite and thenardite are not in equilibrium. With the open-system, constant-fugacity condition placed on CO_2, the choices of thenardite vs. anhydrite and calcite vs. portlandite have a limited effect on pH during evaporation or redissolution (Assumption 5.5.1).

Next, any remaining chloride is precipitated as tachyhydrite ($CaMg_2Cl_6O_{10}{\cdot}12H_2O$), which was observed in the laboratory tests with synthetic porewater. Calcite is then used to precipitate the remaining Ca, and thermonatrite is used to precipitate the remaining Na. Any remaining magnesium is precipitated as either Mg-calcite or dolomite, which are represented stoichiometrically by magnesite ($MgCO_3$).

Silica

The final species to precipitate is amorphous silica (SiO_2), which was detected in all of the laboratory samples derived from the synthetic J-13 water (Table 45 and Table 46). Amorphous silica is used to precipitate all the remaining silica, leaving only trace species and minor amounts of major species, all of which have limited influence on bulk chemical conditions.

The normative approach described in Table 55 and Equation 37 is implemented in two spreadsheet software routines that are used to calculate the amounts of precipitates that form where evaporation is complete, or nearly so, as determined from thermal-hydrology calculations:

- "Zone3-4_L4C4_ui_hiCO2_normativeV1.2.xls" describes precipitation of a normative mineral assemblage in the backfill over the drip shield, during the time interval 300 to 700 yr, for the L4C4 location with the "upper" infiltration distribution.
- "Zone5-6_L4C4_ui_hiCO2_normativeV1.2.xls" describes precipitation of a normative mineral assemblage in the lower backfill and invert, during the time interval 700 to 1500 yr, for the L4C4 location with the "upper" infiltration distribution.

The routines are used in conjunction with thermal-chemical modeling code EQ3/6, for the Chemical Reference Model (Section 6.7).

6.5.6 Supporting Discussion of Mineral Assemblage Stability

Mineral stability is evaluated using reaction equations that relate alternative species or assemblages. For reactions involving H_2O or CO_2, equilibrium between alternatives (i.e., between both sides of the equation) implies fugacity values. These can be compared with independent information about the EBS environment to infer whether equilibrium can exist or, if not, which alternative is more plausible. This approach is not exhaustive but can be used to compare specified alternatives.

Anhydrite vs. Gypsum

Equilibrium between anhydrite and gypsum involves water of hydration and can be written as follows:

$$CaSO_4 : 2H_2O = CaSO_4(s) + 2H_2O(g)$$

(Eq. 38)

where (s) and (g) signify solid minerals and gas (or vapor), respectively. This can be rewritten in terms of the constituent reactions

$$CaSO_4 : 2H_2O(s) = Ca^{2+}(aq) + SO_4^{2-}(aq) + 2H_2O(aq) \quad \log K_{gypsum,100°C} = -4.9034$$

(Eq. 39)

$$CaSO_4(s) = Ca^{2+}(aq) + SO_4^{2-}(aq) \quad \log K_{anhydrite,100°C} = -5.3851$$

(Eq. 40)

where (aq) denotes dissolved aqueous species, and log K is the base 10 logarithm of the equilibrium constant for the reaction (subscripts indicate 100°C). Log equilibrium constant values used in this discussion are taken directly from the file "data0.com.R2" supplied with EQ3/6 V7.2b. For example, the equilibrium constant for Equation 39 is

$$K_{gypsum-anhydrite,100°C} = \frac{CaSO_4(s)(H_2O)^2}{CaSO_4 : 2H_2O(s)} = (H_2O)^2$$

(Eq. 41)

Expressions in parentheses are chemical activities, and the activities for the $CaSO_4{:}2H_2O$ and $CaSO_4$ solids are defined as unity. Reversing Equation 40 and adding to Equation 40 yields Equation 39, with equilibrium constant

$$\log K_{gypsum-anhydrite,100°C} = \log K_{gypsum,100°C} - \log K_{anhydrite,100°C} = 4.9034 + 5.3851 = 0.4817$$

(Eq. 42)

$$H_2O = 10^{0.4817/2} = 1.7412 \text{ atm}$$

(Eq. 43)

For gypsum and anhydrite to exist in equilibrium requires water vapor pressure of 1.741 atm, and, at 100°C, anhydrite is more stable than gypsum at lower pressures. At 60°C, the log K values yield

$$\log K_{gypsum,60°C} = -4.6093$$

(Eq. 44)

$$\log K_{anhydrite,60°C} = -5.7587$$

(Eq. 45)

$$H_2O = 10^{0.1494/2} = 1.188\,\text{atm}$$

(Eq. 46)

which confirms that anhydrite is favored at elevated temperatures less than boiling.

Calcite vs. Portlandite

Equilibrium between calcite and portlandite involves H_2O and CO_2 and can be written as follows:

$$CaCO_3(s) + H_2O(g) = Ca(OH)_2(s) + CO_2(g)$$

(Eq. 47)

This can be rewritten in terms of the constituent reactions:

$$CaCO_3(s) = CaO(s) + CO_2(g) \qquad \log K_{calcite\text{-}lime,100°C} = -16.6246$$

(Eq. 48)

$$CaO(s) + H_2O(g) = Ca(OH)_2(s) \qquad \log K_{lime\text{-}portlandite,100°C} = 7.7745$$

(Eq. 49)

The equilibrium constant for Equation 47 is

$$K_{calcite-portlandite,100°C} = \frac{Ca(OH)_2(s)(CO_2)}{CaCO_3(s)(H_2O)} = \frac{(CO_2)}{(H_2O)}$$

(Eq. 50)

The activities for the $Ca(OH)_2$ and $CaCO_3$ solids are defined as unity. Adding Equations 48 and 49 yields reaction Equation 47, with equilibrium constant

$$\log K_{calcite-portlandite,100°C} = \log K_{calcite-lime,100°C} + \log K_{lime-portlandite,100°C} = -8.8501$$

(Eq. 51)

$$\frac{(CO_2)}{(H_2O)} = 10^{-8.8501} = 1.412 \times 10^{-9}$$

(Eq. 52)

Calcite and portlandite existing in equilibrium requires CO_2 fugacity that is much smaller than H_2O fugacity (approximately 1 atm at 100°C). The CO_2 fugacities predicted in Section 6.2 of this report are much greater than 10^{-9} atm, as are those predicted by other methods, as discussed in Section 7.2 Accordingly, calcite is favored over portlandite at CO_2 conditions expected in the repository. At 60°C, the log K values yield

$$\log K_{calcite-lime,60°C} = -19.6249$$

(Eq. 53)

$$\log K_{lime-portlandite,60°C} = 9.6004$$

(Eq. 54)

$$\frac{(CO_2)}{(H_2O)} = 10^{-10.0245} = 9.452 \times 10^{-11}$$

(Eq. 55)

which shows that calcite is favored over portlandite at all temperatures of interest.

Thenardite+Calcite vs. Thermonatrite+Anhydrite

Equilibrium between thermonatrite+anhydrite and between thenardite+calcite involves CO_2 and can be written as follows:

$$Na_2CO_3 : H_2O(s) + CaSO_4(s) = Na_2SO_4(s) + CaCO_3(s) + H_2O(g)$$

(Eq. 56)

This can be rewritten in terms of the constituent reactions:

$$Na_2CO_3 : H_2O(s) + H^+ = 2Na^+ + HCO_3^- + H_2O(g) \quad \log K_{thermonatrite,100°C} = 9.9856$$

(Eq. 57)

$$CaSO_4(s) = Ca^{2+} + SO_4^{2-} \quad \log K_{anhydrite,100°C} = -5.3851$$

(Eq. 58)

$$Na_2SO_4(s) = 2Na^+ + SO_4^{2-} \quad \log K_{thenardite,100°C} = -0.7048$$

(Eq. 59)

$$Ca(OH)_2(s) + 2H^+ = Ca^{2+} + 2H_2O \quad \log K_{portlandite,100°C} = 18.0609$$

(Eq. 60)

$$CaCO_3(s) = CaO(s) + CO_2(g) \quad \log K_{calcite\text{-}lime,100°C} = -16.6246$$

(Eq. 61)

$$CaO(s) + H_2O(g) = Ca(OH)_2(s) \quad \log K_{lime\text{-}portlandite,100°C} = 7.7745$$

(Eq. 62)

$$CO_2(g) + H_2O = H^+ + HCO_3^- \quad \log K_{CO2-HCO3,100°C} = -8.3574$$

(Eq. 63)

The equilibrium constant for Equation 56 is

$$K_{thermonatrite-thenardite,100°C} = \frac{Na_2SO_4(s)CaCO_3(s)(H_2O)}{Na_2CO_3 : H_2O(s)CaSO_4(s)} = (H_2O)$$

(Eq. 64)

The activities for solids are defined as unity. Reversing Equations 59 through 63 and adding Equations 57 through 63 yields reaction Equation 57, with equilibrium constant

$$\log K_{\text{thermonatrite-thenardite},100°C} = 4.4519$$

(Eq. 65)

$$H_2O = 10^{4.4519} = 2.831 \times 10^4$$

(Eq. 66)

Driving reaction Equation 56 to the left, stabilizing thermonatrite and anhydrite, requires unrealistically large water fugacity (Equation 66). Thenardite and calcite (the right-hand side of Equation 56) can coexist at reasonable water pressures and are therefore the favored assemblage at or near 100°C. At 60°C, the log K values yield

$$\log K_{\text{thermonatrite},60°C} = 10.4500$$

(Eq. 67)

$$\log K_{\text{anhydrite},60°C} = -4.7587$$

(Eq. 68)

$$\log K_{\text{thenardite},60°C} = -0.4382$$

(Eq. 69)

$$\log K_{\text{portlandite},60°C} = 20.1961$$

(Eq. 70)

$$\log K_{\text{calcite-lime},60°C} = -19.6249$$

(Eq. 71)

$$\log K_{\text{lime-portlandite},60°C} = 9.6004$$

(Eq. 72)

$$\log K_{CO2-HCO3,60°C} = -8.0527$$

(Eq. 73)

$$(H_2O) = 10^{4.0106} = 1.0247 \times 10^4$$

(Eq. 74)

which shows that, at temperatures of interest, the assemblage thenardite+calcite is favored over anhydrite and portlandite.

6.5.7 Application of Normative Model to Laboratory Test Results

In this section, the normative approach described previously and summarized in Table 55, is applied quantitatively to the complete evaporation of synthetic J-13 water and synthetic porewater used in laboratory tests (Table 45 and Table 52).

These tests best represent waters that enter the EBS and evaporate in quartz sand. Quartz has low solubility relative to other phases in the host rock (e.g., cristobalite) that contribute Si, and the dissolution and precipitation rates for quartz are kinetically limited; thus, interaction of quartz with rapidly evaporating waters is likely to be minor. The expression of quartz dissolution would be increased dissolved silica, which might enhance precipitation of silicates and SiO_2. However, as will be shown in following text, the formation of aluminosilicates is limited by availability of aluminum, and the entering waters already contain excess Si that precipitates as amorphous silica. Therefore, quartz is considered to be relatively inert in the normative approach.

Precipitates formed upon evaporation of synthetic J-13 water and synthetic porewater are modeled using spreadsheet routines "normative_hiCO2_synJ13V1.2.xls" and "normative_hiCO2_SPWV1.2.xls," respectively. The normative solutions are compared with qualitative observations from the laboratory tests in Table 56 and Table 57. The results are summarized as follows:

- Calcite, halite, niter, and thermonatrite are identified as products of J-13 evaporation in both models.
- Observation of aragonite indicates that different carbonates are precipitated at different stages of evaporation of synthetic J-13 water.
- For synthetic J-13 water, thenardite is identified in the normative assemblage in lieu of gypsum and anhydrite.
- Minor species such as sylvite (or an alternative potassium-bearing phase) identified by the normative model for synthetic J-13 water may not have been detected by XRD.
- Minor species such as the niters, fluorite, halite, and calcite identified by the normative model for synthetic porewater may not have been detected by XRD. (The highly

deliquescent salts such as niter may have dissolved from exposure to humidity, prior to XRD.)

The normative model for evaporation of synthetic porewater produces a residual amount of chloride (approximately 4.03×10^{-4} mol/kg, as shown in file "normative_hiCO2_SPWV1.2.xls"; worksheet: Evaporation). This amount is small and could result from charge imbalance associated with analytical error.

Table 56. Normative Model for Precipitates Formed from Evaporating 1 kg of Synthetic J-13 Water, Compared with Qualitative Laboratory Observations

Predicted Normative Species	Predicted Moles/kg	Observed Species
Species Constituting >90% of Total Molality		
silica (amorphous)	3.702E–04	SiO_2 (amorphous)
thermonatrite ($Na_2CO_3{\cdot}H_2O$)	6.917E–04	thermonatrite ($Na_2CO_3{\cdot}H_2O$)
halite (NaCl)	1.975E–04	halite (NaCl)
thenardite (Na_2SO_4)	1.926E–04	gypsum ($CaSO_4{\cdot}2H_2O$)[a]
		anhydrite ($CaSO_4$)[a]
niter (KNO_3)	1.274E–04	niter (KNO_3)
calcite/Aragonite ($CaCO_3$)	8.208E–05	calcite ($CaCO_3$)
		aragonite ($CaCO_3$)
Remaining Species		
magnesite ($MgCO_3$)[b]	8.638E–05	hectorite ($Na_{0.33}Mg_3Si_4O_{10}(F,OH)_2$)[a]
fluorite (CaF_2)	6.263E–05	
sylvite (KCl)	5.594E–06	

DTN: LL991008104241.042 (observed species)

NOTES: [a] A minor constituent; identification is uncertain.

[b] Magnesium may precipitate as Mg-calcite but is represented stoichiometrically as magnesite.

Table 57. Normative Model for Precipitates Formed from Evaporating 1 kg of Synthetic Porewater, Compared with Laboratory Qualitative Observations.

Predicted Normative Species	Predicted Moles/kg	Observed Species
Species Constituting >90% of Total Molality		
Gypsum/anhydrite ($CaSO_4$)	8.734E–04	gypsum ($CaSO_4{:}2H_2O$)
Tachyhydrite ($CaMg_2Cl_6O_{10}{:}12H_2O$)	2.427E–04	tachyhydrite ($CaMg_2Cl_6O_{10}{:}12H_2O$)
Silica (amorphous)	3.702E–04	
Calcite ($CaCO_3$)	2.567E–04	
Halite (NaCl)	3.021E–04	
Remaining Species		
Niter (KNO_3)	1.023E–04	
Na-niter ($NaNO_3$)	7.025E–05	
fluorite (CaF_2)	5.684E–05	

DTN: LL991008004241.041 (observed species)

6.5.8 Normative Model Validation

In this section, the normative approach described previously and summarized in Table 55, is applied quantitatively to the complete evaporation of synthetic J-13 water and synthetic porewater used in laboratory tests (Table 56 and Table 57). In these tables, compositionally equivalent predicted species (e.g. calcite and aragonite) are grouped. Also, observed and predicted species are grouped for comparison, even where they have different composition (e.g. thenardite and gypsum or anhydrite).

The comparisons shown in Tables 56 and 57 show that the normative approach can produce qualitative agreement for the synthetic J-13 water and synthetic porewater. Silica, thermonatrite, halite, niter, and calcite (or aragonite) are identified as major products of J-13 evaporation in both the predictions and observed data. The normative model predicts thenardite to form where gypsum and anhydrite are observed, so there evidently is some sensitivity to the relative availability of Ca and Na, which is not accounted for in the model. Minor species such as sylvite (or an alternative potassium-bearing phase) identified by the normative model for synthetic J-13 water may not have been detected by XRD. Similarly, minor species such as the niters, fluorite, halite, and calcite, and amorphous silica, which are predicted by the normative model for synthetic porewater, were not detected by XRD.

From the above discussion, the normative model is valid for its intended use. It provides a valid approximation to the major species formed on complete evaporation of waters with composition similar to J-13 water, and matrix porewater. It does not account for mineral replacement (e.g., gypsum vs. anhydrite) caused by commingling of precipitates with concentrated solutions. Accordingly, for species identification (e.g. salts that can form on the drip shield) this should be taken into account by inclusion of all possible minerals that can form.

6.5.9 Summary

6.5.9.1 Evaporation of Synthetic J-13 Water and Synthetic Porewater

The trends in solution chemistry for the evap1 and evap2 tests using synthetic J-13 water (Table 41 through Table 44) are consistent with the XRD results for solid precipitates produced. The presence of the tuff allows for more geochemical processes to occur, particularly mineral dissolution an d precipitation and silicate buffering.

Test results for synthetic J-13 water are sensitive to the ambient atmospheric CO_2 fugacity, which limited pH to the range 10 to 11 for evaporative concentration values up to 150× and probably greater. Smaller values for the CO_2 fugacity will tend to cause higher pH. Thus, if corrosion processes are sensitive to high pH, the 10.59 value measured in this set of tests (Table 41) is a lower bound.

Bicarbonate-type waters such as J-13 water are more sensitive to CO_2 fugacity, particularly during evaporative concentration, and are more likely to produce high-pH conditions than are sulfate-type waters such as the synthetic porewater investigated. The synthetic J-13 results are therefore bounding with respect to high-pH conditions at the surface of the drip shield or the waste package during the thermal period. Sulfate-type or chloride-type waters tend to produce much lower pH values when concentrated evaporatively (4 pH units lower than bicarbonate-type waters, in the laboratory tests) and are therefore not bounding compositions (Assumption 5.1.6). The J-13 water composition (Harrar et al. 1990) is therefore used as the compositional boundary condition for the Chemical Reference Model (Section 6.7).

Experimental results for synthetic J-13 water (with and without tuff) show that evaporative concentration factors greater than 150× are required for pH >10. Thus, the potential volumes and flow rates of affected solutions will be small. Saturation of the backfill in affected regions will be small, as will the relative permeability, and the consequent mobility of concentrated solutions.

If a water composition that is similar to, but more dilute than, J-13 water (e.g., condensate) is used, the results will be similar to the synthetic J-13 results presented here; however, greater evaporative concentration factors would be required to achieve the same high pH values. Thus, the mass of solute involved, and the potential volume of high-pH liquid, would be smaller.

6.5.9.2 Normative Model Uncertainties

The principal uncertainty associated with this model is caused by simplification of the reaction path that culminates in complete evaporation. Precipitates that form relatively early in the evolution of the mineral assemblage, are exposed to aqueous solution conditions, and are therefore available to redissolve and participate in further precipitation reactions. The implication is that salts can form other than those predicted. For example, the normative model predicts thenardite to form where gypsum and anhydrite are observed, so there evidently is some sensitivity to the relative availability of Ca and Na, which is not accounted for. Minor species such as sylvite (or an alternative potassium-bearing phase) identified by the normative model for synthetic J-13 water may not have been detected by XRD. Similarly, species such as the niters, fluorite, halite, and calcite, and amorphous silica, which are predicted by the normative model for synthetic porewater, were not always detected by XRD. Comparison to test data is therefore

important with this approach, and extension to alternative starting solution compositions should be verified by testing.

Another uncertainty for low-CO_2 conditions that may be encountered in the potential repository during the thermal period, it is that sufficient CO_2 will be present to produce thermonatrite and calcite (Assumption 5.5.1). If this assumption is incorrect, portlandite or NaOH could precipitate in the EBS (e.g., on the drip-shield surface). This could have different implications for corrosion of metallic barriers. Thermodynamic equilibrium calculations show that sufficient CO_2 is likely to be available to prevent hydroxide formation, but test data for low-CO_2 conditions are unavailable.

6.5.9.3 Summary Remarks

The normative model for precipitate formation incorporates observations from the laboratory tests on synthetic J-13 water, synthetic porewater, and thermodynamic insights. A set of mineral precipitates is identified (Table 55) that can accommodate all the major ions and many of the minor species that constitute waters similar to J-13. Application of the model to the laboratory test results (Table 56 and Table 57) shows qualitative agreement with most major precipitates identified by XRD, while incorporating other species (not detected) as needed for mass balance.

From the foregoing discussion, the normative model is determined to be valid and have an appropriate level of confidence suited for its intended use. It provides a valid approximation to the major species formed on complete evaporation of waters with composition similar to J-13 water, and matrix porewater. It does not account for mineral replacement (e.g., gypsum vs. anhydrite) caused by commingling of precipitates with concentrated solutions. Accordingly, for species identification (e.g. salts that can form on the drip shield) this should be taken into account by inclusion of all possible minerals that can form.

6.6 EBS COLLOIDS MODEL

This model bounds the impact of ferric-oxide and ferric-oxyhydroxide colloids on RN transport in the invert, specifically considering the impacts resulting from use of steel in the EBS. The results show that the effect of steel in the EBS is bounded, depending on the affinity of corrosion products for radionuclides of interest (e.g. Pu).

In this model the size distribution and maximum concentration of colloids are estimated from natural analogs, and assumed to be entirely hematite colloids. Other colloid types may be present including clays, silica, and waste form colloids (spent fuel or waste glass). Laboratory results discussed below indicate that ferric-oxide colloids have greater affinity for radionuclides of interest than silica or clays. However, waste form colloids have the potential to transport radionuclides and are not considered in this model, therefore the model may not bound the overall potential for colloidal transport.

6.6.1 Introduction

Aqueous colloids are suspensions of solid particles in water. The diameters of the particles typically range from a few nanometers to a few thousand nanometers, which produces a very large surface area per unit mass of material. The behavior of colloids is, accordingly, controlled

by surface forces and processes, including electrostatic repulsion or attraction and surface chemical reactions with species in solution. Colloids' stability and capacity to adsorb radionuclides are complex functions of solution chemistry, temperature, and other variables.

Radionuclide-bearing colloids can adversely affect repository performance because they can travel large distances in groundwater with little or no retardation. Radioactive colloids include intrinsic colloids (i.e., radionuclides provide the dominant metal species in the particles, as in hydrous actinide polymers or colloidal actinide silicates and phosphates) and pseudocolloids (formed by the sorption, entrainment, or other incorporation of radionuclides on or within colloidal particles of other materials).

Laboratory studies (e.g. as discussed by CRWMS M&O 1997) demonstrate that Pu is readily sorbed by pseudocolloids, hence, the bounding analysis that follows will focus on the behavior of radioactive pseudocolloids, and the term "colloid" should be understood to mean pseudocolloids in the remainder of this discussion.

The most important colloid-forming materials, based on their prospective abundance in the potential repository environment, and measured sorption of radionuclides, include clay minerals (e.g., smectites) and colloidal iron oxides such as hematite (see discussion of sorption data in Section 6.6.3.2). Radionuclides can also be sorbed on colloidal silica, but with a generally smaller sorption coefficient than with clays and iron oxides. Colloidal iron compounds may be generated from the large quantities of iron-bearing alloys used within the waste package as well as in the EBS outside the waste package. As shown in Table 27, even without including the iron content of the waste package and its internals, there is more than one metric ton (approximately 1185 kg) of iron per meter of emplacement drift.

A conceptual model for colloid generation, mobility, and affinity for radionuclides within the EBS is combined with available data on colloidal transport and sorption capacity for radionuclides to produce a bounding analysis of the degree to which colloids may increase the aqueous concentrations of radionuclides above their respective solubility limits.

6.6.2 Conceptual Model

The following discussion is based on CRWMS M&O (1997) which is a more comprehensive treatment of factors affecting radionuclide transport. Colloids are considered stable if they do not agglomerate and settle out of a static suspension over the time period of interest. The stability of colloids suspended or entrained in groundwater (i.e., their tendency to remain suspended) is a function of pH, oxygen potential (Eh), ionic strength, composition of the colloidal particles, temperature, flow velocity, and composition and structure of the media through which the groundwater is moving. The temporal evolution of these variables after repository closure cannot be predicted in great detail. However, the available information permits a bounding analysis comprising the following elements:

- Colloid particle size distributions have been measured and reported in groundwater samples pumped from 18 well intervals in the vicinity of Yucca Mountain (Table 22 and Table 23). These data provide a conservative estimate of the concentration of colloidal material that can actually be transported in groundwater along flow pathways

between the potential repository and the accessible environment. The concentrations may be higher than would be observed in undisturbed natural groundwater flow because water velocity near a pumping well is much higher than it is naturally.

- The abundance of iron in the EBS provides a large source of oxides and hydroxides as EBS components corrode. Because there is no compelling argument to preclude the formation of colloids from these corrosion products, it is conservative to assume that all of these products are of colloidal size. Entrainment of colloids in the groundwater and release to the host rock will occur only after sufficient water reenters the drift to support advective flow.

- When their release begins, the size distribution of iron colloids is assumed to be identical to the size distributions of natural colloids referenced previously (Assumption 5.6.1). The underlying assumption is that colloids outside the observed range will not be transported over long distances, either because they are unstable or because they become attached to the porous media through which the water flows.

- The total concentration of radionuclides is the sum of the concentration in solution and the mass adsorbed on colloidal particles. It can be expressed as an enhancement factor (a simple function of colloid mass concentration and sorption coefficient) multiplied by the solubility limit for the radionuclide.

- Sorption of actinides on iron colloids is irreversible, and the sorption coefficient can be bounded by laboratory data (Section 6.6.3.2).

- Sorption on silica and clays is reversible and of smaller magnitude than sorption on iron colloids. Treating the total concentration of suspended colloids as iron colloids, can conservatively bound long-distance colloid transport, if the total concentration of suspended colloids is a fixed parameter.

6.6.3 Bounding Analysis

6.6.3.1 Colloid Size Distribution and Concentration.

Data for size distribution and colloid concentration are given in Table 22 and Table 23 and are analyzed in Attachment XVI. Particle concentrations in counts per mL are given for sizes ranging from 50 to 200 nm at 10-nm increments. Analysis of the data showed that the normalized distribution (fraction of particles within each size range) is closely approximated by a log-normal distribution for each of the samples; it also showed that the parameters of these distributions are close enough to the same values that a single distribution can be used to approximate adequately the size distribution of colloids that can be transported in the vicinity of Yucca Mountain. Figure 30 shows the distribution data for each of the 18 intervals, along with two composite log-normal curves (one for nine Nye County well samples from Table 22 and one for nine Yucca Mountain well samples from Table 23). The two composite curves are almost identical, which lends some credibility to the notion that a single distribution can represent colloid size data for the entire groundwater system around Yucca Mountain.

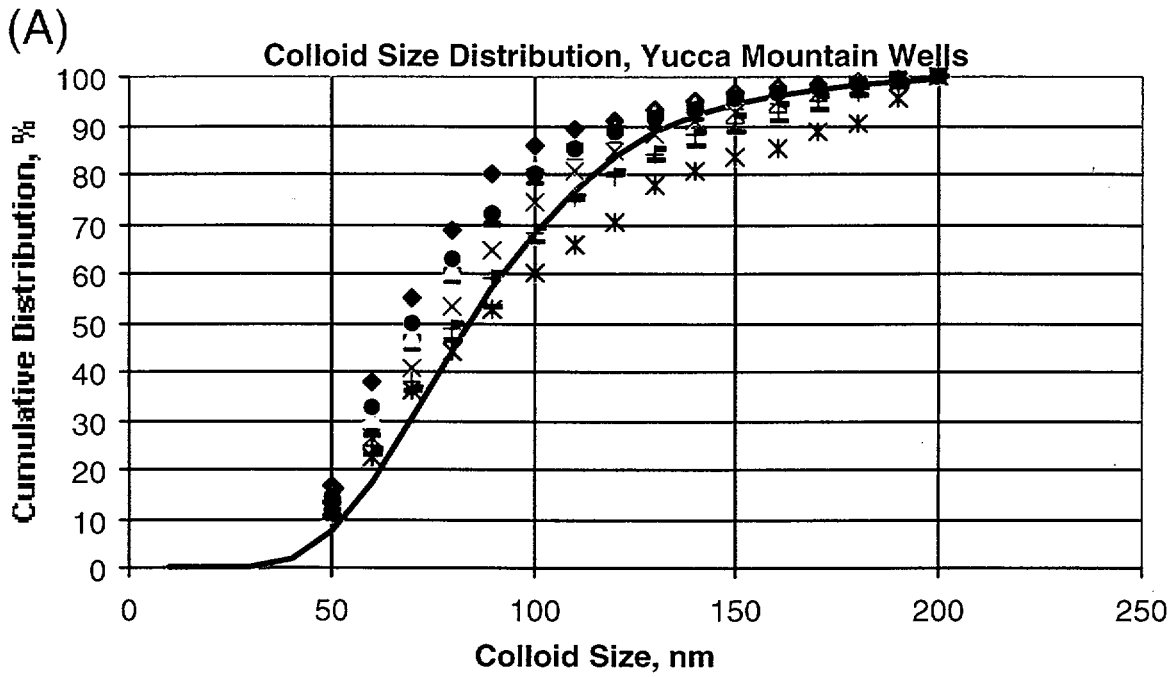

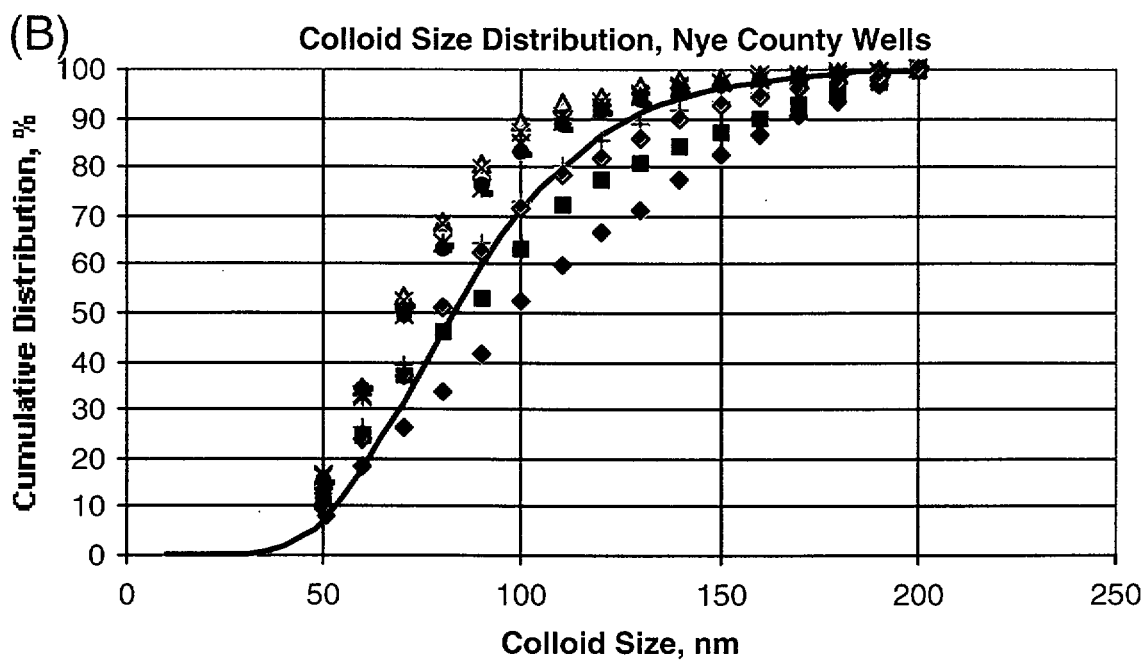

Source: "GwcolloidsV1.2.xls" Worksheets: "NC Cumulative" and "YM Cumulative" (Attachment I)

NOTES: A Data from Nye County wells are tabulated in Table 22.

B Data from Yucca Mountain wells are tabulated in Table 23.

C Each of the symbols used corresponds to a different sampled well interval.

The curve in A is for a log-normal distribution with $\mu = 4.436448$ and $\sigma = 0.360222$, based on averaging statistics from each Yucca Mountain well interval. The curve in B is for a log-normal distribution with $\mu = 4.41515$ and $\sigma = 0.34167$, based on averaging statistics from each Nye County well interval.

Figure 30. Particle Size Distribution for Colloids in Groundwater Samples near Yucca Mountain

Mathematically, the distributions can be represented as follows:

$$F(D_c) = \Phi\left(\frac{\ln(D_c) - \mu_c}{\sigma_c}\right)$$

(Eq. 75

where

D_c = colloid particle diameter, nm

μ_c = mean of the natural log of the colloid particle diameter, nm

σ_c = standard deviation of the natural log of the colloid particle diameter, nm

$\Phi(x)$ = normal probability integral for any variable x

Log-normal parameters for the 18 observed, normalized-size distributions are summarized in Table 58. As noted previously, average values of the parameters for the two data sets are nearly the same. Accordingly, the final parameters recommended for the normalized colloid size distribution are given by the following averages (± one standard deviation):

$$\mu_c = \frac{4.4152 + 4.4364}{2} \pm \frac{0.1030 + 0.0740}{2} = 4.4258 \pm 0.0885$$

(Eq. 76)

$$\sigma_c = \frac{0.3417 + 0.3602}{2} \pm \frac{0.0410 + 0.0311}{2} = 0.3509 \pm 0.0361$$

(Eq. 77)

Table 58. Log-Normal Parameters for Normalized Colloid Size Distributions in Samples from Nine Nye County Wells and Nine Yucca Mountain Wells.

Nye County Wells		Yucca Mountain Wells	
μ_c (nm)	σ_c (nm)	μ_c (nm)	σ_c (nm)
4.6189	0.4027	4.3217	0.3211
4.5136	0.3999	4.3969	0.3382
4.3135	0.2861	4.3807	0.3369
4.3278	0.3016	4.4381	0.3581
4.3468	0.3170	4.5506	0.4239
4.3515	0.3228	4.3724	0.3412
4.4446	0.3563	4.4828	0.3767
4.3546	0.3293	4.4780	0.3637
4.4650	0.3592	4.5068	0.3822
4.4152	**0.3417**	**4.4364**	**0.3602**
±0.1030	**±0.0410**	**±0.0740**	**±0.0311**

Source: "GwcolloidsV1.2.xls" Worksheets: "Nye Co Normalized" and "YM Normalized" (Attachment I)

NOTES: The calculations to determine these parameters are summarized in Attachment XVI. The first boldface row at the bottom of the table gives the means of the respective parameters, and the second boldface row gives the standard deviations.

The total number of colloid particles per mL in the 18 intervals sampled is also closely approximated by a log-normal distribution, which is given by

$$F(N) = \Phi\left(\frac{\ln(N) = m_N}{\sigma_N}\right) \qquad \text{(Eq. 78)}$$

where

N = total number of colloid particles, counts per mL

μ_N = mean of the natural log of the total number of colloid particles per mL

σ_N = standard deviation of the natural log of the total number of colloid particles per mL

$\Phi(x)$ = normal probability integral for any variable x

Analyses of the data are documented in Attachment XVI. Two methods of determining the parameters of the distribution were used: The first method uses a linear regression of the observed cumulative distribution function on a normal probability scale, resulting in $\mu = 17.5936$ and $\sigma = 2.0441$; the second simply determines the parameters by direct calculation of the natural log mean and natural log standard deviation from the data, resulting in $\mu = 17.8089$ and $\sigma = 1.9911$. There is no particular theoretical reason for choosing one set over the other. For

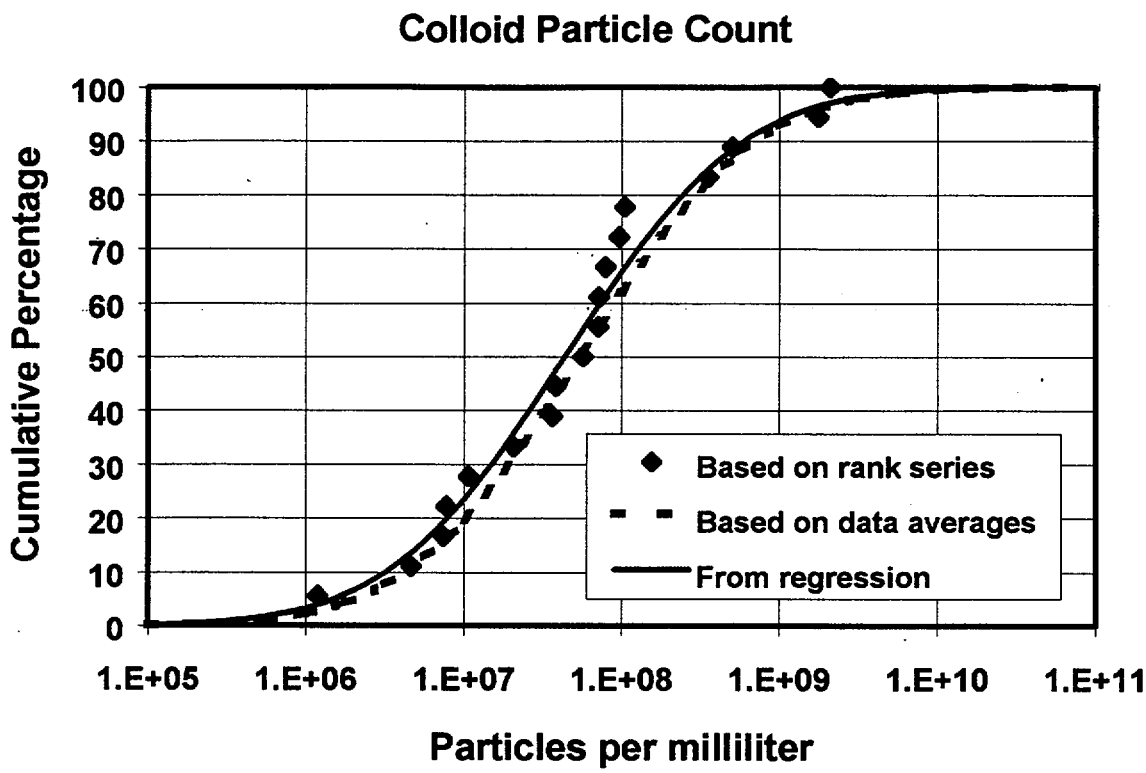

NOTE: Two log-normal distributions are shown: The solid curve is based on linear regression analysis of Nye County and Yucca Mountain data, combining colloid concentration vs. size data from a total of 18 well intervals. The dashed curve is a cumulative distribution developed by averaging log-normal statistics representing data from each of the 18 well intervals. The discrete points are values developed directly from rank series analysis of the combined well data. The distributions are almost indistinguishable, and the parameters are not significantly different at the 95% confidence level.

Figure 31. Distribution of Total Number of Colloid Particles per Milliliter in Groundwater Samples Near Yucca Mountain

simplicity, the second set will be used in further analyses. As can be seen in Figure 31, the curves are nearly identical.

6.6.3.2 Sorption Coefficients

Iron compounds as corrosion products are of particular importance because they have high affinity for actinides, and tend to form colloids during metal corrosion. At least one of the common corrosion products (hematite) has high sorption coefficients, and the sorption on these minerals as discussed below, is probably irreversible. Corrosion products of other metals that may form colloids are expected to be much less important than Fe compounds because Fe accounts for most of the total metal content within the drift.

The sorption coefficient and colloid stability are complex functions of the chemistry of the water and of the nature of the colloidal material. However, bounding values for 239Pu and 243Am can be extracted from recent laboratory work (DTN: LA0003NL831352.002 and DTN: LA0005NL831352.001). These experiments used both natural well water from J-13 (NAT-J-13) and synthetic groundwater (SYN-J-13). Suspensions of colloids in each of these two dilute electrolytes were prepared for hematite, montmorillonite, and silica materials. Sorption coefficients based on these data are shown in Table 59. The tabulated data are bounding values, for representative environmental conditions.

Table 59. Sorption Coefficient (K_d) Values in mL/g for Sorption of Pu and Am on Hematite, Montmorillonite, and Silica Colloids

		Sorption Coefficient Values		
Radionuclide	**Water**	**Hematite**	**Montmorillonite**	**Silica PST-1**
Pu (see note)	Natural J-13	1.1×10^5	2.7×10^4	3.0×10^4
	Synthetic J-13	7×10^5	2.4×10^4	2.1×10^4
^{243}Am	Natural J-13	1×10^7	1×10^5	2.1×10^4
	Synthetic J-13	6.2×10^6	1×10^5	3.2×10^4

DTN: LA0003NL831352.002 and LA0003NL831352.003

NOTES: Representative maximum measured K_d values are tabulated
Pu data are maximum sorption coefficients from Tables S00189.001 and S00189.002, from source DTN: LA0003NL831352.002.

In addition to the sorption measurements, data were reported on the desorption of Pu from loaded samples of hematite, montmorillonite, and silica colloids. After extended agitation in natural or synthetic J-13 water, desorption was far from complete. These results suggest that sorption of actinides on hematite and other oxides such as goethite should be considered irreversible. It is possible that sorption on montmorillonite (and, presumably, other clays) and silica would be reversible over shorter times, although the assumption of complete reversibility is not evident from the reported data. However, given the large amount of ferric material in the emplacement drifts, iron colloids are likely to be more important for sorption of Pu in this environment than clays and silica particle.

6.6.3.3 Bounding Values of Radionuclide Solubility Enhancement Factor

The enhancement factor for colloidal transport represents the factor by which the total amount of a radionuclide in groundwater is increased over the amount in solution at the time the radionuclide was adsorbed. For irreversible adsorption, the amount in solution may be equal to, less than, or greater than the solubility limit at any point along the flow path after the colloid is "loaded" with radionuclide. Mathematically, the enhancement factor E is defined by

$$E = \frac{C_{Total}}{C_0} = 1 + K_d M_C$$

(Eq. 79)

C_{Total} = total radionuclide concentration in solution and suspension (units consistent with C_0)

C_0 = radionuclide solubility limit (units consistent with C_{Total})

K_d = sorption coefficient, mL/g colloid

M_C = mass concentration of colloids, g/mL of suspension.

Assuming spherical particles (Assumption 5.6.2), the mass concentration of colloids is given by

$$M_C = \frac{\pi \rho D_C^3}{6} \cdot N$$

(Eq. 80)

where ρ is the density of the colloid particles, assumed constant. In this equation, both D_C and N are log-normally distributed random variables, with parameters given in Section 6.6.3.1. These random variables appear to be independent, exhibiting little or no correlation in the data. The distribution of particle diameter is rather narrow, which implies that most of the uncertainty or variability arises from the total particle count. For a bounding analysis, one can average the mass concentration over the particle diameter distribution, as follows:

$$\langle M_C \rangle_{D_C} = \frac{\pi \rho \langle D_C^3 \rangle}{6} \cdot N$$

(Eq. 81)

where the left-hand side is a random variable representing the mass concentration averaged over the particle diameter distribution. The notation $\langle X \rangle$ denotes the average of the random variable x over its distribution. For a log-normal distribution with parameters μ and σ, the average of x^3 is given by

$$\langle x^3 \rangle = \exp\left(3\mu + \frac{9\sigma^2}{2}\right)$$

(Eq. 82)

Using the parameters for the size distribution results in

$$\left\langle D_C^3 \right\rangle = \exp\left(3 \cdot 4.4258 + \frac{9 \cdot 0.3509^2}{2}\right) = 1.0161 \text{ x } 10^6 \text{ nm}^3$$

(Eq. 83)

The density of anhydrous hematite (5.24 g/mL; Weast and Astle 1981, p. B-109) is an upper bound on the density of hydrous hematite. This value is used to obtain an order of magnitude estimate for the mass of a spherical colloid particle with a diameter cubed equal to 1.0161×10^6 nm^3, using Equation 83. The result is 2.7878×10^{-9} μg per particle.

All that remains is to calculate the total mass of colloids per mL of suspension, which requires a value for the total number of particles per mL. As noted previously, N is also log-normally distributed, with parameters μ = 17.8089238 and σ = 1.9911. Specific values for the enhancement factor require selecting a fractile on the cumulative distribution function (CDF) of N. Calculations for several fractiles are documented in Attachment XVI and are summarized in Table 60. At the 99th percentile, this analysis predicts an enhancement factor of less than 20.

Table 60. Summary of Calculations for the Colloid Mass at Different Fractiles of the Log-Normal Distribution for the Number of Particles per mL

CDF for Number of Particles per mL	Standardized Normal Variable	Colloid Particles per mL	Colloid Mass, (μg/mL)	Enhancement Factor for $K_d = 7 \times 10^5$
0.99000	2.3263	5.6E+09	1.6E+01	11.87
0.97500	1.9600	2.7E+09	7.5E+00	6.24
0.95000	1.6449	1.4E+09	4.0E+00	3.80
0.90000	1.2816	7.0E+08	1.9E+00	2.36
0.84027	0.9956	2.1E+08	5.8E-01	1.41
0.75000	0.6745	5.4E+07	1.5E-01	1.11
0.50000	0.0000	3.9E+08	1.1E+00	1.77

Source: file "GWcolloidsV1.2.xls" Worksheet: "Mass Conc." (Attachment I)

NOTE: The enhancement factor estimate is based on the largest value of K_d (7×10^5 mL/g) reported in Table 59.

At the 99th percentile, the estimated total mass of colloidal hematite is 15.5 mg/L. For comparison, the total dissolved solids (TDS) content of J-13 water averages about 250 mg/L. Water compositions calculated in Sections 6.7.2 and 6.7.3 show that dissolved solids will equal or exceed that of J-13 water throughout the thermal evolution of the potential repository. In addition, when waters are evaporatively concentrated, or affected by dissolution of precipitates and salts, the ionic strength will increase, which destabilizes colloidal suspensions and will decrease the colloid concentration. Therefore, except for the extreme right tail ($p>0.95$) of the colloid mass CDF at conditions unaltered by evaporative concentration or precipitates and salts, colloids will be less than 10% of the TDS content.

Calculation of the enhancement factor as a function of K_d, at the 99th percentile gives the following results:

- For $K_d = 10^6$, $E = 16.5$
- For $K_d = 10^5$, $E = 2.6$
- For $K_d = 10^4$, $E = 1.2$

Because factors of 2 are not considered significant in radionuclide release and transport calculations for repository performance assessment, this bounding analysis suggests that colloid-enhanced radionuclide transport will be important only if the colloid has a sorption coefficient substantially greater than 10^5 mL/g.

6.6.3.4 Bounding Values for Colloid Diffusion Coefficient

One potential function of the invert ballast is to provide, under the drip shield, a diffusion barrier between the waste package and the host rock. If water is successfully diverted by the backfill/drip-shield system and effectively drained from the drift into the host rock, little or no water would flow beneath the waste package. Potentially, the water content in this region could be kept so low that diffusion rather than advection would dominate radionuclide transport.

A model for diffusivity of dissolved radionuclides is documented in CRWMS M&O (2000h).

For an invert material with 50% porosity and 5% water saturation, the diffusion coefficient of a dissolved ion will be about three orders of magnitude below its value in bulk solution (i.e., with no porous medium present).

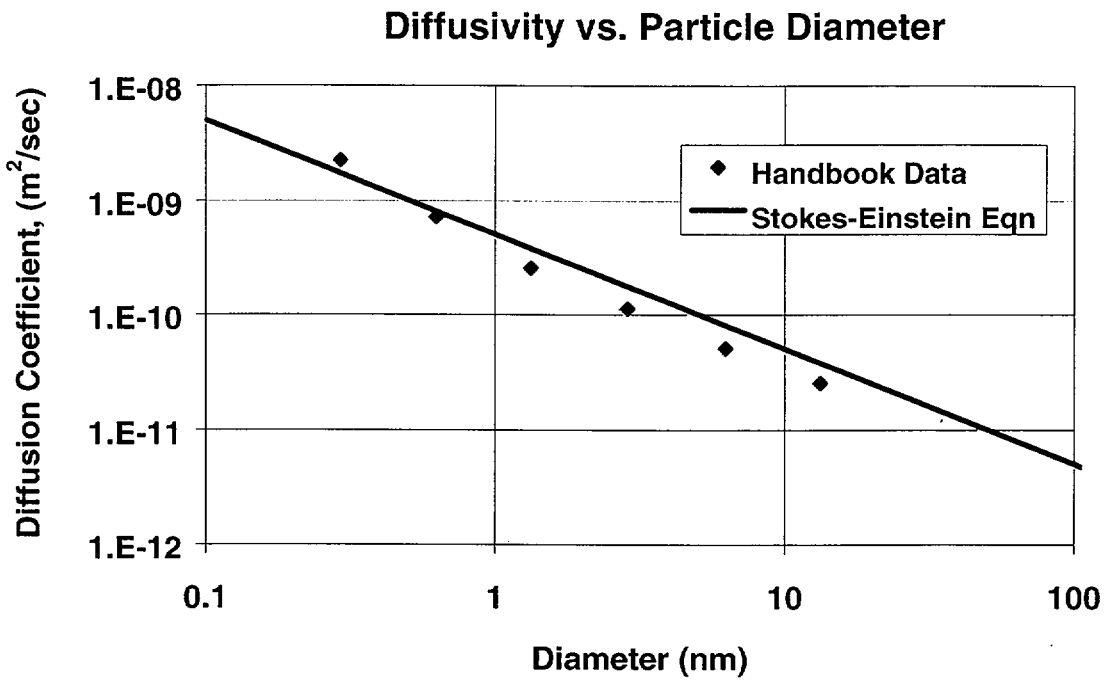

Source: file "GWcolloidsV1.2.xls" Worksheet: "Colloid Diffusivity" (Attachment I)
NOTES: Values shown with points are from Perry and Chilton (1973)
Line is Stokes-Einstein equation for water @ 25°C (Bird et al. 1960)

Figure 32. Estimated Diffusion Coefficient as a Function of Particle Size Using the Stokes-Einstein Equation, Compared with Handbook Values from Table 23

It might be supposed that no colloidal transport would be possible without advective flow. However, diffusion along a surface film of water is possible, at least for the smaller sizes of colloids. Figure 32 summarizes values for the diffusion coefficient in dilute suspensions as a function of particle diameter, over a range covering colloids, based on the Stokes-Einstein equation:

$$\frac{D_{AB}\mu_B}{\kappa T} = \frac{1}{6\pi R_A} = \frac{1}{3\pi D_A}$$

(Eq. 84)

where

D_{AB} = Diffusivity of species A in solvent B (m^2/sec)

μ_B = Viscosity of solvent B, water (Pa-sec)

κ = Boltzman's constant (1.380658×10^{-23} joule/°K)

T = Absolute temperature (°K)

R_A = Radius of species (m)

D_A - Diameter of species (m)

The calculations used to develop Figure 32 are documented in Attachment XVI. These diffusivity values apply in bulk suspensions and are reduced from typical values for dissolved species by two to three orders of magnitude. Even with an enhancement factor of 10 or so, diffusion-controlled radionuclide mass release would be from 10 to 100 times lower than the diffusion of dissolved species. Actual diffusivity in a water film may be even lower because the Stokes-Einstein equation assumes no interaction of the diffusing particle with any substance other than the solvent. Therefore, diffusion of colloids through the invert can be neglected entirely in performance assessment.

6.6.3.5 Discussion and Summary

The foregoing discussion has shown that transport of Pu and possibly other actinides, may be affected by iron colloids produced from corrosion of steel in the waste package and elsewhere in the EBS. Sorption is probably irreversible, and sorptive affinity of iron oxides for Pu is high, so the effect of corroded steel could be to increase irreversible, pseudocolloidal Pu transport at the expense of dissolved Pu. Given a particular concentration of dissolved Pu, the total concentration associated with iron colloids could be an order of magnitude greater under certain conditions. (This would require commensurate dissolution of the waste form, to provide sufficient dissolved Pu to "load up" the iron colloids.) Analysis shows that diffusive transport of colloidally bound radionuclides is not important to performance.

This model is based on inferences relating the abundance and size of natural colloids in Yucca Mountain groundwaters, with the concentrations of ferric-oxide and ferric-oxyhydroxide colloids in the EBS. In addition, sorption coefficients and reversibility are inferred from laboratory tests on hematite colloids.

As stated previously, the intended use of this model is to bound the effect of steel in the EBS, on the potential for colloidal transport of radionuclides. The model is bounding because the entire mobile colloid load in EBS waters is assigned to hematite colloids, which have relatively high affinity for radionuclides such as Pu. Other colloids such as clays and silica will be present and tend to decrease the hematite colloid concentration. The model is also bounding because sampling of groundwater from wells is more dynamic than percolation in the EBS will be, so colloids tend to be mobilized at greater concentrations. Another important bounding aspect of this model is that sorption of Pu is considered irreversible, so that once sorbed, the enhanced mobility of pseudo-colloidal transport in the groundwater system persists for the lifetime of the radionuclide.

Whereas hematite is the most stable Fe-oxide likely to form in the potential repository, other solids such as goethite and ferrihydrite could also be present. These "lower" oxides can have greater surface area and sorption capacity for radionuclides. It is possible that these phases will mature to hematite with time in the repository, however, the endpoints and timing of such evolution are not established. It is likely that the bounding approximations mentioned above, would encompass any differences in potential radionuclide transport that could be attributed to the lower oxides.

From this discussion it is concluded that the EBS Colloids Model is bounding, and valid for its intended use.

6.6.4 EBS Colloids Model Validation

This model is based on inferences relating the abundance and size of natural colloids in Yucca Mountain groundwaters, with the concentrations of ferric-oxide and ferric-oxyhydroxide colloids in the EBS. In addition, sorption coefficients and reversibility are inferred from laboratory tests on hematite colloids.

As stated previously, the intended use of this model is to bound the effect of steel in the EBS, on the potential for colloidal transport of radionuclides. The model is bounding because the entire mobile colloid load in EBS waters is assigned to hematite colloids, which have relatively high affinity for radionuclides such as Pu. Other colloids such as clays and silica will be present and tend to decrease the hematite colloid concentration. The model is also bounding because sampling of groundwater from wells is more dynamic than percolation in the EBS will be, so colloids tend to be mobilized at greater concentrations. Another important bounding aspect of this model is that sorption of Pu is considered irreversible, so that once sorbed, the enhanced mobility of pseudo-colloidal transport in the groundwater system persists for the lifetime of the radionuclide.

Whereas hematite is the most stable Fe-oxide likely to form in the potential repository, other solids such as goethite and ferrihydrite could also be present. These "lower" oxides can have greater surface area and sorption capacity for radionuclides. It is possible that these phases will mature to hematite with time in the repository, however, the endpoints and timing of such evolution are not established. It is likely that the bounding approximations mentioned above, would encompass any differences in potential radionuclide transport that could be attributed to the lower oxides.

From this discussion it is concluded that the EBS Colloids Model is bounding, and valid for its intended use. It is also shown that the model has an appropriate level of confidence suitable for its intended use.

6.7 CHEMICAL REFERENCE MODEL

The Chemical Reference Model combines input from the Thermal Hydrology Model (Section 6.1), Gas Flux and Fugacity Model (Section 6.2), Normative Precipitates and Salts Model (Section 6.5), and other aspects of the EBS Physical and Chemical Environment Model to produce a description of chemical processes in the EBS. The overall objective is an integrated view of chemical conditions in the drift; following are specific objectives:

- Describe the evolution of water composition and solid precipitates in the backfill above the drip shield and waste package (Zone 3/4) and above the invert and the lower part of the backfill (Zone 5/6).

- Evaluate the effects of corrosion products from structural steel, leachate from cementitious materials, and degradation products from other human-made, introduced materials, on the EBS bulk chemical environment.

- Assess the effects of microbial processes on the bulk chemical environment.

- Assess the effects of colloid formation and transport on the bulk chemical environment.

Reaction cells corresponding to the composite zones of Table 24, are used to estimate the chemical evolution of the bulk environment. The number of such cells is limited by the computational effort required to calculate the evolution of the EBS environment for 10,000 yr or longer. The three composite zones in Table 24 are based on the six zones calculated with the TH model. They constitute the smallest number of zones that can be used to represent compositionally similar regions: host rock above the drift, backfill above the drip shield, and the backfill/invert in the lower part of the drift.

6.7.1 Simulation of Water Composition in Zone 1/2

The host rock above the drift is represented by a compositional boundary condition at Zone 0 and by a reaction cell at Zone 1/2. The flux of water from Zone 0 to Zone 1/2 is calculated by the TH Model (Section 6.1); the composition of this flux is similar to that of J-13 water (DTN LL980711104242.054). Previous work has shown that J-13 water composition is chemically analogous to fracture waters in the host rock (Harrar et al. 1990) and is suitable for reasonable-bound treatment of pH effects from evaporative concentration (Sections 4.1.5 and 6.5.8.1).

Using EQ3/6 for Zone 1/2, the J-13 water composition is modified by elevated temperature, P_{CO2}, evaporative concentration, and mineral interaction. Separate models for each time period were prepared using the input data shown in Table 25. These are equilibrium models based on EQ3NR (Wolery 1992b;this code is part of the EQ3/6 code package). The approach is justified because the starting (Zone 0) composition is already close to solubility equilibrium with host rock minerals. Estimates of reactive surface area for the host rock are not required.

The calculations for Zone 0 and Zone 1/2 waters are based on a conceptual model for J-13 water in which the HCO_3^-, H^+, and Ca^{2+} components are mutually controlled by the fugacity of CO_2, equilibrium with calcite, and electrical charge balance. The model also assumes that the minor Al^{3+}, Fe^{2+}, and Mg^{2+} components are controlled by equilibrium with selected ideal clay minerals and that minor Mn^{2+} is controlled by equilibrium with pyrolusite (MnO_2). Other components are taken to follow specified concentrations based on Harrar et al. (1990), corrected for a specified degree of evaporative concentration in the case of Zone 1/2 waters (but not in that of Zone 0 waters).

Major and minor host rock minerals are included in the calculations (silica polymorphs, hematite, MnO_2, smectites, calcite, etc. as indicated in the "data0.elh" file used for the

calculations). Feldspars are not included because they dissolve slowly. Hematite could be used to control ferric iron instead of nontronite clay, but this would make little difference to the Fe concentration or the bulk chemical environment. Micas and Al-oxides are not included because they are very unlikely to occur. The clays are much more active as possible precipitates, and as preexisting minerals in the host rock. Kaolinite could have been used to control Al instead of smectite, but kaolinite is uncommon, and this substitution also would have little effect on the bulk chemical environment.

In addition to the above rationale, other phases have been excluded for particular reasons, such as exclusion of quartz in modeling the equilibrium of fracture water with the host rock at elevated temperature. These specially excluded phases, and the underlying reasons, are indicated in the EQ3/6 input files for those problems.

Applied to ordinary ambient J-13 water, using the observed subsurface CO_2 fugacity of 1×10^{-3} bar (Section 6.2), this model yields almost exactly the observed Ca^{2+} concentration and a pH of about 8.1. The model is also attractive because the actual groundwater coexists with calcite, and equilibrium with that mineral is highly likely. The calculated pH is higher than the average value of 7.41 reported by Harrar et al. (1990).

Table 61. Calculated Water Composition in Zone 1/2 for Time Periods 1 through 5

	Nominal Time (years)				
	100	500	1000	2000	5000
Temperature (°C)	80.81	90.05	88.42	79.96	51.69
P_{CO2} (atm)	9.084E-07	1.805E-06	1.536E-06	5.405E-06	3.314E-05
P_{O2} (atm)	2.384E-04	4.736E-04	4.030E-04	1.416E-03	8.608E-03
Evaporation/ Condensation Factor	1.088	0.9778	0.8782	0.9895	0.9995
pH	9.318	9.139	9.162	9.140	9.243
I (molal)	4.273E-03	4.041E-03	3.961E-03	2.924E-03	2.486E-03
Al^{3+}	1.940E-06	2.407E-06	2.265E-06	1.417E-06	2.904E-07
$B(OH)_3(aq)$	1.365E-05	1.227E-05	1.101E-05	1.242E-05	1.255E-05
Ca^{2+}	6.365E-04	6.392E-04	6.866E-04	2.385E-04	4.316E-05
Cl^-	2.191E-04	1.969E-04	1.769E-04	1.993E-04	2.013E-04
F^-	1.249E-04	1.122E-04	1.007E-04	1.135E-04	1.147E-04
Fe^{2+}	8.812E-16	4.994E-16	5.449E-16	9.124E-16	5.698E-15
HCO_3^-	2.250E-05	2.305E-05	2.194E-05	6.406E-05	7.237E-04
K^+	1.403E-04	1.260E-04	1.132E-04	1.276E-04	1.288E-04
Li^+	7.492E-06	6.771E-06	6.051E-06	6.771E-06	6.915E-06
Mg^{2+}	3.148E-10	3.464E-10	3.460E-10	8.011E-10	7.715E-09
Mn^{2+}	1.363E-14	3.649E-14	2.911E-14	2.578E-14	3.708E-15
NO_3^-	1.541E-04	1.385E-04	1.244E-04	1.401E-04	1.415E-04
Na^+	2.167E-03	1.948E-03	1.750E-03	1.971E-03	1.991E-03
SO_4^{2-}	2.084E-04	1.873E-04	1.682E-04	1.895E-04	1.914E-04
$SiO_2(aq)$	3.584E-03	3.741E-03	3.665E-03	2.804E-03	1.275E-03
Sr^{2+}	5.022E-07	4.451E-07	3.995E-07	4.565E-07	4.565E-07

Source: EQ3NR output files for Zone 1/2 (Attachment I)

NOTES: All concentrations in mol/kg H_2O unless otherwise specified

The expected thermodynamic controls on the solution composition can be extrapolated up to approximately the boiling point of the water. One new constraint is required to deal with aqueous silica. This is set to be the greater of the concentration reported by Harrar et al. (1990) or that corresponding to solubility equilibrium with cristobalite. Values of the CO_2 fugacity from Section 6.2, and small corrections for evaporative concentration (of Zone 1/2 waters only) are also applied here.

6.7.1.1 Water Composition in Zone 1/2

The water compositions calculated for Zone 1/2, for each time period, are shown in Table 61. Water compositions are affected principally by temperature-dependent solubility and P_{CO2}. Prograde solubility of cristobalite increases the silica concentration with temperature.

Note that lower CO_2 fugacities result in higher pH values (in the range 8.7–9.2). This pH increase corresponds to the loss of CO_2, which is an acid anhydride. These pH values represent somewhat more alkaline conditions than would be calculated for ambient temperature (e.g., 31°C) owing to the contraction of the upper end of the practical pH range at elevated temperatures. The pH is effectively controlled by the $H_3SiO_4^-$/cristobalite buffer (noting that solubility of aqueous SiO_2 is controlled by cristobalite) and not by the HCO_3^-/CO_3^{2-} buffer. There is a loss of dissolved Ca^{2+} in these calculations for these waters that is effectively due to the precipitation of calcite. The minor dissolved components Al^{3+}, Fe^{2+}, Mg^{2+}, and Mn^{2+} do vary (the concentration of Al^{3+} basically increases with pH) but remain minor.

Minor changes in concentrations of relatively conservative species such as Cl^-, F^-, SO_4^{2-}, NO_3^-, Na^+, and K^+ are caused by evaporative concentration (as prescribed in Table 25).

6.7.2 Simulation of Mineral Precipitation and Water Composition in Zone 3/4

According to the TH Model results (Table 25 in Section 4.1.7.4), water from Zone 1/2 does not enter Zone 3/4 (backfill above the springline) until Time Period 2. During this time period (300 to 700 yr), the liquid influx is exactly balanced by vapor outflux, and the calculated liquid water mass in Zone 3/4 is small. The cumulative liquid influx during the time period is approximately 40,000 times the resident mass of 0.8462 kg (for a half-drift model). Accordingly, the formation of precipitates is calculated ignoring the liquid residue. This is justified because such a small quantity of liquid will be dispersed in the backfill.

6.7.2.1 Normative Assemblage of Evaporative Minerals Formed in Zone 3/4 During Time Period 2

Using the Zone 1/2 water composition for Time Period 2, an assemblage of minerals is calculated using the approach described in Section 6.5. The results are shown in Table 62 for a half-drift model. Approximately 20 kg of various precipitates, on a full-drift basis, mostly consisting of amorphous silica, is predicted to accumulate in the backfill above the springlines.

Table 62. Normative Evaporative Mineral Assemblage Predicted to Accumulate in Zone 3/4 During Time Period 2 (300 to 700 yr)

Mineral	Formula	Moles of Precipitates (mol/m) [a]	Molar Mass (kg/mol) [a]	Mass of Precipitates (kg/m) [a]
Niter	KNO_3	3.993E+00	1.011E-01	4.038E-01
Na-niter	$NaNO_3$	3.934E-01	8.500E-02	3.344E-02
Fluorite	CaF_2	1.778E+00	7.808E-02	1.388E-01
Villiaumite	NaF	0.000E+00	4.199E-02	0.000E+00
Sylvite	KCl	0.000E+00	7.455E-02	0.000E+00
Halite	NaCl	6.239E+00	5.844E-02	3.646E-01
Mg-smectite [b]	$Mg_{0.165}Al_{2.33}Si_{3.67}O_{10}(OH)_2$	6.652E-05	3.667E-01	2.439E-05
Ca-smectite [b]	$Ca_{0.165}Al_{2.33}Si_{3.67}O_{10}(OH)_2$	3.266E-02	3.676E-01	1.201E-02
Na-smectite [b]	$Na_{0.333}Al_{2.33}Si_{3.67}O_{10}(OH)_2$	0.000E+00	1.420E-01	0.000E+00
Thenardite	Na_2SO_4	5.934E+00	1.420E-01	8.429E-01
Anhydrite	$CaSO_4$	0.000E+00	1.361E-01	0.000E+00
Tachyhydrite	$CaMg_2Cl_6O_{10}:12H_2O$	0.000E+00	6.776E-01	0.000E+00
Calcite	$CaCO_3$	1.847E+01	1.001E-01	1.848E+00
Magnesite	$MgCO_3$	0.000E+00	8.431E-02	0.000E+00
Thermonatrite	$Na_2CO_3:H_2O$	2.161E+01	1.240E-01	2.679E+00
Amorphous Silica	SiO_2	1.184E+02	6.009E-02	7.116E+00
Total				1.344E+01

Source: file "normative_hiCO2_L4C4_ui-zone34-500V1.2.xls" (Attachment I)

NOTES: [a] Values correspond to accumulation in a half-drift model. Multiply by two to obtain accumulation in the full drift cross-section.

6.7.2.2 Surface Area of Quartz Sand Backfill in Zone 3/4

The surface area of quartz sand is estimated from a measured-size fraction analysis (Section 4.1.7.5, DTN: MO9912EBSPWR28.001). The sand mass is accounted for using spherical particles, with the mean diameter for each size category, and honoring the proportion of total mass present in each category. Surface area is calculated by summing the areas of the spheres. The calculation is performed in spreadsheet routine "OvertonSandAreaV1.2" (Attachment I). The results are tabulated in terms of sand surface area per mass of liquid in Zone 3/4 and Zone 5/6 in each time period (Table 63).

Table 63. Surface Area Calculation for Quartz-Sand Backfill in Composite Zones 3/4 and 5/6, Expressed as Surface Area per Mass of Solvent

	Composite Zones	
	Zone 3/4	Zone 5/6
	Sand Surface (m^2/m)	
	1.102E+05	2.073E+04
Liquid Mass (kg/m)		
Time Period 1	0.000E+00	0.000E+00
Time Period 2	2.500E+00	0.000E+00
Time Period 3	2.553E+02	7.242E+00
Time Period 4	3.933E+02	2.043E+02
Time Period 5	4.412E+02	2.232E+02
Ratio of Sand Surface Area to Liquid Mass (m^2/kg)		
Time Period 1		
Time Period 2	4.406E+04	
Time Period 3	4.316E+02	2.863E+03
Time Period 4	2.802E+02	1.015E+02
Time Period 5	2.497E+02	9.290E+01

Source: file "OvertonSandAreaV1.2.xls" (Attachment I)

This calculation provides a lower bound on the quartz surface area because (a) real sand particles have more surface area than do spheres with the same mass, and (b) the mass of particles passed through the 0.053 mm sieve was not taken into account.

6.7.2.3 Kinetics of Quartz Precipitation

The kinetics of quartz precipitation is an important issue because of the use of Overton sand (a quartz sand) as backfill. In the rock surrounding the drift, quartz—and its less stable polymorph, cristobalite—coexist out of chemical equilibrium on a geologically long-term basis because the growth rate of quartz is quite small (Rimstidt and Barnes 1980). The concentration of dissolved silica corresponds to near-equilibrium with cristobalite (and supersaturation with respect to quartz). This condition is maintained in the rock at Yucca Mountain because of the slow growth kinetics of quartz. That condition may be replaced in the sand backfill by one of near-equilibrium with quartz, resulting in a significant drop in dissolved silica. This has some implications for pH and pH-buffer capacity. At sufficiently low fugacity of CO_2, the pH may rise to high values (>10), and buffers such as $H_3SiO_4^-/SiO_2(aq)$, and $NaH_3SiO_4(aq)$/cristobalite, and $NaH_3SiO_4(aq)$/quartz may become controlling.

The precipitation and dissolution of silicate minerals is generally accepted to be a surface area-mediated process (i.e., the rate is proportional to the area of the mineral-water interface). The kinetics for quartz and other SiO_2 minerals was studied by Rimstidt and Barnes (1980). Their rate law and data for quartz growth were used to examine the rate of quartz growth (via overgrowths) in the backfill. In the backfill, the surface area of quartz far exceeds that available in the surrounding rock (per unit mass or volume of groundwater). Contact of influent water with

the sand backfill may result in a rapid development of quartz overgrowths and a significant drop in dissolved silica (from near cristobalite solubility to near quartz solubility). As the water passes back into the rock, the dissolved silica would be expected to rise again because of the dissolution of cristobalite.

6.7.2.4 Redissolution of Evaporative Minerals in Zone 3/4

All calculations in Zone 3/4 (and Zone 5/6) were conducted using the EQ6 code (Wolery and Daveler 1992; this is another code in the EQ3/6 package). This code directly simulates processes involving water reacting with other substances.

The evaporative mineral assemblage comprises minerals with solubilities greater than 1 molal (e.g., niter, halite, thermonatrite). It is possible for much of the accumulated mineral mass described in Table 62 to be redissolved by a small amount of water. However, it is also possible that spatially heterogeneous liquid permeability, and the limited solubility of amorphous silica, could impede rapid dissolution. For this model, redissolution is assumed to occur congruently, with a final-solution ionic strength of 1 molal (Assumption 5.7.1).

Redissolution is modeled by introducing the water composition from Zone 1/2 into Zone 3/4 at the start of Time Period 3 (700 to 1500 yr). In the EQ6 model, the evaporative mineral assemblage is titrated into 1 kg of liquid water until the ionic strength is 1 molal (within 1%). Quartz is present as the major component of the sand backfill; in the final model calculations, equilibrium with this mineral is assumed to control the concentration of dissolved silica.

The 1 molal ionic strength limit is artificial and corresponds to the upper limit of practical usage of the B-dot activity coefficient model. This probably underestimates the efficiency of inflowing groundwater in redissolving the evaporite mineral assemblage because higher ionic strengths are likely to be achieved. The time period required to effectively remove this assemblage (Time Period 3A), using this estimate of removal efficiency, is therefore an upper bound. It nevertheless indicates a relatively rapid removal (the duration of Time Period 3A is less than 14.6 yr, which is much less than that of Time Period 3B, the remainder of Time Period 3).

A calculation using EQ6 and the Rimstidt and Barnes (1980) rate law and kinetic data for quartz growth (coupled with a geometric estimate of the appropriate surface area) was made, starting with fluid in which the other processes had already been completed. This computation yielded a decline in dissolved silica to a value closely corresponding to quartz solubility in less than one year. Because the actual effective surface area might be three times higher because of surface roughness, just one-third of a year might produce the same result. Also, the decline in dissolved silica follows an exponential decay pattern in which most of the decline takes place early in the process; thus, most of the effect could be achieved in even less time. Because of these factors, the other calculations of processes in Zone 3/4 (and later in Zone 5/6) were made assuming instantaneous equilibration with quartz (an easier calculational constraint to deal with).

The results from EQ6 modeling of precipitate redissolution and other processes in Time Period 3A are shown in Table 64. In Time Period 3A, quartz and calcite are precipitated as the evaporative precipitates (apart from calcite) are redissolved. Both of these minerals are present at the start of this time period, and more of each is deposited. CO_2 is initially evolved during

Table 64. Composition of Water in Zone 3/4 After Return of Liquid Water Through-Flow and Starting with Redissolution of Evaporative Precipitates in Time Period 3A.

	Time Period			
	3A	3B	4	5
Temperature (°C)	96.05	96.05	86.95	56.95
P_{CO2} (atm)	1.536E-06	1.536E-06	5.405E–06	3.314E–05
P_{O2} (atm)	4.030E-04	4.030E-04	1.416E–03	8.608E–03
Evaporation/Condensation Factor	10.635	10.635	1.0950	1.004
pH	11.081	9.920	9.276	9.319
I (molal)	1.001E+00	2.025E–02	2.812E–03	2.502E–03
Al^{3+}	1.815E-03	2.410E-05	1.551E-06	2.915E-07
$B(OH)_3(aq)$	1.170E-04	1.172E-04	1.360E-05	1.260E-05
Ca_2^+	7.280E-06	3.548E-05	1.194E-04	3.061E-05
Cl^-	1.485E-01	1.882E-03	2.182E-04	2.021E-04
F^-	6.836E-02	1.072E-03	1.243E-04	1.152E-04
Fe^{2+}	5.788E-15	5.372E-15	9.990E-16	5.721E-15
HCO_3	7.208E-02	1.549E-04	7.878E-05	8.148E-04
K^+	9.502E-02	1.205E-03	1.397E-04	1.293E-04
Li^+	6.427E-05	6.439E-05	7.414E-06	6.943E-06
Mg^{2+}	5.583E-13	4.525E-11	8.771E-10	7.746E-09
Mn^{2+}	5.583E-13	3.098E-13	2.823E-14	3.722E-15
NO_3^-	1.044E-01	1.323E-03	1.534E-04	1.421E-04
Na^+	1.469E+00	1.862E-02	2.158E-03	1.999E-03
SO_4^{2-}	1.412E-01	1.790E-03	2.075E-04	1.922E-04
$SiO_2(aq)$	7.139E-01	7.821E-03	1.481E-03	5.339E-04
Sr^{2+}	9.846E-08	8.840E-07	4.998E-07	3.648E-07
Moles Dissolved (<0 = Formed) per 1 kg Influent H_2O				
Halite	1.380E-02			
Niter	8.833E-03			
$NaNO_3$	8.706E-04			
Mg-smectite	1.472E-07			
Thenardite	1.313E-02			
Thermonatrite	4.781E-02			
SiO_2 (amophous)	2.620E-01			
Fluorite [a]	3.170E-03			
Ca-smectite	7.227E-05			
Calcite	-3.900E-03	-6.832E-04	-1.295E-04	-1.267E-05
Quartz	-1.988E-01	-2.930E-03	-1.451E-03	-7.432E-04
Moles Evolved (<0 = Used) per 1 kg Influent H_2O				
CO_2 (g)	3.720E-02	-6.800E-04	-1.400E-04	-1.000E-04

Source: EQ6 output files for Zone 3/4 (Attachment I)

NOTES: All concentrations in mol/kg H_2O unless otherwise specified.

Normative species with zero predicted abundance are not reported in this table.

Fluorite is solubility-limited and slow to dissolve; the figure shown results in removal of ~80% of the accumulated fluorite.

redissolution (including titration of calcite into solution) but is consumed in Time Period 3B (note that an "open-system," or constant-fugacity, CO_2 boundary condition is used). The pH rises to about 10.8 in Time Period 3A (the maximum value encountered in the calculations presented here). This is mainly because of the strong evaporative concentration (90.6%), which concentrates the OH^- component in solution to about 0.62 molal. In later time periods, the extent of evaporation is not so great, and the pH does not rise so high.

Approximately 14 yr are needed to redissolve the accumulated precipitates with 1 molal ionic strength (calculated in spreadsheet file: "normative_hiCO2_L4C4_ui-zone34-500.xls"; worksheet: 700 to 1500 yr).

6.7.2.5 Water Composition in Zone 3/4 After Redissolution of Evaporative Minerals

After Time Period 3, the water composition in Zone 3/4 returns to conditions that are similar to those of Zone 1/2 (host rock) except for the effects of achieving equilibrium or near-equilibrium with quartz and evaporative concentration, which remains strong. More calcite continues to precipitate, and CO_2 continues to be consumed.

6.7.3 Simulation of Mineral Precipitation and Water Composition in Zone 5/6

According to the TH Model results (Table 25 in Section 4.1.7.4 and Section 6.1), water from Zone 3/4 does not enter Zone 5/6 (backfill below the springline plus crushed tuff invert) until Time Period 3. During this time period (700 to 1500 yr), the liquid influx is exactly balanced by vapor outflux, and the calculated liquid water mass in Zone 5/6 is limited. The cumulative liquid influx during the time period is approximately 3600 times the resident mass of 7.242 kg (for a half-drift model). The formation of precipitates is calculated ignoring the liquid mass because of the large accumulation (100 kg) of precipitate (Table 65).

Table 65. Normative Evaporative Mineral Assemblage Predicted to Accumulate in Zone 5/6 During Time Period 3 (700 to 1500 yr)

Mineral	Formula	Moles Precipitates Time Period 3A (mol/m) [A]	Moles Precipitates Time Period 3B (mol/m) [A]	Total Moles Precipitates (mol/m) [A]	Molar Mass (kg/mol) [A]	Mass of Precipitates (kg/m) [A]
Niter	KNO_3	6.228E+01	3.081E+01	9.309E+01	1.011E-01	9.413E+00
Na-niter	$NaNO_3$	6.140E+00	3.037E+00	9.177E+00	8.500E-02	7.800E-01
Fluorite	CaF_2	4.772E-03	9.075E-01	9.123E-01	7.808E-02	7.123E-02
Villiaumite	NaF	4.480E+01	2.560E+01	7.040E+01	4.199E-02	2.956E+00
Sylvite	KCl	0.000E+00	0.000E+00	0.000E+00	7.455E-02	0.000E+00
Halite	NaCl	9.733E+01	4.813E+01	1.455E+02	5.844E-02	8.501E+00
Mg-smectite [b]	$Mg_{0.165}Al_{2.33}Si_{3.67}O_{10}(OH)_2$	2.218E-09	7.014E-06	7.016E-06	3.640E-01	2.554E-06
Ca-smectite [b]	$Ca_{0.165}Al_{2.33}Si_{3.67}O_{10}(OH)_2$	0.000E+00	0.000E+00	0.000E+00	3.667E-01	0.000E+00
Na-smectite [b]	$Na_{0.333}Al_{2.33}Si_{3.67}O_{10}(OH)_2$	5.106E-01	2.646E-01	7.752E-01	3.676E-01	2.850E-01
Thenardite	Na_2SO_4	9.259E+01	4.578E+01	1.384E+02	1.420E-01	1.965E+01
Anhydrite	$CaSO_4$	0.000E+00	0.000E+00	0.000E+00	1.361E-01	0.000E+00
Tachyhydrite	$CaMg_2Cl_6O_{10}{:}12H_2O$	0.000E+00	0.000E+00	0.000E+00	0.67764	0.000E+00
Calcite	$CaCO_3$	0.000E+00	0.000E+00	0.000E+00	1.001E-01	0.000E+00
Magnesite	$MgCO_3$	0.000E+00	0.000E+00	0.000E+00	8.431E-02	0.000E+00
Thermonatrite	$Na_2CO_3{:}H_2O$	3.146E+02	1.539E+02	4.685E+02	1.240E-01	5.810E+01
Amorphous Silica	SiO_2	4.660E+02	1.990E+02	6.651E+02	6.009E-02	3.996E+01
Total						1.397E+02

Source: file "normative_hiCO2_l4c4_ui-zone56-1000V1.2.xls" (Attachment I)

NOTE: [A] Values correspond to accumulation in a half-drift model. Multiply by two to obtain accumulation in the full drift cross-section.

6.7.3.1 Normative Assemblage of Evaporative Minerals Formed in Zone 5/6 During Time Period 3

Using the Zone 3/4 water composition for both Time Period 3A and Time Period 3B, an assemblage of minerals is calculated using the approach described in Section 6.5. The results are shown in Table 65 for a half-drift model. Hundreds of kilograms of precipitates and salts, on a full-drift basis, are calculated to accumulate in the lower backfill and invert, per each meter of drift. These precipitates/salts consist mostly of amorphous silica, and also include calcite, halite, and other species.

6.7.3.2 Surface Area of Quartz-Sand Backfill in Zone 5/6

Values for the surface area per liquid mass used to model Zone 5/6 are tabulated in Table 63. The calculation is discussed in Section 6.7.2.1 and is performed in spreadsheet routine "OvertonSandAreaV1.2" (Attachment I).

6.7.3.3 Redissolution of Evaporative Minerals in Zone 5/6

The evaporative mineral assemblage comprises minerals with solubilities greater than 1 molal (e.g., niter, halite, thermonatrite). As discussed for Zone 3/4, it is possible for much of the accumulated mineral mass described in Table 65 to be redissolved by a small amount of water. For this model, redissolution is assumed to occur congruently, with final solution ionic strength of 1 molal (Assumption 5.7.1).

Redissolution is modeled by introducing the water composition from Zone 3/4 into Zone 5/6 at the start of Time Period 4 (1500 to 2500 yr). In the EQ6 model, the evaporative mineral assemblage is titrated into 1 kg of liquid water until the ionic strength is 1 molal (within 1%). Equilibrium with quartz is again assumed because of the large surface area presented by the sand backfill. Some crushed tuff is present at the bottom of Zone 5/6 (in the invert). It is likely that the concentration of silica may rise once the water reaches this material. However, the surface area is much smaller, relatively speaking. Therefore, such a potential increase in dissolved silica has been ignored in the present calculations.

The evaporite minerals are redissolved in the short Time Period 4A analogous to Time Period 3A. The processes and results for Zone 5/6 during Time Period 4A are qualitatively very similar to those for Zone 3/4 during Time Period 3A.

The results from EQ6 modeling of precipitate redissolution and other processes are shown in Table 64. Quartz and calcite precipitated as the evaporative precipitates (apart from calcite) are redissolved. CO_2 is initially evolved during redissolution (including titration of calcite into solution) but is consumed in Time Period 3B (note that an open-system, or constant-fugacity, CO_2 boundary condition is used).

Approximately 40 yr are required to redissolved the accumulated precipitates with 1 molal ionic strength (calculated in spreadsheet file: "normative_hiCO2_L4C4_ui-zone56-1000.xls"; worksheet: 1500 to 2500 yr, Attachement I).

Table 66. Composition of Water in Zone 5/6 After Return of Liquid Water Through-Flow and Starting with Redissolution of Evaporative Precipitates in Time Period 4A

	Time Period		
	4A	4B	5
Temperature (°C)	88.46	88.46	58.90
P_{CO2} (atm)	5.405E–06	5.405E–06	3.314E–05
P_{O2} (atm)	1.416E–03	1.416E–03	8.608E–03
Evaporation/Condensation Factor	1.046	1.046	1.003
pH	10.952	9.268	9.320
I (molal)	9.999E-01	2.931E-03	2.504E-03
Al3+	1.477E-03	1.622E-06	2.924E-07
B(OH)3(aq)	1.419E-05	1.423E-05	1.264E-05
Ca^{2+}	7.209E-06	1.219E-04	2.987E-05
Cl^-	1.188E-01	2.282E-04	2.027E-04
F^-	5.949E-02	1.300E-04	1.155E-04
Fe^{2+}	1.042E-15	1.045E-15	5.738E-15
HCO_3^-	1.538E-01	7.555E-05	7.912E-04
K^+	7.605E-02	1.461E-04	1.297E-04
Li^+	7.734E-06	7.755E-06	6.964E-06
Mg^{2+}	2.381E-13	8.473E-10	7.769E-09
Mn^{2+}	2.945E-14	2.953E-14	3.733E-15
NO_3^-	8.355E-02	1.605E-04	1.425E-04
Na^+	1.176E+00	2.257E-03	2.005E-03
SO_4^{2-}	1.130E-01	2.170E-04	1.928E-04
SiO_2(aq)	4.039E-01	1.543E-03	5.355E-04
Sr^{2+}	8.039E-08	5.228E-07	3.659E-07
Moles Dissolved (<0 = formed) per 1 kg Influent H_2O			
SiO_2 (amophous)	5.171E–01		
Halite	1.137E–01		
Niter	7.277E–02		
$NaNO_3$	7.173E–03		
Fluorite	7.906E–04		
Villiaumite	5.533E–02		
Mg-smectite	6.084E–09		
Na-smectite	6.069E–04		
Thenardite	1.082E–01		
Thermonatrite	3.661E–01		
Calcite	–9.031E–04	-2.856E-06	-8.281E-07
Quartz	–1.336E–01	-5.682E-06	0.000E+00
Moles Evolved (<0 = Used) per 1 kg Influent H_2O			
CO_2 (g)	2.178E–01	0.000E+00	0.000E+00

Source: EQ6 output files for Zone 5/6 (Attachment I)

NOTES: All concentrations in mol/kg H_2O unless otherwise specified.
Normative species with zero predicted abundance are not reported in this table.

6.7.3.4 Water Composition in Zone 5/6 After Redissolution of Evaporative Minerals

After Time Period 4, the water composition in Zone 5/6 returns to conditions that are similar to those in Zone 1/2 (host rock); this can be verified by comparing water compositions for Time Period 4B and Time Period 5 in Table 61 and Table 66. Quartz and calcite precipitation and CO_2 consumption in Time Period 4 are less than in Zone 3/4 during Time Period 5, probably because the influent waters to Zone 5/6 have already reacted to elevated temperature and contact with quartz in the previous zone.Steel Corrosion

Corrosion of structural steel used in ground support, the invert, and conveyances within the emplacement drifts is important as a potential sink for oxygen and as a source for ferric precipitates and colloids. Alloy A572 has been identified for use in ground support and the invert (CRWMS M&O 2000a) (TBV-3902). The mass and surface area of steel are shown in Table 27.

Structural steel corrosion is important not because the steel will fail, which is certain during the first few hundreds or thousands of years after repository closure, but because corrosion consumes oxygen. Depending on the corrosion rate, oxygen fugacity in the EBS could decrease to levels that promote production of hydrogen as the steel corrodes, which in turn can promote corrosion of CRMs.

6.7.4 Scoping Calculation of Oxygen Demand

A simple mass balance provides perspective on the potential chemical oxygen demand by steel in the EBS. Corrosion-resistant materials (i.e. titanium and Alloy-22) are not considered in the oxygen calculation because their demand is low (Assumption 5.7.5) From Table 27, the total mass of steel in all zones is 1185 kg per meter of drift. Assuming a half-reaction of the form

$$Fe(s) + H_2O + \frac{O_2}{2} = FeOOH(s) + H^+ + e^-$$

(Eq. 85)

the reactant mole ratio is Fe:O. The required mass of oxygen is

$$m_{O2} = m_{Fe} \cdot \frac{FW_{O2}}{FW_{Fe}}$$

(Eq. 86)

where

m_{Fe} = mass of iron (1185 kg/m)

FW_{O2} = formula weight of molecular oxygen (16.0 g/mol)

FW_{Fe} = formula weight of iron (55.8 g/mol)

Substituting values gives a total oxygen demand of m_{O2} = 339 kg/m. Dividing by the molecular weight of O_2 gas (32.0 g/mol) converts this value to 1.06×10^4 mol O_2/m, or 238 m^3 of O_2 gas at standard temperature and pressure (0°C, 1 atm). Taking the gas-filled porosity of the host rock as 1 percent, this mass of oxygen is contained in 2.38×10^4 m^3 of host rock, which is approximately equal to the entire volume of rock above the repository.

The cumulative flux of O_2 gas into an emplacement drift, is calculated for the L4C4 location and "upper" infiltration, using different approaches as shown in Figure 28. The figure also indicates the total oxygen required for complete corrosion of EBS carbon steel as calculated above. It shows that the cumulative flux of O_2 will eventually be sufficient to satisfy the oxygen demand, but this may not occur until several thousand years after closure. Corrosion will begin when relative humidity conditions permit (RH > 0.7), which will begin after only a few hundred years, for most locations in the potential repository. Therefore there may be a decrease in the O_2 fugacity in the drifts. The Gas Flux and Fugacity Model (Figure 25) suggests that the decrease could be an order of magnitude or more, if the O_2 consumption rate approaches the calculated maximum flux, compared with fugacity conditions without consumption. The oxygen demand will actually be satisfied by gas-phase transport throughout the repository block, i.e. multi-dimensional transport, which will moderate the fugacity decrease.

In summary, this scoping calculation shows the needed oxygen is available in the host rock and can be replaced by natural processes, at a rate that is comparable to the rate of corrosion discussed below.

Corrosion Rate for Structural Steel

Whereas Alloy A572 has not been tested under controlled conditions representing repository service, long-term corrosion testing of compositionally similar A516 has been performed for the waste-package program (CRWMS M&O 2000b) (TBV-4586). An empirical rate expression for A516 corrosion in a vapor-phase environment is used to represent A572 in repository emplacement drifts (Assumption 5.7.2). In the expression, the corrosion rate depends on temperature and on the pH and NaCl concentration of the aqueous phase (Section 4.1.7.7). The corrosion rate does not depend on the cumulative extent of corrosion (Assumption 5.7.3). In this model, the onset of corrosion is delayed until RH increases to 70% (Assumption 5.7.4). Also, while precipitates are redissolved in the EBS, the corrosion rate is calculated for the chemical conditions present for most of the time period (Time Period 3B and Time Period 4B) rather than at the beginning (Assumption 5.7.5). Finally, when the threshold RH criterion for corrosion is reached before there is water through-flow (i.e., for Zone 5/6, Time Period 3), the influent water composition controls the corrosion rate (Assumption 5.7.6).

Order-of-magnitude estimates for steel corrosion rate and O_2 consumption are calculated in an attached spreadsheet routine (file: "th+gas_model-L4C4-ui-04.xls"; worksheet: Steel). These results indicate the following:

- Steel present in the drifts can completely corrode in a few hundreds to thousands of years

- The rate of steady-state oxygen consumption can exceed the maximum 1-D flux calculated to intercept the 5.5-m diameter drift

- Corrosion rate is especially sensitive to pH, which varies by approximately 2 pH units with time, and across the EBS. Equation 10 shows that the pH effect is an order of magnitude greater than the temperature effect and is greater than the salt concentration effect except when C_{NaCl} exceeds approximately 1% (which only occurs when evaporative precipitates are dissolved).

These results indicate that oxygen fugacity in the EBS could be decreased through a combination of steel corrosion and the air-mass-fraction effect discussed in Section 6.2. Steel corrosion rates calculated in this model (file: "th+gas_model-L4C4-ui-04.xls"; worksheet: Steel) may be lower bounds for the potential repository because of the stated assumptions and because of the choice of the L4C4 location with the "upper" infiltration distribution as the reference TH Model (Section 6.1). If so, the magnitude of O_2 depletion would be less, but the duration could be extended.

6.7.5 Effects of Microbial Activity

Microbial activity has been shown to accelerate the corrosion rate for carbon steel by a factor of approximately six (Assumption 5.4.5; Section 6.4). Thus, microbial activity could further decrease the oxidation potential in the EBS. Occurrence of suboxic conditions could also lead to changes in the microbial ecology of the host rock.

6.7.6 Corrosion-Resistant Materials

Slow consumption of oxygen by corrosion of Ti-7 or Alloy-22 could contribute slightly to depletion of oxygen in the EBS. However, the potential rate of consumption is a small fraction of the oxygen availability calculated from the Gas Flux and Fugacity Model. For example, a Ti drip shield with surface area of 10 m^2/m corroding to TiO_2 at a rate of 1 μm/yr would require an oxygen flux of

$$O_2 \text{ Mass Flux} = Ar\rho_{Ti} \cdot \frac{MW_{O2}}{MW_{Ti}}$$

(Eq. 87)

where

A	= area (e.g., 10 m^2/m)
r	= general corrosion penetration rate (e.g., 10^{-6} m/yr = 3.17×10^{-14} m/sec)
ρ_{Ti}	= Ti density (4.5×10^3 kg/m^3; (Weast and Astle 1981, p. B-159)
MW_{O2}	= molecular weight of O_2 (0.032 kg/mol; (Weast and Astle 1981, p. B-126)
MW_{Ti}	= formula weight of Ti (0.0479 kg/mol; (Weast and Astle 1981, p. B-159)

Substituting these values gives a mass flux of 9.5×10^{-10} kg of oxygen per yr per meter of drift. This is less than 2% of the maximum flux calculated with the reasonable-bound model of Section 6.2. In addition to oxygen consumption, other potential impacts on the EBS bulk chemical environment, from corrosion of the drip shield and waste package, are assumed to be negligible in the 10,000-yr performance period (Assumption 6.7.7).

6.7.7 CO_2 Consumption in the Engineered Barrier System

In this model, CO_2 is consumed or produced by several type of chemical processes:

- Evaporation/condensation processes whereby solution conditions change, and CO_2 is exchanged with the EBS environment
- Precipitation/dissolution reactions involving such species as calcite and thermonatrite
- Cement leaching in which alkaline fluids are discharged to the EBS environment and exchange CO_2

The first two of these processes are summarized in Table 67, which combines results from EQ3 models of Zone 1/2 water composition, the CO_2 demand represented by precipitation of the normative mineral assemblage in Zone 3/4 and Zone 5/6, and the EQ6 models for the redissolution of these precipitates and the subsequent flow of water through the EBS.

These results show that throughout the EBS and the host rock, CO_2 production and consumption are minor, except for interaction with precipitates and salts formed by evaporation during the thermal period (Figure 33). Demand is greatest during formation of the normative assemblage of evaporative precipitates, and dissolution of these precipitates in the next time period.

6.7.7.1 Effects of Cementitious Materials

The CO_2 balance is expanded to include leachate from rockbolts (Table 67). The leachate flow rate and chemistry are described by the Cementitious Materials Model. The results show that the CO_2 demand on equilibration of the leachate with CO_2 and quartz sand in the EBS is small compared with consumption and production from other causes. This is primarily controlled by the small volume of leachate, which in turn is related to the permeability of the grout. The leachate flow, and the consequent rate of CO_2 consumption, could increase by approximately one order of magnitude without substantially affecting the cumulative CO_2 balance shown in Table 67. This can be concluded by comparing the cumulative 1-D CO_2 flux through an 81-m wide pillar, with the cumulative in-drift CO_2 production, with cement. The availabe CO_2 flux (considering the pillar in addition to the rock directly over the drift opening) far exceeds the difference between the in-drift cumulative CO_2 production, with and without cement.

Table 67. CO_2 Consumption in the Engineered Barrier System from Evaporation and Dissolution/Precipitation Processes

Rate of CO_2 Production

Time Period	Nominal Time (yr)	Maximum 1-D CO_2 Flux to Potential Repository (kg/m-sec)	In-Drift (Full-Drift) Total CO_2 Budget Produced (kg/m-sec)	Incl. Host Rock (wrt Zone 0) CO_2 Budget Produced (kg/m-sec)	In-Drift with Cement CO_2 Budget Produced (kg/m-sec)	Percent Change in CO_2 Budget w/ Cement (%)
1	100	8.03E-10	0.00E+00	-1.84E-10	0.00E+00	0.0
2	500	8.03E-10	-1.73E-10	-1.05E-10	-1.74E-10	1.1
3A	1000	8.03E-10	-7.63E-09	-6.94E-09	-7.64E-09	0.1
3B	1000	8.03E-10	-8.24E-10	-1.29E-10	-8.33E-10	1.0
4A	2000	8.03E-10	4.45E-08	6.39E-08	4.45E-08	0.0
4B	2000	8.03E-10	-4.47E-11	1.99E-11	-5.10E-11	14.1
5	5000	8.03E-10	-2.29E-11	3.51E-11	-3.95E-11	72.4

Cumulative CO_2 Production

Time Period	Time Period Duration (yr)	Cumulative 1-D CO_2 Flux through an 81-m Pillar (kg CO_2/m)	In-Drift (Full-Drift) Total Cumulative CO_2 Produced (kg CO_2/m)	Incl. Host Rock (wrt Zone 0) Cumulative CO_2 Produced (kg CO_2/m)	In-Drift with Cement Cumulative CO_2 Produced (kg CO_2/m)
1	250	6.34E+00	0.00E+00	-1.45E+00	0.00E+00
2	400	1.65E+01	-2.18E+00	-2.78E+00	-2.20E+00
3A	14	1.68E+01	-5.55E+00	-5.84E+00	-5.58E+00
3B	783	3.67E+01	-2.59E+01	-9.03E+00	-2.62E+01
4A	40	3.77E+01	3.03E+01	7.17E+01	3.00E+01
4B	892	6.03E+01	2.90E+01	7.22E+01	2.86E+01
5	5000	1.87E+02	2.54E+01	7.78E+01	2.24E+01

Source: file "CO2balanceV1.2.xls" (Attachment I)

NOTES: Positive values for CO_2 production signify release of CO_2 to the gas phase; negative production signifies net consumption.
Half-drift (symmetry model) results are multiplied by two to obtain full-drift results.

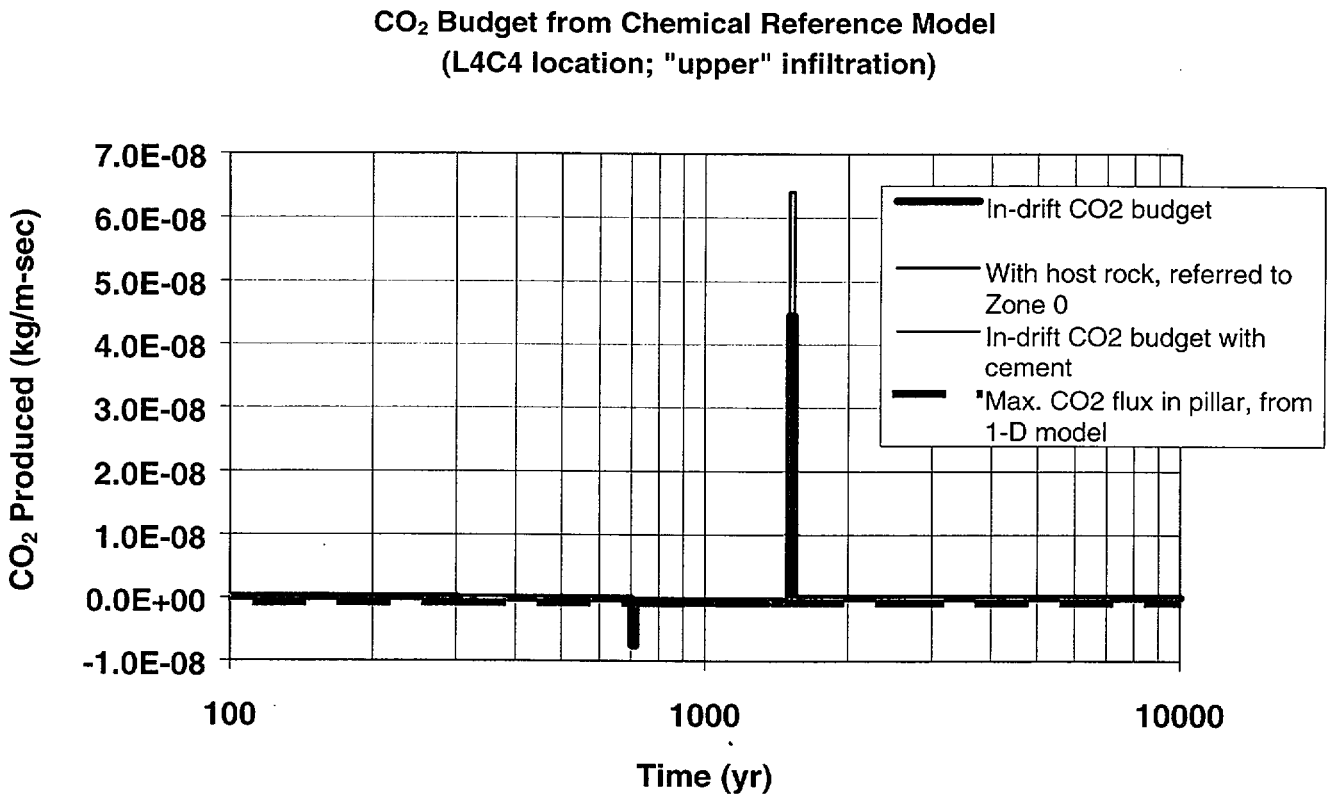

Figure 33. CO_2 Budget for Reference Model (L4C4 location; "upper" infiltration)

Leachate composition is similar to the water composition that evolves when evaporative precipitates are redissolved (compare Table 64 compositions with the Cementitious Materials Model, Table 39).

6.7.8 Chemical Reference Model Validation

The reference model is valid for its intended use at conceptual level, which is to improve understanding of changes in the EBS bulk chemical environment during thermal evolution of the potential repository, and to support post-closure aspects of the design basis for the drip shield and waste package. The Chemical Reference Model combines inputs from the submodels including TH Model, Gas Flux and Fugacity Model, Normative Precipitates and Salts Model, and other aspects of the EBS Physical and Chemical Environment Model to produce a description of chemical processes in the EBS. Model validation for these submodels or components of the Chemical Reference Model was provided in Sections 6.1 through 6.6. Based the validation results of the submodels, the Chemical Reference Model provides valid predictions of solution composition and mineral precipitation and dissolution at conceptual level . These predictions are based on use of EQ3/6 software implemented in accordance with past

practices. The thermodynamic and kinetic data used were taken from widely used sources. There are uncertainties associated with the reference model, particularly the discretization discussed previously. However, these are bounding, or are caused by calculating the average composition of the bulk environment, and are therefore consistent with the intended use of the model at conceptual level.

6.7.9 Discussion and Summary of the Bulk Chemical Environment

Chemical reaction-cell modeling shows that mobile water in the backfill can approach pH 11 when evaporative salts and precipitates are present. Higher pH may occur locally in waters that are saturated with respect to salts such as thermonatrite, but which have high ionic strength ($I >> 1$ molal) and were not modeled in this report. As relative humidity increases during cooldown, the salt-saturated brines will eventually become diluted, and pH will decrease. The principal uncertainties associated with this model arise from heterogeneity of hydrologic processes, and from spatial and temporal discretization.

Calculations show that precipitates can be readily redissolved and removed, by seepage fluxes which are comparable in magnitude to those which evaporated to produce the precipitates in the first place. There are no chemical constraints that would prevent rapid redissolution of precipitates and salts, however, there may be hydrologic factors such as flow heterogeneity that limit access of water to soluble salts.

The reference model is chosen to maximize seepage influx, evaporative solution concentration, and formation of precipitates and salts. Some important comments on the reference model results are as follows:

- Temporal and spatial discretization may cause overestimation of the total mass of precipitated salts, and the residence time of salts in the backfill and invert. Spatial granularity also causes averaging of the calculated chemical conditions in the host rock, backfill, and invert.

- Redissolution of precipitates and salts may occur faster (with higher pH and dissolved solids) or slower (lower pH and dissolved solids) than predicted by the reference model.

- Saturated brines will form when precipitates and salts are present, and there is sufficient humidity. The reference model considers the chemical effects when precipitated salts are diluted to 1 molal ionic strength by seepage, however, because of hydrologic uncertainty the bounding chemical condition is the continued presence of salts which are in equilibrium with the humidity in the drift environment.

For application of the reference model to bounding conditions for corrosion of the drip shield, saturated brine would be present after the start of Time Period 2 (300 to 700 years), when relative humidity exceeds 50 percent (for nitrate salts) or 85 percent (for other salts). The different salts can occur separately, or in mixtures. Brine concentration will decrease as the relative humidity increases.

Based on the foregoing discussion, relative humidity can be used as a "master variable" in bounding models for water composition in contact with the drip shield or waste package. Evolution of relative humidity at the drip shield surface, for the four TH models calculated in Section 6.1, is shown in Figure 34. In general, it is shown that the model has an appropriate level of confidence suitable for its intended use.

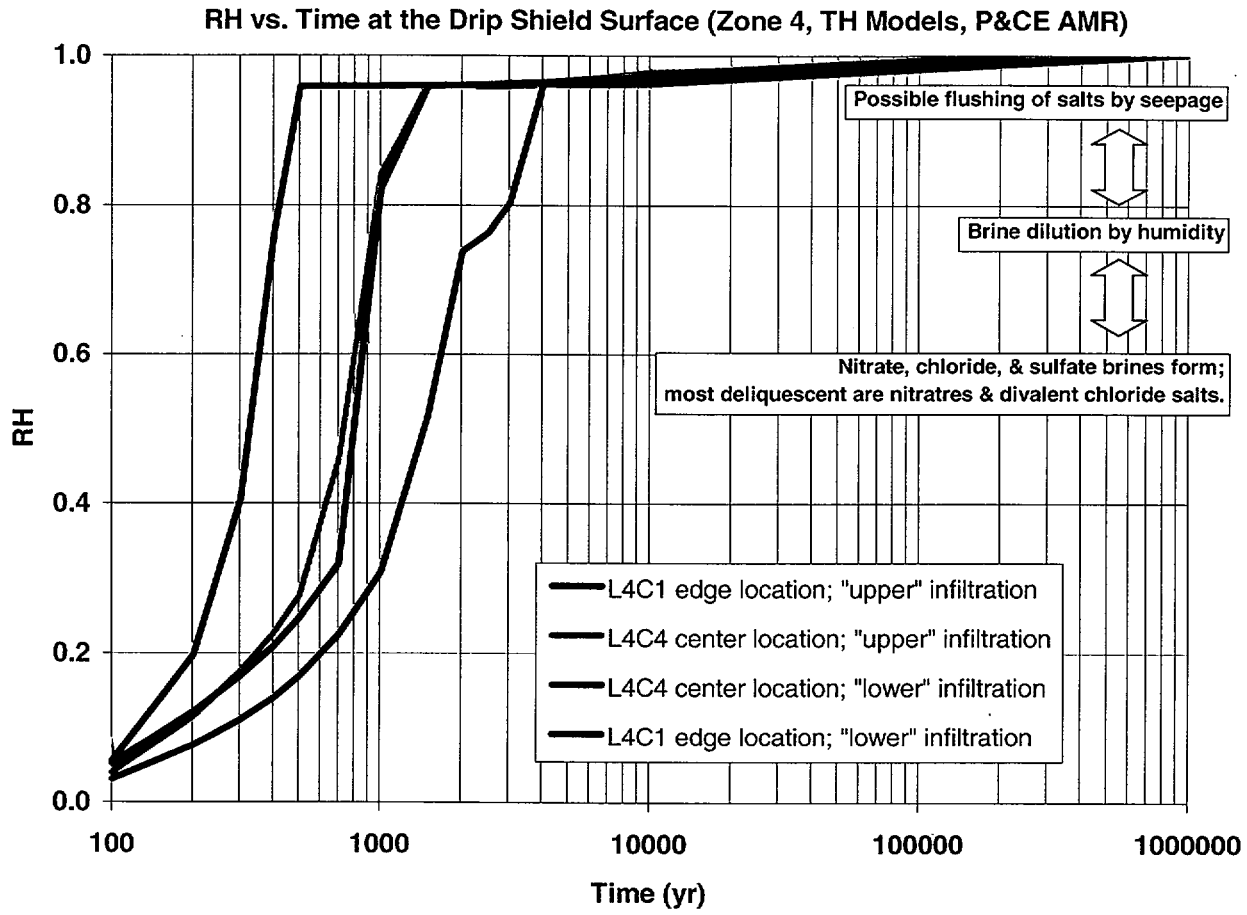

Figure 34. Relative Humidity vs. Time Averaged in the Backfill Region Just Above the Upper Drip Shield Surface (Zone 4)

7. CONCLUSIONS

This report follows the work scopes presented in Section 1 and fulfill the specific tasks and activities included in the development plan (CRWMS M&O 1999c) as documented in previous sections. The following sections summarize the results and conclusions from the constituent models of the EBS P&CE Model:

- Thermal Hydrology Model
- Gas Flux and Fugacity Model
- Cementitious Materials Model
- Microbial Effects Model
- Normative Precipitates and Salts Model
- EBS Colloids Model
- Chemical Reference Model

Descriptions of the models listed above were provided in Sections 6.1 through 6.7. The model validation includes provision of scientific literature, parameter input, assumptions, simplifications, initial and boundary conditions; explanation of how the software are used; expected source of uncertainty (i.e.TBV tracking); comparison with data from measurements or from alternative conceptual models; and computer data files to allow independent repetition of the model simulation. It is determined that these models are validated for their intended use at conceptual level. The uncertainties and restrictions of the models are provided in the summary sections of each model in Section 6.

These results and conclusions form the basis for specifying the environment in which the drip shield and waste package must perform and for EBS performance-assessment calculations. (Note that although the models described in this report develop data, but it is not expected to be directly used as inputs for other technical products. It is expected that only a summary of information will be used. Therefore no DTNs are provided for model output at this time.)

The software and most of the inputs used in this AMR are TBV; therefore all conclusions are unqualified. The use of any unqualified technical information or results from this model as input in documents supporting construction, fabrication, or procurement, or as part of a verified design to be released to another organization, is required to be identified and controlled in accordance with appropriate procedure.

The impact of uncertainty of some of the key input variables (e.g., infiltration flux and thermal conductivity of the host-rock units) were addressed in previous section of this AMR. Changes to the inputs and/or software will require reproducing this model. This document may be affected by techincal product input information that requires confirmation. Any changes to the document that may occur as a result of completing confirmation activities will be reflected in subsequent revisions. The status of the input information quality may be confirmed by reviw of the Document Input Reference System database.

7.1 THERMAL HYDROLOGY

The environmental conditions needed for chemical modeling were evaluated for six zones representing the in-drift environment and the surrounding host rock. Zone-averaged conditions

were calculated for five time intervals representing the postclosure period from 50 to 10,000 yr after waste emplacement. Four TH cases were run using NUFT V3.0s.

Zone fluxes, evaporation, and analysis of the hypothetical migration of a conservative solute were used to choose one case as a reasonable-bound representation of TH conditions to carry forward in a bounding analysis of the chemical environment. This is the L4C4 location from the multiscale TH Model with the "upper" infiltration distribution. This reasonable-bound case tends to maximize the liquid water flux in the EBS during the thermal period, which enhances the rate of evaporation and the potential for chemical precipitation. The residence time of liquid water in the EBS tends to be minimized because of the liquid flux, and the air mass-fraction tends to be minimized because of the rate of evaporation.

Based on these results, the zone-averaged temperature, liquid masses, and gas- and liquid-phase fluxes are specified for chemical modeling of three composite zones representing the host rock, backfill, and invert.

Temperature

Cooldown occurs sooner for conditions representing the repository edge.

Low-flux conditions produce greater peak temperatures and slower cooldown because less liquid water is available to evaporate and transfer latent heat.

Liquid Saturation and Dryout

The spatial extent of dryout (zero or low liquid saturation) is greater for low-flux conditions.

Water returns to the EBS environment sooner for high-flux conditions and for repository-edge conditions.

After cooldown, the liquid water saturation in the upper part of the backfill is approximately 10 percent to 20 percent, depending on "lower" or "upper" infiltration conditions, respectively.

Evaporation Rate and Air Mass-Fraction

Evaporation tends to be localized to a narrow zone above the dryout zone; this narrow zone recedes toward the drip-shield surface as the heat-source strength decays with time.

The rate of evaporation from all zones is much smaller than the total thermal output of the waste packages for the first few hundred years. When the extent of dryout stabilizes, depending on the timing and magnitude of infiltration flux, more than half of the thermal output is converted to latent heat by evaporation. For the "upper" infiltration distribution, there is more sustained

evaporation than for the "lower" infiltration. The peak in evaporation rate occurs sooner for the repository edge than for the center.

The minimum air mass-fraction is approximately 10^{-3} when evaporation rate is maximized for the reasonable-bound case.

Gas-Phase Mass Flux

For the NUFT V3.0s models used in this report, the gas-phase mass flux is driven by evaporation of water vapor. The maximum upward mass flux during the thermal period occurs in the host rock directly above the drift; it does not necessarily occur at the drift-wall, but may occur several meters within the host rock.

There is a slight circulation whereby the mass flux is downward in the pillar and upward near the drift at the drift elevation. The magnitude of the downward flux is much smaller than that of the upward flux.

Potential for Salt Accumulation

When zones have no liquid outflow, substantial accumulation of soluble salts may occur from evaporation (the zones need not be dry for this to occur).

Solute mass on the order of 2×10^5 times the solute mass present in 1 kg of reference composition may accumulate in Zone 4 (drip-shield surface). For example, if chloride is present in the reference water at 7 mg/L (typical for J-13 water), the accumulated mass of chloride in the backfill could approach 1.5 kg per meter of drift.

For the repository-edge location, the potential accumulation of soluble salts is less than at the center because there is less heat available for evaporation.

For the "lower" infiltration results, there is greater potential for solute accumulation in the invert.

7.2 GAS FLUX AND FUGACITY

A mass-transfer model was developed for gas-phase transport of CO_2 and O_2 gases in the unsaturated zone, and it was calibrated to ^{14}C data for ambient conditions. The model is used to develop linear flux–fugacity relations for CO_2 and O_2, which are used in chemical modeling. It is an approximate model for which the assumptions and limitations are discussed in Section 5.2.

Discussion of Conservatism in the Bounding Estimates

The gas-phase CO_2 and O_2 fugacities, and their variation with mass flux, represent reasonable lower-bound availability for chemical reactivity in the drifts for the following reasons:

- Aqueous fluxes of CO_2, are neglected in the model.
- One-dimensional transport is assumed, but there are indications from TH modeling (Section 6.1) that multidimensional gas-phase occurs. The wide drift spacing

associated with the EDA II design concept allows for cooler temperatures in the pillars, which promotes convective circulation.

- Retrograde solubility is neglected in the model; hence, the gas-liquid phase partitioning does not change as a function of temperature. With higher temperature, the distribution coefficient K_d actually decreases, which promotes CO_2 transport.

The Gas Flux and Fugacity Model neglects chemical processes that control partitioning of CO_2 between solid, liquid, and gas phases. However, as shown in the Chemical Reference Model, there is likely to be net production of CO_2 in the gas phase associated with heating; therefore, the neglected processes would tend to increase the CO_2 fugacity and, thus, the model provides lower-bound values.

7.3 CEMENTITIOUS MATERIALS

This model provides reasonable-bound estimates for flow rate and chemistry of grout leachate and for the interaction of leachate with backfill and CO_2 in the EBS. For as long as the grout remains substantially intact inside the rockbolt holes, the flow of water that interacts directly with grout is projected to be a small fraction of the seepage inflow into the drifts. As grout leachate chemically equilibrates with CO_2 and quartz backfill in the EBS, the composition approaches that of seepage water, except for the high sulfate produced by ettringite dissolution at elevated temperature. When mixed with other waters in the EBS, the sulfate (which tends to act as a conservative species) is diluted, and the leachate becomes a minor contributor to the EBS bulk chemical environment.

Composition of Grout Leachate

Leachate pH values of 10.2 to 11.5 are predicted, depending primarily on the solubility of portlandite, which increases at lower temperature. These elevated pH values for leachate will probably not occur at the drip shield or at the waste package because of mixing with other water in the EBS and because of reaction with quartz-sand backfill and gas-phase CO_2.

After equilibration with CO_2 and quartz-sand backfill, pH of approximately 8.5 is predicted. This result does not take into account evaporative concentration in the backfill, which is important during Time Period 2 and Time Period 3. However, the composition of the equilibrated leachate is similar to seepage waters during the same time periods, and the quantity of leachate is a small fraction of the seepage, so the impact on the bulk chemical environment will be minor.

Sulfate concentrations as great as 1200 mg/L in grout leachate are predicted at the highest temperatures because of the temperature-dependent solubility of ettringite. The total mass of sulfate depends on the flow rate, which may vary from less than one to several hundred mL/yr per rockbolt.

Factors Limiting Chemical Effects from Rockbolt Grout

The grout permeability is small (Assumption 5.3.8), which limits chemical interaction of the grout with the EBS environment while increasing the longevity of the grout to dissolution. Very

small flow rates, on the order of few mL/yr per rockbolt, are obtained using the saturated permeability of the grout.

A more conservative bounding approach was developed, based on the ratio of rockbolt cross-sectional area to the drift diameter, to estimate the average flow rate for leachate into the drift. This method produces flow rates on the order of 75 to 330 mL/yr per rockbolt, or a few percent of the total seepage inflow to the drifts. These estimates are valid for as long as most of the grout is contained in the rockbolt holes, which is directly related to grout longevity.

For the reference model, neither ettringite nor portlandite completely dissolves for at least 1500 yr. Other phases (brucite, tobermorite) are more stable to dissolution and will tend to alter in place to more thermodynamically stable minerals. These results are based on the reference TH Model (Section 6.1), which provides a reasonable upper bound on the seepage flow rate and, therefore, tends to maximize the rates of dissolution for ettringite and portlandite.

7.4 MICROBIAL EFFECTS

Bacteria and fungi are present in the host rock at Yucca Mountain, and laboratory testing has shown that when moisture and nutrient sources are available, microbial activity can produce MIC of carbon steel and waste-package materials.

Microbial growth and activity in the host rock at ambient (prerepository) conditions are limited by the availability of water and nutrients, particularly phosphate. Dryout of the EBS during the repository thermal period will further limit water, arresting microbial growth and activity. Based on known microbial responses, the time until return of microbial growth and activity can be estimated from environmental factors. Observations of temperature-dependence reported in published literature show that no microbial activity will occur at temperatures greater than 120°C in aqueous environments. Reported dependence on humidity shows that growth and activity do not generally occur at less than approximately 90% RH. When salts are present, the threshold RH could decrease, depending on deliquescent behavior of the salts (Figure 35).

In principle, bacteria are capable of degrading all EBS materials. The primary electron donors in the EBS will be metals (such as steel) or metal ions in reduced form (such as the ferrous ion, and also hydrogen or methane if available). The primary electron acceptors will be sulfate, nitrate, and gas-phase oxygen. The backfill will consist of clean, washed quartz sand, which is not an energy source.

EBS water-diversion features, including the drip shield, will protect the waste package during the thermal period and beyond. No salts or necessary nutrients such as phosphate will be deposited on the waste package as long as the drip shield is intact and functions as intended. Even if RH is greater than 90% under the drip shield, MIC of the waste package will be insignificant until drip-shield failure occurs. This assumes that the dust deposited on the waste package surface will not sustain significant growth and activity.

When the drip shield is exposed to sufficient humidity or liquid water, MIC can occur, as observed in laboratory tests. When the drip shield allows liquid water penetration, or the waste package comes into direct contact with backfill or invert materials, MIC of the waste package can occur. In laboratory microcosm tests, MIC has been observed to accelerate the corrosion of

carbon steel (C1020) by a factor of approximately six. This may be an upper bound because the test cells were saturated and had crushed tuff and glucose added.

7.5 PRECIPITATES AND SALTS

A normative model for precipitate formation has been developed; it incorporates laboratory data from evaporation of synthetic J-13 water and synthetic porewater, plus thermodynamic insights. A set of mineral precipitates is identified that can accommodate all the major ions and many of the minor species that constitute J-13 water and similar waters. Application of the model to the laboratory test results shows qualitative agreement with most major precipitates identified in the laboratory tests, while incorporating other species (not detected) as needed for mass balance.

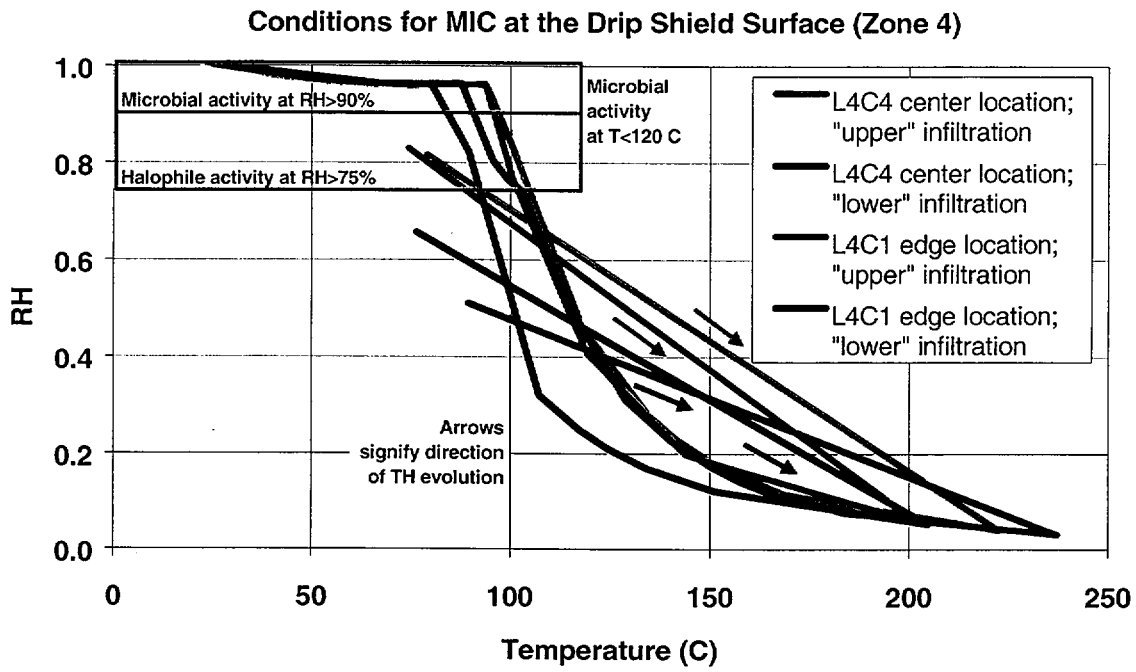

Figure 35. Conditions for MIC at the Drip Shield Surface

Empirical Basis for Normative Model of Precipitate Formation

Test results for synthetic J-13 water are sensitive to the CO_2 fugacity. The tests were performed under atmospheric CO_2 conditions, which limited pH to the range 10 to 11 for evaporative concentration values as great as 150× and greater. Smaller values for the CO_2 fugacity will tend to cause higher pH. Thus, if corrosion processes are sensitive to high pH, the measured pH values are lower bounds.

Bicarbonate-type waters, such as J-13 water, are more sensitive to CO_2 fugacity during evaporative concentration and are more likely to produce high-pH conditions than are sulfate-type waters, such as the synthetic porewater investigated. The synthetic J-13 results are therefore bounding with respect to high-pH conditions at the surface of the drip shield or the waste package during the thermal period. Sulfate-type or chloride-type waters tend to produce much lower pH values when concentrated evaporatively (4 pH units difference was observed).

Limited Volume of Concentrated Waters

Experimental results for synthetic J-13 water (with and without tuff present) show that, for pH to exceed 10, evaporative concentration factors greater than 150× are required. Thus, the potential volumes and flow rates of affected solutions will be small. Saturation of the backfill in affected locations will be small, and the relative permeability and consequent mobility of these solutions will be limited.

If a water composition that is similar to but more dilute than J-13 water is used (e.g., condensate), the results will be similar to the synthetic J-13 results presented here. However, greater evaporative concentration factors would be required to achieve the same pH values. The mass of solute involved, and the potential volume of high-pH liquid, would be even smaller than for J-13.

7.6 COLLOIDS

Colloids are important in assessing repository performance only if they irreversibly sorb radionuclides and the resulting radioactive colloids are physically stable enough to survive flow and transport through the groundwater system to the accessible environment.

Although the mass of iron-bearing corrosion products retained within the drift at any time will change the local bulk fluid and solid chemistry, entrained colloids are not expected to materially affect bulk chemistry along the downstream flow paths. Based on the bounding analysis presented in Section 6.6, there is less than 5% probability that the total mass of entrained colloids will exceed 10% of the total dissolved solids content of J-13 water (Section 6.6.3.3).

The increase in radionuclide content from sorption on colloids is likely to be less than 10× the solubility limit of the radionuclide, unless the sorption coefficient exceeds 10^5 mL/g.

Under the chemical conditions expected within the drift, actinides are less strongly sorbed and more rapidly desorbed by siliceous colloids than by hematite and goethite. Measured sorption coefficients for Pu on silica colloids (10^3 to 10^4 mL/g) are lower by about two orders of magnitude than for Pu sorption on hematite colloids (10^5 mL/g).

Chemical and hydrologic conditions within the drift cannot be predicted with sufficient certainty to exclude the formation of stable colloids of hematite or goethite. Based on relatively high values of measured sorption coefficients and the paucity of evidence for reversible sorption of Pu and Am on iron colloids, an upper bound on the total radionuclide content of 10 to 100 times the solubility limit is recommended for use in performance assessment.

Sorption on clays and silica colloids is not likely to be significant.

7.7 CHEMICAL REFERENCE MODEL

Calculations show that pH will be in the approximate range of 8.5 to 11 in the EBS bulk chemical environment during the thermal period (Figure 36). There is the potential for tens to hundreds of kilograms of mineral precipitates—comprising mostly silica, sulfate salts, carbonates, and halite—to accumulate in the EBS. Ionic strength is dilute (e.g., less than 0.1 molal) during the thermal period, except for evaporative concentration, and redissolution of precipitates and salts (Figure 37).

Redissolution of precipitates is difficult to model accurately because thermochemical models lack data support for extreme concentration and temperature conditions and because the distribution of flow in the EBS depends on changes in backfill properties and the nature of seepage from the host rock. Accordingly, a bounding model for chemical conditions on the drip shield surface would include the presence of precipitates and the aqueous conditions at equilibrium with these precipitates, given the extant TH conditions in the EBS.

CO_2 Consumption in the EBS

On the whole, throughout the EBS and the host rock, CO_2 is produced rather than consumed during the thermal period. CO_2 demand is greatest during formation of the normative assemblage of evaporative precipitates, but is more than equaled by production in the host rock as formation water warms and is exposed to lower fugacity.

Effects of Cementitious Materials

Cement leachate composition is similar to the water composition that evolves when evaporative precipitates are redissolved (Section 6.3.8). CO_2 demand frmo equilibration of leachate with CO_2 and quartz sand in the EBS is small compared with consumption and production from other causes (Section 6.7.7.1). This is primarily controlled by the small flow of leachate, which in turn is related to the grout permeability (Assumption 5.3.8). The leachate flow could increase by as much at least an order magnitude without impacting the CO_2 balance.

Corrosion of Structural Steel

Steel present in the drifts can completely corrode in a few decades or a few centuries.

The oxygen necessary for corrosion is available in the host rock and will be readily replaced by natural processes; however, oxygen fugacity in the EBS could be substantially decreased through a combination of steel corrosion and the air mass-fraction effect.

The important issue for predicting the EBS environment is the relation between the corrosion rate for steel and the O_2 fugacity. Advancement in modeling of gas transport in the host rock will be of limited value in elucidating the O_2 fugacity in the drifts. Improved prediction will be based on new data or interpretation of corrosion rate vs. P_{O2} for structural steel.

Effects of Microbial Activity

Microbial activity has been shown to accelerate the corrosion rate for carbon steel by a factor of approximately six. Thus, microbial activity could further decrease the oxidation potential in the EBS, and anoxic conditions could lead to proliferation of organisms that may not presently be important contributors to microbial ecology of the host rock.

Corrosion-Resistant Materials

Slow consumption of oxygen by corrosion of Ti-7 or Alloy-22 could contribute slightly to depletion of oxygen in the EBS. However, the potential rate of consumption is a small fraction of the calculated oxygen availability.

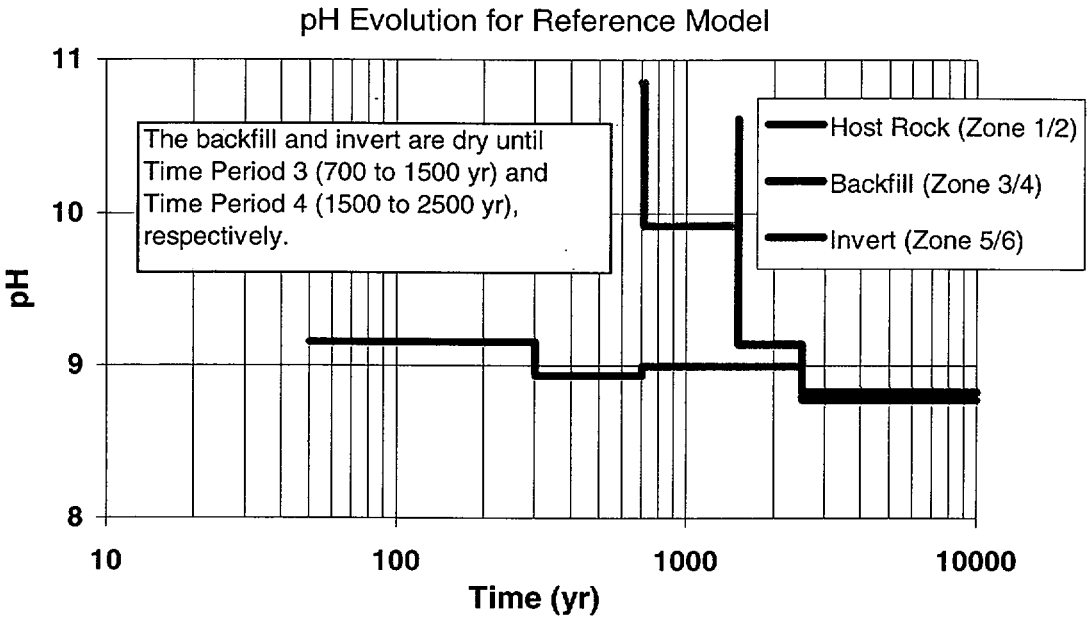

Figure 36. pH vs. Time for the Chemical Reference Model

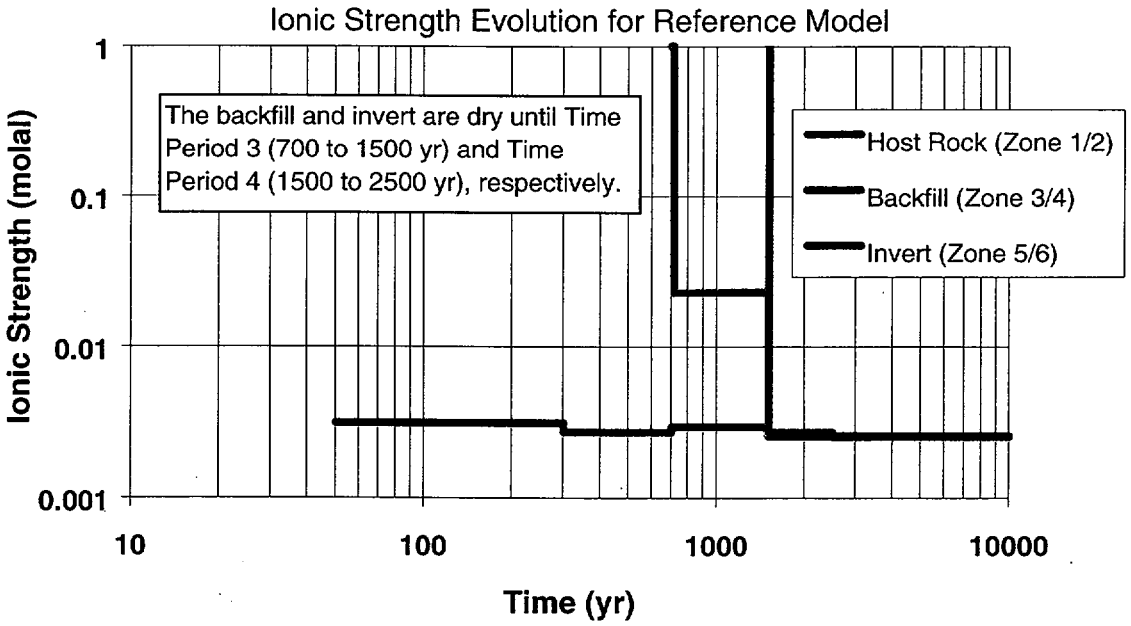

Figure 37. Ionic Strength vs. Time, for the Chemical Reference Model

8. INPUTS AND REFERENCES

8.1 DOCUMENTS CITED

AISC (American Institute of Steel Construction) 1989. *Manual of Steel Construction, Allowable Stress Design.* 9th Edition. Chicago, Illinois: American Institute of Steel Construction. TIC: 205770.

Atkins, P.W. 1990. *Physical Chemistry.* (4th edition) New York, New York: W.H. Freeman & Co. TIC: 245483.

Atlas, R.M. and Bartha, R. 1981. *Microbial Ecology: Fundamentals and Applications.* Reading, Massachusetts: Addison-Wesley Publishing. TIC: 246870.

Bear, J. 1988. *Dynamics of Fluids in Porous Media.* New York, New York: Dover Publications. TIC: 217568.

Bird, R.B., Stewart, W.E., and Lightfoot, E.N. 1960. *Transport Phenomena.* New York, New York: John Wiley & Sons, Inc. TIC: 208957.

Bodvarsson, G.S.; Bandurraga, T.M.; and Wu, Y.S., eds. 1997. *The Site-Scale Unsaturated Zone Model of Yucca Mountain, Nevada, for the Viability Assessment.* LBNL-40376. Berkeley, California: Lawrence Berkeley National Laboratory. ACC: MOL.19971014.0232.

Borenstein, S.W. 1994. *Microbiologically Influenced Corrosion Handbook.* p. 288. New York, New York: Industrial Press. TIC: 241092.

Brooks, R.H. and Corey, A.T. 1966. "Properties of Porous Media Affecting Fluid Flow." *Journal of the American Society of Civil Engineers, Irrigation and Drainage Division, 92,* (IR2), 61-89. New York, New York: American Society of Civil Engineers. TIC: 216867.

Brown, A.D. 1976. "Microbial Water Stress." *Bacteriological Reviews, 40,* (4), 803-846. Baltimore, Maryland: Williams & Wilkins Co. TIC: 247692.

Broxton, D.E.; Warren, R.G.; Byers, F.M.; and Scott, R.B. 1989. "Chemical and Mineralogic Trends Within the Timber Mountain-Oasis Valley Caldera Complex, Nevada: Evidence for Multiple Cycles of Chemical Evolution in a Long-Lived Silicic Magma System." *Journal of Geophysical Research, 94,* (B5), 5961-5985. Washington, D.C.: American Geophysical Union. TIC: 225928.

Buscheck, T.A.; Shaffer, R.J.; and Nitao, J.J. 1997. *Pretest Thermal-Hydrological Analysis of the Drift-Scale Thermal Test at Yucca Mountain.* Livermore, California: Lawrence Livermore National Laboratory. ACC: MOL.19980507.0359.

CRWMS M&O 1998a. "Thermal Hydrology." Chapter 3 of *Total System Performance Assessment-Viability Assessment (TSPA-VA) Analyses Technical Basis Document.* B00000000-01717-4301-00003 REV 01. Las Vegas, Nevada: CRWMS M&O. ACC: MOL.19981008.0003.

CRWMS M&O 1998b "Waste Package Degradation Modeling and Abstraction." Chapter 5 of *Total System Performance Assessment-Viability Assessment (TSPA-VA) Analyses Technical Basis Document.* B00000000-01717-4301-00005 REV 01. Las Vegas, Nevada: CRWMS M&O. ACC: MOL.19981008.0005.

CRWMS M&O 1998c. "Near-Field Geochemical Environment." Chapter 4 of *Total System Performance Assessment-Viability Assessment (TSPA-VA) Analyses Technical Basis Document.* B00000000-01717-4301-00004 REV 01. Las Vegas, Nevada: CRWMS M&O. ACC: MOL.19981008.0004.

CRWMS M&O 1999a. *Engineered Barrier System Performance Modeling (WP#12012383MX).* Activity Evaluation, July 12, 1999. Las Vegas, Nevada: CRWMS M&O. ACC: MOL.19990719.0317.

CRWMS M&O 1999b. *Classification of the MGR Ex-Container System.* ANL-XCS-SE-000001 REV 00. Las Vegas, Nevada: CRWMS M&O. ACC: MOL.19990928.0221.

CRWMS M&O 1999c. *Development Plan for EBS Physical & Chemical Environment Model.* TDP-EBS-MD-000008. Las Vegas, Nevada: CRWMS M&O. ACC: MOL.19990810.0565.

CRWMS M&O 1999d. *Natural Environment Data for Engineered Barrier System (EBS) Base Case.* Input Transmittal EBS-NEP-99273.T. Las Vegas, Nevada: CRWMS M&O. ACC: 19990920.0108.

CRWMS M&O 1999e *Surface Area and Masses for Steel Used in Repository Emplacement Drifts.* EBS-EBS-99322.T. Las Vegas, Nevada: CRWMS M&O. ACC: MOL.19991027.0150.

CRWMS M&O 1999f. Software User's Manual (UM) for PHREEQC Version 2.0 (beta). 10068-UM-2.0-00. Las Vegas, Nevada: CRWMS M&O. ACC: MOL.20000114.0118.

CRWMS M&O 2000a. *Request for a Copy of PA-SSR-99218.Ta.* 00220.T. Las Vegas, Nevada: CRWMS M&O. ACC: MOL.20000412.0941.

CRWMS M&O 2000b. *Vapor-Phase Corrosion Data and Correlation Model for A516 Steel.* Input Transmittal 00215.T. Las Vegas, Nevada: CRWMS M&O. ACC: MOL.20000412.0940.

CRWMS M&O 2000c. *Emplacement Drift System Description Document.* SDD-EDS-SE-000001 REV 00. Las Vegas, Nevada: CRWMS M&O. ACC: MOL.20000121.0119.

CRWMS M&O 2000d. *Drift-Scale Coupled Processes (DST and THC Seepage) Models.* MDL-NBS-HS-000001 REV 00. Las Vegas, Nevada: CRWMS M&O. Submit to RPC URN-0042.

CRWMS M&O 2000e. *Unsaturated Zone Flow and Transport Model Process Model Report.* TDR-NBS-HS-000002 REV 00. Las Vegas, Nevada: CRWMS M&O. ACC: MOL.20000320.0400.

CRWMS M&O 2000f. *Multiscale Thermohydrologic Model.* ANL-EBS-MD-000049 REV 00. Las Vegas, Nevada: CRWMS M&O. URN-0019

CRWMS M&O 2000g. *Water Diversion Model.* ANL-EBS-MD-000028 REV 00. Las Vegas, Nevada: CRWMS M&O. ACC: MOL.20000107.0329.

CRWMS M&O 2000h. *Invert Diffusion Properties Model.* ANL-EBS-MD-000031 REV 00. Las Vegas, Nevada: CRWMS M&O. ACC: MOL.20000203.0694.

Cussler, E.L. 1997. *Diffusion: Mass Transfer in Fluid Systems.* 2nd Edition. Cambridge, United Kingdom: Cambridge University Press. TIC: 241150.

Diercks, M.; Sand, W.; and Bock, E. 1991. "Microbial Corrosion of Concrete." *Experientia, 47,* 514-516. Basal, Switzerland: Birkhauser Verlag. TIC: 244488.

DOE (U.S. Department of Energy) 2000. *Quality Assurance Requirements and Description.* DOE/RW-0333P, Rev. 10. Washington, D.C.: U.S. Department of Energy, Office of Civilian Radioactive Waste Management. ACC: MOL.20000427.0422.

Ehrlich, H.L. 1996. *Geomicrobiology.* 3rd Edition. New York, New York: Marcel Dekker, Inc. TIC: 247746.

Fenchel, T., and Blackburn, T.H. 1979. *Bacteria and Mineral Cycling.* New York, New York: Academic Press. Library Tracking Number-247767.

Freeze, R.A., and Cherry, J.A. 1979. *Groundwater.* Englewood Cliffs, New Jersey: Prentice-Hall. TIC: 217571.

Fritz, P. and Fontes, J.Ch. 1980. *Handbook of Environmental Isotope Geochemistry.* The Terrestrial Environment, A. Volume 1, p. 545. New York, New York: Elsevier Scientific Publishing Company. TIC: 243187.

Garrels, R.M. and Christ, C.L. 1965. *Solutions, Minerals and Equilibria.* Boston, Massachusetts: Jones and Bartlett. TIC: 223483.

Ghani, A.; Rajan, S.S.; and Lee, A. 1994. "Enhancement of Phosphate Rock Solubility Through Microbial Processes." *Soil Biology & Biochemistry, 26,* (1), 127-136. Rotterdam, The Netherlands: Elsevier Science. TIC: 247717.

Hardin, E.L., Blair, S.C., Buscheck, T.A., Chesnut, D.A., DeLoach, L.D., Glassley, W.E., Johnson, J.W., Knapp, R.B., Lee, K., Meike, A., Myers, K., Nitao, J.J., Palmer, C.E., Rogers, L.L., Rosenberg, N.D., Viani, B.E., Wang, H.F., Wittwer, C., and Wolery, T.J. 1998. Near-Field/Altered-Zone Models Report. Milestone report for the CRWMS Management and Operating Contractor, U.S. Department of Energy. UCRL-ID-129179. SP3100M3. Livermore, California: Lawrence Livermore National Laboratory. ACC: MOL.19980630.0560.

Harrar, J.E.; Carley, J.F.; Isherwood, W.F.; and Raber, E. 1990. *Report of the Committee to Review the Use of J-13 Well Water in Nevada Nuclear Waste Storage Investigations.* UCID-21867. Livermore, California: Lawrence Livermore National Laboratory. ACC: NNA.19910131.0274.

He, Z.L.; Baligar, V.C.; Martens, D.C.; and Ritchey, K.D. 1997. "Effect of Phosphate Rock, Lime, and Cellulose on Soil Microbial Biomass in Acidic Forest Soil and its Significance in Carbon Cycling." *Biology and Fertility of Soils, 24,* (3), 329-334. Heidelberg, Germany: Springer International. TIC: 247442.

Heinen, W. and Lauwers, A.M. 1988. "Leaching of Silica and Uranium and Other Qualitative Aspects of the Lithobiotic Colonization in a Radioactive Thermal Spring." *Microbial Ecology, 15,* (1), 135-149. New York, New York: Springer-Verlag. TIC: 247443.

Hiebert, F.K. and Bennett, P.C. 1992. "Microbial Control of Silicate Weathering in Organic-Rich Ground Water." *Science, 258,* 278-281. Washington, D.C.: American Association for the Advancement of Science. TIC: 247444.

Horn, J.A. 1999. *Approach and Supporting Data for MIC Modeling.* Deliverable WP267DM5. Livermore, California: Lawrence Livermore National Laboratory. ACC: MOL.20000125.0687.

Horn, J.M.; Davis, M.; Martin, S.; Lian, T.; and Jones, D. 1998a. *Assessing Microbiologically Induced Corrosion of Waste Package Materials in the Yucca Mountain Repository.* URCL-JC-130567. Livermore, California: Lawrence Livermore National Laboratory. TIC: 244465.

Horn, J.M.; Rivera, A.; Lian, T.; and Jones, D. 1998b. "MIC Evaluation and Testing for the Yucca Mountain Repository." *Proceedings of Corrosion 98, National Association of Corrosion Engineers, March 22-27, San Diego, California.* 152/2 to 152/14. Houston, Texas: NACE International. TIC: 237146.

Horn, J.; Martin, S.; Masterson, B.; and Lian, T. 1999a. "Biochemical Contributions to Corrosion of Carbon Steel and Alloy 22 in a Continual Flow System." *Corrosion 99, 54th Annual Conference and Expo, San Antonio, Texas, April 25-30, 1999.* Houston, Texas: National Association of Corrosion Engineers. ACC: MOL.20000316.0533.

Horn, J.M., Davis, M., Masterson, B., Rivera, A., Miranda, A., and Martin, S. 1999b. "Bacterial growth and nutrient availability in a subsurface nuclear waste repository environment." In proceedings from 99th Annual Meeting of the American Society of Microbiology. Chicago, Illinois: May 30–June 3, 1999. American Society of Microbiology. Library Tracking Number-247797.

Incropera, F.P. and Dewitt, D.P. 1996. *Fundamentals of Heat and Mass Transfer.* 4th Edition. New York, New York: John Wiley & Sons. TIC: 243950.

Kieft, T.L.; Kovacik, W.P., Jr.; Ringelberg, D.B.; White, D.C.; Haldeman, D.L.; Amy, P.S.; and Hersman, L.E. 1997. "Factors Limiting Microbial Growth and Activity at a Proposed High-Level Nuclear Repository, Yucca Mountain, Nevada." *Applied and Environmental Microbiology, 63,* (8), 3128-3133. Washington, D.C.: American Society for Microbiology. TIC: 236444.

Kristjansson, J.K. and Hreggvidsson, G.O. 1995. "Ecology and Habitats of Extremophiles." *World Journal of Microbiology and Biotechnology, 11,* (1), 17-25. Oxford, England: Rapid Communications of Oxford Ltd in Association with UNESCO. On Order Library Tracking Number-1625.

Lian, T.; Martin, S.; Jones, D.; Rivera, A.; and Horn, J. 1999. "Corrosion of Candidate Container Materials by Yucca Mountain Bacteria." *Corrosion 99. Paper No. 476,* Houston, Texas: NACE International. TIC: 245833.

Little, B. and Wagner, P. 1997. "Myths Related to Microbiologically Influenced Corrosion." *Materials Performance, 36,* (6), 40-44. Houston, Texas: National Association of Corrosion Engineers. TIC: 247475.

Little, B.; Wagner, P.; and Mansfeld, F. 1991. "Microbiologically Influenced Corrosion of Metals and Alloys." *International Materials Reviews, 36,* (6), 253-272. Materials Park , Ohio: ASM International. TIC: 242236.

Liu, H.H.; Doughty, C.; and Bodvarsson, G.S. 1998. "An Active Fracture Model for Unsaturated Flow and Transport in Fractured Rocks." *Water Resources Research, 34,* (10), 2633-2646. Washington, D.C.: American Geophysical Union. TIC: 243012.

MathSoft 1998. *Mathcad 8, User's Guide.* Cambridge, Massachusetts: MathSoft. TIC: 242289.

Mattimore, V. and Battista, J.R. 1996. "Radioresistance of Deinococcus Radiodurans: Functions Necessary to Survive Ionizing Radiation are Also Necessary to Survive Prolonged Desiccation." *Journal of Bacteriology, 178,* (3), 633-637. Washington, D.C.: American Society for Microbiology. TIC: 247491.

McCann, M.P.; Kidwell, J.P.; and Matin, A. 1991. "The Putative Sigma Factor KatF has a Central Role in Development of Starvation-mediated General Resistance in Eschericia Coli." *Journal of Bacteriology, 173,* 4188-4194. Washington, D.C.: American Society for Microbiology. TIC: 247735.

McCright, R.D. 1998. *Corrosion Data and Modeling.* Volume 3 of *Engineered Materials Characterization Report.* UCRL-ID-119564 Rev. 1.1. Livermore, California: Lawrence Livermore National Laboratory. ACC: MOL.19980806.0177.

McLaren, A.D. 1969. "Radiation as a Technique in Soil Biology and Biochemistry." *Soil Biology & Biochemistry, 1,* 63-73. Rotterdam, The Netherlands: Elsevier Science. TIC: 247735.

Mualem, Y. 1976. "A New Model for Predicting the Hydraulic Conductivity of Unsaturated Porous Media." *Water Resources Research, 12,* (3), 513-522. Washington, D.C.: American Geophysical Union. TIC: 217339.

Murphy, W.M. 1995. "Contributions of thermodynamic and mass transport modeling to evaluation of groundwater flow and groundwater travel time at Yucca Mountain, Nevada." *Scientific Basis for Nuclear Waste Management XVIII, Symposium held October 23-27, 1994, Kyoto, Japan.* Murakami, T. and Ewing, R.C., eds. *353,* 419-426. Pittsburgh, Pennsylvania: Materials Research Society. TIC: 216341.

Nitao, J.J. 1993. "The NUFT Code for Modeling Nonisothermal, Multiphase, Multicomponent Flow and Transport in Porous Media." *Eos, 74,* (43), 313. Washington, D.C.: American Geophysical Union. TIC: 226135.

NRC (U.S. Nuclear Regulatory Commission) 1999. *Issue Resolution Status Report Key Technical Issue: Evolution of the Near-Field Environment.* Rev. 2. Washington, D.C.: U.S. Nuclear Regulatory Commission. ACC: MOL.19990810.0640.

Onofrei, M.; Gray, M.N.; Coons, W.E.; and Alcorn, S.R. 1992. "High Performance Cement-Based Grouts for Use in a Nuclear Waste Disposal Facility." *Waste Management, 12,* 133-154. New York, New York: Pergamon Press. TIC: 245401.

Perfettini, J.V.; Revertegat, E.; and Langomazino, N. 1991. "Evaluation of Cement Degradation Induced by the Metabolic Products of Two Fungal Strains." *Experientia, 47,* 527-532. Basel, Switzerland: Birkhauser Verlag. TIC: 239327.

Perry, R.H. and Chilton, C.H., eds. 1973. *Chemical Engineers' Handbook.* 5th Edition. New York, New York: McGraw-Hill. TIC: 242591.

Potts, M. 1994. "Desiccation tolerance of prokaryotes." Microbiol. Rev., 58(4):755–805. American Society for Microbiology. TIC: 247743.

Reeve, J.N. 1994. "Thermophiles in New Zealand." ASM News, 60,(10),541–545. TIC: 247744.

Rimstidt, J.D. and Barnes, H.L 1980. "The Kinetics of Silica-Water Reactions." *Geochimica et Cosmochimica Acta, 44,* 1683-1699. Oxford, England: Pergamon Press. TIC: 219975.

Robie, R.A.; Hemingway, B.S.; and Fisher, J.R. 1979. "Thermodynamic Properties of Minerals and Related Substances at 298.15 K and 1 Bar (10[5] Pascals) Pressure and at Higher Temperature." *Bulletin 1452,* . Denver, Colorado: U.S. Geological Survey. TIC: 230505.

Sand, W., and Bock, E. 1991. "Biodeterioration Of Ceramic Materials By Biogenic Acid." *Intl. Biodeterioration,* 175–182. Great Britain: Elsevier Science Pub. Ltd. Library Tracking Number-1704.

Stotzky, G. and Pramer, D. 1973. "Activity, Ecology, and Population Dynamics of Microorganisms in Soil." *Critical Reviews in Microbiology.* 59-137. Cleveland, Ohio: Chemical Rubber Company. TIC: 244209.

Straus, D.B., Walter, W.A., and Gross, C.A. 1987. "The Heat Shock Responses Of E. Coli Is Regulated By Changes In Concentration Of Sigma-32." *Nature,* 329:348–351. Library Tracking Number-1706.

Stumm, W. and Morgan, J.J. 1981. *Aquatic Chemistry – An Introduction Emphasizing Chemical Equilibria in Natural Waters.* New York, New York: John Wiley & Sons. TIC: 208448.

Thorstenson, D.C. 1993. "The Composition and CO_2 Carbon Isotope Signature of Gases from Borehole USW UZ-6, Yucca Mountain, Nevada." *Proceedings of Workshop V: Flow and Transport through Unsaturated Fractured Rock - Related to High-Level Radioactive Waste Disposal, Held at Radisson Suite Hotel, Tucson, Arizona, January 7-10, 1991.* Evans, D.D. and Nicholson, T.J., eds. *NUREG/CP-0040,* 184-188. Washington, D.C.: U.S. Nuclear Regulatory Commission. TIC: 207128.

van Genuchten, M.T. 1980. "A Closed-Form Equation for Predicting the Hydraulic Conductivity of Unsaturated Soils." *Soil Science Society American Journal, 44,* (5), 892-898. Madison, Wisconsin: Soil Science Society of America. TIC: 217327.

Weast, R.C. and Astle, M.J., eds. 1981. *CRC Handbook of Chemistry and Physics: A Ready Reference Book of Chemical and Physical Data.* 62nd Edition. Boca Raton, Florida: CRC Press. TIC: 240722.

Wildenschild, D. and Roberts, J. 1999. *Experimental Tests of Enhancement of Vapor Diffusion in Topopah Spring Tuff.* UCRL-JC-134850. Livermore , California: Lawrence Livermore National Laboratory. TIC: 246923.

Wilkins, D.R. and Heath, C.A. 1999. "Direction to Transition to Enhanced Design Alternative II." Letter from Dr. D.R. Wilkins (CRWMS M&O) and Dr. C.A. Heath (CRWMS M&O) to Distribution, June 15, 1999, LV.NS.JLY.06/99-026, with enclosures, "Strategy for Baselining EDA II Requirements" and "Guidelines for Implementation of EDA II." ACC: MOL.19990622.0126; MOL.19990622.0127; MOL.19990622.0128.

Wolery, T.J. 1992a *EQ3/6, A Software Package for Geochemical Modeling of Aqueous Systems. Package Overview and Installation Guide (Version 7.0).* UCRL-MA-110662 PT I. Livermore, California: Lawrence Livermore National Laboratory. TIC: 205087.

Wolery, T.J. 1992b. *EQ3NR, A Computer Program for Geochemical Aqueous Speciation-Solubility Calculations. Theoretical Manual, User's Guide, and Related Documentation (Version 7.0).* UCRL-MA-110662 PT III. Livermore, California: Lawrence Livermore National Laboratory. TIC: 205154.

Wolery, T.J. and Daveler, S.A. 1992. *EQ6, A Computer Program for Reaction Path Modeling of Aqueous Geochemical Systems: Theoretical Manual, User's Guide, and Related Documentation (Version 7.0).* UCRL-MA-110662 PT IV. Livermore, California: Lawrence Livermore National Laboratory. TIC: 205002.

YMP (Yucca Mountain Project) 1998. *Q-List.* YMP/90-55Q, Rev. 5. Las Vegas, Nevada: Yucca Mountain Site Characterization Office. ACC: MOL.19980513.0132.

8.2 CODES, STANDARDS, REGULATIONS, AND PROCEDURES

AP-2.13Q, Rev. 0, ICN1. Technical Product Development Planning. Washington, District of Columbia: U.S. Department of Energy, Office of Civilian Radioactive Waste Management. ACC: MOL.19991115.0230.

AP-3.10Q, Rev. 2, ICN 0. Analyses and Models. Washington, District of Columbia: U.S. Department of Energy, Office of Civilian Radioactive Waste Management. ACC: MOL.20000217.0246.

AP-3.15Q, Rev. 1, ICN 1. Managing Technical Product Inputs. Washington, District of Columbia: U.S. Department of Energy, Office of Civilian Radioactive Waste Management. ACC: MOL.20000218.0069.

AP-SI.1Q, Rev. 2, ICN4. Software Management. Washington, District of Columbia: U.S. Department of Energy, Office of Civilian Radioactive Waste Management. ACC: MOL.20000223.0508.

ASME (American Society of Mechanical Engineers) A.207. 1995. *1995 Boiler and Pressure Vessel Code - Section II Materials - Part A Material Specification-Ferrous - SA-516/SA-516M Specification for Pressure Vessel Plates, Carbon Steel, for Moderate- and Lower- Temperature Service (ASTM A 516/A 516M-90).* New York, New York: American Society for Testing and Materials. TIC: 245287.

ASTM B 575-94. 1994. *Standard Specification for Low-Carbon Nickel-Molybdenum-Chromium, Low-Carbon Nickel-Chromium-Molybdenum, and Low-Carbon Nickel-Chromium-Molybdenum-Tungsten Alloy Plate, Sheet, and Strip.* Philadelphia, Pennsylvania: American Society for Testing and Materials. TIC: 237683.

ASTM A572/A572M-97. 1997a. *Standard Specification for High-Strength Low-Alloy Columbium-Vanadium Structural Steel.* Philadelphia, Pennsylvania: American Society for Testing and Materials. TIC: 241041.

ASTM A 240/A 240M-97a. 1997b. *Standard specification for heat-resisting chromium and chromium-nickel stainless steel plate, sheet, and strip for pressure vessels.* West Conshohocken, PA: American Society for Testing and Materials. TIC: 241744.

QAP-2-0, Rev. 5, ICN1. Conduct of Activities. Las Vegas, Nevada: CRWMS M&O. ACC: MOL.19991109.0221.

QAP-2-3, Rev. 10. Classification of Permanent Items. Las Vegas, Nevada: CRWMS M&O. ACC: MOL.19990316.0006.

8.3 SOURCE DATA

8.3.1 Thermal Hydrology Model (See Section 6.1)

DTN: MO9911MWDEBSWD.000. EBS Water Drainage Model. Submittal date: 11/29/99.

DTN: LB990861233129.001 "Drift Scale Calibrated 1-D Property Set, FY99." (Base-case infiltration). Submittal date: 08/06/1999.

DTN: LB990861233129.002 "Drift Scale Calibrated 1-D Property Set, Fy99." (Upper-bound infiltration). Submittal date: 08/06/1999.

DTN: LB990861233129.003 "Drift Scale Calibrated 1-D Property Set, Fy99." (Lower-bound infiltration). Submittal date: 08/06/1999.

DTN: SN9908T0872799.004. Tabulated In-Drift Geometric and Thermal Properties Used in Drift-Scale Models for TSPA-SR (Total System Performance Assessment-Site Recommendation). Submittal date: 08/30/1999.

DTN: SN9907T0872799.001. Heat Decay Data and Repository Footprint for Thermal-Hydrolgic and Conduction-Only Models for TSPA-SR (Total System Performance Assessment-Site Recommendation). Submittal date: 07/27/1999.

DTN: LB99EBS1233129.001. Natural Environment Data for Engineered Barrier System (EBS) Basecase. Submittal date: 11/29/99.

DTN: LB99EBS1233129.004. Natural Environment Data for Engineered Barrier System (EBS) Basecase. Submittal Date: 11/29/99.

DTN: LL980810004244.067. The Drift Scale Test Effect Of The Chemistry Of Pore Gases And Pore Water. Submittal date: 08/24/98.

8.3.2 Gas Flux and Fugacity Model (See Section 6.2)

DTN: GS930508312271.021. Analysis of Gaseous-Phase Stable and Radioactive Isotopes in the Unsaturated Zone, Yucca Mountain, Nevada. Submittal date: 04/30/1993.

DTN: GS940708312261.005. Carbon Dioxide, Methane, Carbon 13/12, and Oxygen 18/16 Results from USW UZ-6, USW UZ-6S, USW UZ-N27, USW UZ-N62, USW UZ-N64, USW UZ-N75, USW UZ-N93, USW UZ-N94, USW UZ-N95, UE-25 NRG#2B, UE-25 NRG#4, UE-25 NRG#5, and USW NRG-6. Submittal date: 07/25/1994.

DTN: GS941208312261.008. Carbon Dioxide, Methane, Carbon 14, and Carbon 13/12 Data from USW NRG-6 and USW NRG-7 for May and June 1994; and Carbon 14 Data from USW Wells NRG#5, UZ-6S, UZ-N27, UZ-N62, UZ-N64, UZ-N93, UZ-N94, and UZ-N95 from March 1994. Submittal date: 12/16/1994.

DTN: GS950808312261.004. Carbon 14 Results from Gas Samples Collected in February and March 1995. Submittal date: 08/29/1995.

DTN: GS960208312261.002. Carbon-14 Results from Gas Samples Collected; Carbon Dioxide, Carbon 13/12, Oxygen 18/16, and Carbon-14 Results from Gas Samples Collected; and Carbon Dioxide, Methane, Carbon 13/12 and Oxygen 18/16 Results from Gas Samples Collected. Submittal date: 02/16/1996.

DTN: GS961108312271.002. Chemical and Isotopic Composition of Pore Water and Pore Gas, 1994–96, from Boreholes USW UZ-1, USW UZ-14, UE-25 UZ#16, USW NRG-6, USW NRG-7A, USW SD-7, USW SD-9, ESF-AL#3-RBT#1, and ESF-AL#3-RBT#4, and ESF Rubble. Submittal date: 12/04/1996.

DTN: GS970283122410.002. Gas and Water Chemistry Data from Samples Collected at Boreholes UE-25 NRG#5 and USW SD-7 on Yucca Mountain, Alcove 5, and Borehole ESF-NAD-GTB#1A in Alcove 6, ESF, between 8-11-96 and 1-14-97. Submittal date: 02/21/1997.

DTN: GS970908312271.003. Unsaturated Zone Hydrochemistry Data, 2-1-97 to 8-31-97, Including Chemical Composition and Carbon, Oxygen, and Hydrogen Isotopic Composition: Porewater from USW NRG-7A, SD-7, SD-9, SD-12 and UZ-14; and Gas from USW UZ-14. Submittal date: 09/08/1997.

DTN: MO9811MWDGFM03.000. Input Data to Geologic Framework Model GFM3.0. Submittal date: 11/30/1998.

DTN: LB990861233129.001. Drift Scale Calibrated 1-D Property Set, FY99. Submittal date: 08/06/1999.

DTN: LL990702804244.100. Pore Water Data. Submittal date: 7/13/1999.

DTN: LL980711104242.054. Report of the Committee to Review the Use of J-13 Well Water in Nevada Nuclear Waste Storage Investigations. Submittal date: 08/05/1998.

8.3.3 Cementitious Materials Model (See Section 6.3)

DTN: LL980711104242.054. Report of the Committee to Review the Use of J-13 Well Water in Nevada Nuclear Waste Storage Investigations. Submittal date: 08/05/1998.

DTN: GS961108312271.002. Chemical and Isotopic Composition of Pore Water and Pore Gas, 1994–96, from Boreholes USW UZ-1, USW UZ-14, UE-25 UZ#16, USW NRG-6, USW NRG-7A, USW SD-7, USW SD-9, ESF-AL#3-RBT#1, and ESF-AL#3-RBT#4, and ESF Rubble. Submittal date: 12/04/1996.

DTN: GS970908312271.003. Unsaturated Zone Hydrochemistry Data, 2-1-97 to 8-31-97, Including Chemical Composition and Carbon, Oxygen, and Hydrogen Isotopic Composition: Porewater from USW NRG-7A, SD-7, SD-9, SD-12 and UZ-14; and Gas from USW UZ-14. Submittal date: 09/08/1997.

8.3.4 Microbial Effects Model (See Section 6.4)

DTN: LL980711104242.054. Report of the Committee to Review the Use of J-13 Well Water in Nevada Nuclear Waste Storage Investigations. Submittal date: 08/05/1998.

DTN: LL991203505924.094. Approach and Supporting Data for MIC Modeling. Submittal date: 12/13/1999.

8.3.5 Normative Precipitates and Salts Model (See Section 6.5)

DTN: LL980711104242.054. Report of the Committee to Review the Use of J-13 Well Water in Nevada Nuclear Waste Storage Investigations. Submittal date: 08/05/1998.

DTN: LL991008004241.041. Evaporation of Topopah Spring Tuff Pore Water. Submittal date: 10/21/1999. Submit to RPC URN-0268
DTN: LL991008104241.042. Evaporation of J13 Water: Laboratory Experiments and Geochemical Modeling. Submittal date: 10/21/1999. Submit to RPC URN-0269

DTN: MO9912EBSPWR28.001. Particle Size Data, Water Retention Data, and Hydraulic Conductivity Data for Overton Sand Used in the Water Diversion Model AMR (ANL-EBS-MS-000028 REV 00). Submittal date: 12/02/1999.

8.3.6 EBS Colloids Model (See Section 6.6)

DTN: LA0002SK831352.001. Total Collidal Particles Concentration And Size Distribution In Groundwaters From The Nye County Early Warning Drilling Program. Submittal date: 02/02/2000.

DTN: LA0002SK831352.002. Total Colloidal Particles Concentration And Size Distribution In Groundwaters Around Yucca Mountain. Submittal date: 02/25/2000.

DTN: LA0003NL831352.002. The KD Values of 239PU on Colloids of Hematite, Ca-Montmorillonite and Silica in Natural and Synthetic Groundwater. Submittal date: 03/29/2000.

DTN: LA0005NL831352.001. The KD Values of 243AM on Colloids of Hematite, Montmorillonite and Silica in Natural and Synthetic Groundwater. Submittal date: 05/03/2000. URN-0293.

DTN: LB991200DSTTHC.001. Pore Water Composition And Co2 Partial Pressure Input To Thermal-Hydrological-Chemical (Thc) Simulations: Table 3 Of Amr N0120/U0110, "Drift-Scale Coupled Processes (Drift-Scale Test And Thc Seepage) Models. Submittal date: 03/11/2000.

8.3.7 Chemical Reference Model (See Section 6.7)

No input data from the Technical Database Management System were used in Section 6.7.

8.4 SOFTWARE SOURCES

Lawrence Livermore National Laboratory. 1999. *Software Code: NUFT V3.0s.* V3.0s. STN: 10088-3.0s-00.

Lawrence Livermore National Laboratory. 2000. *Software Routine: CONVERTCOORDS V1.1.* V1.1. STN: 10209-1.1-00.

Lawrence Livermore National Laboratory. 2000. *Software Routine: YMESH V1.53.* V1.53. STN: 10172-1.53-00.

Lawrence Livermore National Laboratory. 2000. *Software Routine: XTOOL V10.1.* V10.1. STN: 10208-10.1-00.

CRWMS M&O. 1999. *Software Code: PHREEQC.* V2.0. STN: 10068-2.0-00.

CRWMS M&O. 1998. *Software Code: EQ3/6.* V7.2b. STN: LLNL:UCRL-MA-110662.